

MEASUREMENT OF THE $e^+e^- \rightarrow \pi^+\pi^-2\pi^0$ AND $e^+e^- \rightarrow \pi^+\pi^-3\pi^0$
CROSS SECTIONS USING INITIAL STATE RADIATION AT
BABAR

KONRAD GRIESSINGER

geboren am 28.02.1984 in Scherzingen (Schweiz)

Mainz, 08.12.2016

Dissertation

zur Erlangung des Grades „Doktor der Naturwissenschaften“
am Fachbereich Physik, Mathematik und Informatik
der Johannes Gutenberg-Universität Mainz

Konrad Grißinger: Measurement of the $e^+e^- \rightarrow \pi^+\pi^-2\pi^0$ and
 $e^+e^- \rightarrow \pi^+\pi^-3\pi^0$ Cross Sections Using Initial State Radiation at
BABAR

Datum der mündlichen Prüfung: 29.03.2017

Is justified true belief knowledge? – Edmund L. Gettier

SUMMARY

The muon anomalous magnetic moment $g_\mu - 2$ is one of the most precisely measured quantities in particle physics. Yet, its measured value deviates from the prediction by the Standard Model of Particle Physics by approximately three standard deviations.

The cross section of the process $e^+e^- \rightarrow \pi^+\pi^-2\pi^0$ is one of the main contributors to the uncertainty of the Standard Model prediction of $g_\mu - 2$. Therefore an improved understanding of this process is fundamental to gaining closer insight into the $g_\mu - 2$ puzzle.

The cross section $e^+e^- \rightarrow \pi^+\pi^-3\pi^0$ has never been measured accurately, yielding another uncertainty of $g_\mu - 2$. This also hinders the analysis of $e^+e^- \rightarrow \pi^+\pi^-2\pi^0$ to which it presents a background.

This thesis closes both gaps by analyzing the channels $e^+e^- \rightarrow \pi^+\pi^-2\pi^0$ and $e^+e^- \rightarrow \pi^+\pi^-3\pi^0$.

The analyses are performed on data taken at the *BABAR* experiment, which operated at SLAC National Accelerator Laboratory between 1999 and 2008. It gathered a total integrated luminosity of approximately 500 fb^{-1} at center-of-mass energies around 10.58 GeV , the rest mass of the $Y(4S)$ resonance.

This data is used in the present thesis work via the initial state radiation technique, which enables cross section measurements over a continuous energy range. In comparison to energy scan experiments, this results in small and consistent systematic uncertainties over the full range. Due to the extremely high luminosity, ISR processes, even though suppressed by the fine-structure constant α , are produced in large numbers, leading to small statistical uncertainties.

This effects the opportunity of measuring the aforementioned cross sections with unprecedented accuracy. At the inception of this thesis, the goal was a systematic accuracy of less than 5 % for the analysis of the process $e^+e^- \rightarrow \pi^+\pi^-2\pi^0$ in its peak region. The final result achieves 3.1 % accuracy, considerably exceeding the original goal. The analysis of the channel $e^+e^- \rightarrow \pi^+\pi^-3\pi^0$ was not planned at the beginning, and now 25 to 32 % accuracy have been reached. In both cases the contribution to $g_\mu - 2$ is evaluated as well as the effect on the running of the fine-structure constant $\Delta\alpha$. Furthermore, their intermediate resonance structure is studied, yielding among other results the previously unmeasured branching fractions for the processes $J/\psi \rightarrow \pi^+\pi^-2\pi^0$ and $J/\psi \rightarrow \pi^+\pi^-3\pi^0$.

ZUSAMMENFASSUNG

Das anomale magnetische Moment des Myons, $g_\mu - 2$, ist eine der am genauesten gemessenen Größen der Teilchenphysik. Jedoch weicht sein gemessener Wert um etwa drei Standardabweichungen von der Vorhersage des Standardmodells der Teilchenphysik ab.

Der Wirkungsquerschnitt des Prozesses $e^+e^- \rightarrow \pi^+\pi^-2\pi^0$ ist einer der Hauptbeiträge zur Unsicherheit der Standardmodellvorhersage von $g_\mu - 2$. Daher ist ein verbessertes Verständnis dieses Prozesses essentiell um nähere Erkenntnis über $g_\mu - 2$ zu gewinnen.

Der Wirkungsquerschnitt des Prozesses $e^+e^- \rightarrow \pi^+\pi^-3\pi^0$ ist noch nie genau vermessen worden, woraus sich eine weitere Unsicherheit von $g_\mu - 2$ ergibt. Zusätzlich stellt dies ein Hindernis für die Analyse von $e^+e^- \rightarrow \pi^+\pi^-2\pi^0$ dar, wozu er einen Untergrund beisteuert.

Durch diese Dissertation werden beide Lücken geschlossen, da sowohl $e^+e^- \rightarrow \pi^+\pi^-2\pi^0$ als auch $e^+e^- \rightarrow \pi^+\pi^-3\pi^0$ analysiert sind.

Die Analysen werden auf Grundlage der Daten des *BABAR*-Experiments durchgeführt, welches zwischen 1999 und 2008 am SLAC National Accelerator Laboratory stattfand. Es sammelte insgesamt eine integrierte Luminosität von etwa 500 fb^{-1} bei Schwerpunktenenergien um 10.58 GeV , der Ruhemasse der $Y(4S)$ -Resonanz.

In dieser Arbeit werden die Daten mittels der ISR-Technik verwendet, welche Wirkungsquerschnittsmessungen über ein stetiges Energieintervall ermöglicht, ohne Veränderung der Beschleunigerparameter. Im Vergleich zu Scan-Experimenten ergeben sich daraus kleine und konsistente systematische Unsicherheiten über den gesamten Energiebereich. Auf Grund der extrem hohen Luminosität werden ISR-Ereignisse, trotz ihrer Unterdrückung um die Feinstrukturkonstante α , in sehr großer Zahl produziert, was zu kleinen statistischen Unsicherheiten führt.

Daraus entsteht die Möglichkeit, Wirkungsquerschnitte mit bisher unerreichter Präzision zu bestimmen. Zu Beginn dieser Dissertation bestand das Ziel darin, in der Analyse des Prozesses $e^+e^- \rightarrow \pi^+\pi^-2\pi^0$ eine systematische Unsicherheit von weniger als 5 % in dessen Peakbereich zu erreichen. Im Endergebnis werden 3.1 % verwirklicht, was das ursprüngliche Ziel deutlich übertrifft. Die Analyse des Kanals $e^+e^- \rightarrow \pi^+\pi^-3\pi^0$ war am Anfang der Arbeit nicht geplant und inzwischen wird eine Präzision von 25 bis 32 % erreicht. In beiden Fällen wird der Beitrag zu $g_\mu - 2$ ermittelt, sowie der Einfluss auf das Laufen der Feinstrukturkonstante $\Delta\alpha$. Desweiteren werden ihre Zwischenresonanzen untersucht, unter anderem die bislang ungemessenen Verzweigungsverhältnisse von $J/\psi \rightarrow \pi^+\pi^-2\pi^0$ und $J/\psi \rightarrow \pi^+\pi^-3\pi^0$.

CONTENTS

1	INTRODUCTION	3
1.1	The g -Factor	6
1.2	Experimental Measurement of $g_\mu - 2$	6
1.2.1	Essentials of Spin Dynamics	7
1.2.2	The E821 Experiment	8
2	THEORETICAL PREDICTION OF g AND α	13
2.1	QED Contributions	14
2.2	Electroweak Contributions	16
2.3	Leading Order Hadronic Vacuum Polarization	17
2.3.1	From the Optical Theorem to Vacuum Polarization	18
2.3.2	Derivation of the Dispersion Relation	20
2.3.3	Connection of a_ℓ to the Matrix Element	23
2.3.4	Schwinger's Result	24
2.3.5	Putting the Puzzle Together	25
2.3.6	Hadronic Cross Sections	28
2.3.7	Final State Rad. Correction to $g - 2$	32
2.3.8	Resulting Value of $a_\mu^{\text{had,LO}}$	34
2.4	Higher Order Hadronic Vacuum Polarization	35
2.5	Light by Light Scattering	35
2.6	Summary of Contributions to a_μ	37
2.7	Outlook on a_μ	37
2.8	Running of the Fine-Structure Constant α	39
3	THE ISR TECHNIQUE FOR CROSS SECTIONS	43
3.1	Radiative Return	43
4	THE BABAR EXPERIMENT	47
4.1	Introduction: SLAC, PEP-II, and BABAR	47
4.2	Silicon Vertex Tracker	50
4.3	Drift Chamber	50
4.4	Detector of Internally Reflected Cherenkov Light	55
4.5	Electromagnetic Calorimeter	56
4.6	Instrumented Flux Return	59
4.7	Trigger and Data Acquisition	60
5	GENERAL PROCEDURE & DATA SET	63
5.1	General Analysis Procedure	63
5.2	Data Set and Simulation Samples	64
5.3	Preselection	66
5.4	Track and Photon Requirements	67
5.5	Kinematic Fit	68

5.6	Particle Identification Selectors	73
5.7	Common Event Selection	74
5.7.1	Kinematic Requirements	75
5.7.2	Background Reduction via PID	75
6	THE CHANNEL $\pi^+\pi^-3\pi^0\gamma_{\text{ISR}}$	83
6.1	Event Selection	85
6.2	Background Subtraction	86
6.2.1	Continuum Background	86
6.2.2	Sideband Subtraction	89
6.3	Acceptance and Efficiency	92
6.3.1	Correction of Track and π^0 Detection	96
6.4	Relative Fractions of $\omega 2\pi^0\gamma$ and $\eta\pi^+\pi^-\gamma$	96
6.5	Cross Section	108
6.6	Systematic Uncertainties of the Cross Section	109
6.7	J/ψ Branching Fraction	109
7	THE CHANNEL $\pi^+\pi^-2\pi^0\gamma_{\text{ISR}}$	113
7.1	Event Selection	113
7.2	Background Subtraction	117
7.2.1	Continuum Background	117
7.2.2	$e^+e^- \rightarrow \tau^+\tau^-(\gamma)$	123
7.2.3	$e^+e^- \rightarrow \mu^+\mu^-2\pi^0$	124
7.2.4	ISR Background Channels	126
7.2.5	ISR Background Subtraction Uncertainty	131
7.3	Precision Efficiency Corrections and Mass Resolution	135
7.3.1	Correction of Track, γ and π^0 Detection	135
7.3.2	The $\chi^2_{4\pi}$ Requirement	136
7.3.3	Dependence on Resonance Weight	139
7.3.4	Unfolding the Mass Resolution	143
7.4	Radiative Corrections	151
7.4.1	NLO ISR Corrections	151
7.4.2	FSR Correction of the Mass Spectrum	152
7.5	The Resulting Cross Section	157
7.6	Intermediate Resonances	160
7.6.1	Production of $\rho^0 f_0$	160
7.6.2	Production of $\rho^+\rho^-$	162
7.6.3	Production of $\omega\pi^0$	170
7.6.4	J/ψ Branching Fraction	170
8	CALCULATION OF a_μ AND $\Delta\alpha$	177
A	KINEMATIC CONSIDERATIONS	185
A.1	Equivalence $1 - \frac{s'}{s} = \frac{2E_\gamma^*}{\sqrt{s}}$	185
A.2	Equivalence of Restricting the ISR Photon Energy and the Invariant Hadronic Mass	185

B	INTERMEDIATE CALCULATIONS IN THE DERIVATION OF a_ℓ	187
B.1	Replacing the Vacuum Polarization Tensor by the Amplitude	187
B.2	Extracting the Kinematic Factor $s + 2m^2$	188
B.3	Including the Vacuum Polarization Amplitude into the Photon Propagator	189
C	SPECIFICS OF THE ANALYSES	191
C.1	Calculation of Uncertainties in Background-reduced Proportions	191
C.2	μ -PID Correction	192
C.3	Additional Plots on the Continuum Subtraction from the Final State $\pi^+\pi^-2\pi^0\gamma$	193
C.4	Efficiency Corrections	196
C.4.1	Tracking	196
C.4.2	γ Efficiency Correction	196
C.4.3	π^0 Efficiency Correction	197
C.5	$e^+e^- \rightarrow \pi^+\pi^-2\pi^0$ Cross Section Table	200
D	NUMERICAL STABILITY OF THE KERNEL FUNCTION	205
E	COPYRIGHT	207
E.1	Creative Commons Legal Code	207
E.1.1	Attribution-NonCommercial-ShareAlike 4.0 International	207

PREAMBLE

In 1935 a strongly interacting particle was famously predicted by Hideki Yukawa at a mass of approximately $100 \text{ MeV}/c^2$ [1]. One year later, Carl D. Anderson and Seth Neddermeyer found evidence [2] for a particle in this mass range in cosmic radiation data. Their colleagues' conclusion that the *mesotron* exists [3] was therefore justified, and from today's perspective this can be accepted as true, although it is now called π *meson* or *pion*. Hence the belief that the pion exists was true and justified already in 1936, but did Anderson and Neddermeyer or their colleagues *know* that it exists?

Knowledge is the ultimate goal of science. Unfortunately certainty is unattainable in physics, being an empirical science. Therefore philosophers have tried for millenia to form a proper definition of knowledge. The classical definition, *justified true belief*, dates back to Plato, despite his own scepticism. A mere half-century ago Edmund Gettier published his essay "Is Justified True Belief Knowledge?" [4], wherein he describes several cases in which a person is justified in their belief and this belief turns out to be true, yet it would never be considered knowledge. To demonstrate, his *Case I* can be summarized as follows: Smith is justified in believing that Jones will get a promotion and, independently, that Jones has ten coins in his pocket. Thus he is justified in believing that the person who gets the promotion has ten coins in his pocket. This turns out to be true, yet only because Smith himself surprisingly gets the job and has ten coins in his pocket.

This example is strikingly similar to many cases in research, maybe most prominently the alleged discovery of the pion. Nowadays we are reasonably sure that the pion exists, thus the conclusion was correct, although Anderson and Neddermeyer actually observed muons. Despite some criticism of Gettier's examples, his essay triggered a debate, still raging today, on how to improve the definition of knowledge. In this sense, the quest to achieve insight and hence knowledge for the natural sciences hinges on the justification. Our beliefs are parametrized by theories or models. And while we can never be certain that a statement is indeed true, we can assess whether the proposed theory is justified.

Although for a data analyst this raises the question of which significance is sufficient to claim proof, the more fundamental problem is *how* to justify a proposition. Repeatedly questioning the validity of the alleged proof or reason for a proposed theory leads to Agrippa's trilemma: the possibilities of providing proof are

- Circular reasoning,
- Axiom/Postulate/Dogma,
- Infinite regress.

Circular reasoning can be reduced to “A is true because A is true” (usually obscured by several intermediate steps) and thus yields no further information.

Postulates or axioms are used as a starting point for some models. While a particular model may be useful to explain certain effects, no insight beyond the axiom can be achieved.

Infinite regress is the mechanism that drives new insight in fundamental research. (In combination with falsifiability of said theories.) In the process of continued inquiry the questions become increasingly general and the explanations encompass a wider range of scenarios. This can be illustrated by starting with just about any curiosity about nature, e.g. the renowned question “why is the sky blue?” The obvious answer seems to be that the characteristics of Rayleigh (or more generally Mie) scattering lead to the effect, but a perceptive counterpart might demand an explanation of this theory. Deriving the scattering formula from Maxwell’s equations will carry the argument one step forward, but pursuing this path a little further – passing QED-town and Electroweak Unification City along the way – one eventually ends up at the Standard Model of Particle Physics, which additionally encompasses Quantum Chromodynamics. This is also the point (combined with Gravitation), where almost all inquiries of this type come to an end at the moment.

The Standard Model is incredibly comprehensive in its explanatory power, but coming back to the original question: is it justified to believe this model and thus its implications? In order to examine this, the Standard Model (like any other theory) is subjected to every conceivable test. It may not be possible to prove that the model is correct (or true) but it can be falsified by comparing its predictions with the observations found in nature. The most compelling evidence for deviation from the Standard Model in particle physics at the moment stems from the anomaly of the muon magnetic moment $g_\mu - 2$. The SM prediction is fueled by experimentally measured hadronic cross sections, of which two of the most important channels for improving the precision of the $g_\mu - 2$ calculation are $e^+e^- \rightarrow \pi^+\pi^-\pi^0\pi^0$ and $e^+e^- \rightarrow \pi^+\pi^-\pi^0\pi^0\pi^0$.

This is also the main topic of the presented thesis: the analysis of cross sections composed of four and five times Yukawa’s particle.

INTRODUCTION

According to the modern understanding, four fundamental forces exist in nature, two well known in everyday life – the electromagnetic and gravitational forces – and two occurring at microscopic level – the weak and strong nuclear forces. Without the latter two forces, matter as we know it could not exist, since the electrostatic repulsion between two protons is much stronger than their gravitational attraction, such that every atomic nucleus would fall apart immediately. The strong force is responsible for keeping matter stable on the nuclear scale, since it binds nucleons together at short distances, thus counteracting the electromagnetic repulsion of the protons in the nucleus. This force is a consequence of the interaction between the quarks within the nucleon, which is described by the theory of Quantum Chromodynamics (QCD). The weak interaction is responsible for effects like the nuclear β -decay, where a proton turns into a neutron or vice versa. Beginning in 1960, it was discovered that electromagnetic and weak force both can be described by the same (“electroweak”) theory [5–8]. Together with QCD, this forms the fundamental theory at the core of the Standard Model of Particle Physics, whose constituents are shown in Fig. 1.

In the Standard Model (SM), all forces are transmitted by mediator particles. In the case of QCD, the mediator particle is the gluon, discovered in 1978 at DESY [9]. Since the strong interaction applies only to color-charged objects, gluons exist in eight different states by combination of the three essential colors red, blue and green. The mediator of the electromagnetic interaction is the photon, while the weak interaction is transmitted by the two electrically charged W^\pm and the neutral Z^0 particles, first discovered in 1983 [10–14]. All these particles – the gluon, photon, W^\pm and Z^0 – make up one category of the particles found in the Standard Model, the interaction particles or gauge bosons.

There exists yet another category, consisting of matter particles, named quarks and leptons. The six known quarks are subject to all forces of the Standard Model: electromagnetic, weak and strong. They are organized in three “generations” of two quarks each with very different masses. Three of the quarks have an electrical charge of $+2e/3$, while the rest has $-e/3$. The six leptons, on the other hand, only interact weakly and electromagnetically, and are also grouped into three generations, but half is charged with $-e$, while the rest is electrically neutral.

The distinction between matter and interaction particles coincides with the categorization by particle spin, the intrinsic angular

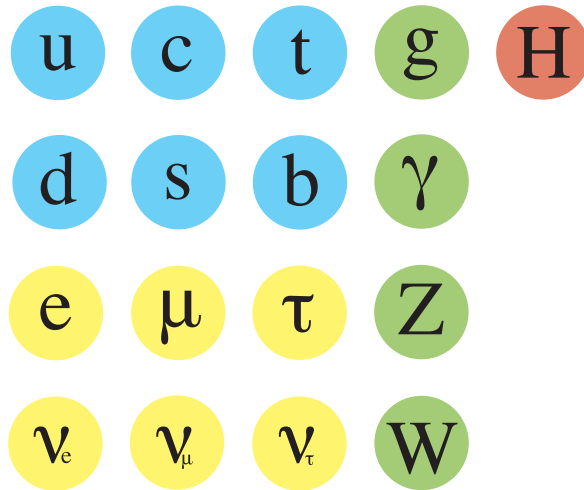


Figure 1.: Schematic listing of the particles in the Standard Model: Quarks in blue, leptons in yellow, gauge bosons in green and the Higgs boson in red.

momentum. All matter particles are fermions (with spin $1/2$), while interaction particles have integer spin, making them bosons.

The last particle necessary to complete the Standard Model is the Higgs boson. It plays a somewhat different role than the other bosons, as it is not a gauge boson, since its symmetry is spontaneously broken. The Higgs mechanism enables particles to have mass and especially explains why the W^\pm and Z^0 bosons are massive, yet photons and gluons are massless. The existence of the Higgs boson is a byproduct of this mechanism.

Incorporating solely the aforementioned particles and forces, the Standard Model of Particle Physics is astonishingly successful in predicting physical observables. The recent results of the discovery of a particle widely suspected to be the Higgs boson [15, 16] and the branching fraction of $B_s^0 \rightarrow \mu^+ \mu^-$ [17, 18] show how well it describes our world. Apart from various astrophysical phenomena, there are only very few tests left in particle physics which show a discrepancy between the direct measurement and the Standard Model prediction. The most important instance at the moment is the anomaly of the gyromagnetic factor g (introduced in Sec. 1.1) of the muon. In combination with the astrophysical observations, this indicates the possible necessity of extensions to the theory as it is known today.

In the particular case of the muon anomalous magnetic moment $g_\mu - 2$, the direct measurement differs from the SM prediction by 3σ (see Sec. 2.6), thus representing evidence of a deviation between

theory and experiment.¹ Many mechanisms have been suggested to explain this discrepancy, spanning a wide field from anomalous couplings [19], an additional boson [20–22], supersymmetric extensions of the Standard Model [23, 24], to the possible existence of at least one leptoquark [25–27]. Therefore it is of utmost importance to improve the significance of this deviation in order to determine whether a fluctuation or an actual physical effect is seen.

The most precise direct measurement was performed at the Brookhaven National Laboratory in experiment E821. It shall be described briefly in Sec. 1.2.

For the SM prediction, experimental input is needed to reach a similar level of accuracy. There are several contributions to the SM prediction of $g - 2$: QED, weak interaction, and the hadronic part, which is in focus here. The QED and weak parts can be calculated term by term in perturbative series as sketched in Sec. 2.1 and Sec. 2.2.

For the calculation of the hadronic contribution a perturbation ansatz only works for high energies, due to the running coupling α_s . For the overwhelmingly important low to medium energy range, a dispersion relation in connection with the optical theorem is used to relate $g - 2$ to the corresponding cross section, which is derived in Sec. 2.3.

Therefore, it is essential to have a precise measurement of all relevant individual hadronic channels.

Higher order hadronic contributions are summarized in Secs. 2.4 (higher order vacuum polarization) and 2.5 (light-by-light scattering). Both also require experimental input to reach satisfactory precision. A summary of all contributions to $g_\mu - 2$ is given in Sec. 2.6. Furthermore, the effect of vacuum polarization on the fine-structure constant α is discussed in Sec. 2.8.

Initial State Radiation – presented in Ch. 3 – is exploited to measure cross sections over a wide energy range at fixed energy colliders like *BABAR*.

Following this rather theoretical groundwork, the experimental and analytical part is structured as follows:

- Outline of the *BABAR* experiment and especially the detector in Ch. 4
- Summary of the data set collected at *BABAR* and the event selection common to the $\pi^+\pi^-2\pi^0\gamma$ and the $\pi^+\pi^-3\pi^0\gamma$ analysis in Ch. 5
- Analysis of the cross section $e^+e^- \rightarrow \pi^+\pi^-3\pi^0$ in Ch. 6

¹ It should be noted that considering the entirety of observables measured to test the SM, predominantly good agreement with the SM is seen, such that merely a minuscule hint at a deficiency in the Standard Model remains.

- Analysis of the cross section $e^+e^- \rightarrow \pi^+\pi^-2\pi^0$ in Ch. 7
- Numerical method to compute the contribution to $g - 2$ given a cross section developed and applied to both measured channels in Ch. 8
- Followed by a brief conclusion.

1.1 THE g -FACTOR

The magnetic moment $\vec{\mu}$ of an object is determined by its potential energy due to an external magnetic field \vec{B} [28]:

$$E_{\text{pot}} = -\vec{\mu} \cdot \vec{B}. \quad (1)$$

A charged, point-like spin- $1/2$ particle (also called Dirac particle) possesses a magnetic moment given by [29]

$$\vec{\mu} = g \cdot \frac{q}{2m} \vec{s}, \quad (2)$$

where q is its charge, m its mass and \vec{s} its spin vector. The proportionality factor g is also a fundamental property of the particle and must be known precisely to calculate the magnitude of the magnetic moment. For leptons, Dirac theory [30, 31] predicts $g = 2$, yet this is shown to be inaccurate via higher order Standard Model calculations in Sec. 2 and by the experimental means summarized in the following sections.

1.2 EXPERIMENTAL MEASUREMENT OF $g_\mu - 2$

In the most precise experimental determinations of $g_\mu - 2$, the particle spin's precession in a magnetic field is measured. This requires a method to detect the direction of a particle's spin. In the case of the muon, the correlation between the direction into which the positron is ejected and the muon spin direction in the decay $\mu^+ \rightarrow e^+ \nu_e \bar{\nu}_\mu$ facilitates a means of measurement.

Overview of Existing Experimental Measurements

Several experiments have been performed to measure the value of $a_\mu := g_\mu/2 - 1$. They are listed in Tab. 1, which also shows how the precision of the succeeding experiments has improved due to more sophisticated setups. In the following, we will focus on the most recent experiment, E821, which was performed at Brookhaven National Laboratory, while employing the same general technique as the preceding experiments at CERN.

Table 1.: Results with uncertainties of existing a_μ measurements.

Experiment	$a_\mu \times 10^{11}$	Precision (ppm)
CERN I [32]	114500000 ± 2200000	4300
CERN II [33]	116616000 ± 31000	270
CERN III [34]	116592400 ± 850	7.3
BNL E821 [35]	116592080 ± 63	0.5

1.2.1 Essentials of Spin Dynamics

Charged particles with a velocity perpendicular to a magnetic field move on circular orbits with the angular cyclotron frequency

$$\vec{\omega}_c = -\frac{q\vec{B}}{\gamma m}, \quad (3)$$

where q is the particle charge, m its mass, and γ the relativistic Lorentz factor. During this motion their magnetic moment and spin undergo precession around the direction of the magnetic field. The spin precession frequency is given by Larmor and Thomas precession [28] as

$$\vec{\omega}_s = -\left(\frac{g-2}{2} + \frac{1}{\gamma}\right)\frac{q\vec{B}}{m}, \quad (4)$$

with the gyromagnetic factor g . Hence, the ‘‘anomaly’’ given by the difference of precession and motion frequency

$$\vec{\omega}_a = \vec{\omega}_s - \vec{\omega}_c = -\frac{g-2}{2}\frac{q\vec{B}}{m} \quad (5)$$

is directly proportional to the anomaly of the gyromagnetic factor g defined as $a \equiv \frac{g-2}{2}$. If an additional electric field is present (also perpendicular to the particle velocity $\vec{v} = c\vec{\beta}$), the ‘‘anomalous frequency’’ is given by the Bargmann-Michel-Telegdi (BMT) equation [28, 36]

$$\vec{\omega}_a = -\frac{q}{m}\left(a\vec{B} - \left[a - \frac{1}{\gamma^2 - 1}\right]\frac{\vec{\beta} \times \vec{E}}{c}\right). \quad (6)$$

The second contribution, dependent on the electric field, can be minimized by choosing the particle velocity such that $\gamma = \sqrt{1 + 1/a}$. For the important case of the muon, this results in $\gamma \approx 29.3$, corresponding to the ‘‘magic’’ particle momentum² of approximately 3.094 GeV/c.

Knowing the BMT equation, determining $g - 2$ of the muon becomes a question of measuring the spin direction after precession.

² The idea of the ‘‘magic’’ γ /momentum first appears in the proposal for the CERN III $g_\mu - 2$ experiment [37], which drastically improved precision to 7 ppm [34].

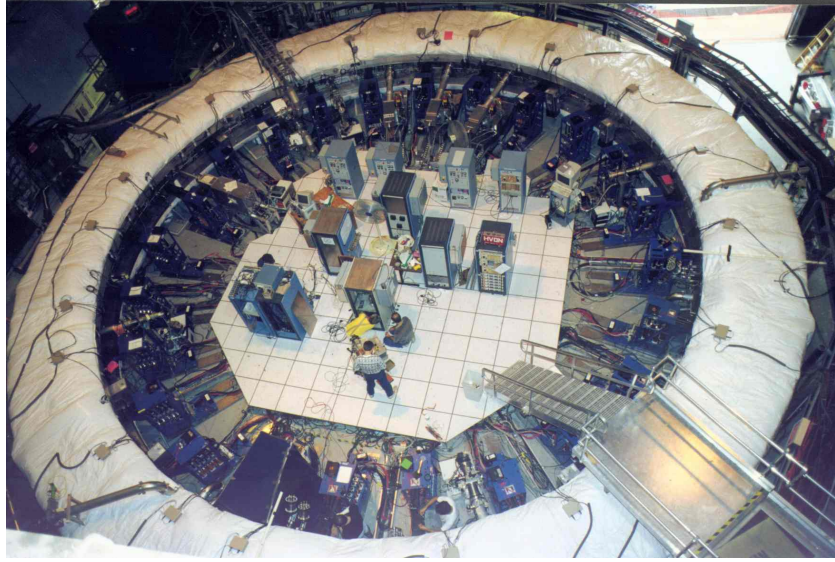


Figure 2.: Bird's-eye view of the E821 experiment at Brookhaven National Laboratory from Ref. [39]. ©The Royal Swedish Academy of Sciences. Reproduced by permission of IOP Publishing. All rights reserved.

For this purpose, it is observed that in the μ rest frame the direction of motion of the positron in the decay

$$\mu^+ \rightarrow e^+ \nu_e \bar{\nu}_\mu \quad (7)$$

is predicted to be correlated to the direction of the muon spin due to conservation of angular momentum and lepton number. (Likewise for the charge-conjugated process.) The decay probability P as a function of the angle θ^* between the muon spin direction and the positron momentum in the μ rest frame can be parametrized [38] as

$$\frac{dP(\theta^*)}{d\cos(\theta^*)} \propto 1 + \kappa \cos(\theta^*), \quad (8)$$

with a constant kinematic factor κ . Hence determining the most probable decay positron direction for a muon orbiting in an electromagnetic field is equivalent to measuring the muon $g - 2$.

1.2.2 The E821 Experiment

The concept outlined above has been realized most recently by the E821 experiment at Brookhaven National Laboratory (BNL), pictured in Fig. 2. As schematically illustrated in Fig. 3, in the first step, protons are accelerated to 24 GeV/c and collide with a fixed nickel target. At this point, pions moving in the same direction as the protons are produced. These enter a dedicated pion-decay channel, where, due to their rather short lifetime of about 2.6×10^{-8} s, most pions decay in flight. The dominant decay $\pi^+ \rightarrow \mu^+ \nu_\mu$ includes a

neutrino, so that its spin constellation is fixed, as the neutrino is always left-handed. Therefore, a polarized muon beam is produced, which is filtered to contain only muons of the “magic” momentum 3.094 GeV/c and then directed into a storage ring. While orbiting, the muons decay into positrons and neutrinos, which leave the storage ring due to the excess momentum from the decay. The exiting positrons are counted by calorimeters inside the storage ring as seen in Fig. 4, which record the time and position of the particle. The count rate distribution in Fig. 5 can be fitted with a function [40] of the form

$$N(t) = N_0 \exp(-t/\gamma\tau_\mu) (1 - A \cos(\omega_a t + \phi)) , \quad (9)$$

thereby extracting the value of the “anomalous frequency” ω_a (the fit parameters N_0 , A , ϕ are of no concern and the values of the muon lifetime τ_μ and the relativistic Lorentz factor γ are precisely known). The anomaly of the muon gyromagnetic factor can then be calculated as

$$a_\mu = \frac{\omega_a}{\omega_L - \omega_a} , \quad (10)$$

where $\omega_L = -\frac{g}{2} \frac{qB}{m}$ is the Larmor frequency, which is measured independently [41]. According to the original publication [35] the result is

$$a_\mu(\text{exp}) = (116592080 \pm 54 \pm 33) \times 10^{-11} , \quad (11)$$

where the first uncertainty is statistical and the second systematic.³ The Particle Data Group rescales the value to account for an improved Larmor frequency measurement (relative to the proton) [42] and obtains [43]

$$a_\mu(\text{exp}) = (116592089 \pm 54 \pm 33) \times 10^{-11} . \quad (12)$$

As shown in Tab. 1, the result from the E821 experiment improves the precision of the experimental a_μ value by more than an order of magnitude. In the future, two experiments aim to improve the precision by another factor four: the Muon $g - 2$ collaboration at Fermilab [44] using a similar approach as before and the $g - 2$ /EDM collaboration at J-PARC using a completely new concept [45].

³ In the calculation of the uncertainties the effect of a possible electric dipole moment is considered (by taking into account its current limits), which would distort the comparison between theory and experiment. The effect is found to be negligible.

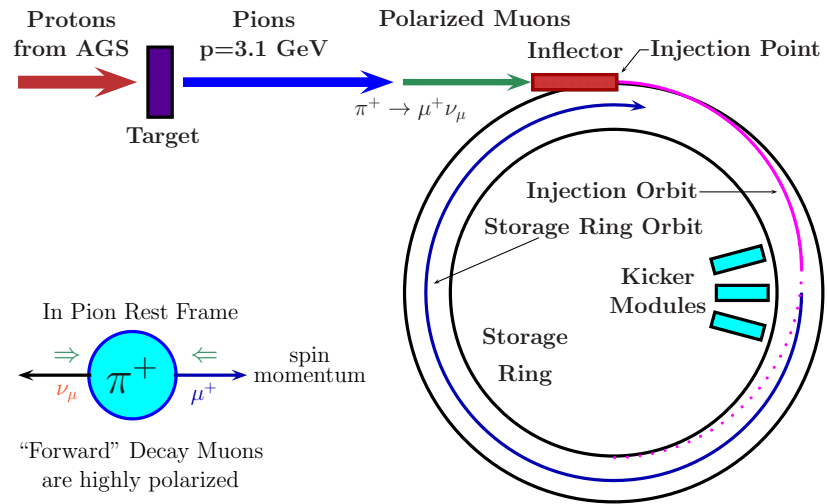


Figure 3.: Schematic representation of the E821 experiment from π^+ production to μ^+ decay. Reprinted from Ref. [46], ©2009, with permission from Elsevier.

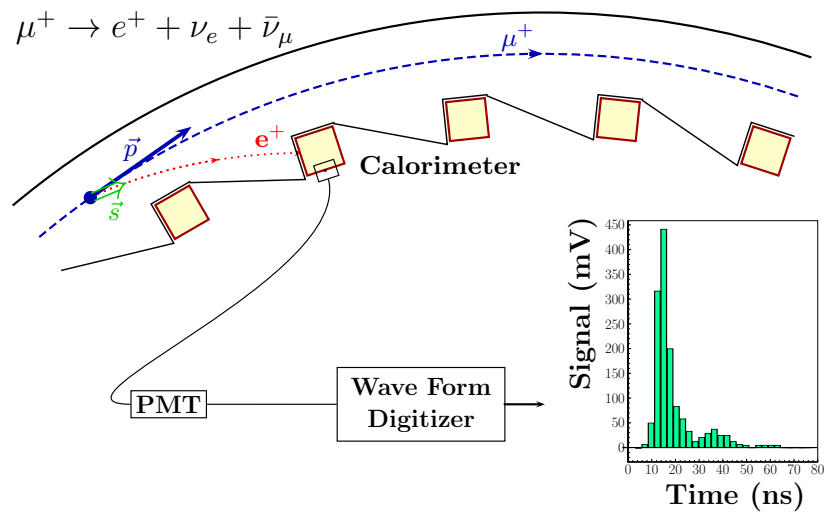


Figure 4.: The calorimeter setup used in the E821 experiment for decay counting. Reprinted from Ref. [46], ©2009, with permission from Elsevier.

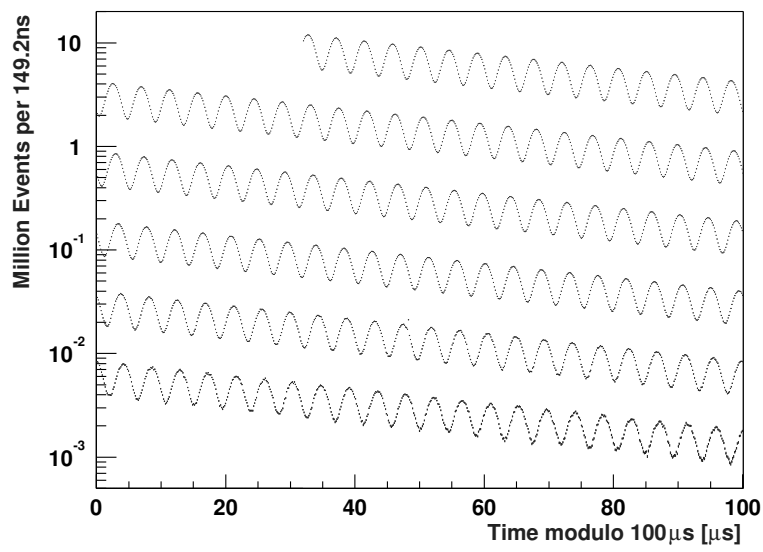


Figure 5.: Damped oscillations in the decay rate measured by the E821 experiment. Reprinted with permission from Ref. [35], ©2006 by the American Physical Society.

THEORETICAL PREDICTION OF g AND α

In this chapter the theoretical predictions of the anomalous muon magnetic moment and the running of the fine-structure constant are introduced. First, the contributions to $g - 2$ from QED and electroweak processes are summarized, followed by the connection between hadronic cross sections and the anomalous muon magnetic moment is proven. Finally, the same type of relation is derived for the running of the fine-structure constant.

In the Standard Model the interaction of matter with a force is mediated by a force carrier, such as the photon for the electromagnetic interaction. Therefore, the coupling g_ℓ (introduced in Sec. 1.1) between an external magnetic field and the lepton spin is determined by the combination of all possible processes between a lepton and a photon. The tree diagram shown in Fig. 6 yields also the result of Dirac theory [30, 31]: $g_\ell^{\text{Dirac}} = 2$. To get the complete value of g_ℓ , the single vertex in Fig. 6 has to be replaced by a “blob” containing all possible intermediate processes in the Standard Model from electromagnetic, weak and strong interaction. Hence, the anomalous gyromagnetic factor g_ℓ can be decomposed into

$$\frac{g_\ell^{\text{SM}} - 2}{2} =: a_\ell^{\text{SM}} = a_\ell^{\text{QED}} + a_\ell^{\text{weak}} + a_\ell^{\text{hadronic}}. \quad (13)$$

The QED and weak parts are evaluated perturbatively as summarized in Sec. 2.1 and Sec. 2.2, respectively, while the hadronic contribution has to be assessed using a semi-phenomenological approach derived in Sec. 2.3 to achieve comparable precision.

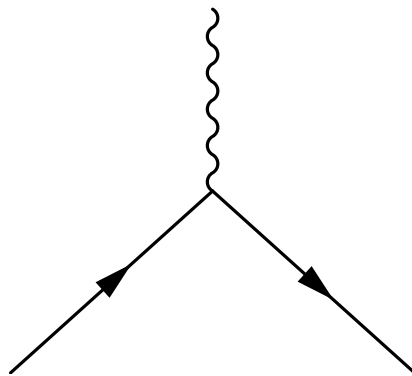


Figure 6.: Feynman diagram of the tree level interaction.¹

¹ Here and in the following Feynman diagrams, curled lines indicate photons, straight solid lines leptons, and straight dashed lines W or Z bosons.

2.1 QED CONTRIBUTIONS

Since the QED coupling is small – $\alpha \approx \frac{1}{137.036}$ – electromagnetic effects can generally be computed with high precision as perturbative expansions, e.g. in $\frac{\alpha}{\pi}$. For $g = 2$, the first (one-loop) summand of the series is Schwinger’s famous result calculated in 1947 [47, 48] and derived in Sec. 2.3.4, which amounts to $\frac{1}{2} \frac{\alpha}{\pi} \approx 1.161 \times 10^{-3}$.

At the two-loop level, the systematic process of evaluating higher orders was begun by Karplus and Kroll [49], who derived the part universal to all lepton flavors (note the important correction calculated by Sommerfield [50, 51] and Petermann [52, 53]). It was continued by Suura, Wichmann [54] and Petermann [55] with the mass-dependent contribution depicted in Fig. 7a (for a different lepton flavor in the internal loop than in the external legs). For the muon, the result [56] is

$$\begin{aligned}
a_{\mu}^{\text{QED}(4)} &= \left(\frac{\alpha}{\pi}\right)^2 \left(\frac{197}{144} + \frac{\pi^2}{12} + \frac{3}{4} \zeta(3) - \frac{\pi^2}{2} \ln 2 \right. \\
&\quad + \int_0^1 dx \int_0^1 dy \frac{x^2(1-x)y^2(1-y^2/3)}{x^2(1-y^2) + 4 \frac{m_e^2}{m_{\mu}^2} (1-x)} \\
&\quad \left. + \int_0^1 dx \int_0^1 dy \frac{x^2(1-x)y^2(1-y^2/3)}{x^2(1-y^2) + 4 \frac{m_{\tau}^2}{m_{\mu}^2} (1-x)} \right) \\
&= (-0.328 + 1.094 + 7.808 \times 10^{-5}) \left(\frac{\alpha}{\pi}\right)^2 \\
&= 0.765857425(17) \left(\frac{\alpha}{\pi}\right)^2 \\
&= 4.13217628(92) \times 10^{-6},
\end{aligned}$$

where ζ denotes the Riemann zeta function [57, 58] with $\zeta(3) = 1.202\dots$ and m_e , m_{μ} , and m_{τ} are the masses of the electron, muon, and tau, respectively. The arising integrals can be calculated [59, 60] exactly² using dilogarithms [58, 61], such that the uncertainties are exclusively due to the lepton mass ratios. (The numerical values in the intermediate steps are truncated for readability.)

At the three-loop level or sixth order (Fig. 7b), processes involving both other leptons appear, such that the problem becomes even more challenging (beyond the scope of this summary), but is still analytically calculated in terms of polylogarithms [61]. Detailed calculations can be found in Refs. [62–67], which result in

$$a_{\mu}^{\text{QED}(6)} = 24.05050996(32) (\alpha/\pi)^3 = 3.014190246(40) \times 10^{-7}.$$

The complexity and number of diagrams – like the one in Fig. 7c – grows even further at order eight [68–73], such that numerical

² Care has to be exercised in the evaluation of the analytical result at big mass ratios since numerical instabilities arise due to large cancellations.

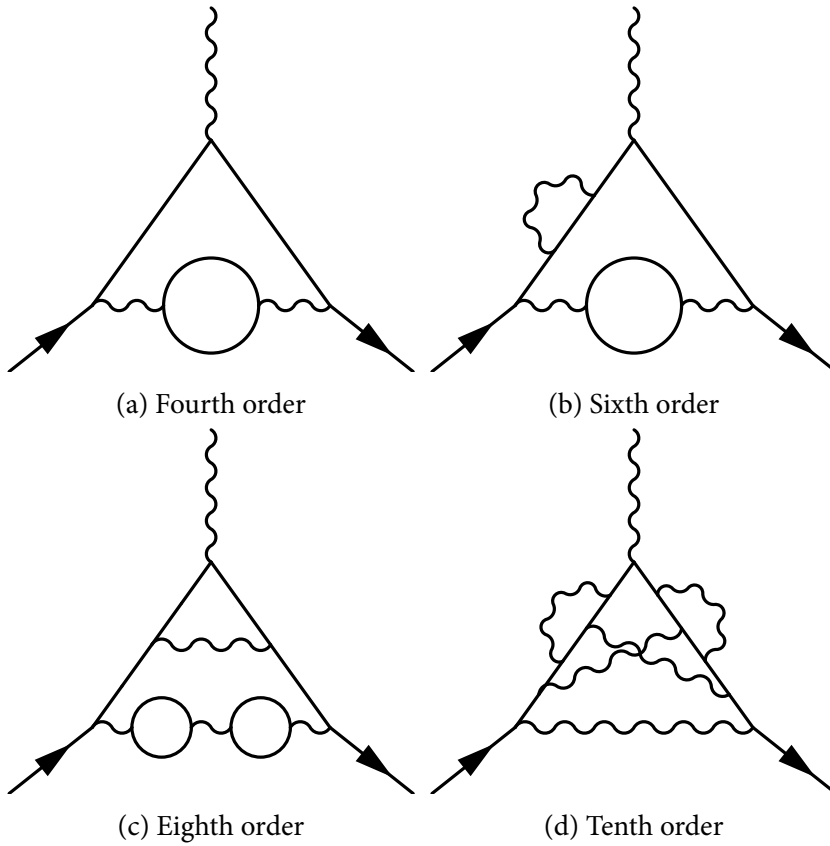


Figure 7: Examples of possible QED processes contributing to $g-2$.

calculations are required as analytic solutions have only been found for certain classes of diagrams [74, 75]. These methods yield

$$a_{\mu}^{\text{QED}(8)} = 130.8796(63)(\alpha/\pi)^4 = 3.810077(183) \times 10^{-9}.$$

To date, the electromagnetic part of $g-2$ has been calculated up to tenth order (Fig. 7d), which contains an impressive 9080 diagrams. As summarized in Refs. [56, 73] and references therein, the result is

$$a_{\mu}^{\text{QED}(10)} = 753.29(104)(\alpha/\pi)^5 = 5.0938(70) \times 10^{-11}.$$

The total QED contribution up to order ten is given by [56]

$$a_{\mu}^{\text{QED}} = 116584718.951(80) \times 10^{-11}.$$

It is noteworthy that although the value of the additional correction applied to $g-2$ appears to be decreasing for rising loop-order k , the coefficient multiplied by $(\alpha/\pi)^k$ keeps increasing due to terms involving large logarithms $\ln \frac{m_{\mu}}{m_{\ell}}$, where m_{ℓ} is the electron or τ mass. Therefore, it has been estimated that the six-loop correction $a_{\mu}^{\text{QED}(12)}$ might be as large as 10^{-12} , possibly exceeding the uncertainty of the current QED calculation.

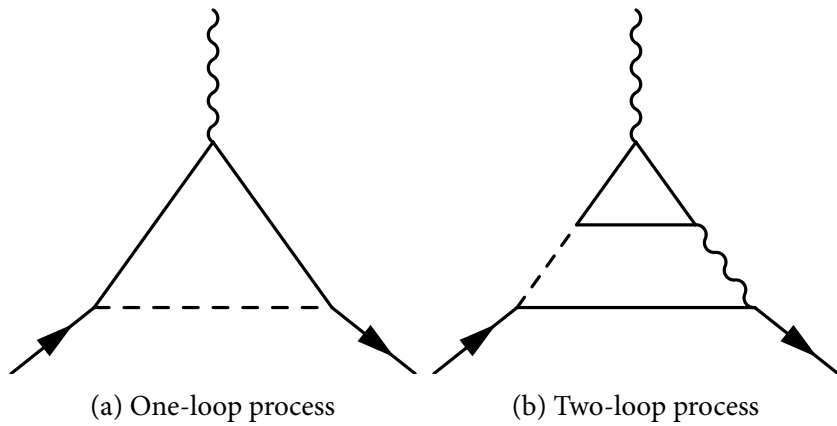


Figure 8.: Examples of electroweak processes contributing to $g - 2$.

2.2 ELECTROWEAK CONTRIBUTIONS

The electroweak part of the Standard Model prediction of $g - 2$ includes all processes containing a W^\pm , Z^0 or Higgs boson (in unitary gauge [76, 77]). Similar to QED, its contribution can be expanded diagram by diagram into a perturbative series³. The one-loop processes – exemplarily shown in Fig. 8a – is calculated [60, 82] to

$$\begin{aligned}
 a_\mu^{\text{EW}(1)} = & \frac{5G_F m_\mu^2}{24\sqrt{2}\pi^2} \left(1 + \frac{1}{5}(1 - 4\sin^2\theta_W)^2 + \mathcal{O}\left(\frac{m_\mu^2}{M_W^2}\right) \right. \\
 & \left. + \mathcal{O}\left(\frac{m_\mu^2}{M_Z^2} \ln\left(\frac{M_Z^2}{m_\mu^2}\right)\right) + \mathcal{O}\left(\frac{m_\mu^2}{M_H^2} \ln\left(\frac{M_H^2}{m_\mu^2}\right)\right) \right), \quad (14)
 \end{aligned}$$

where G_F is the Fermi constant, θ_W the Weinberg angle and M_W , M_Z , and M_H the mass of the W^\pm , Z^0 and Higgs boson, respectively. The complete one-loop contribution can be calculated in closed form as shown in Ref. [83], although the latter three terms in Eq. 14 are negligible as they are suppressed by m_μ^2/M_B^2 (where M_B is the mass of any of the bosons).

There are 1678 two-loop diagrams akin to Fig. 8b, which have been assessed in their entirety in a remarkable calculation [79, 84]. Interestingly, the expected [60] approximate suppression by $\alpha/\pi \approx 1/431$ with respect to the one-loop term is not observed, instead the magnitude is about 20 % of the first order contribution, yet with the opposite sign. The enhancement is again due to large logarithms, in this case of the form $\ln\frac{M_B}{m_\mu}$.

For a long time, evaluating these contributions hinged on the uncertainty of only knowing broad upper and lower bounds for the

³ At the two-loop level and beyond, vacuum polarization contributions involving strong interaction appear, which cannot be calculated perturbatively. These will not be described here since their contribution accounts for only about 10 % of the total electroweak component. They are, however, considered in the results and uncertainties. For detailed discussions see Refs. [78–81].

Higgs mass. After the recent discovery and subsequent mass measurement of a particle theorized to be a Higgs boson, the prediction of the electroweak part of a_μ was updated [85]. At the one-loop level, the result is

$$a_\mu^{\text{EW}(1)} = 194.80(1) \times 10^{-11},$$

while the two-loop correction now yields

$$a_\mu^{\text{EW}(2)} = -41.23(74) \times 10^{-11}.$$

Processes including three or more loops are estimated as

$$a_\mu^{\text{EW}(3+)} = 0.00(20) \times 10^{-11}.$$

This amounts to a global electroweak contribution to a_μ of

$$a_\mu^{\text{EW}} = 153.6(10) \times 10^{-11}$$

with a noteworthy total uncertainty of 1×10^{-11} , which is dominated by the effects of hadronic vacuum polarization.

2.3 LEADING ORDER HADRONIC VACUUM POLARIZATION

The contributions to a_μ from QED and weak interactions can be calculated perturbatively over the whole energy spectrum. This is not possible in the case of the QCD part of a_μ because the running coupling of the strong interaction α_s [38] at low energies is too large to permit sufficiently fast – if any – convergence of the perturbative series [86, 87].

The dominating hadronic contribution consists of two distinct components: hadronic vacuum polarization and light-by-light scattering. The latter is summarized in Sec. 2.5. Hadronic vacuum polarization is further subdivided into a leading order (LO) part and higher order corrections. Since the leading order process is a major motivation for this analysis, it is developed in the following sections, while the higher order effects are summarized in Sec. 2.4.

The low energy region of QCD is dominated by the light hadronic states, but neither perturbative QCD, nor lattice gauge theory, nor chiral perturbation theory reach sufficient precision for the calculation of a_μ^{had} . Instead, a semi-phenomenological approach is taken, where precisely measured hadron production in e^+e^- annihilation is used to evaluate a dispersion integral for a_μ .

At first glance it may seem counterintuitive to use hadronic cross sections produced by one lepton flavor (e) as input for the extraction of the hadronic contribution to the magnetic moment of another lepton flavor (μ). Therefore, this correspondence needs to be proven. On the input side, a corollary of the optical theorem

will be derived, which allows to use cross sections to calculate the scattering amplitude, a universal quantity independent of the initial state of the process. On the output side, a_μ is connected to the scattering amplitude by decomposing the process of a lepton coupling to an electromagnetic field into form factors, which are in turn related to the scattering amplitude.

More specifically, we first show how to extract the imaginary part of a scattering amplitude from the corresponding cross section (Sec. 2.3.1). Then we derive how to retrieve the full amplitude from its imaginary part (Sec. 2.3.2). Lastly, we connect the scattering amplitude to the anomalous lepton magnetic moment (Sec. 2.3.3, 2.3.4, 2.3.5). In conclusion, we will have derived the famous relation⁴ $a_\ell \approx \frac{1}{4\pi^3} \int K_\ell(s) \sigma(s) ds$ between a cross section and the corresponding contribution to a_ℓ , which is the main result of this section.

2.3.1 From the Optical Theorem to Vacuum Polarization

The total cross section of a process is connected to the imaginary part of the S -matrix by the *optical theorem*. Subsequently, a relation between the S -matrix element and the scattering amplitude is derived. Hence, the net result of this section is a relation between the imaginary part of the scattering amplitude and the cross section, produced with any lepton in the initial state, although we focus on the electron here.

The optical theorem is a result of the unitarity of the S -matrix. The S - or *scattering matrix* relates the initial state and the final state of a scattering process:

$$|\phi(\infty)\rangle = S |\phi(-\infty)\rangle.$$

The wave function ϕ at $t = -\infty$ corresponds to the initial state $|i\rangle$ and at $t = \infty$ to the final state $|f\rangle$. From this relation it is clear that in order to ensure conservation of probability, S has to be unitary, $S^\dagger S = \mathbb{1}$. Therefore, the absolute square of any matrix element gives the probability of the corresponding final state to be produced from the given initial state. Since the S -matrix describes the full process including the interaction-free part (parametrized by the identity matrix), the interaction is isolated in the T -matrix defined by $S \equiv \mathbb{1} + iT$. This definition and the unitarity of the S -matrix lead to

$$T^\dagger T = i(T^\dagger - T).$$

By comparing the imaginary part of the matrix element for forward scattering $|i\rangle \rightarrow |i\rangle$ to the general relation between T -matrix and

⁴ The lepton flavors are completely universal in this section. To distinguish the two leptons involved, throughout this section the general index ℓ is used for the magnetic moment, while the cross section initial state is set to the electron (e), which could of course also be replaced by any other lepton.

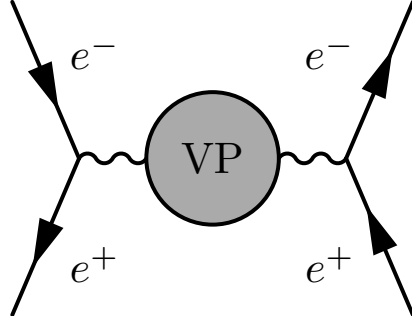


Figure 9.: Feynman diagram of lepton annihilation including vacuum polarization.

total cross section (with two particles of rest mass m_e in the initial state, as in electron-positron annihilation), the optical theorem is found [88, 89]:

$$\text{Im } T_{ii} = s \sqrt{1 - \frac{4m_e^2}{s}} \cdot \sigma_{\text{tot}}. \quad (15)$$

On the other hand, applying the Feynman rules to the process shown in Fig.9 yields⁵ (in Feynman gauge)

$$i T_{ii} = \bar{v}(-ie)\gamma^\mu u \frac{-ig_{\mu\nu}}{s + i\epsilon} (i\Pi^{\nu\rho}) \frac{-ig_{\rho\sigma}}{s + i\epsilon} \bar{u}(-ie)\gamma^\sigma v.$$

Due to current conservation, the vacuum polarization tensor $\Pi^{\nu\rho}$ must be transversal [90] and can thus be expressed as

$$\begin{aligned} \Pi^{\nu\rho}(q) &= -(q^2 g^{\nu\rho} - q^\nu q^\rho) \cdot (\Pi(q^2) - \Pi(0)) \\ &= -(q^2 g^{\nu\rho} - q^\nu q^\rho) \cdot \Pi_{\text{ren}}(q^2), \end{aligned}$$

where $\Pi(q^2)$ is the vacuum polarization amplitude, which defines the renormalized amplitude $\Pi_{\text{ren}}(q^2) := \Pi(q^2) - \Pi(0)$. The relation

$$\begin{aligned} i T_{ii} &= \bar{v}(-ie)\gamma^\mu u \frac{-ig_{\mu\nu}}{s + i\epsilon} (i\Pi^{\nu\rho}) \frac{-ig_{\rho\sigma}}{s + i\epsilon} \bar{u}(-ie)\gamma^\sigma v \\ &= \bar{v}(-ie)\gamma^\mu u \frac{ig_{\mu\sigma}\Pi_{\text{ren}}(s)}{s + i\epsilon} \bar{u}(-ie)\gamma^\sigma v \\ &= \frac{-ie^2\Pi_{\text{ren}}(s)}{s + i\epsilon} (\bar{v}\gamma^\mu u) (\bar{u}\gamma_\mu v) \end{aligned}$$

then follows as shown in App.B.1 and can be used to get rid of the vacuum polarization tensor $\Pi^{\nu\rho}$ and instead work with the renormalized vacuum polarization amplitude Π_{ren} .

Using the equivalence derived in App.B.2

$$(\bar{v}\gamma^\mu u) (\bar{u}\gamma_\mu v) = -s \left(1 + \frac{2m_e^2}{s} \right),$$

⁵ Throughout this chapter, the definitions from Ref. [90] for $u, \bar{u}, v, \bar{v}, g_{\mu\nu}, \gamma^\mu, \sigma^{\mu\nu}$ etc. are used unless otherwise stated. e denotes the elementary charge.

noting that $\text{Im } \Pi(0) = 0$ such that $\text{Im } \Pi_{\text{ren}}(s) = \text{Im } \Pi(s)$, we find for $s > 0$, $\varepsilon \rightarrow 0^+$

$$\text{Im } T_{ii} = e^2 \left(1 + \frac{2m_e^2}{s} \right) \text{Im } \Pi(s)$$

Comparing to Eq. 15 the relation between the total cross section and the vacuum polarization amplitude emerges:

$$\sigma_{\text{tot}}(s) = 4\pi\alpha \frac{1 + \frac{2m_e^2}{s}}{\sqrt{1 - \frac{4m_e^2}{s}}} \frac{\text{Im } \Pi(s)}{s}. \quad (16)$$

While the above cross section is valid for electrons in the initial state, this relation also holds for cross sections produced using other lepton pairs if the electron mass m_e is replaced by the mass of the chosen lepton.

2.3.2 Derivation of the Dispersion Relation

A dispersion relation connects a scattering amplitude to an integral over the imaginary part of the scattering amplitude, so that knowing the imaginary part enables us to calculate the full amplitude.⁶ This is useful for the prediction of the hadronic contribution to $g - 2$ since the imaginary part of the scattering amplitude is determined by the corresponding cross section as shown in Sec. 2.3.1, enabling us to use experimental data as input to compute the full amplitude. The corresponding dispersion relation, an analogue of the Kramers-Kronig relations [91, 92], is given by

$$\Pi_{\text{ren}}(k^2) := \Pi(k^2) - \Pi(0) = \frac{k^2}{\pi} \lim_{\varepsilon \rightarrow 0} \int_{s_{\text{min}}}^{\infty} ds \frac{\text{Im } \Pi(s)}{s(s - k^2 + i\varepsilon)}. \quad (17)$$

The amplitude $\Pi(s)$ is a function defined on the real axis ($s, k^2 \in \mathbb{R}$), but can be extended analytically into the upper half of the complex plane⁷. Using the Schwarz reflection principle [93], the analytic continuation into the lower half-plane can be constructed as

$$\Pi(s^*) = \Pi^*(s) \quad (18)$$

for $s \in \mathbb{C}$. Consequently, Π is analytic in \mathbb{C} except along the positive real axis above the production threshold s_{min} ($s > s_{\text{min}} > 0$), where it has a branch cut discontinuity as evident from the optical theorem (Sec. 2.3.1). The analyticity properties of the amplitude follow from causality [94]. Furthermore, we observe $\text{Im } \Pi(s) = 0 \forall s \leq s_{\text{min}}$ from the optical theorem.

⁶ In other contexts, such as optics, the term ‘‘dispersion relation’’ may be used differently.

⁷ Therefore, $\lim_{\varepsilon \rightarrow 0} \Pi(s + i\varepsilon) \equiv \Pi(s) \forall s, \varepsilon \in \mathbb{R}, \varepsilon > 0$.

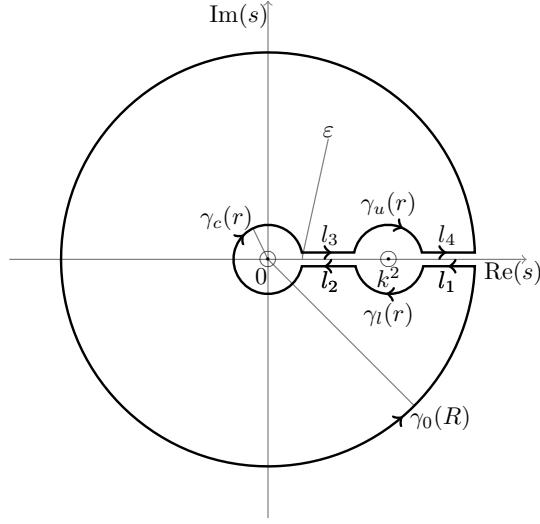


Figure 10.: Contour used for the dispersion integral.

Let us prove the dispersion relation. Since $\frac{\Pi(s)}{s(s-k^2)}$ is analytic in the complex plane except for $s = 0$, $s = k^2$, and along the branch cut discontinuity $s > s_{\min}$, $s \in \mathbb{R}$, the residue theorem cannot be applied directly. Therefore, the contour \mathcal{C} shown in Fig. 10 is chosen instead, such that following from the Cauchy theorem [95]

$$\oint_{\mathcal{C}} ds \frac{\Pi(s)}{s(s-k^2)} = 0. \quad (19)$$

Splitting up the integration path into the segments defined in Fig. 10 we observe the following:

$$\lim_{R \rightarrow \infty} \int_{\gamma_0(R)} ds \frac{\Pi(s)}{s(s-k^2)} = 0$$

because $|\Pi(s)/s| \rightarrow 0$ for $|s| \rightarrow \infty$,

$$\lim_{r \rightarrow 0} \int_{\gamma_c(r)} ds \frac{\Pi(s)}{s(s-k^2)} = -2\pi i \operatorname{Res} \left(\frac{\Pi(s)}{s(s-k^2)}, s=0 \right) = 2\pi i \frac{\Pi(0)}{k^2},$$

$$\begin{aligned} \lim_{r \rightarrow 0} \int_{\gamma_l(r)+\gamma_u(r)} ds \frac{\Pi(s)}{s(s-k^2)} &= -2\pi i \operatorname{Res} \left(\frac{\Pi(s)}{s(s-k^2)}, s=k^2 \right) \\ &= -2\pi i \frac{\Pi(k^2)}{k^2}, \end{aligned}$$

where Res is the residue,

$$\begin{aligned}
& \int_{l_1+l_2+l_3+l_4} ds \frac{\Pi(s)}{s(s-k^2)} = \\
& = \int_r^{k^2-r} ds \left(\frac{\Pi(s+i\varepsilon)}{(s+i\varepsilon)(s+i\varepsilon-k^2)} - \frac{\Pi(s-i\varepsilon)}{(s-i\varepsilon)(s-i\varepsilon-k^2)} \right) \\
& + \int_{k^2+r}^R ds \left(\frac{\Pi(s+i\varepsilon)}{(s+i\varepsilon)(s+i\varepsilon-k^2)} - \frac{\Pi(s-i\varepsilon)}{(s-i\varepsilon)(s-i\varepsilon-k^2)} \right).
\end{aligned}$$

From the relation $\Pi^*(s) = \Pi(s^*)$, which holds for all $s \in \mathcal{C}$, $\operatorname{Re}(\Pi(s)) = \operatorname{Re}(\Pi(s^*))$ and $\operatorname{Im}(\Pi(s)) = -\operatorname{Im}(\Pi(s^*))$ follow directly. Using this, we obtain

$$\begin{aligned}
& \int_{l_1+l_2+l_3+l_4} ds \frac{\Pi(s)}{s(s-k^2)} = \\
& = \lim_{r \rightarrow 0} 2i \int_r^{k^2-r} ds \operatorname{Im} \left(\frac{\Pi(s+i\varepsilon)}{(s+i\varepsilon)(s+i\varepsilon-k^2)} \right) \\
& + \lim_{r \rightarrow 0} 2i \int_{k^2+r}^R ds \operatorname{Im} \left(\frac{\Pi(s+i\varepsilon)}{(s+i\varepsilon)(s+i\varepsilon-k^2)} \right) \\
& = 2i \int_0^R ds \operatorname{Im} \left(\frac{\Pi(s+i\varepsilon)}{(s+i\varepsilon)(s+i\varepsilon-k^2)} \right).
\end{aligned}$$

Considering $\operatorname{Im}(f \cdot g) = \operatorname{Re}(f) \cdot \operatorname{Im}(g) + \operatorname{Im}(f) \cdot \operatorname{Re}(g)$, we see that

$$\begin{aligned}
& \lim_{\varepsilon \rightarrow 0} \operatorname{Im} \left(\frac{\Pi(s+i\varepsilon)}{(s+i\varepsilon)(s+i\varepsilon-k^2)} \right) = \\
& = \lim_{\varepsilon \rightarrow 0} \left(\underbrace{\operatorname{Re}(\Pi(s+i\varepsilon))}_{\|\cdot\| < \infty} \cdot \underbrace{\operatorname{Im} \left(\frac{1}{(s+i\varepsilon)(s+i\varepsilon-k^2)} \right)}_{\rightarrow 0} \right) \\
& + \lim_{\varepsilon \rightarrow 0} \left(\operatorname{Im}(\Pi(s+i\varepsilon)) \cdot \operatorname{Re} \left(\frac{1}{(s+i\varepsilon)(s+i\varepsilon-k^2)} \right) \right) \\
& = \lim_{\varepsilon \rightarrow 0} \left(\operatorname{Im}(\Pi(s+i\varepsilon)) \cdot \frac{1}{(s+i\varepsilon)(s+i\varepsilon-k^2)} \right)
\end{aligned}$$

with $\varepsilon > 0$, $\varepsilon \in \mathbb{R}$, $k^2 \in \mathbb{R}^+$, $s \in \mathbb{R}^+ \setminus \{0, k^2\}$. Thus for $R \rightarrow \infty$

$$\lim_{\varepsilon \rightarrow 0} \int_{l_1+l_2+l_3+l_4} ds \frac{\Pi(s)}{s(s-k^2)} = \lim_{\varepsilon \rightarrow 0} 2i \int_0^\infty ds \left(\frac{\operatorname{Im}(\Pi(s+i\varepsilon))}{(s+i\varepsilon)(s+i\varepsilon-k^2)} \right).$$

Summing up the contributions from all parts of the contour and comparing to the full contour, the following is obtained:

$$o = \Pi(o) - \Pi(k^2) + \lim_{\varepsilon \rightarrow 0} \frac{k^2}{\pi} \int_o^\infty ds \left(\frac{\text{Im}(\Pi(s + i\varepsilon))}{(s + i\varepsilon)(s + i\varepsilon - k^2)} \right).$$

Since $\text{Im} \Pi(s) = o$ for $s < s_{\min}$, $s \in \mathbb{R}$, this evaluates to

$$o = \Pi(o) - \Pi(k^2) + \lim_{\varepsilon \rightarrow 0} \frac{k^2}{\pi} \int_{s_{\min}}^\infty ds \left(\frac{\text{Im}(\Pi(s))}{s(s - k^2 + i\varepsilon)} \right) \quad \square \quad (20)$$

2.3.3 Connection of a_ℓ to the Matrix Element

After the correspondence between the cross section and the scattering amplitude has been established, the following sections will show how the scattering amplitude is related to the anomalous lepton magnetic moment.

Since the gyromagnetic factor g of a particle is the constant of proportionality connecting its spin \vec{s} and magnetic moment $\vec{\mu}$ via

$$\vec{\mu} = g \cdot \frac{e}{2m} \vec{s},$$

it can be derived (following [90]) by analyzing the scattering of the particle off a magnetic field. Hence, without loss of generality, for a lepton the corresponding scattering matrix element can be written as⁸

$$\begin{aligned} i\mathcal{M} &= -ie\bar{u}(p')\Gamma^\mu(p', p)u(p)\tilde{A}_\mu(q) \\ &= ie\bar{u}(p') \left(\gamma^i F_1(q^2) + \frac{i\sigma^{iv}q_v}{2m} F_2(q^2) \right) u(p)\tilde{A}_i(\vec{q}), \end{aligned} \quad (21)$$

where $q = p' - p$ and \tilde{A}_μ is the Fourier transform (since we are working in momentum space) of the electromagnetic potential A_μ , with $A_\mu = (o, \vec{A})$ for this purely magnetic case. The form factors $F_j(q^2)$ can be extracted by decomposition into contributions proportional to γ^μ and $\sigma^{\mu\nu}q_\nu$ for $q^\mu \rightarrow o$, where $F_1(q^2) = 1$ and $F_2(q^2) = o$ in lowest order. The above expression for \mathcal{M} vanishes for $\vec{q} = o$, so in an expansion for $q^\mu \rightarrow o$ it is sufficient to consider only terms up to first order. In this linear approximation the nonrelativistic limit is used for the spinors $u(p)$

$$u(p) = \begin{pmatrix} \sqrt{\vec{p} \cdot \vec{\sigma}} \xi \\ \sqrt{\vec{p} \cdot \vec{\sigma}} \xi \end{pmatrix} \approx \sqrt{m} \begin{pmatrix} (1 - \vec{p} \cdot \vec{\sigma}/2m) \xi \\ (1 + \vec{p} \cdot \vec{\sigma}/2m) \xi \end{pmatrix},$$

⁸ \mathcal{C} and \mathcal{P} invariance are assumed here, otherwise further form factors arise. Moreover, the decomposition into terms proportional to γ^μ and $\sigma^{\mu\nu}q_\nu$ is not unique. Alternatively, Γ^μ can be decomposed into terms proportional to γ^μ and $(p + p')^\mu$, resulting in different form factors commonly denoted as $F(q^2)$ and $G(q^2)$. For a detailed treatment see Ref. [96].

where ξ is a two-component spinor normalized to unity and σ^i are the standard Pauli matrices.

Simplifying the matrix element yields for $q \rightarrow 0$

$${}_1\mathcal{M} = -2ime\xi^{\prime\dagger} \left(\frac{-1}{2m} \sigma^k (F_1(0) + F_2(0)) \right) \xi \tilde{B}^k(\vec{q}) \quad (22)$$

with the definition of the Fourier transform of the magnetic B -field $\tilde{B}^k(\vec{q}) = -i\epsilon^{ijk} q^i \tilde{A}^j(\vec{q})$. Therefore, in the limit $q^\mu \rightarrow 0$, this can be interpreted as the Born approximation of a potential corresponding to a weak, static magnetic B -field

$$V(\vec{x}) = -\vec{\mu} \cdot \vec{B}(\vec{x}) \quad (23)$$

where the magnetic moment can hence be identified as

$$\begin{aligned} \vec{\mu} &= \frac{e}{m} (F_1(0) + F_2(0)) \xi^{\prime\dagger} \frac{\vec{\sigma}}{2} \xi \equiv g \frac{e}{2m} \vec{s} \\ \Rightarrow g &= 2(F_1(0) + F_2(0)). \end{aligned} \quad (24)$$

After renormalization to remove divergences in F_1 , it can be shown that $F_1(0) = 1$ also holds in higher orders of α . F_2 is not divergent, so the first order correction of g only depends on F_2 :

$$a_\ell := \frac{g_\ell - 2}{2} = F_2(0). \quad (25)$$

In summary, in order to calculate the anomaly of the gyromagnetic factor, $g/2 - 1$, the term proportional to $\sigma^{\mu\nu} q_\nu$ has to be evaluated for $q^2 \rightarrow 0$, here denoted by $F_2(0)$.

2.3.4 Schwinger's Result

In 1947 Julian Schwinger derived [47, 48] the first order radiative correction to the lepton magnetic moment in Dirac theory $g_\ell = 2$, resulting in $\frac{\alpha}{2\pi}$ (despite the misprint in the original publication). The derivation is instrumental in understanding higher order corrections, and hence shall be summarized here. The calculation can be found in greater detail in Ref. [90].

The only possible QED-correction of $\mathcal{O}(\alpha)$ is the exchange of one virtual photon between the incoming and outgoing lepton, Schwinger's process in the Feynman diagram in Fig. 11. Thus considering exclusively this graph's contribution as $\delta\Gamma^\mu$ in Eq. 21, the following is obtained by applying Feynman rules & gauge⁹

$$\begin{aligned} \bar{u}(p') \delta\Gamma^\mu u(p) &= \int \frac{d^4k}{(2\pi)^4} \frac{-i g_{\nu\rho}}{(k-p)^2 + i\epsilon} \\ &\cdot \bar{u}(p') (-ie\gamma^\nu) \frac{i(\not{k}' + m)}{k'^2 - m^2 + i\epsilon} \gamma^\mu \frac{i(\not{k} + m)}{k^2 - m^2 + i\epsilon} (-ie\gamma^\rho) u(p). \end{aligned} \quad (26)$$

⁹ Dimensional regularization has to be applied to remove infrared and ultraviolet divergences affecting F_1 , yet not F_2 .

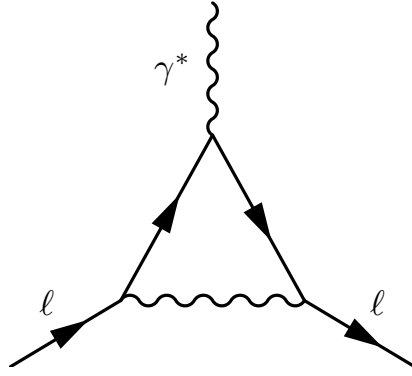


Figure 11.: Feynman diagram of the Schwinger's first order QED-correction.

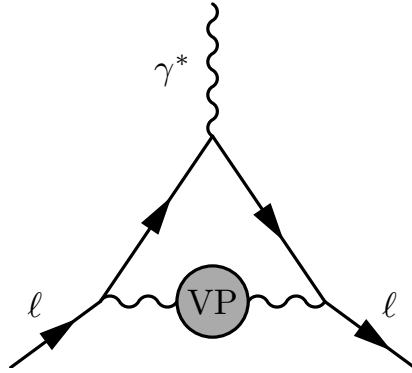


Figure 12.: Feynman diagram of the vacuum polarization term.

After quite a bit of algebra involving the method of Feynman parameters and a Wick rotation, the expression can be decomposed into coefficients of γ^μ and $\sigma^{\mu\nu}q_\nu$, as expected from Eq. 21. Evaluating the latter contribution in the limit $q^2 \rightarrow 0$, Schwinger's result is regained:

$$a_\ell \equiv \frac{g_\ell - 2}{2} = F_2(0) = \frac{\alpha}{2\pi} . \quad (27)$$

2.3.5 Putting the Puzzle Together

The contribution of interest for this work is the graph containing an additional hadronic loop as shown in Fig. 12. This term's correction to $g - 2$ can be calculated by modifying the photon propagator $\frac{-ig_{\nu\rho}}{q^2}$ in Eq. 26 with the (renormalized) vacuum polarization amplitude $\Pi_{\text{ren}}(q^2)$ yielding $\frac{i g_{\nu\rho}}{q^2} \Pi_{\text{ren}}(q^2)$, as shown in App.B.3. The corresponding vacuum polarization correction to the vertex function then becomes

$$\begin{aligned} \delta^{(2)}\Gamma^\mu = & \int \frac{d^4k}{(2\pi)^4} \frac{i g_{\nu\rho}}{(k-p)^2 + i\epsilon} \Pi_{\text{ren}}((p-k)^2) \\ & \cdot (-ie\gamma^\nu) D_F(k') \gamma^\mu D_F(k) (-ie\gamma^\rho) \end{aligned}$$

with $D_F(k) := \frac{i(k+m)}{k^2-m^2+i\varepsilon}$. Applying the dispersion relation (Eq.17), the correction becomes

$$\delta^{(2)}\Gamma^\mu = \int \frac{d^4k}{(2\pi)^4} \frac{i g_{\nu\rho}}{(k-p)^2 + i\varepsilon} \frac{(k-p)^2}{\pi} \cdot \int_{s_{\min}}^{\infty} ds \frac{\text{Im } \Pi(s)}{s(s-(k-p)^2 - i\varepsilon)} (-ie\gamma^\nu) D_F(k') \gamma^\mu D_F(k) (-ie\gamma^\rho) .$$

Canceling $(k-p)^2$ against $(k-p)^2 + i\varepsilon$ is applicable since the singularity at this point is effectively removed. Interchanging the order of integration (Fubini's theorem [97]) gives

$$\delta^{(2)}\Gamma^\mu = \int_{s_{\min}}^{\infty} ds \frac{\text{Im } \Pi(s)}{\pi s} \int \frac{d^4k}{(2\pi)^4} \frac{ie^2 g_{\nu\rho} \gamma^\nu D_F(k') \gamma^\mu D_F(k) \gamma^\rho}{(k-p)^2 - s + i\varepsilon} .$$

The inner integral possesses a structure similar to the Schwinger case, apart from the fact that the photon has gained the “mass” \sqrt{s} . Hence it can similarly be decomposed into parts proportional to γ^μ and $\sigma^{\mu\nu} q_\nu$, respectively. The latter contribution corresponds to the form factor F_2 we are interested in. It is derived directly using a set of simplifications for general momentum integrals (see Ref. [98]) resulting in the integral shown in Ref. [99]¹⁰. Alternatively, it can be worked out involving a Wick rotation and Feynman parameters analogous to the Schwinger case [90] but retaining the photon “mass” \sqrt{s} . Either approach results in

$$\frac{\pi}{\alpha} F_2(q^2) = \int_{s_{\min}}^{\infty} ds \frac{\text{Im } \Pi(s)}{\pi s} \int_0^1 dx dy dz \frac{\delta(x+y+z-1) m^2 z(1-z)}{m^2(1-z)^2 - q^2 xy + sz}$$

with $q^2 = (p' - p)^2 = (k' - k)^2$ and the Dirac distribution δ [102]. Since a_ℓ is F_2 evaluated at $q^2 = 0$, this simplifies to

$$\begin{aligned} \frac{\pi}{\alpha} F_2(0) &= \int_{s_{\min}}^{\infty} ds \frac{\text{Im } \Pi(s)}{\pi s} \int_0^1 dx dy dz \delta(x+y+z-1) \frac{z(1-z)}{(1-z)^2 + \frac{s}{m^2} z} \\ &= \int_{s_{\min}}^{\infty} ds \frac{\text{Im } \Pi(s)}{\pi s} \int_0^1 dz \frac{z^2(1-z)}{z^2 + \frac{s}{m^2}(1-z)} . \end{aligned}$$

¹⁰ In Ref. [99], the effect of a possible QED cutoff [100, 101] on a_ℓ is studied, resulting in an equivalent integral independent of hadron production.

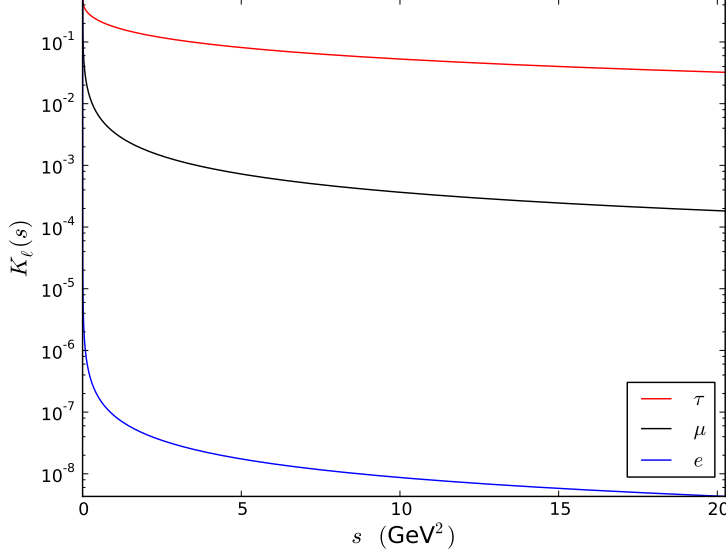


Figure 13.: The Kernel function for each lepton flavor.

The inner integral is known as the Kernel function $K_\ell(s)$, which for any given lepton ℓ is defined with $m \equiv m_\ell$. Writing out the integral explicitly gives [103]

$$K_\ell(s) = \begin{cases} \frac{1}{h^2} \left(4(h-2) \ln \frac{h}{4} - h \left(4 - \frac{h}{2} \right) \right. \\ \quad \left. - 2(h^2 - 8h + 8) \frac{\arctan(\sqrt{h-1})}{\sqrt{h-1}} \right) & s < 4m_\ell^2 \\ \frac{1}{h^2} \left(4(h-2) \ln \frac{h}{4} - h \left(4 - \frac{h}{2} \right) \right. \\ \quad \left. - 2(h^2 - 8h + 8) \frac{\operatorname{arctanh}(\sqrt{1-h})}{\sqrt{1-h}} \right) & s > 4m_\ell^2 \end{cases} \quad (28)$$

with $h := \frac{4m_\ell^2}{s}$. The singularity at $h = 1$ is removable by $K_\ell(4m_\ell^2) = 8 \ln(2) - \frac{11}{2} \approx 0.045$. The result can be studied in Fig. 13 for all lepton flavors.

Using the optical theorem for the vacuum polarization amplitude (Eq. 16), $\operatorname{Im} \Pi(s)/s$ may now be replaced by

$$\frac{\operatorname{Im} \Pi(s)}{s} = \frac{\sqrt{1 - \frac{4m_\ell^2}{s}}}{4\pi\alpha \left(1 + \frac{2m_\ell^2}{s} \right)} \cdot \sigma_{e^+e^- \rightarrow \text{had}}(s).$$

The result¹¹

$$a_\ell^{\text{had}} \equiv F_2(0) = \frac{1}{4\pi^3} \int_{s_{\min}}^{\infty} K_\ell(s) \cdot \frac{\sqrt{1 - \frac{4m_e^2}{s}}}{1 + \frac{2m_e^2}{s}} \cdot \sigma_{e^+e^- \rightarrow \text{had}}(s) ds \quad (29)$$

enables us to calculate the contribution to a_ℓ (for any lepton flavor ℓ) given by each hadronic channel using measured e^+e^- data (or other estimates) for the cross section. The factor $\sqrt{1 - \frac{4m_e^2}{s}} / \left(1 + \frac{2m_e^2}{s}\right)$ is often approximated as unity if $s_{\min} \gg 4m_e^2$. The production threshold energy squared s_{\min} is $m_{\pi^0}^2$ for the minimal hadronic case $e^+e^- \rightarrow \pi^0\gamma$, $4(m_{\pi^\pm} + m_{\pi^0})^2$ for $e^+e^- \rightarrow \pi^+\pi^-2\pi^0$, and $(2m_{\pi^\pm} + 3m_{\pi^0})^2$ for $e^+e^- \rightarrow \pi^+\pi^-3\pi^0$.

2.3.6 Hadronic Cross Sections

As shown above, a reliable total hadronic cross section is necessary¹² for precise standard model predictions of $g - 2$ and – as outlined in Sec. 2.8 – the running of α . This can be achieved by measuring the R -ratio defined as

$$R(s) := \frac{\sigma_{e^+e^- \rightarrow \text{had}}(s)}{\sigma_{e^+e^- \rightarrow \mu^+\mu^-}(s)},$$

where $\sigma_{e^+e^- \rightarrow \text{had}}$ is the total hadronic cross section, $\sigma_{e^+e^- \rightarrow \mu^+\mu^-}$ the muon pair cross section, and s the squared center-of-mass energy. Fig. 14 shows that R exhibits a plateau-structure with additional resonances and has been measured over a large energy range [43].

To achieve even higher accuracy, each single channel can be analyzed exclusively. As observed in Fig. 14, hadron production is largest at low energies. Additionally, the low energy region is weighted more strongly (cf. Fig. 13) in the relation to a_ℓ (Eq. 29). Due to these two effects the region between 0 and 1 GeV accounts for more than 75 % of the value of a_μ^{had} , depicted by the largest slice in Fig. 15 (left), which shows a pie chart of the contributions to a_μ^{had} from several energy regions.

At these low energies, the channel $e^+e^- \rightarrow \pi^+\pi^-$ is at least an order of magnitude larger than other contributions. (At very low energies, $e^+e^- \rightarrow \pi^0\gamma$ is the only competing process and has a much smaller cross section [103].) For this reason, the cross section of $e^+e^- \rightarrow \pi^+\pi^-$ has been measured with tremendous effort and remarkable precision. Early precision measurements of this channel were carried out by the CMD-2 [112, 113] and SND [114]

¹¹ This type of relation was first suggested in Ref. [104], where the effect on a_μ of lepton and pion pair production is studied using spectral functions instead of cross sections.

¹² It should be noted that τ decay data [105–108] can also be used as input, leading to a discrepancy [109, 110] if the $\rho^0 - \gamma$ mixing is not taken into account [111].

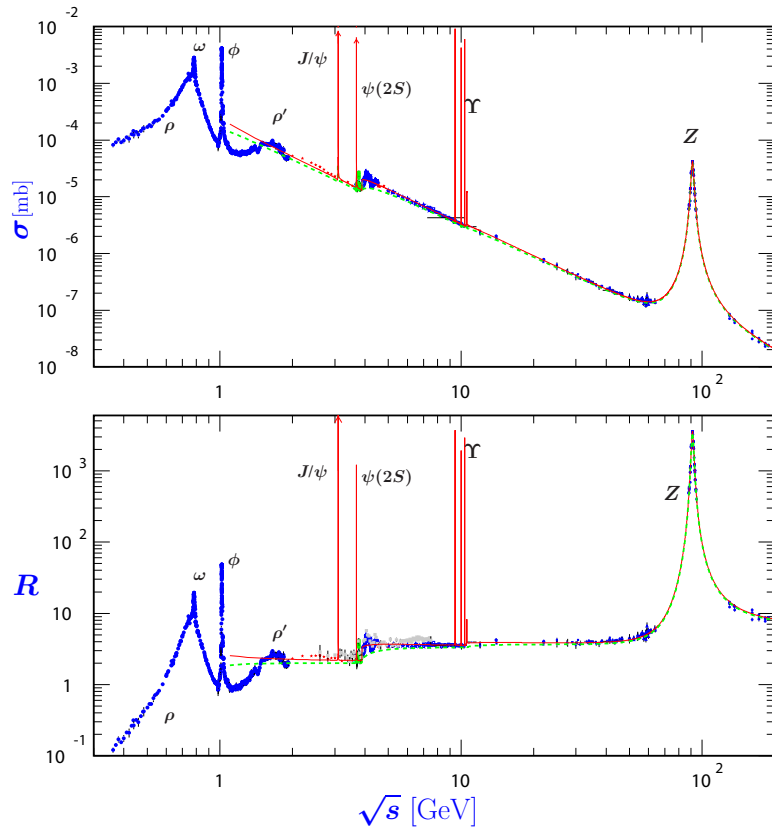


Figure 14.: The total inclusive hadronic cross section (top) and R -ratio (bottom) compiled from various experiments [43].

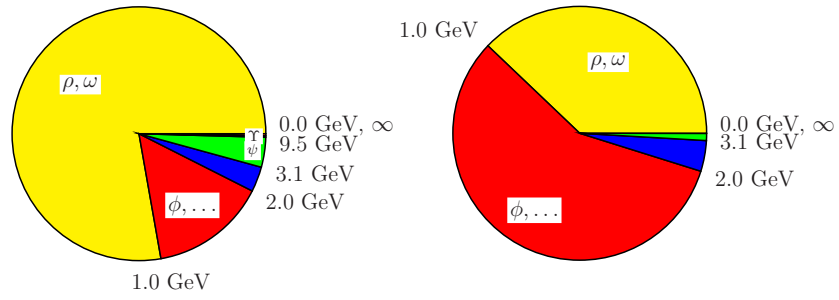


Figure 15.: Relative contributions to the value of a_μ^{had} (left) and its squared uncertainty (right). Reprinted from Ref. [46], ©2009, with permission from Elsevier.

experiments with systematic uncertainties of 0.8 % and 1.3 %, respectively. The measurement by *BABAR* reaches down to 0.5 % [115] systematic accuracy, while KLOE achieves 0.7 % [116]. Recently, BES-III published a measurement in the energy region between 0.6 GeV and 0.9 GeV, with a systematic uncertainty of 0.9 % [117]. Besides the high precision attained by each single measurement, in part of the energy range there is a systematic discrepancy of more than one standard deviation between *BABAR* and the other experiments, which is yet to be resolved.

The high precision of the measurements in the low energy region leads to the effect seen in the right panel of Fig. 15, which depicts the relative contributions to the squared uncertainty of a_μ^{had} for several energy ranges: at present, the leading contributor to the uncertainty of a_μ is not the low energy region, but rather the range between 1 GeV and 2 GeV. In this region there is a contribution from $e^+e^- \rightarrow \pi^+\pi^-\pi^0$ which was measured by SND [118, 119] and *BABAR* [120], with accuracy down to 3.6 % in the ϕ peak. But as seen in Fig. 16, which shows the hadronic cross sections measured by *BABAR* to date (note the logarithmic scale), the dominant cross sections above the ϕ resonance correspond to the 4-pion channels. The fully charged 4π -mode was recently measured [121] at *BABAR* with less than 3 % uncertainty in its peak region.

Conversely, the channel $e^+e^- \rightarrow \pi^+\pi^-\pi^0\pi^0$ is still only known with accuracy worse than 10 % [122] and over a very limited energy range, as shown in Fig. 17. The previously existing data was collected by the experiments SND [123, 124], ADONE MEA [125–127], ADONE $\gamma\gamma 2$ [128], ACO [129, 130], DCI-M3N [131], ND [132], and OLYA [133]. Therefore, the channel $e^+e^- \rightarrow \pi^+\pi^-\pi^0\pi^0$ remains a leading source of uncertainty for the SM prediction of $g_\mu - 2$. The present analysis fills this void.

Furthermore, the channel $e^+e^- \rightarrow \pi^+\pi^-3\pi^0$ has only been measured with accuracy in the range of 50 % to 100 %. The most accurate analysis was performed at the DCI-M3N experiment in Orsay [131] in the year 1979 and its cross section result is shown in

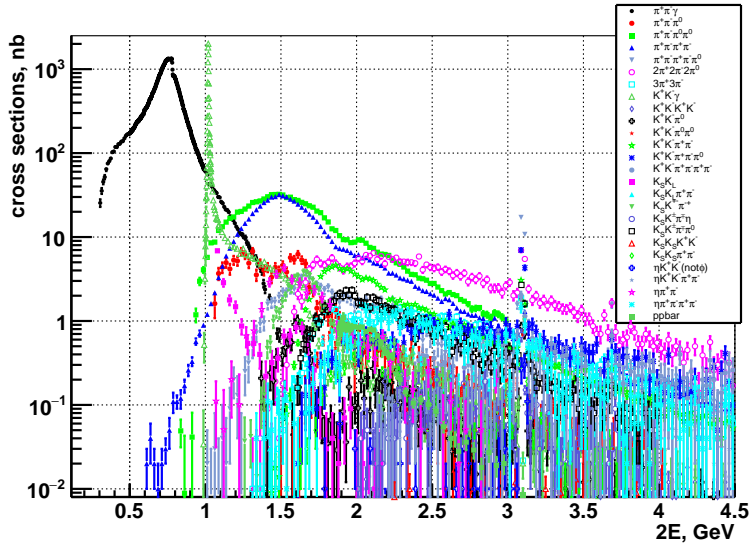


Figure 16.: *BABAR* measurements of exclusive channels contributing to the inclusive hadronic cross section (with $2E = \sqrt{s}$). Note that the entries for $\pi^+ \pi^- 2\pi^0$ and $K_s K^+ \pi^- \pi^0$ are preliminary and some channels have the charmonia contributions removed. Figure courtesy of F. Ignatov, BINP Novosibirsk.

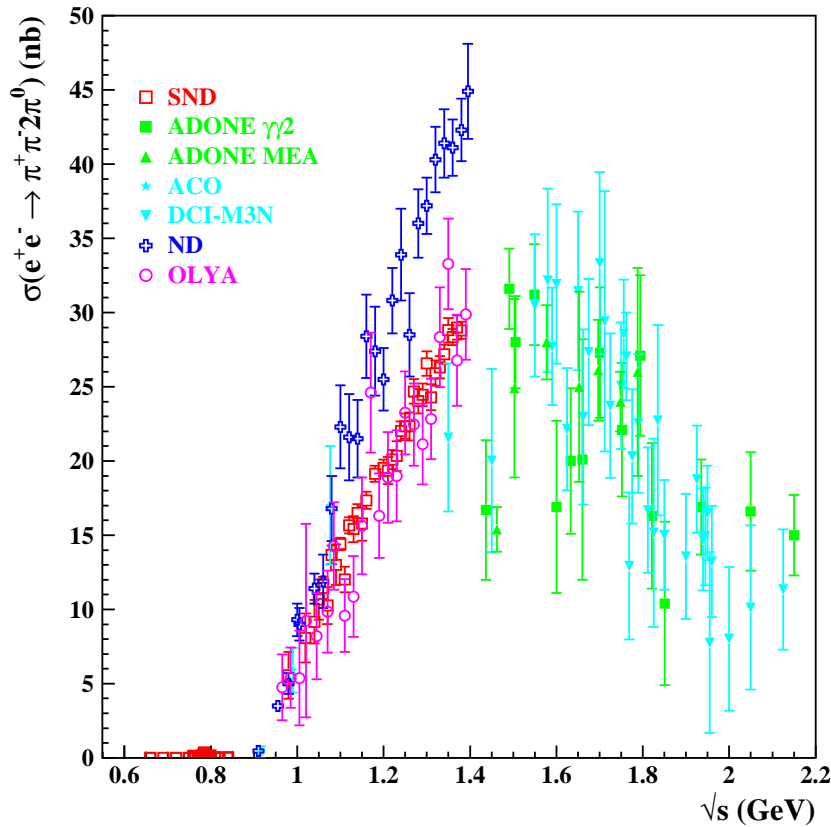


Figure 17.: The $\pi^+ \pi^- 2\pi^0$ cross section data published before *BABAR* (see text for references).

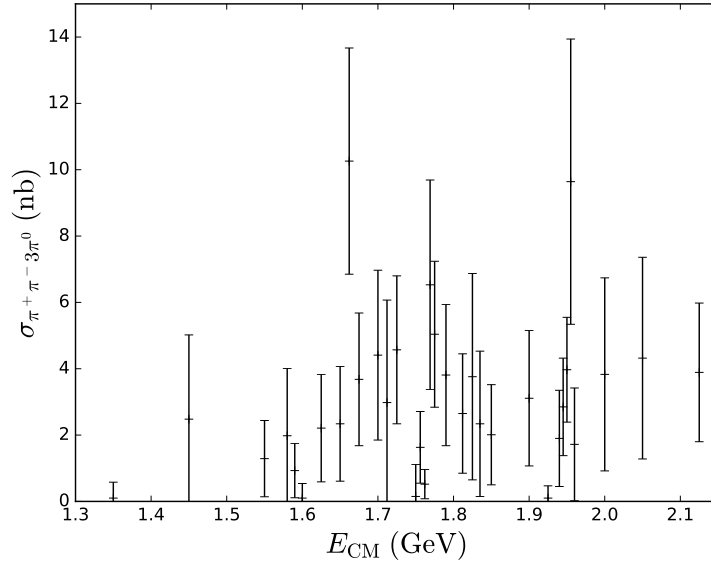


Figure 18.: The $e^+e^- \rightarrow \pi^+\pi^-3\pi^0$ cross section measured by the DCI-M3N experiment [131], data as listed in [122] ($E_{\text{CM}} = \sqrt{s}$). Statistical uncertainties shown only.

Fig. 18. Despite the comparatively small cross section, its contribution to a_μ is still very poorly known because at the moment it has to be evaluated (due to the large uncertainties of the measured cross section) by using measurements of processes related via isospin equivalence. Hence this channel needs to be investigated more accurately.

To extract the cross section over the full energy range from *BABAR* data, one needs to employ the method of *Initial State Radiation*, since the *BABAR* experiment operated at a fixed CM energy. This technique lowers the effective CM energy, thus giving access to all energies below 10.58 GeV, and is summarized in Sec. 3.

2.3.7 Final State Radiation Correction to $g - 2$

Measured cross sections are corrected to reconstruct the energy at which the final state (excluding the initial state radiation photon, if this method was employed) was produced despite the possible emission of additional radiation. Nonetheless, this means that events emitting a photon from the final state are counted. For the calculation of $g - 2$, including events with final state radiation (FSR) means that not only the contribution due to leading order vacuum polarization (Fig. 12) is evaluated, but the combination of all processes with vacuum polarization and photon loops modifying the VP-process, such as the one shown in Fig. 19.

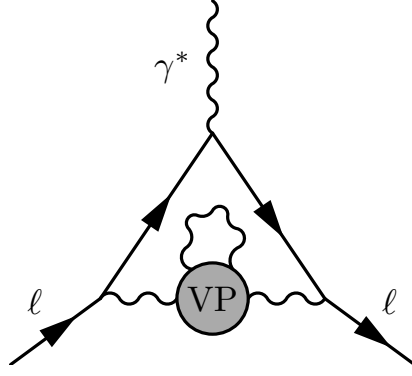


Figure 19.: Feynman diagram of the vacuum polarization term with an additional FSR photon loop.

For the two-pion case, this effect has been calculated [134, 135] to first order in α using scalar QED, approximating pions as point-like particles, so that it can be corrected¹³. The contribution due to the additional diagrams in that case is given as

$$\begin{aligned}
 \eta(s) = & \frac{1 + \beta^2}{\beta} \left(4 \text{Li}_2 \left(\frac{1 - \beta}{1 + \beta} \right) + 2 \text{Li}_2 \left(-\frac{1 - \beta}{1 + \beta} \right) \right. \\
 & \left. - 3 \ln \left(\frac{2}{1 + \beta} \right) \ln \left(\frac{1 + \beta}{1 - \beta} \right) - 2 \ln(\beta) \ln \left(\frac{1 + \beta}{1 - \beta} \right) \right) \\
 & - 3 \ln \left(\frac{4}{1 - \beta} \right) - 4 \ln(\beta) \\
 & + \frac{1}{\beta^3} \left(\frac{5}{4} (1 + \beta^2)^2 - 2 \right) \ln \left(\frac{1 + \beta}{1 - \beta} \right) + \frac{3}{2} \frac{1 + \beta^2}{\beta^2},
 \end{aligned} \tag{30}$$

$\beta = \sqrt{1 - \frac{4m_\pi^2}{s}}$, $\text{Li}_2(x) = -\int_0^x \ln(1-t)/t dt$ (the dilogarithm [61]), and the result is shown in Fig. 20. The cross section must be divided by $(1 + \frac{\alpha}{\pi} \eta(s))$ in order to get the $g-2$ contribution due to vacuum polarization without an additional photon loop. In Fig. 20 it is observed that the correction of first order in α is below one percent for $\sqrt{s} \geq 0.5$ GeV. Therefore higher order corrections can safely be neglected in this mass range as they would be suppressed by another factor α , resulting in sub-permil corrections.

Yet, as this correction corresponds to the two-pion case, it cannot be applied to the four- and five-pion cross sections measured here, for which it has not been calculated to date. Hence, we will not extract the $g-2$ contribution solely due to pure vacuum polarization, but restrict ourselves to calculating the contribution due to the combination of all leading order vacuum polarization processes, regardless of additional photon loops.

¹³ To get rid of the unphysical singularity for $\beta \rightarrow 0$ ($s \rightarrow 4m_\pi^2$), the correction has to be resummed, but this additional effect is negligible in the energy range considered here.

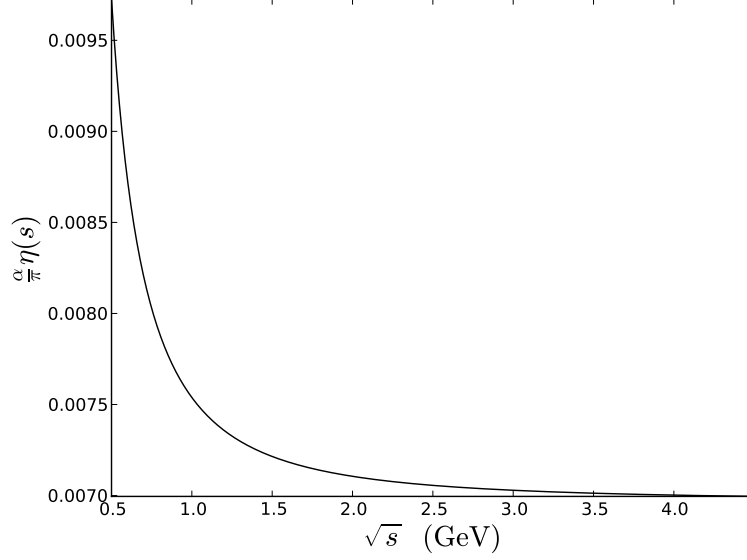


Figure 20.: The leading order FSR correction function $\frac{\alpha}{\pi} \eta(s)$ for $g - 2$ [134, 135].

2.3.8 Resulting Value of $a_\mu^{\text{had,LO}}$

Considering all measured hadronic channels results in a leading order contribution of

$$a_\mu^{\text{had,LO}} = 6923(42) \times 10^{-11}$$

to the Standard Model prediction [136].¹⁴ The uncertainty of 42×10^{-11} must be improved to draw a conclusion about the nature of the muon $g - 2$ puzzle, as will be outlined in Sec. 2.6.

The contribution from the $\pi^+ \pi^- 2\pi^0$ channel determined from previously existing measurements is $167.6(133) \times 10^{-11}$ [137] in the energy range from 1.02 GeV to 1.8 GeV. Hence its uncertainty is almost one third of the size of the uncertainty of the total value.

The latest published value for the a_μ contribution from the complete process $e^+ e^- \rightarrow \pi^+ \pi^- 3\pi^0$ is extracted from data employing isospin relations [109] and gives $12.9(22) \times 10^{-11}$ in the energy range from 1.019 GeV to 1.8 GeV. Due to the fact that the number is estimated using isospin relations, an undetermined systematic uncertainty is present. This result differs significantly from the value obtained by combining newer measurements [136, 138] of $e^+ e^- \rightarrow \pi^+ \pi^- \pi^+ \pi^- \pi^0$ and $e^+ e^- \rightarrow \eta \pi^+ \pi^-$, which give an estimate¹⁵ of $a_\mu(\pi^+ \pi^- 3\pi^0) = 7.4(7) \times 10^{-11}$ below 1.8 GeV, but are also subject to undetermined systematic uncertainties due to the isospin

¹⁴ The recent BES-III result for the channel $e^+ e^- \rightarrow \pi^+ \pi^-$ is not included in this compilation, which was published earlier.

¹⁵ For details see Sec. 8.

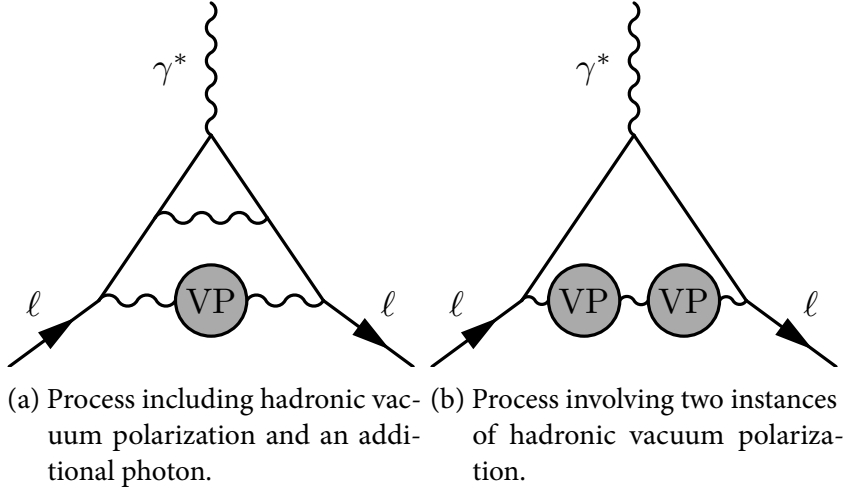


Figure 21.: Examples of NLO hadronic vacuum polarization diagrams.

model. The fact that the discrepancy of $\sim 5.5 \times 10^{-11}$ between these two values, both extracted using isospin relations, is of the same order of magnitude as the values themselves shows that a direct measurement of $a_\mu(\pi^+\pi^-3\pi^0)$ is indispensable.

2.4 HIGHER ORDER HADRONIC VACUUM POLARIZATION

In addition to diagrams of the form shown in Fig. 12 there are contributions from hadronic effects at higher orders. As mentioned in Sec. 2.2, the diagrams involving weak and strong interactions are subsumed into the electroweak contribution. Besides that, diagrams consisting of at least three loops involving only hadronic and QED processes have to be evaluated separately, also using measured cross sections for the hadronic vacuum polarization. The three-loop or next-to-leading order (NLO) component – shown in Fig. 21 – yields [139]

$$a_\mu^{\text{had,NLO}} = -98.7(9) \times 10^{-11},$$

while the four-loop (NNLO) diagrams – Fig. 22 – amount to

$$a_\mu^{\text{had,NNLO}} = 12.4(1) \times 10^{-11}.$$

In total, this gives the estimate for higher order hadronic contributions

$$a_\mu^{\text{had,HO}} = -86.3(10) \times 10^{-11}.$$

2.5 LIGHT BY LIGHT SCATTERING

The hadronic contributions to $g - 2$ manifest in different forms. Besides vacuum polarization, there is also hadronic light-by-light

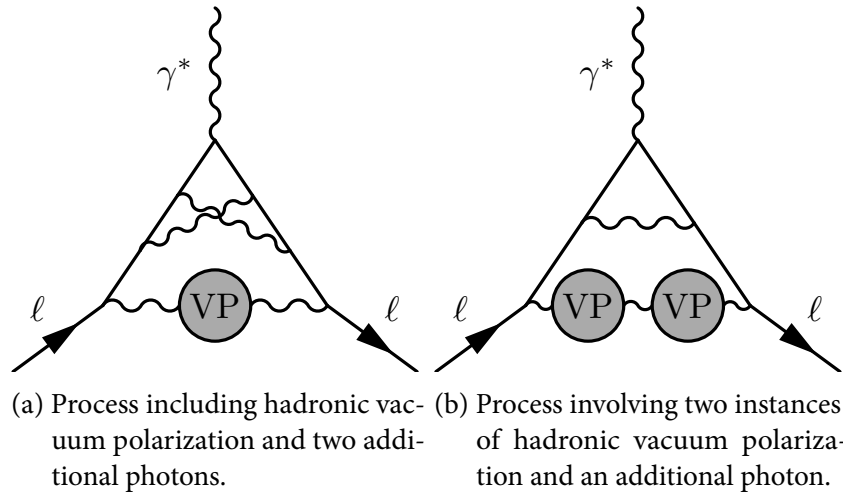


Figure 22.: Examples of NNLO hadronic vacuum polarization diagrams.

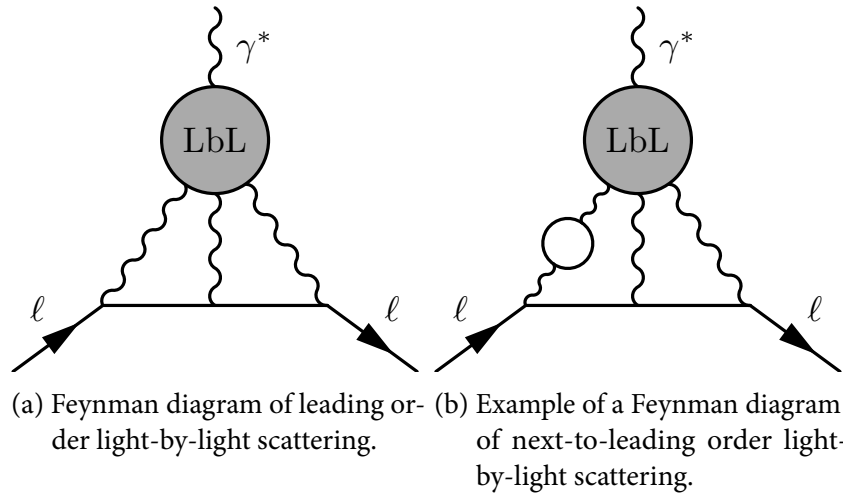


Figure 23.: Feynman diagrams of light-by-light scattering processes contributing to $g - 2$.

scattering (hLbL), in which the magnetic field (via a virtual photon) couples to the hadronic process, not directly to the lepton. The hadronic process in turn couples to the lepton via three photons as shown in Fig. 23a. Due to the number of photons involved in the diagram it is clear that light by light scattering starts at order α^3 , one order above the leading vacuum polarization effect. Recently, lattice field theory computations have been performed [140, 141] but still lack accuracy, such that this effect must be calculated using different methods. For very low energies, there are approaches from chiral perturbation theory to calculate the hLbL contribution, while for very high energies perturbative QCD is used. Since the hLbL contribution is not directly related to any measurable observable, the intermediate energy region has to be evaluated via models, introducing an additional uncertainty. Over the full energy range,

the largest fraction of the light-by-light scattering component is due to the production of pseudoscalar mesons like π^0 , η or η' . Including all processes, the leading hLbL contribution is estimated as [46]

$$a_\mu^{\text{hLbL,LO}} = 116(39) \times 10^{-11}.$$

It should be noted that the value of this contribution is much smaller than in hadronic vacuum polarization, while its uncertainty is of the same order of magnitude.

Hadronic light-by-light scattering processes can also arise at order α^4 , e.g. via diagrams including an additional lepton loop as shown in Fig. 23b. This leads to further suppression, such that the resulting contribution to a_μ is small [142]:

$$a_\mu^{\text{hLbL,NLO}} = 3(2) \times 10^{-11}.$$

Given the large uncertainty of the leading LbL contribution, this result confirms that higher order terms are negligible.

Therefore the total contribution to a_μ from hadronic light-by-light scattering can be estimated as

$$a_\mu^{\text{hLbL}} = 119(41) \times 10^{-11}.$$

2.6 SUMMARY OF CONTRIBUTIONS TO a_μ

To compare the experimental value of a_μ from Sec. 1.2.2 to the Standard Model prediction, the theoretical contributions must be collected. Table 2 lists all components as well as their sum and the deviation between experiment and theory, which amounts to a relative discrepancy of 3.0σ , assuming Gaussian statistics.

It should be noted that the particular value of the discrepancy between Standard model prediction and experiment varies between publications. This depends on which data set is evaluated and which theoretical model is used to calculate the hadronic light-by-light processes, resulting in different contributions and uncertainties. While combining the references quoted in Tab. 2 results in 3.0σ , different choices of the set of contributions may lead to relative discrepancies of 3.3σ [143] or 3.6σ [136]. After including the new BES-III data, discrepancies of up to 4.0σ have been reported at conferences [144], but the corresponding compilations are not published yet, hence their results should be taken with a grain of salt.

2.7 OUTLOOK ON a_μ

Besides improving the theoretical prediction of a_μ by performing new measurements especially for the hadronic contribution, the experimental value of a_μ will also be improved. Two new experiments

Table 2.: Compilation of contributions to a_μ .

	$a_\mu \times 10^{11}$	$\delta a_\mu \times 10^{11}$
QED [56]	116584718.951	0.080
EW [85]	153.6	1
hadronic VP LO [136]	6923	42
hadronic VP HO [139]	-86.3	10
hadronic LbL [46, 142]	119	41
total theory	116591828	60
E821 experiment [43]	116592089	63
deviation exp-theo	261	87

are planning to achieve a fourfold improvement of precision compared to the current value. At Fermilab, experiment E989 [44] will use the same method as the E821 experiment at Brookhaven, but aims to increase statistics by a factor 20 and decrease the systematic uncertainties to one third. The Muon $g-2$ /EDM Collaboration [45] at J-PARC will use a different technique. Here, an ultra-cold muon beam is injected into a storage magnet and the decay positrons are counted. Due to its new method, this experiment will be very valuable as an independent verification of existing experimental results.

Should the discrepancy between the experimental value of a_μ and its Standard Model prediction persist after the precision of experiment and theory have been improved such that it is proven that a physical phenomenon is observed, this would constitute evidence for physics beyond the Standard Model or “New Physics”. Several approaches exist to explain the effect.

The most basic question is whether theory and experiment are evaluating exactly the same quantity. One effect of this type is explored on the experimental side [35] by estimating how a nonzero electric dipole moment (EDM) of the muon would distort the measured frequency, which would not be due exclusively to the anomalous magnetic moment any more. Using the current upper limit for the muon EDM this is found to be a small effect. It is included in the systematic uncertainty, but physics beyond the Standard Model could result in a larger muon EDM than currently estimated. It is also worth recalling that in the theoretical derivation of a_μ \mathcal{C} and \mathcal{P} invariance are assumed when separating the vertex function into two form factors (Sec. 2.3.3). This assumption may become void in the presence of New Physics, such that the extracted observable would not correspond purely to the anomalous magnetic moment.

As an extension to the Standard Model, an additional boson [20] has been suggested, sometimes called “dark photon”. This boson would mediate between Standard Model matter and Dark Matter, and in addition could explain the $g_\mu - 2$ discrepancy if its mass and coupling fall into a specific corridor. Most of this parameter

range has been ruled out via experimental searches for a signature of this type of interaction, most recently by measurements at the A1 Experiment [21] and at BABAR [22], with an additional constraint from BES-III expected soon.

Another possible explanation could be substructure in leptons, quarks or the W^\pm/Z^0 bosons [19]. This would result in form factors and modified interactions leading to anomalous couplings.

Furthermore, supersymmetric extensions of the Standard Model are explored [23, 24]. In Supersymmetry, each Standard Model particle is assigned a “superpartner”, a particle from the supersymmetric extension of the Standard Model. In the Minimal Supersymmetric Model (MSSM), the additional contribution to a_μ would be proportional to $\tan(\beta)/M_{\text{SUSY}}^2$, where M_{SUSY} is the mass scale of the superparticles and $\tan(\beta)$ is a central yet unknown parameter of the model. Hence Supersymmetry could explain the $g_\mu - 2$ puzzle with a suitable value of the above ratio.

Recently, a different type of solution has been developed, which predicts the existence of leptoquarks [25, 27] or leptomesons [26]. A leptoquark is a hypothetical particle carrying lepton number and color and a leptomeson would be a leptoquark-antileptoquark bound state. Their existence could explain the $g_\mu - 2$ discrepancy between experiment and theory and it has been suggested to search for these particles in current and future experiments.

2.8 RUNNING OF THE FINE-STRUCTURE CONSTANT α

Two of the fundamental parameters of the Standard Model are the elementary charge e and the electromagnetic coupling α . They are both not constant but exhibit an energy dependence which can be predicted.¹⁶

Vacuum polarization occurring with increasing energy shields a charged particle from electromagnetic fields, as shown in Fig. 24a. This screening alters the effective charge of the particle. Thus, a running charge must be introduced [38]:

$$e^2(q^2) = \frac{e^2}{1 + \Pi(q^2) - \Pi(0)}, \quad (31)$$

where q^2 is the momentum transfer, e the elementary charge at zero momentum transfer, and Π the vacuum polarization amplitude. This expression is already renormalized such that $e^2(0) = e^2$.

Just like the elementary charge, the fine structure constant is also energy-dependent since $\alpha = \frac{e^2}{4\pi}$. This effectively modifies the electromagnetic interaction to include not only a plain photon,

¹⁶ The prediction of $\alpha(q^2)$ is not detailed as extensively as the theory behind $g - 2$, hence this section appears considerably shorter. This is merely due to the fact that this section relies heavily on the derivation developed for $g - 2$.

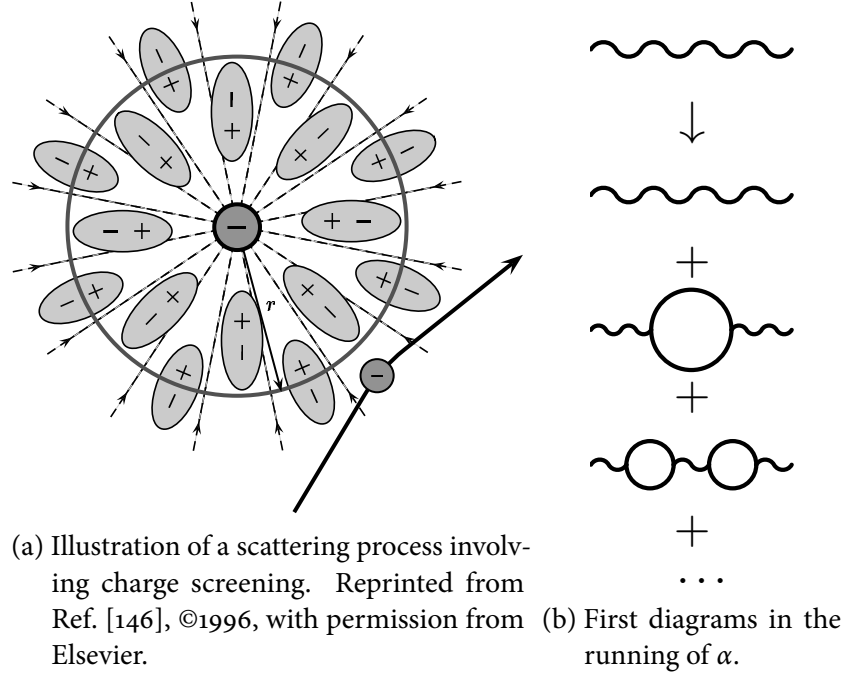


Figure 24.: Schematic representations of effective charge and coupling.

but also additional loop corrections indicated in Fig. 24b. In a renormalized expression [145] this effect is parameterized as

$$\alpha(q^2) = \frac{\alpha}{1 - \Delta\alpha(q^2)}, \quad (32)$$

$$\Delta\alpha(q^2) \equiv -(\Pi(q^2) - \Pi(0)),$$

with $\alpha = 7.2973525698(24) \times 10^{-3}$ [43] the fine structure constant at zero momentum transfer. The correction $\Delta\alpha$ is given by additional contributions from processes involving QED, electroweak, and strong interaction (plus possibly unknown components): $\Delta\alpha = \Delta\alpha_{\text{QED}} + \Delta\alpha_{\text{EW}} + \Delta\alpha_{\text{strong}} + \dots$. The leptonic and electroweak parts can be calculated perturbatively with high accuracy. Conversely, the hadronic contribution is not calculable with sufficient precision at low energies due to the large coupling of the strong interaction, necessitating an alternative approach. As in the case of $g - 2$, the dispersion relation Eq. 17 holds, and comparing to Eq. 32 yields

$$\Delta\alpha(q^2) = -\frac{q^2}{\pi} \int_0^\infty ds \frac{\text{Im} \Pi(s)}{s(s - q^2)}. \quad (33)$$

Applying the general corollary of the Optical Theorem (Eq. 16) results in the connection between σ , a cross section in e^+e^- annihilation, and the corresponding contribution to $\Delta\alpha$:

$$\Delta\alpha_X(q^2) = \frac{1}{4\pi^2\alpha} \int_{s_{\min}^X}^\infty ds \frac{\sqrt{1 - \frac{4m_e^2}{s}}}{1 + \frac{2m_e^2}{s}} \frac{\sigma_{e^+e^- \rightarrow X}(s)}{1 - \frac{s}{q^2}}. \quad (34)$$

Due to the singularity at $s = q^2$, the integral has to be evaluated as a Cauchy principal value [102] denoted by \mathcal{P} .

It should be noted that for large q^2 the low-energy range contributes a smaller fraction than in the case of $g - 2$, where the Kernel function $K_\ell(s)$ increases for $s \rightarrow 0$ unlike $1/(1 - s/q^2)$, the weight of the integrand for $\Delta\alpha$.

Resulting from this behavior, in the region below 1.8 GeV the channel $e^+e^- \rightarrow \pi^+\pi^-2\pi^0$ contributes about 8 % to the hadronic part of the running of α at the Z -pole $\Delta\alpha(M_Z^2c^2)$, yet only around 2.8 % to a_μ^{had} [136]. Likewise, the uncertainty of $\pi^+\pi^-2\pi^0$ amounts to 28 % of the total uncertainty of the hadronic part of a_μ^{had} , yet to more than 43 % in the case of $\Delta\alpha(M_Z^2c^2)$ at the Z -pole. Similar scaling of the effects is expected for the channel $e^+e^- \rightarrow \pi^+\pi^-3\pi^0$. It is estimated [147] that the sum of all contributions over the full energy range amounts to $\Delta\alpha(M_Z^2c^2) = 0.059105(255)$, of which the hadronic part is $\Delta\alpha^{\text{had}}(M_Z^2c^2) = 0.027607(225)$, accounting for most of the total uncertainty.

Using the purely electroweak reactions $e^+e^- \rightarrow \mu^+\mu^-$ and $e^+e^- \rightarrow e^+e^-\mu^+\mu^-$, the TOPAZ experiment measured the inverse fine-structure constant as $\alpha^{-1} = 128.5 \pm 1.8_{\text{stat}} \pm 0.7_{\text{syst}}$ [148] at a momentum transfer of 57.77 GeV/c, in agreement with the SM prediction 129.6 ± 0.1 .

Outlook on the Running of the Fine-Structure Constant α

Since the electromagnetic coupling α is a fundamental constant of the Standard Model, it is used for improving the precision of the other parameters of the electroweak interaction. This is achieved by fitting a set of electroweak parameters to their measured values under the constraints given by the theory. One group performing this type of analysis is the Gfitter collaboration. In their latest report [149] several variables still had sizeable uncertainties, such that improved input for $\Delta\alpha$ would be very valuable. Especially the fitted value of the effective leptonic weak mixing angle would profit significantly from an improved determination of $\Delta\alpha$. Since the hadronic contribution to $\Delta\alpha$ accounts for most of its total uncertainty, it is essential to improve this part. As discussed above, the channels $e^+e^- \rightarrow \pi^+\pi^-2\pi^0$ and $e^+e^- \rightarrow \pi^+\pi^-3\pi^0$ are major contributors to this uncertainty, hence their precise cross section measurements are fundamental to achieving this goal.

SUMMARY OF THEORETICAL PREDICTIONS

In the above chapter, two relations were derived, which connect cross sections measured in lepton annihilation to $g - 2$ and $\Delta\alpha$, respectively. Since hadronic processes are difficult to calculate pertur-

batively, this allows us to improve the Standard Model predictions of both observables by precisely investigating the production of hadronic final states. It is further outlined that accurate measurements for most major hadronic contributors exist, yet not for the channel $e^+e^- \rightarrow \pi^+\pi^-2\pi^0$, which at the moment is responsible for a large fraction of the total uncertainty in both cases. The channel $e^+e^- \rightarrow \pi^+\pi^-3\pi^0$ contributes to a lesser extent, but its uncertainty is basically unknown as no useable cross section measurement exists. Both problems will be solved by the following analyses.

THE ISR TECHNIQUE OF MEASURING CROSS SECTIONS

In general, total cross sections σ are extracted according to

$$\sigma = \frac{N}{\mathcal{L}}, \quad (35)$$

where \mathcal{L} denotes the integrated luminosity and N the number of events. More precisely, since we cannot measure the number of events with perfect efficiency or free of background:

$$\sigma = \frac{N_{\text{tot}} - N_{\text{bkg}}}{\varepsilon \cdot \mathcal{L}}, \quad (36)$$

here N_{tot} is the total number of selected events, N_{bkg} the number of background events and ε the global efficiency (including acceptance).

In this chapter, it will be explained how a non-radiative cross section is extracted from a measurement involving initial state radiation (ISR).

3.1 RADIATIVE RETURN

The *BABAR* experiment operated at a fixed CM energy, such that a special technique has to be used to extract cross sections over a broad energy range. The method of *Initial State Radiation (ISR)* or *Radiative Return* – devised roughly half a century ago [150, 151] – takes advantage of the fact that high-energetic lepton pairs may radiate real photons in addition to annihilating.¹

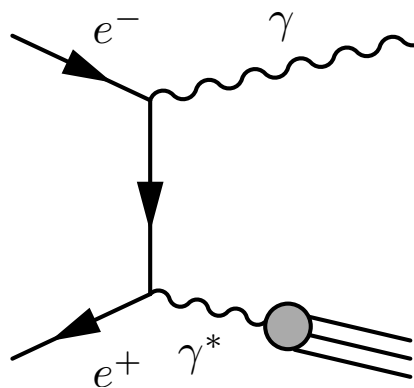


Figure 25.: Feynman diagram of an LO-ISR process producing a hadronic final state.

¹ In this chapter, merely a summary of the aspects instrumental to the analyses is presented. For a more detailed review, see e.g. Ref. [152] and references therein.

At leading order (LO), one photon is emitted from either of the incoming leptons as shown in Fig. 25. The final state (excluding the ISR-photon) now has the invariant mass $M \equiv \sqrt{s'} = \sqrt{(1-x)s}$, $x = \frac{2E_\gamma^*}{\sqrt{s}}$ (see App. A.1), where E_γ^* is the center-of-mass energy of the ISR photon, with s the square of the original CM energy of the experiment, e.g. $\sqrt{s} = 10.58$ GeV for PEP-II.

Hence, a *radiative cross section* can be measured (differentially in M) by detecting all events of a given final state plus an additional photon² and extracting their energy distribution. Yet, to calculate the cross section, the number of measured events must be normalized to the number of collisions at the energy of the final state $\sqrt{s'}$, i.e. to the luminosity.

The probability of radiating one photon such that the original energy \sqrt{s} is lowered to $\sqrt{s'}$ can be derived [153] by calculating the ratio of the cross section of any final state via the ISR process divided by the cross section via direct annihilation without emitting an additional photon. The leptonic part ($e^+e^- \rightarrow \gamma^*(\gamma)$) of the process can be calculated using the Feynman rules and is independent of the decay of the virtual photon γ^* into the final state in question under the assumption of factorization. The hadronic decay $\gamma^* \rightarrow \text{had}$ is therefore left as an arbitrary function of s' and cancels out when building the ratio of the two cross sections (with and without ISR). The ratio of the cross sections (at the same s') then yields the probability of producing the same final state via LO-ISR and is often referred to as the leading order *radiator function* W shown in Fig. 26 and given [152, 154] by

$$W(s, x, \theta_\gamma^*) = \frac{\alpha}{\pi x} \cdot \left[(2 - 2x + x^2) \cdot \ln \frac{1+C}{1-C} - Cx^2 \right], \quad (37)$$

for $\theta_\gamma^* > 0$, where the ISR photon is radiated into the CM polar angular range $|\cos(\theta_\gamma^*)| < C$ from the beam axis, with $C < 1$.

The radiator function including several photons is calculated in a similar manner, as shown in Ref. [155] for the next-to-leading order (NLO) case, but does not possess a convenient closed-form expression any more. The corrections due to higher order radiation can reach several percent of the leading order value. In this analysis, higher order effects are suppressed. The luminosity used to extract the cross section includes NLO effects by applying a correction to the LO formula as outlined in Sec. 7.4.1.

With the radiator function available, the measured radiative differential cross section can be converted into the original cross section [152]:

$$\frac{d\sigma_{\text{FS}\gamma}(M)}{dM} = \frac{2M}{s} \cdot W(s, x, \theta_\gamma^*) \cdot \sigma_{\text{FS}}(M). \quad (38)$$

² Not strictly necessary, so-called *untagged* measurements do not require detecting the ISR photon.

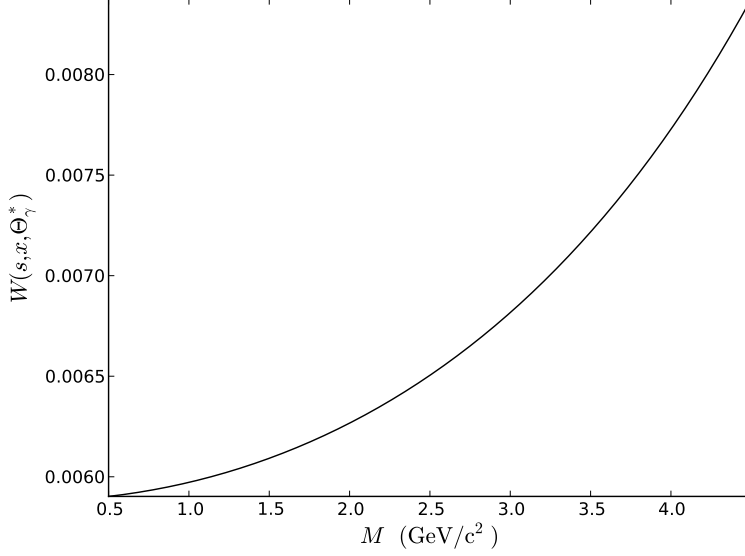


Figure 26.: The leading order radiator function W for $C = \cos(20^\circ)$ and $\sqrt{s} = 10.58$ GeV.

Using the ISR technique, the left hand side of Eq. 38 can be measured similarly to Eq. 36 but as a function of the invariant final state mass M :

$$\frac{d\sigma_{\text{FS}\gamma}(M)}{dM} = \frac{dN_{\text{FS}\gamma}(M)}{dM} \cdot \frac{1}{\varepsilon(M)\mathcal{L}(1+\delta)}. \quad (39)$$

Here, $N_{\text{FS}\gamma}$ represents the effective number of signal events after subtraction of all backgrounds, the efficiency ε is also energy-dependent and δ takes into account radiative corrections explained in Sec. 7.4. Combining Eq. 38 with Eq. 39, the non-radiative cross section is extracted:

$$\sigma_{\text{FS}}(M) = \frac{dN_{\text{FS}\gamma}(M)}{dM} \cdot \frac{s}{2M \cdot \mathcal{L} \cdot W(s, x, \theta_\gamma^*) \cdot \varepsilon(M) \cdot (1+\delta)}. \quad (40)$$

For *BABAR* analyses, the ISR luminosity

$$\mathcal{L}_{\text{ISR}}(M) = \frac{2M}{s} \cdot W(s, x, \theta_\gamma^*) \cdot \mathcal{L} \quad (41)$$

is shown in Fig. 27 (top) for $\mathcal{L} = 454.3 \text{ fb}^{-1}$ and the leading order radiator function W with $\sqrt{s} = 10.58$ GeV and $C = \cos(20^\circ)$. In the early stages of this analysis, a phenomenological polynomial fit to $e^+e^- \rightarrow \mu^+\mu^-\gamma$ data was used to describe the radiator function. Its deviation from the more precise current method is shown in Fig. 27 (bottom) and reaches $\pm 2\%$, the relative RMS deviation [156] being 1.3%.

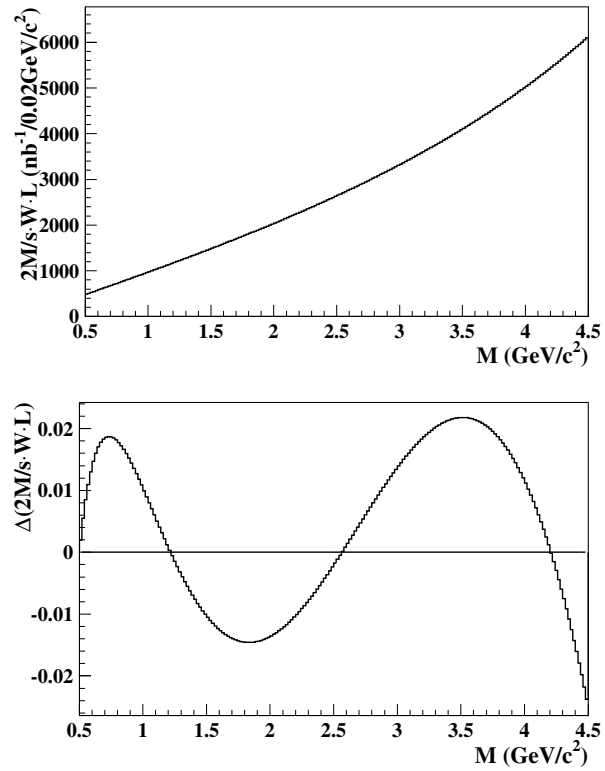


Figure 27.: The combined luminosity and radiator function (top) and its relative difference to the less precise fit method (bottom) in dependence of $M = \sqrt{s'}$.

THE BABAR EXPERIMENT

In the following chapter, an overview of the experiment is given. The first stage of the setup consists of the accelerator feeding into the storage rings, where the collision is achieved. The particles produced at the interaction point are captured by the *BABAR* detector, whose components are outlined individually below. If desired, more details are found in Refs. [157, 158].

4.1 INTRODUCTION: SLAC, PEP-II, AND *BABAR*

The *BABAR* experiment was carried out at the SLAC National Accelerator Laboratory¹ in Menlo Park, California. It consists of a 3 km-long linear accelerator (Linac), shown in Fig. 28, leading into the PEP-II storage rings (successor of the Positron Electron Project PEP). The main purpose of the experiment was the study of *CP*-violation in the decay of *B* mesons. To achieve the maximum number of $B\bar{B}$ pairs, the accelerator operated at a center-of-mass energy of 10.58 GeV, equivalent to the invariant mass of the $\Upsilon(4S)$. This resonance decays to $B\bar{B}$ pairs in more than 96 % of the cases, making *BABAR* a *B Factory*.

Electrons are fed into the Linac at its far end via damping rings to tune their energy precisely to the nominal value. Positrons are injected further downstream. The Linac accelerates the electrons to 9.0 GeV and the positrons to 3.1 GeV, subsequently injecting them into the High Energy Ring and the Low Energy Ring, respectively. The hexagonal storage rings feature bending dipoles at the turns and focussing quadrupoles and sextupoles along the straight sections. The particle energy is kept stable by RF cavities along the PEP-II rings counteracting the energy loss due to synchrotron radiation. In the section named *IR2*, the rings cross each other's path. Through a sophisticated system of magnets, the beams are led to a head-on collision (unlike in the competing Belle experiment [159], which has a crossing angle of 22 mrad), such that the only boost is along the beam-axis due to the differing beam-energies ($\beta\gamma = 0.56$). The boost defines the “forward direction”, a short term for the direction of motion of the electrons, while the “backward direction” points along the direction of motion of the positrons.

The *BABAR* experiment was set up around this point, harnessing the collisions by detecting the produced particles. During its 9 years of running, PEP-II reached a peak luminosity of $1.2 \times 10^{34} \text{ cm}^2 \text{ s}^{-1}$

¹ Originally named Stanford Linear Accelerator Center.

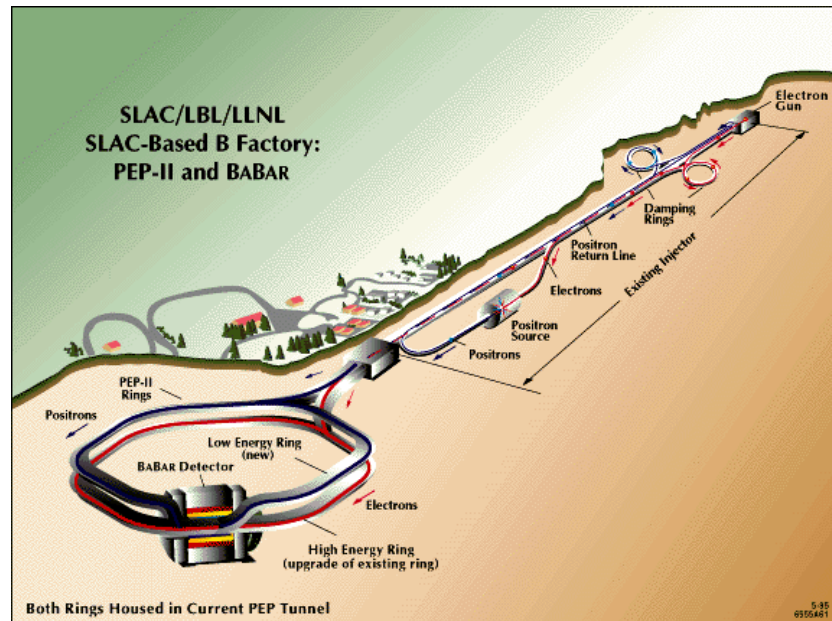


Figure 28.: The *B* Factory at SLAC. (Courtesy of SLAC National Accelerator Laboratory.)

– four times larger than the design luminosity of $3 \times 10^{33} \text{ cm}^2 \text{ s}^{-1}$ – and accumulated the total integrated luminosity of 557 fb^{-1} on the $\Upsilon(4S)$ resonance as well as other energies, as shown in Fig. 29 (the difference of $\sim 4 \text{ fb}^{-1}$ is due to additional energy scan data). The *BABAR* detector recorded 531.43 fb^{-1} , corresponding to 95.4 % detection efficiency. Of the 531.43 fb^{-1} recorded, events corresponding to 513.7 fb^{-1} [160] were successfully reconstructed. For an event to be detected successfully, it has to be registered by at least one of the detector components indicated in Fig. 30:

- Silicon Vertex Tracker (abbreviated as SVT),
- Drift Chamber (DCH),
- Detector of Internally Reflected Cherenkov Light (DIRC),
- Electromagnetic Calorimeter (EMC),
- Instrumented Flux Return (IFR).

The inner components (SVT, DCH & EMC) are encased by a solenoid magnet providing an almost uniform 1.5 T field to facilitate the possibility of transverse momentum measurements for charged particles in the DCH. Upon detection, the event is processed and recorded by the Trigger and Data Acquisition System, which is described at the end of this section.

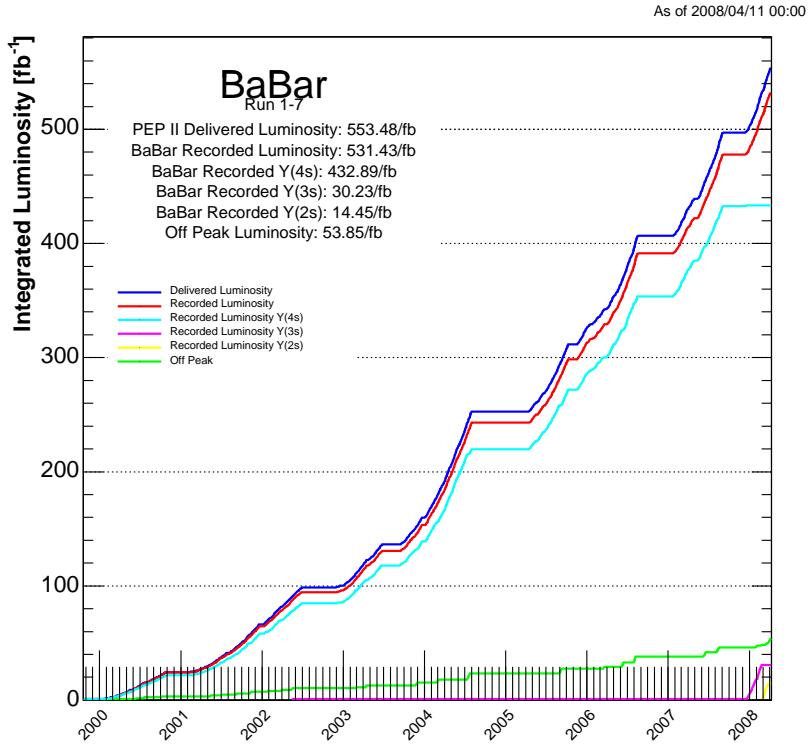


Figure 29.: The integrated PEP-II luminosity and amount of data measured by the *BABAR* detector. (Courtesy of SLAC National Accelerator Laboratory.)

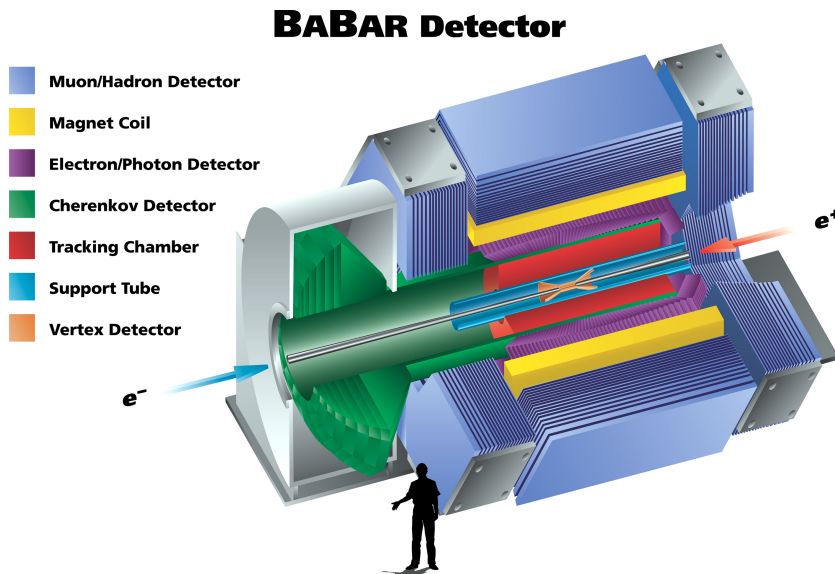


Figure 30.: Overview of the *BABAR* detector. (Courtesy of SLAC National Accelerator Laboratory.)

4.2 SILICON VERTEX TRACKER

The Silicon Vertex Tracker (SVT) is the innermost part of the *BABAR* detector, starting mere millimeters outside the beam pipe and is shown in Figs. 31 & 32. It measures the azimuthal angle ϕ and the longitudinal coordinate z of charged particle tracks with high precision. The SVT consists of five layers of double-sided silicon sensors arranged symmetrically around the z -axis. The three innermost layers form regular hexagonal right prisms at radial distances between ~ 3 cm and ~ 6 cm, while the outer two layers form regular polygonal right prisms with 16 and 18 edges in the radial range $\sim 12 - 15$ cm (see Fig. 31). All layers have been designed with azimuthal overlap in order to guarantee high efficiency without gaps. As shown in Fig. 32, layers 1 – 3 are entirely parallel to the z -axis, while layers 4 and 5 are arch-shaped. This configuration extends the range of angular coverage while using less detector material. Furthermore, it increases the angle of incidence for low-angle tracks, thus improving the precision of the measurements. In this design the SVT has a polar angular coverage of 90 % in the center-of-mass frame.

In total, there are 340 double-sided silicon strip detectors of $300\ \mu\text{m}$ thickness in the SVT. On the inner surface of each layer, the strips are perpendicular to the z -axis to provide z -coordinate measurements. Longitudinal strips reside on the outer surface of each layer, thus providing ϕ measurements.

The SVT can provide stand-alone track reconstruction, and this feature is used for *rolling calibration* during data collection, approximately once per hour. This calibration is achieved by matching each track measured in the SVT with its counterpart reconstructed in the Drift Chamber. For an ensemble of such tracks the average deviations in position and direction are converted into the six parameters of a rigid body transformation (translation and rotation). The coordinates measured by the SVT are then translated into the DCH coordinate system using the extracted parameters of this global alignment procedure. This procedure provides a very precise correction to possible displacement of other detector components relative to the SVT due to exterior influences like temperature changes.

Over the complete *BABAR* data taking period, the SVT achieved an efficiency of more than 95 %. Coordinate resolutions in z and $r\phi$ varied between $15\ \mu\text{m}$ and $40\ \mu\text{m}$.

4.3 DRIFT CHAMBER

The Drift Chamber (DCH, shown in Figs. 33 & 34), in combination with the SVT, is the main component of the tracking system in the *BABAR* Experiment, and thus of crucial importance for the present analysis. For charged-particle tracks, the combination provides

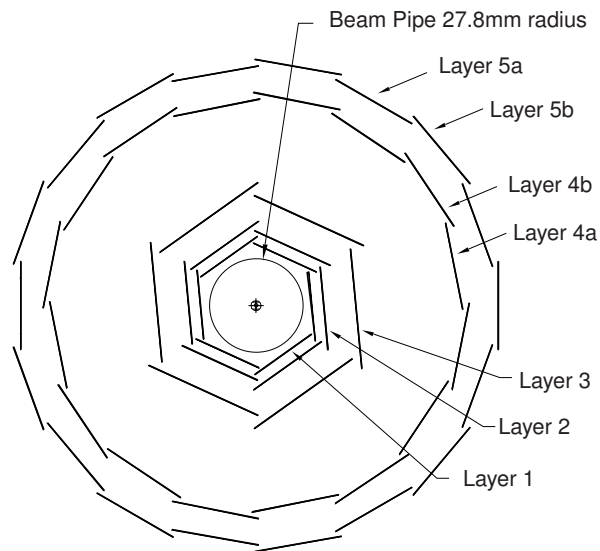
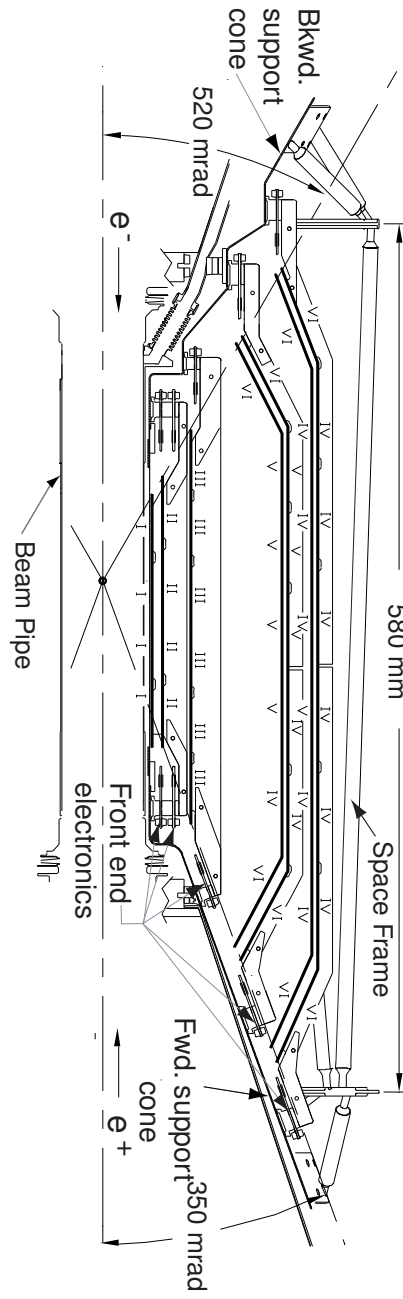


Figure 31.: Schematic drawing of a transverse section through the *BABAR* silicon vertex tracker. (Courtesy of SLAC National Accelerator Laboratory.)

precise three-momentum measurement, and in addition, since specific ionization dE/dx measurements are obtained from the SVT and DCH, it is also an essential part of the *BABAR* particle identification (PID) system for charged particles. This is most important for tracks emitted at small polar angles, since the DIRC (see Sec. 4.4) does not cover such particles.

In *BABAR* coordinates, the z -axis is defined to be parallel to the DCH magnetic field generated by the aforementioned solenoid and points in the forward direction. The x -axis points towards the center of the storage ring and y completes the right-handed orthogonal coordinate system. The collision axis is not parallel to the z -axis, but rotated by ~ 20 mrad in the xz -plane. This configuration provides minimal angles between the fields of the guide magnets in front of and behind the detector and the incoming as well as outgoing beams, thus minimizing perturbation of the beams by the magnetic fields. The DCH – filled with a 80:20 Helium-Isobutane mixture – consists of 40 layers of wire cells (a unit of field wires surrounding a sense wire), which are arranged in cylindrical symmetry around the z -axis. If a charged particle passes through the gas mixture, it ionizes part of the atoms along its path. The produced electron (ion) is accelerated towards the anode (cathode) wire. Once the electron is close enough to the anode, the electric field becomes sufficiently strong to accelerate the electron to high enough energies, such that partial ionization occurs. This process reproduces, causing a *Townsend avalanche*, until the electrons reach the anodic sense wire, and generate a measurable electrical signal. By this mechanism, 40 spatial and ionization loss measurements can be

Figure 32.: Schematic drawing of a longitudinal section through the BABAR Silicon Vertex Tracker. (Courtesy of SLAC National Accelerator Laboratory.)



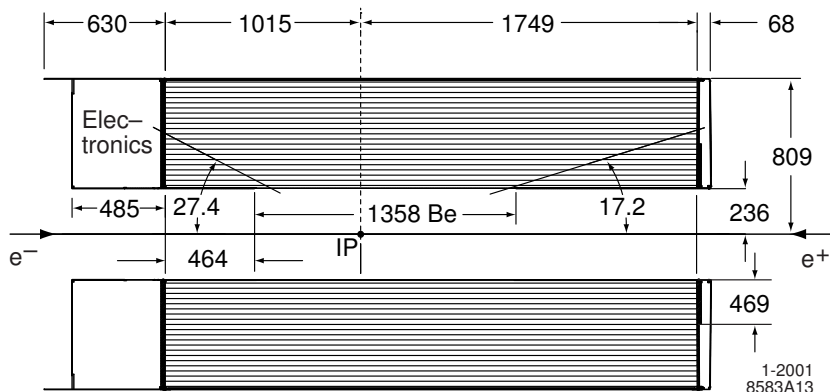
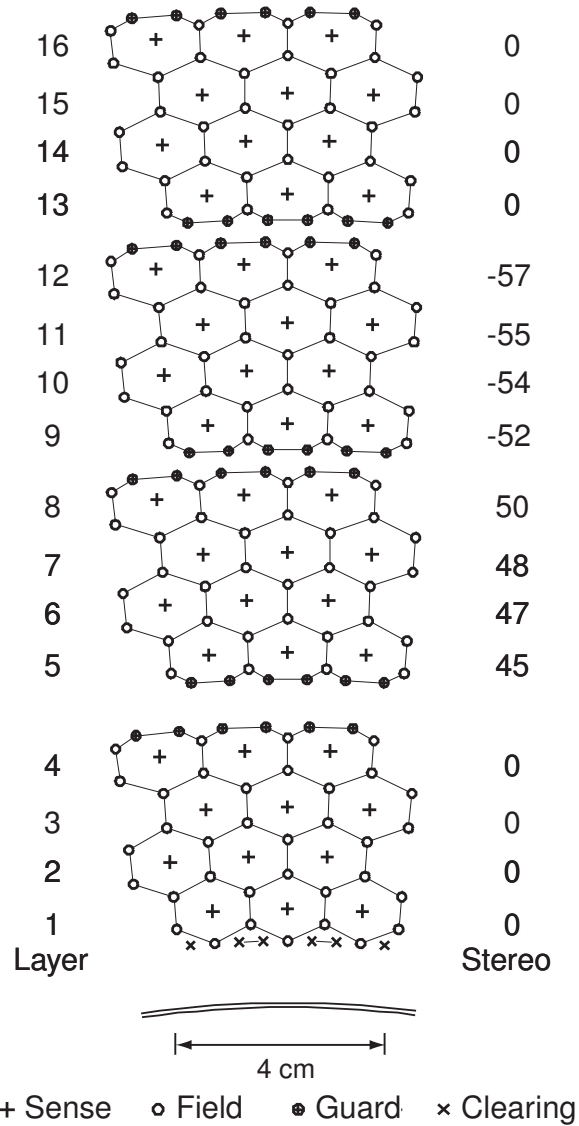


Figure 33.: Schematic drawing of the *BABAR* drift chamber. Distances in mm, angles in $^\circ$, “IP” is the nominal interaction point, and “Be” denotes the beryllium tube in the center of the DCH. (Courtesy of SLAC National Accelerator Laboratory.)

obtained in the DCH for tracks which traverse the entire chamber, i.e. for transverse momenta above ~ 180 MeV/c.

As shown in Fig. 33, the chamber spans 2764 mm. The interaction point (IP) is offset by 37 cm in the backward direction from the center of the chamber to account for the boost resulting from the asymmetric beam energies. The DCH takes the form of a hollow cylinder with inner radius of 236 mm and outer radius of 809 mm with respect to the z -axis, about which it has azimuthal symmetry. Particles emitted from the IP at polar angles of at least 17.2° and 27.4° in forward and backward direction, respectively, traverse at least half of the wire layers. The wires are arranged in hexagonal cells as shown in Fig. 34, such that the cells at a particular radius form a layer. The individual layers are grouped into superlayers consisting of 4 layers, where all layers within a superlayer have the same orientation (positive angles “U”, negative angles “V”, null angle “A”) with slightly varying stereo angles. These layers are skewed by small stereo angles from 45 mrad to 70 mrad with increasing radius to provide z -coordinate information for each measured track. The superlayers are ordered such that the stereo angles follow the pattern “AUVAUVAUVA” with increasing radius.

This results in a single-hit resolution of ~ 100 μm . The measured coordinates can be used to extract the bending radius of a charged track due to the 1.5 T solenoidal magnetic field, yielding a relative transverse momentum resolution of $\frac{\sigma(p_T)}{p_T} = 0.47\%$. The energy loss measurement for a track intersecting ~ 40 layers of the DCH has a relative standard deviation of $\frac{\sigma(dE/dx)}{dE/dx} \approx 8\%$.



1-2001
8583A14

Figure 34.: Layout of the first 16 wire cell layers in the *BABAR* drift chamber. Each group of layers (layers 1-4, 5-8, 9-12, 13-16...) makes up one superlayer. The layer numbers are listed on the left, the stereo angle in mrad of each layer is given in the right column, and the different wire types are marked with specific symbols. (Courtesy of SLAC National Accelerator Laboratory.)

4.4 DETECTOR OF INTERNALLY REFLECTED CHERENKOV LIGHT

Charged particles traversing any medium at a velocity higher than the speed of light in that material, emit a cone of radiation, a phenomenon known as the Cherenkov effect [161]. The angle between the direction of the track and the emitted light is given by $\Theta_C = \arccos(1/n\beta)$, where n is the refractive index of the medium, and $\beta \equiv v/c$ with v the particle velocity and c the speed of light in vacuum. Therefore a measurement of the Cherenkov angle Θ_C directly translates into a measurement of the particle velocity v . Since the momentum p is known from the Drift Chamber, the mass can be extracted ($m_0c = p\sqrt{1/\beta^2 - 1}$), hence identifying the particle.

The *BABAR* DIRC, illustrated in Fig. 35, is a modern type of Cherenkov detector, where fused silica bars serve as radiators as well as transmitters of the produced Cherenkov light. It consists of 144 fused silica bars arranged in bar boxes to form a regular 12-sided polygon at a minimum distance of 836.5 mm around the z -axis. The bars cover a length of 4.9 m, or 83 % of the CM polar angle cosine. Due to small gaps between the bar boxes, 94 % of 2π in azimuth is covered. Part of the radiation cone undergoes total internal reflection if the particle velocity is high enough (the refractive index of fused silica is $n \approx 1.473$, thus $\beta \gtrsim 0.925$ is necessary, corresponding to a pion with a momentum of ~ 340 MeV/ c in the laboratory frame) or the track is sufficiently angled toward the forward or backward direction. The emitted light is reflected at the surfaces of the bar, until it reaches the backward end, as shown in Fig. 36. Light radiated in the forward direction is first reflected by a mirror at the forward end of the bar. Upon reaching the backward end, it is then transmitted through an optical system and the water-filled Standoff Box (SOB) to the array of 10752 photomultiplier tubes (PMTs) for detection. The geometrical configuration of the responding PMTs is then processed by the software to yield the radius of the light cone and thus the Cherenkov angle.

A typical signal produced by a $\mu^+\mu^-$ -event is shown in Fig. 37, where the “smile” (upward facing cone section) and “frown” (downward facing cone section) can be observed clearly. The existence of an inverted image is due to the finite size of the optical system. In order to keep the device compact, a wedge is attached to the back end of each bar; this projects radiation emerging from the bar at very large angles onto PMTs at smaller angles, as this radiation is reflected at the upper edge of the wedge. If only part of the emitted cone hits the upper edge of the wedge, an additional inverted image is produced. Also, the lower surface of the wedge is sloped slightly upwards (6 mrad) in order to focus different parts of the light output onto the same region, as illustrated in Fig. 36. The

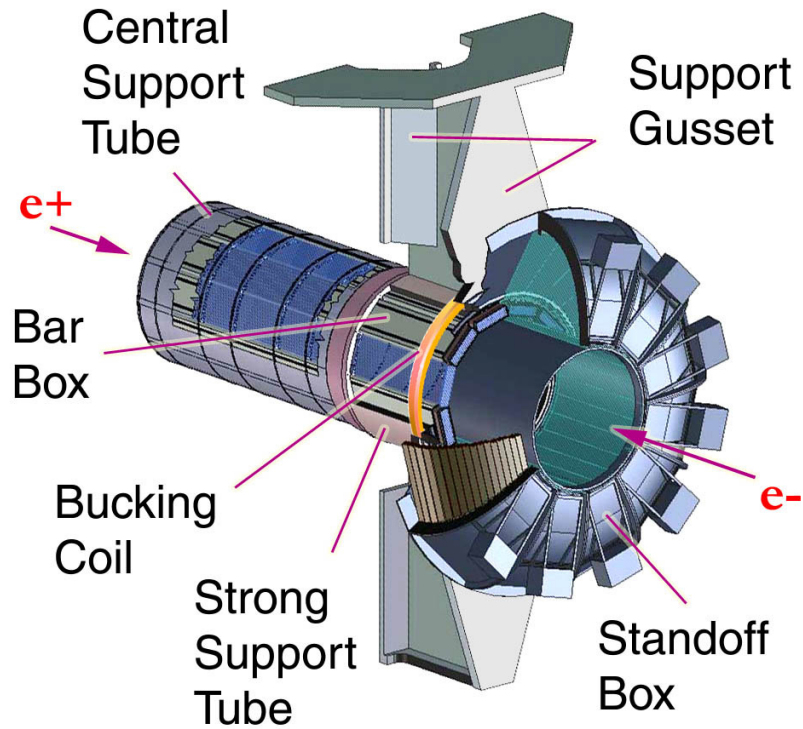


Figure 35.: Overview of the *BABAR* DIRC. (Courtesy of SLAC National Accelerator Laboratory.)

overall single photon angular resolution is about 10 mrad, and is mainly determined by the angular separation of the PMTs and photon dispersion. Depending on the polar angle of the track, between 20 and 65 Cherenkov photons are expected, leading to a track angle resolution of ~ 2.5 mrad. As a result, a 4.2σ separation between pions and kaons is achieved at momenta around 3 GeV/c.

4.5 ELECTROMAGNETIC CALORIMETER

The measurement of photon energies is an essential part of the present analysis, since the ISR photon must be measured accurately, and neutral pions have to be reconstructed by combining two detected photons. Therefore it is fundamental to precisely measure energy and direction of photons.

Electromagnetic Calorimeters (EMC) are designed specifically to quantify the amount of energy deposited by a photon or electron in the form of an electromagnetic shower. This process occurs when a photon of more than a few MeV passes through a material of high nuclear charge (i.e. high atomic number Z), and interacts with the intrinsic electric field. The interaction causes the photon to undergo e^+e^- pair production. The electrons and positrons in turn emit bremsstrahlung photons, starting the process anew, hence cre-

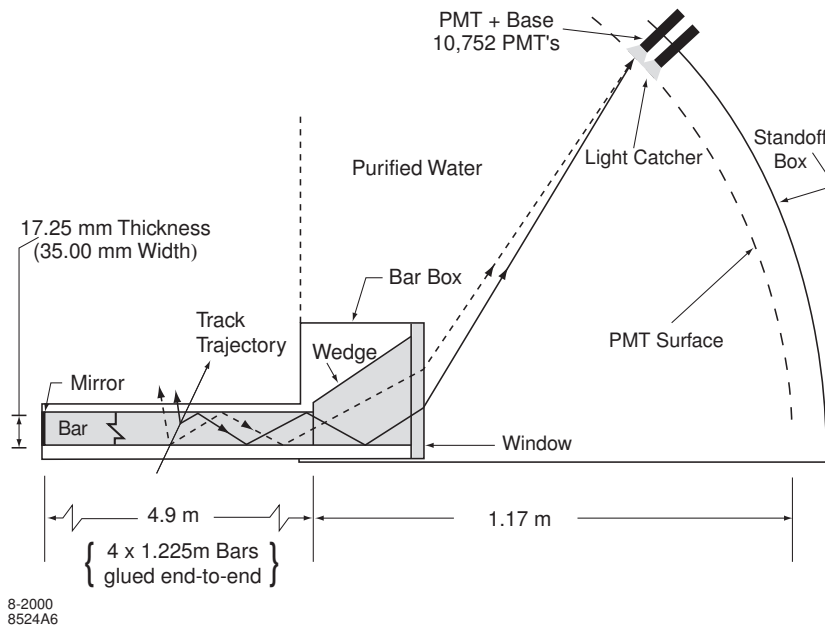


Figure 36.: Schematic drawing of the *BABAR* DIRC. (Courtesy of SLAC National Accelerator Laboratory.)

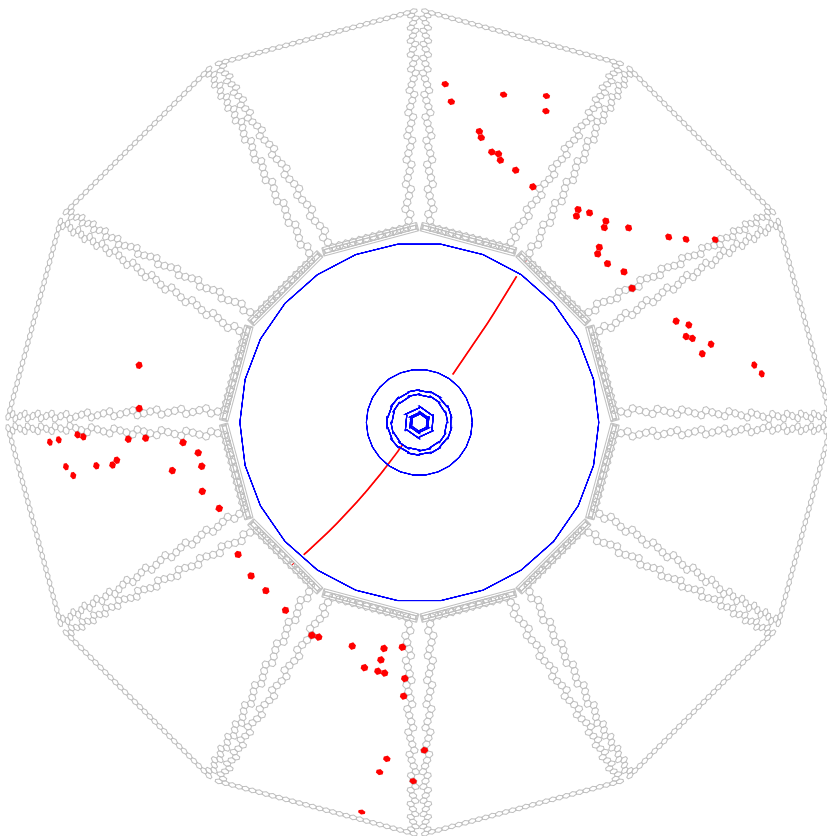


Figure 37.: Typical signal of a $\mu^+ \mu^-$ -event (red dots) in the *BABAR* DIRC as seen along the beam axis. The reconstructed tracks are shown as red lines from the SVT to the DIRC. (Courtesy of SLAC National Accelerator Laboratory.)

ating an *electromagnetic shower*. Through this cascade, the energy of the original photon is divided up until e^+e^- pair production is no longer possible. If the process takes place in an array of scintillating crystals, the incident particle's energy can be determined by counting the number of scintillation photons produced, provided the array is sufficiently deep in terms of radiation length, such that the incoming energy is completely absorbed.

The *BABAR* EMC consists of 6580 CsI crystals doped with Thallium. The barrel section of the EMC is divided into 48 rings of 120 crystals each, while the forward end cap is constructed of 820 crystals in 8 rings. As shown in Fig. 38, in addition to its azimuthal symmetry, the EMC is arranged in a projective geometry, such that each crystal is pointed near the interaction point. Silicon photo diodes are mounted onto the back of each crystal to collect the scintillation light. The combination of these features yields excellent determination of photon energy and position at the inner surface of the EMC with a coverage of around 90 % of the solid angle in the center of mass frame. Assuming that the photon originated at the interaction vertex of the associated event, its direction is also well-measured as shown below.

Electromagnetic showers in the energy range from 20 MeV to 9 GeV can be measured in the *BABAR* EMC with a resolution of

$$\frac{\sigma_E}{E} = \frac{a}{\sqrt[4]{E(\text{GeV})}} \oplus b, \quad (42)$$

where the operator \oplus signifies addition in quadrature. The first term is associated with fluctuations in photon statistics, combined with electronic noise and beam-related backgrounds. The second term accounts for shower leakage, light-collection issues, and further detector imperfections. Calibration with a radioactive source yields $\sigma_E/E = (5.0 \pm 0.8)\%$ at 6.13 MeV, while at higher energies the resolution is measured at multiple points using Bhabha scattering. For instance $\sigma_E/E = (1.9 \pm 0.07)\%$ is achieved at 7.5 GeV. Fitting the resolution function in Eq. 42 to the measurements yields $a = (2.30 \pm 0.30)\%$, and $b = (1.85 \pm 0.12)\%$.

While for energies below 2 GeV the π^0 mass resolution in the decay $\pi^0 \rightarrow 2\gamma$ is dominated by the photon energy uncertainty, at high energies the angular resolution becomes most important. It can be described by

$$\sigma_\theta = \sigma_\phi = \frac{c}{\sqrt{E(\text{GeV})}} + d. \quad (43)$$

From the study of π^0 and η decays the values $c = (3.87 \pm 0.07)$ mrad, and $d = (0.00 \pm 0.04)$ mrad are obtained, resulting in angular resolution of 3-12 mrad.

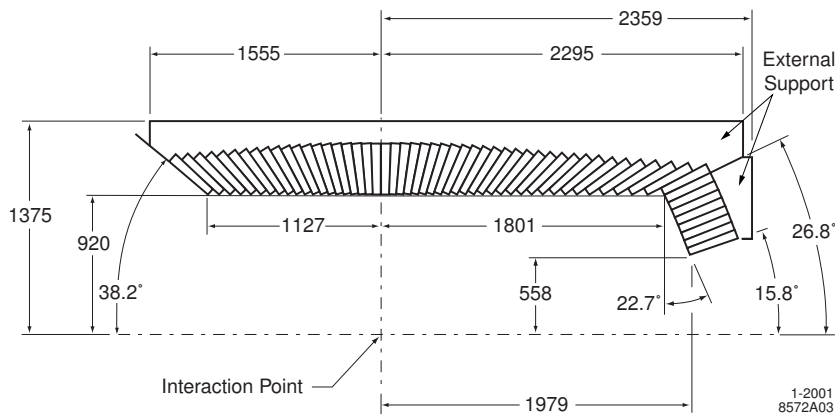


Figure 38.: Cross section of the *BABAR* EMC's top half along the beam-axis. The projective arrangement of the 56 crystal rings is shown, with all dimensions given in mm. (Courtesy of SLAC National Accelerator Laboratory.)

4.6 INSTRUMENTED FLUX RETURN

In order to yield a highly uniform and well-known magnetic field within the detector volume, the magnetic flux has to be fed back into the region interior to the cryostat containing the superconducting solenoid. In the *BABAR* experiment, this is accomplished by means of end-cap iron doors and an iron yoke surrounding the EMC and thus most of the detector. This structure, shown in Fig. 39, can be exploited to identify muons and detect neutral hadrons such as neutrons or K_L mesons by *instrumenting* it.

The *BABAR* Instrumented Flux Return (IFR) was initially equipped exclusively with Resistive Plate Chambers (RPCs) in between the steel plates of the magnet flux return. An RPC consists of two highly resistive parallel plates, one charged negatively (cathode) and the other charged positively (anode), while the volume between the plates is filled with a gas mixture (567:388:45 mix of Argon, Freon R-134a and Isobutane at *BABAR*). If a photon or a charged particle (like a muon) passes through the gas, ionization occurs, as in the drift chamber. Neutral hadrons first interact with the material of the IFR to produce a secondary charged particle or photon. Due to the significantly higher electric field, a controlled *gas-discharge avalanche* (known as a *streamer*) is triggered in an RPC. This means that the produced signal is only weakly dependent on the initial size of the ionization. The discharge avalanche is detected outside the plates via two perpendicular sets of aluminum strips yielding ϕ - and z -coordinates. However, the RPC performance degraded over time, so that many modules had to be replaced by improved RPCs (in the endcaps) and by Limited Streamer Tubes (LSTs) in the barrel [158] shown on the left hand side of Fig. 39. A Limited Streamer Tube consists of multiple PVC-cells (Polyvinyl chloride),

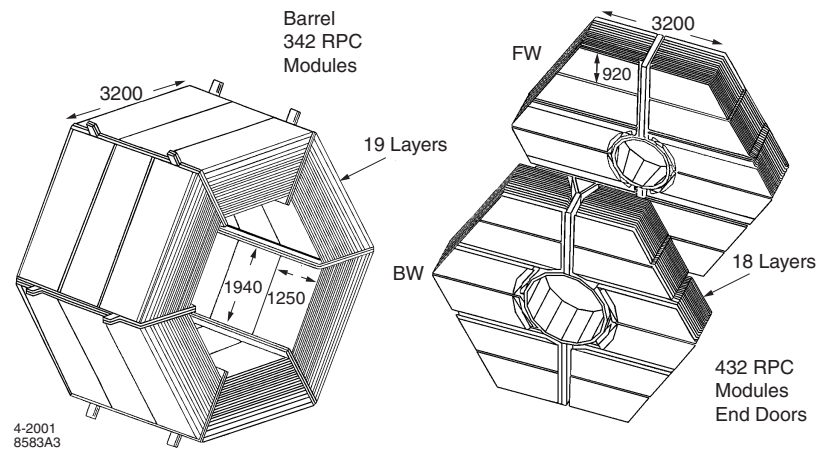


Figure 39.: Schematic picture of *BABAR*'s instrumented flux return. Lengths in mm. (Courtesy of SLAC National Accelerator Laboratory.)

each graphite-coated, around a high voltage wire. The operating principle is similar to that of a drift chamber operating at a voltage slightly above proportional mode (where the electrical signal strength is proportional to the incident particle's energy). The ϕ -coordinate of a detected track is determined directly by the wires which register a signal. The z -coordinate is calculated from the charge induced on external copper readout strips.

In the final configuration the *BABAR* IFR consisted of approximately 1200 LSTs in 12 of the 19 gaps between the plates of the IFR barrel, separated by 2 cm to 10 cm of steel (6 gaps were filled with brass, while one gap was geometrically impossible to retrofit). The endcaps were equipped with 18 layers of RPCs also separated by 2 cm to 10 cm of steel. Each layer consisted of 12 RPCs in total, arranged in chambers of 2 RPCs each.

4.7 TRIGGER AND DATA ACQUISITION

After detection, the trigger system evaluates each event candidate to determine whether it should be recorded. The *BABAR* trigger system is implemented in a two-layer hierarchy, where L1 is the hardware-, and L3 the software-level.² While running on the $\Upsilon(4S)$ resonance, the system achieved an efficiency of 99 % for the $B\bar{B}$ decays desired in a *B* Factory, but also more than 95 % for continuum decays. The trigger also performed extremely well against machine background, providing trigger rates well above the design values in L1 and L3 in the expected conditions. Even as luminosity increased above the design value, the system managed to keep dead time constant around the design value of 1 %.

² Against all intuition, an L2 trigger does not exist.

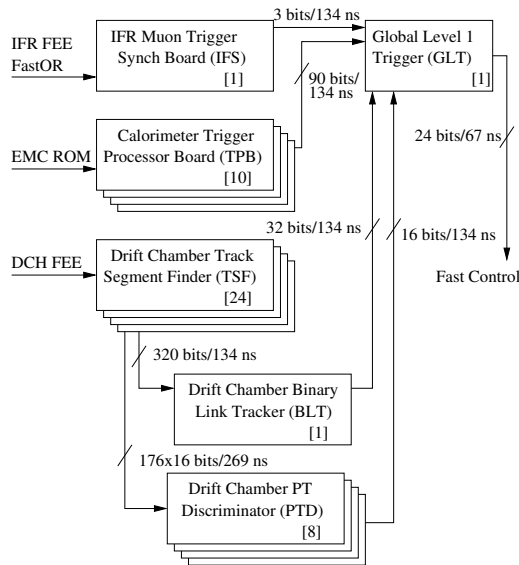


Figure 40.: *BABAR* L1 trigger schematic. (Courtesy of SLAC National Accelerator Laboratory.)

In the L1 trigger information from the DCH (for charged tracks) and from the EMC as well as IFR (for showers) is processed, as shown in Fig. 40. These inputs, listed below, are highly redundant, providing the excellent efficiency and the possibility of precise determination of each separate trigger line's efficiency:

- The Drift Chamber Trigger's Track Segment Finder at first searches line segments of supposed trajectories and then passes this information on to the the Binary Link Tracker (BLT) and the p_T discriminator (PTD). The BLT links the track segments together for events with low transverse momentum ($p_T < 0.8 \text{ GeV}/c$), while the PTD takes care of the high- p_T events. Each of the two sends a signal to the global trigger if a valid track has been detected.
- The Electromagnetic Trigger (EMT) compares the energies detected in 40 azimuthal ϕ sectors summed over various polar θ -ranges to the corresponding thresholds and sends the result to the global trigger.
- The Internal Flux Trigger (IFT) selects $\mu^+\mu^-$ events and cosmic rays. A signal is produced if in one of the 8 pre-defined sectors at least 4 out of 8 layers register a hit.

From all the received information, the global trigger forms specific inputs for the Fast Control and Timing System (FCTS). If the FCTS detects a valid trigger (after masking, prescaling etc.), an L1 accept signal is issued, initiating event readout and feeding it into the L3 trigger.

The L3 trigger software reconstructs and classifies each event in order to filter according to specified background recognition conditions. The procedure consists of three steps: first, inputs are constructed by logical combination of all incoming signals from the FCTS. Then, these inputs are processed using a variety of freely programmable scripts, which are designed to identify specific categories of processes. Finally, the output lines are formed by logically combining the results of the different scripts. These L3 trigger lines are henceforth used to select a certain class of decay or filter out background processes. By suppressing backgrounds like Bhabha events, the amount of information to be processed is reduced by approximately an order of magnitude between L1 and L3.

It is noteworthy that the flexibility of the *BABAR* trigger considerably expands the spectrum of measurements possible at the *BABAR* experiment despite being intended as a *B* Factory. It especially provides the opportunity to study ISR-processes with high precision.

SUMMARY OF THE EXPERIMENTAL SETUP

It should not be taken for granted that an experiment designed as a *B* Factory facilitates the means to measure hadronic cross sections with high precision. Many components need to be versatile enough to not only measure $B\bar{B}$ decays but also an initial state photon and simultaneously several charged tracks and neutral mesons. Hence a drift chamber with a wide momentum range is needed as well as an electromagnetic calorimeter suitable for energy measurements down a few MeV. Accurate vertexing and particle identification via vertex and Cherenkov detector as well as an instrumented flux return further help improve such analyses. Yet all ISR measurements are ultimately only possible due to the fact that the trigger records not only typical $B\bar{B}$ events but is also programmed to store hadronic ISR events, a remarkable feature for an experiment intended for a very different purpose.

GENERAL PROCEDURE & DATA SET

In this chapter, the general analysis procedure of the cross section measurements is introduced. Furthermore, the data set and simulation samples are summarized, followed by an overview of the selection common to both signal channels: $e^+e^- \rightarrow \pi^+\pi^-2\pi^0\gamma_{\text{ISR}}$ and $e^+e^- \rightarrow \pi^+\pi^-3\pi^0\gamma_{\text{ISR}}$. To reduce redundancy, some figures and numbers are only shown for one of the signal channels when the results are similar.

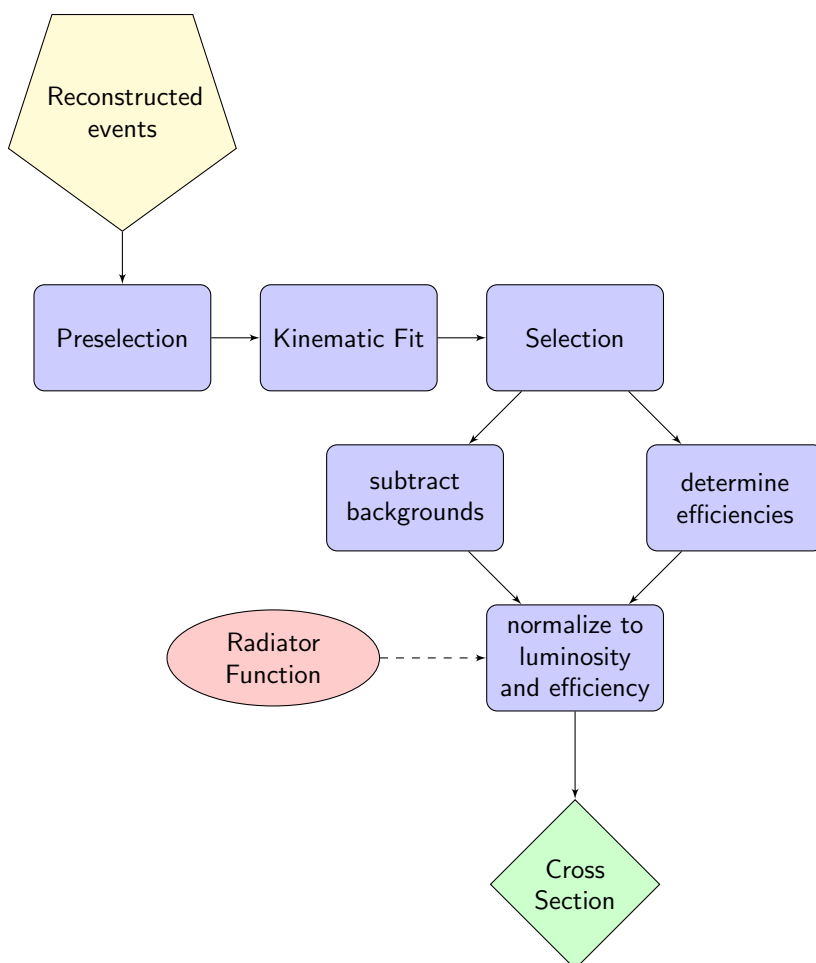


Figure 41.: Schematic chart of the analysis procedure.

5.1 GENERAL ANALYSIS PROCEDURE

The procedure applied to the events in this type of cross section analysis is shown in Fig. 41. The analyses are event-based, so that

as the very first step, a rough preselection (see Sec. 5.3 for details) is applied which should reject background processes whose kinematics are very different from the signal channels without significant loss of signal statistics. The remaining events are subjected to the kinematic fit outlined in Sec. 5.5. Afterwards, the results of the kinematic fit in combination with further event variables is used in the final selection (Sec. 5.7). The resulting event set may still be polluted by competing background processes whose events survive the selection with small probability. These remaining background events are subtracted using the corresponding simulation samples (which have also undergone the full procedure) or a data driven method (Sec. 6.2 & Sec. 7.2). In parallel, the analysis procedure is also applied to the signal simulation and the resulting event distribution is divided by the originally generated distribution. The result is the combination of detector acceptance and efficiency. In the following step, the event set from data is divided by the acceptance and efficiency from simulation, yielding the approximate event rate in nature. The final step is the normalization to the radiative ISR luminosity (Sec. 3), resulting in the cross section.

5.2 DATA SET AND SIMULATION SAMPLES

For this measurement the full $Y(4S)$ on peak data set of 454.3 fb^{-1} is used, incorporating runs 1 through 6. The individual runs are the data taking periods at *BABAR* which usually lasted around one year.

Besides data, simulation samples for signal and background channels are used. These samples are produced using different generators specified below and then processed by the GEANT4-based detector simulation. The main purpose of these samples is to help choose the selection criteria and, in the case of the signal simulation, for the calculation of efficiency and acceptance. The background simulation samples are also used to subtract background contributions remaining after selection.

For the signal channel $e^+e^- \rightarrow \pi^+\pi^-2\pi^0\gamma_{\text{ISR}}$, a dedicated Monte Carlo (MC) sample exists, which is produced with the AFKQed event generator [153, 162]. AFKQed is based on EVA, an early version of the state-of-the-art event generator for ISR processes: PHOKHARA [163, 164]. The production of hadrons is modeled by expressing the hadronic electromagnetic current in terms of form factors. The hadronic tensor (defined as the covariant product of the current with its own complex conjugate) is subsequently contracted with the leptonic tensor (known from QED), giving the differential cross section. Furthermore, initial state radiation is included in the AFKQed generator, but final state radiation (FSR) is not. FSR is included using PHOTOS [165] as outlined in Sec. 7.4.2.

The PHOTOS generator relies on the structure function technique for additional photon radiation.

The same type of simulation exists for the channels $\pi^+\pi^-\pi^0\gamma_{\text{ISR}}$, $\omega 2\pi^0\gamma_{\text{ISR}}$, $\eta\pi^+\pi^-\gamma_{\text{ISR}}$, $2(\pi^+\pi^-)2\pi^0\gamma_{\text{ISR}}$, $K^+K^-2\pi^0\gamma_{\text{ISR}}$, $K_s K^\pm \pi^\mp \gamma_{\text{ISR}}$, which are possible background channels in both analyses.¹

However, no complete simulation of the signal channel $e^+e^- \rightarrow \pi^+\pi^-3\pi^0\gamma_{\text{ISR}}$ exists. Only simulation samples of the subchannels $e^+e^- \rightarrow \omega 2\pi^0\gamma_{\text{ISR}}$ and $e^+e^- \rightarrow \eta\pi^+\pi^-\gamma_{\text{ISR}}$ are available. Both samples are processed such that they only contain the final state $\pi^+\pi^-3\pi^0\gamma_{\text{ISR}}$.

A $\tau^+\tau^-(\gamma)$ background sample was generated with KK2f [166].

In addition to the simulation samples mentioned above, a JETSET [167] production of continuum events is used to subtract non-ISR-background from data. In this generator, the process $e^+e^- \rightarrow \gamma^*/Z^0 \rightarrow q\bar{q}$ is modeled, where q can be any quark. In the present case, the simulation is restricted to γ^* in the intermediate state and $q = u, d, s$. JETSET uses a string-based model for the hadronic decay of the $q\bar{q}$ state. This model exploits QCD confinement: when the two partons of the $q\bar{q}$ pair move away from their common production vertex, the potential energy rises linearly in their distance from each other. Once this distance surpasses a certain threshold, it becomes energetically favorable to split the string into two substrings by generating another quark pair $q'\bar{q}'$. This process repeats for each of the two new strings ($q\bar{q}'$ and $q'\bar{q}$) until on-shell hadrons are produced.

All continuum simulation events including a *true* photon (e.g. ISR or FSR photon, but not a photon from e.g. a π^0 -decay) with MC-true energy $E_\gamma > 3$ GeV are discarded because they are considered ISR events, e.g. the $2\pi 3\pi^0\gamma$ -signal, which is first of all not sufficiently described by JETSET (more precise, dedicated generators for ISR processes exist, thus they should be used for these cases). Secondly, part of the signal channels is also included in the ISR processes of the continuum simulation, but is of course not supposed to be subtracted from data.

All simulation samples are prepared and provided by the *BABAR* Monte Carlo working group, which adjusts the aforementioned generators to the experimental circumstances and processes the generated events in a GEANT4-based detector model. As will be shown in the following chapters, these simulation samples constitute all relevant background processes for the $\pi^+\pi^-2\pi^0\gamma_{\text{ISR}}$ analysis with the exception of $\pi^+\pi^-3\pi^0\gamma_{\text{ISR}}$. This is part of the reason to analyze the channel $\pi^+\pi^-3\pi^0\gamma_{\text{ISR}}$, where a data-driven background subtraction method is employed. The resulting cross section can

¹ Here and throughout this work, in the context of particle combinations the notation “ 2π ” implies a pair of charged pions $\pi^+\pi^-$. The same notation holds for other particles, such as kaons.

then be used for the background subtraction in the $\pi^+\pi^-2\pi^0\gamma_{\text{ISR}}$ analysis.

5.3 PRESELECTION

The following section describes the first step of the selection procedure to extract the signal events from data. Moreover it introduces the different levels of Ntuples, starting with the original *Level-1 Ntuples* (“L1”), which are reduced to *Level-2 Ntuples* (“L2”) by rejecting non-ISR events. For each specific final state *Level-3 Ntuples* (“L3”) are produced, which contain several combined, kinematic variables. At the end, the tight final selection is applied, filtering out most background events.

The initial selection of ISR-events does not include criteria designed to select $\pi^+\pi^-2\pi^0\gamma$ or $\pi^+\pi^-3\pi^0\gamma$ events, but instead all ISR events. The most important criteria for an ISR-event are the existence of at least one charged track² and a high-energetic photon with $E_{\gamma_{\text{ISR}}}^{\text{CM}} > 3 \text{ GeV}$ (in the Center-of-Mass Frame). All events fulfilling these requirements are stored in the *Level-1-Ntuples (L1)*.

For ISR simulations, all produced events are stored until *Level 2 (L2)* to allow efficiency determination, whereas only events satisfying the selection criteria outlined below are stored for data and non-ISR background channels. In *L2*, the selected events have to comply with the following trigger and background filter requirements, standardized by the *BABAR* ISR group:

- MC: at least one particle produced by the generator.
- MC: isrfilter = true: this filter scales down radiative Bhabha events (which are sometimes used for calibration and normalization) to $1/40$ and rejects events that do not fit the topology of an ISR process with a high-energetic photon.
- trgl10 \neq 0 \wedge trgl3 \neq 0 : these trigger lines reject many non-ISR processes by requiring a high energy EMC-cluster (e.g. from the ISR-photon) or another signature from DCH and EMC consistent with the topology of ISR events.
- bkgfilter \neq 0 : this filter mainly excludes events without usable EMC-cluster(s) and without charged tracks coming from the interaction point.
- radbhabha \neq true : this trigger rejects events matching the kinematic properties of Bhabha scattering. Most importantly, events with two tracks, one of which carries a momentum equivalent to more than 70 % of the beam energy are discarded.

² Disregarding channels like $e^+e^- \rightarrow \pi^0\gamma(\gamma_{\text{ISR}})$ etc., which are not of interest to this work.

Overall, the trigger efficiency is very close to 100 % for ISR-events, such that no considerable loss in statistics is suffered through these conditions.

The summary of data and simulation samples used in this work is shown in Tab. 3. A tighter selection, outlined below, is applied to the charged tracks and photons of the remaining events before they are submitted to the kinematic fit.

Table 3.: The available data and simulation samples. N_{exp} is the expected number of events, based on the *BABAR* luminosity. N_{L_2} is the number before selection, only the preselection for the *Level-2-Ntuples* was applied to the *Level-1-Ntuples* as outlined in Sec. 5.3. For the ISR simulations, all events in *L1* are saved in *L2*.

Channel	$\sigma[\text{pb}]$	N_{exp}	N_{L_2}
data			6151886
$\pi^+\pi^-2\pi^0\gamma_{\text{ISR}}$ MC			10276910
uds MC	2090	949541340	1497084
$\tau\tau(\gamma)$ MC	890	404350140	560832
$\pi^+\pi^-\pi^0\gamma_{\text{ISR}}$ MC	2.6	1181248	9711860
$2(\pi^+\pi^-\pi^0)\gamma_{\text{ISR}}$ MC	1.8	835128	150689
$K^+K^-2\pi^0\gamma_{\text{ISR}}$ MC	0.25	113582	98420
$K_s K^\pm \pi^\mp \gamma_{\text{ISR}}$ MC	0.3	136298	3507966
$\eta\pi^+\pi^-\gamma_{\text{ISR}}$ MC	0.25	113582	4837730
$\omega 2\pi^0\gamma_{\text{ISR}}$ MC	0.45	204447	7951921

5.4 TRACK AND PHOTON REQUIREMENTS

Concerning charged tracks, the following selection is required for a track to be flagged as “good” track:

- maximum distance from the interaction point in the xy -plane: $\text{docaXY} < 1.5$ cm,
- maximum distance from the interaction point along the z -axis: $|\text{dZ}| < 2.5$ cm,
- transverse momentum: $p_{\text{trans}} > 0.1$ GeV/c,
- polar angle: $0.4 \text{ rad} \leq \theta^{\text{lab}} \leq 2.45 \text{ rad}$.

Only events with exactly 2 “good” tracks are used in the cross section analysis. It has been studied that after the full selection 1-good-track events with a recoverable second “almost-good” track and 3-good-track events where the worst track (track with the same charge as one of the others and the larger docaXY) is discarded

only increase statistics by $(0.75 \pm 0.02)\%$ and $(0.62 \pm 0.02)\%$ respectively in data and signal simulation for the $\pi^+\pi^-2\pi^0\gamma$ channel, with similar results in the $\pi^+\pi^-3\pi^0\gamma$ case. Thus the clean 2-good-track sample can be used without significantly increasing the statistical uncertainty while avoiding additional systematics. Furthermore, systematic uncertainties due to the subtraction of background channels with predominantly 1 or 3 tracks are minimized.

Concerning the photons, the highest energetic photon in the Center-of-Mass frame is selected as ISR photon and as mentioned above needs to have an energy of at least 3 GeV in CM frame, which suppresses background from B -decays while removing hardly any signal events. All other photons need to have a minimum lab-energy of 50 MeV to be a candidate for a photon from a π^0 decay. One of the π^0 -photons has to have a lab-energy above 100 MeV. This requirement is implemented to exclude low energy photons and machine background.³ Low energy photons are mostly radiated by the initial or final state particles but do not originate from the decay of the π^0 we are trying to detect.

A kinematic fit will be used in the following to determine how well an event is described by the signal hypothesis. The kinematic fit needs two charged tracks and an ISR photon. Additionally, the number of non-ISR photons has to be at least sufficient to reconstruct the hypothetical number of π^0 s in order for the event to enter the kinematic fit. Thus, for the signal hypothesis, at least one ISR-photon and four/six ($\pi^+\pi^-2\pi^0\gamma/\pi^+\pi^-3\pi^0\gamma$) additional photons are required. Furthermore, only events with less than 100 photons are processed. The resulting χ^2 , which can be used as a goodness-of-fit test, is one of the most important measures to distinguish signal from background.

5.5 KINEMATIC FIT

One of the rewards of writing notes on fitting theory is the number of people who stop me in the street to shake my hand, telling me breathless stories of how kinematic fitting changed their lives.

– Prof. Paul Avery

The uncertainties of an event's measured observables can be improved by imposing restrictions exploiting the structure of the reaction under investigation. When one final state is studied exclusively, a kinematic fit can be applied to the measured detector response.

Kinematic fitting is a problem of constrained optimization. A loss function (e.g. χ^2 or negative (Log-)Likelihood) must be mini-

³ Machine background is composed mostly of detector signals not originating from e^+e^- collisions. Example processes include beam particles hitting apertures or photons from Bremsstrahlung with beam gas.

mized by adjusting a set of parameters while fulfilling constraints. Specifically for kinematic fitting this means that the predicted 4-momenta are chosen in such a way that they obey energy-momentum conservation and possibly other physical constraints while staying as close as possible to the originally measured variables. Algorithmically, this is achieved⁴ through the method of *Lagrange multipliers*. The corresponding Lagrangian L can be written as

$$L(\vec{x}, \hat{x}) = S(\vec{x}, \hat{x}) + \vec{\lambda} \cdot \vec{C}(\hat{x}), \quad (44)$$

where \vec{x} is the vector of measured values, \hat{x} its predicted counterpart, S is the loss function which incorporates the detector resolution, $\vec{\lambda}$ are the Lagrange multipliers, and \vec{C} are the constraints, parameterized such that $C_j(\hat{x}) = 0 \forall j$. The optimal vector \hat{x} can now be found by solving the system of equations

$$\begin{aligned} \frac{\partial L}{\partial \lambda_j} &= 0 & \forall j, \\ \frac{\partial L}{\partial \hat{x}_k} &= 0 & \forall k. \end{aligned} \quad (45)$$

For a more detailed derivation see e.g. Ref. [168].

In the kinematic fit to the $2\pi 2\pi^0 \gamma$ ($2\pi 3\pi^0 \gamma$) hypothesis six (seven) constraints are required: four from energy-momentum-conservation of the complete event and two (three) from the photon-photon-masses, which have to equal the π^0 mass. The fit takes the measured momenta of the two charged tracks and the five (seven) photons (ISR + $2(3)\pi^0$) as input and returns their fitted values and a χ^2 as a test of the goodness-of-fit. Subsequently all variables depending on the particle momenta can be computed from the fitted values. Throughout this work, the observables calculated from the fitted values are used unless stated otherwise.

Using the two “good” charged tracks, the algorithm selects all events with at least $2 \cdot n_{\pi^0} + 1$ photons of lab-energy greater than 0.05 GeV. After the photon with the highest CM-energy is picked as γ_{ISR} , out of the remaining total number of photons, all combinations of $2 \cdot n_{\pi^0}$ photons with $E_{\gamma}^{\text{lab}} > 0.05$ GeV (apart from the ISR photon) are then considered as candidates for the π^0 . Within each set of these $2 \cdot n_{\pi^0}$ photons, all partitions of n_{π^0} photon pairs are constructed. If the two-photon masses ($m_{\gamma\gamma}$) are within 0.03 GeV of the true π^0 mass and one of the four/six π^0 -photons has a lab-energy greater than 0.1 GeV, the combination is passed on to the kinematic fit. From a fit to the data ($\pi^+ \pi^- 2\pi^0 \gamma$ simulation) distribution in Fig. 42 the width of the π^0 peak was determined to be 7.3 MeV (7.5 MeV) for the signal channel $\pi^+ \pi^- 2\pi^0 \gamma$, similarly for $\pi^+ \pi^- 3\pi^0 \gamma$. Using the 30 MeV window, reasonable photon combinations enter the kinematic fit (together with the “good” tracks).

⁴ Alternative methods exist, but are not employed in this analysis.

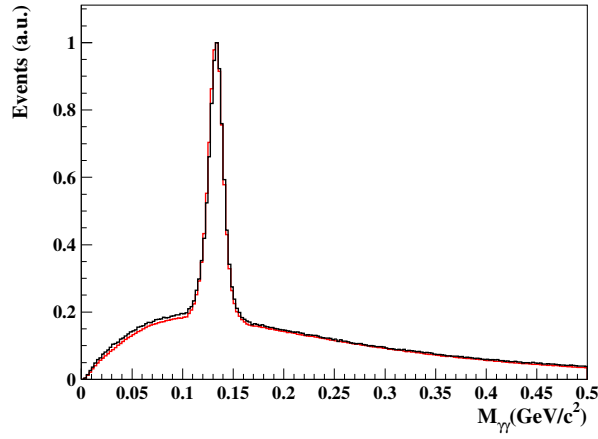


Figure 42.: Distribution of the two-photon masses in data (black) and $\pi^+\pi^-2\pi^0\gamma$ MC (red), peak heights normalized to unity. The photons have to hit the good fiducial volume and $E_\gamma^{\text{lab}} > 0.05$ GeV, two good tracks and $0 < \chi^2_{4\pi} < 30$ are required. (Note that all photon combinations are plotted.)

The angular and energy distributions of the photons can be seen in Fig. 43 and Fig. 44, again for $\pi^+\pi^-2\pi^0\gamma$, showing that the simulation describes data reliably.

The kinematic fit algorithm optimizes the four-momenta of the hypothetical particles such that energy-momentum-conservation is obeyed. This takes into account the uncertainties of each variable via the covariance matrix and subsequently computes the kinematic fit χ^2 as a goodness-of-fit test. The combination of photons giving the smallest kinematic fit χ^2 is subsequently selected. This fit is performed in several hypotheses for each event and the event is only stored in the *Level-2-Ntuples* if the kinematic fit converges in at least one of the available hypotheses: $2\pi\pi^0\gamma$, $2\pi2\pi^0\gamma$, $2\pi\eta\pi^0\gamma$, $2\pi2\eta\gamma$, $2\pi3\pi^0\gamma$, $2\pi3\pi^0$, $2K2\pi^0\gamma$, $2K3\pi^0\gamma$, $2\pi4\pi^0\gamma$, $2\pi4\pi^0$.

The variables computed in the kinematic fit are stored in the *Level-2-Ntuples*. These values may differ slightly from the measured raw values. This can be observed in Fig. 45, which shows the distribution of the variable $M_{\text{inv}} - M_{4\pi}$ in the $2\pi2\pi^0\gamma$ simulation. M_{inv} denotes the invariant hadronic mass on MC generator level, while $M_{4\pi}$ is the reconstructed invariant mass after the kinematic fit. A clear peak with mean $(0.42 \pm 0.02)\text{MeV}/c^2$ and RMS-width $15.47\text{MeV}/c^2$ is visible. This width is compatible with the standard bin width of 20 MeV, resulting in a distribution of 100 events with frequencies of 2, 23, 50, 23, 2 into the center and two adjacent bins. The effect of this mass resolution is investigated in Sec. 7.3.4.

Further derived variables are stored in the *Level-3-Ntuples* and are later used to perform the final event selection and cross section computation.

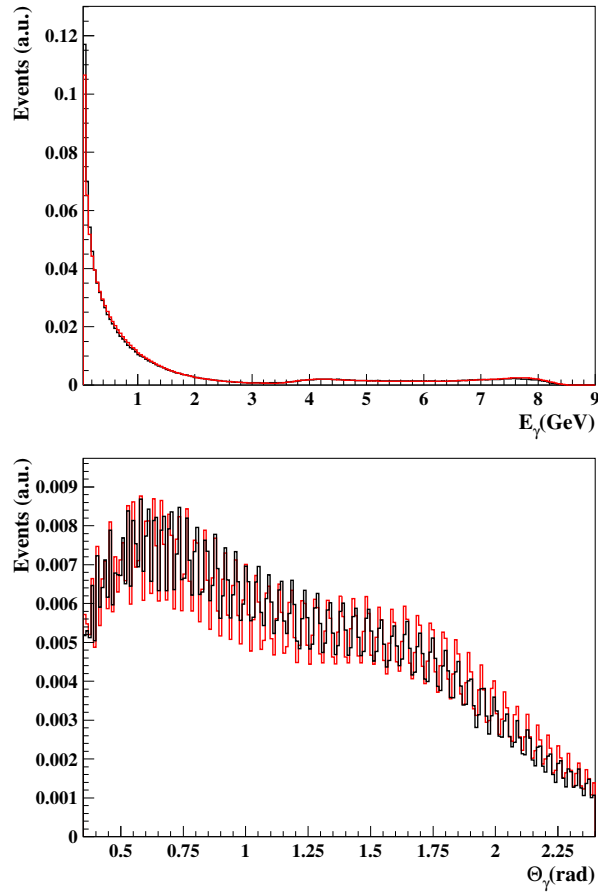


Figure 43.: Distribution of the photon energies E_γ^{lab} (top) and angles $\theta_\gamma^{\text{lab}}$ (bottom) in data (black) and $\pi^+\pi^-2\pi^0\gamma$ MC (red). The photons have to hit the good fiducial volume and $E_\gamma^{\text{lab}} > 0.05$ GeV, two good tracks and $0 < \chi_{4\pi}^2 < 30$ are required. (Note that all photon entries, not only those used to reconstruct the event, are plotted and the distributions are scaled to the same area.)

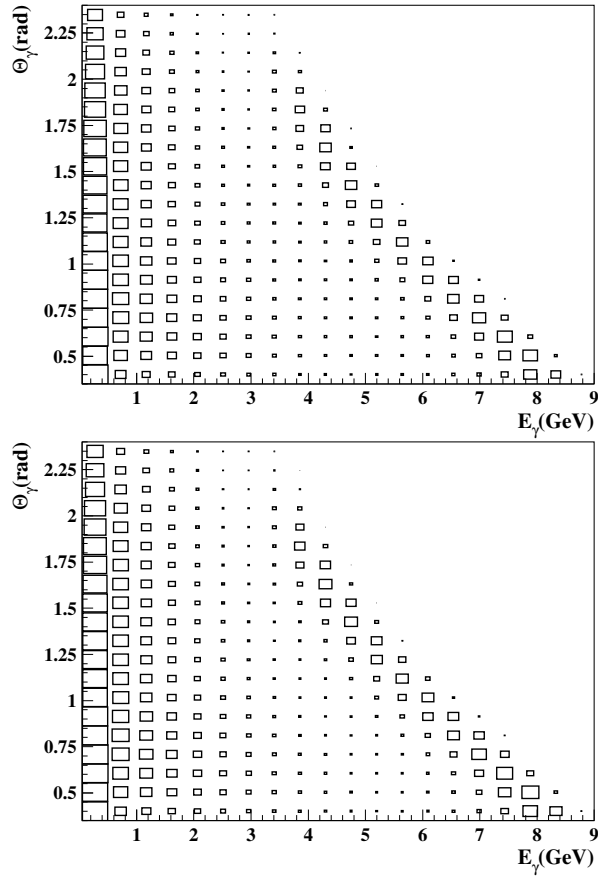


Figure 44.: Distribution of the photon energies E_γ^{lab} vs. angles $\theta_\gamma^{\text{lab}}$ in data (top) and $\pi^+\pi^-2\pi^0\gamma$ MC (bottom). The photons have to hit the good fiducial volume and $E_\gamma^{\text{lab}} > 0.05$ GeV, two good tracks and $0 < \chi_{4\pi}^2 < 30$ are required. (Note that all photon entries are plotted.)

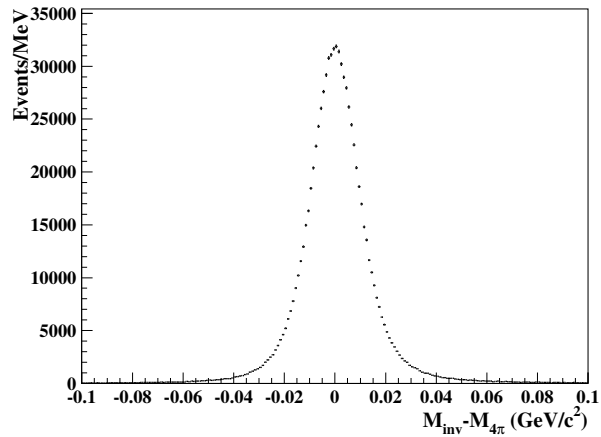


Figure 45.: Distribution of the deviation between the generator-level hadronic mass (M_{inv}) and its counterpart after the kinematic fit ($M_{4\pi}$) in signal simulation. (Full selection applied.)

5.6 PARTICLE IDENTIFICATION SELECTORS

The particle type responsible for a measured charged track can be determined from the signature left in the different detector components. Such Particle Identification (PID) selectors are used to reduce the contribution of background events with kaons (from $K_s K^\pm \pi^\mp \gamma$ and $K^+ K^- 2(3)\pi^0 \gamma$) and muons ($\psi(2S) \rightarrow J/\psi 2(3)\pi^0 \rightarrow \mu^+ \mu^- 2(3)\pi^0$) in the final state. Therefore, kaon and muon vetos are implemented to reject these backgrounds instead of identifying the signal channel with a pion selector (the latter would result in larger absolute systematic uncertainties since the number of signal events is much larger than the number of background events after the remaining selection).

In the *BABAR* experiment, several levels of strictness for identifying a certain particle type have been defined. They are, in descending order: very tight, tight, loose, very loose.

Applying PID selection introduces two types of systematic uncertainty:

1. The PID efficiency may be different between data and simulation, and thus the remaining amount of background subtracted via simulation would differ from the background in data.
2. Due to pion misidentification of the PID selector, signal events are lost and differences between data and simulation lead to a systematic uncertainty.

Thus, the general strategy is to find selection criteria that keep the combined systematic uncertainties of these two effects small.

Likelihood-based Particle Identification

A wide variety of methods exists to identify a detected particle's species from its recorded signal. In some cases, especially when dedicated detector elements are available, rather simple methods like a cut-based approach are sufficient to reach the necessary level of precision, as is the case for muons using IFR-information. But in many cases, more sophisticated formalisms are needed to achieve reliable identification. For this purpose, a diverse host of multivariate classifiers is employed, such as support vector machines, artificial neural networks [169], error-correcting output codes employing bagged decision trees [170, 171], and likelihood selectors. The latter type is used in this analysis to identify charged kaons and shall be explained briefly.

The likelihood of a track to have been caused by a particle of type λ is given as the product of the likelihoods for this hypothesis in all

parts of the detector or more generally in all measured observables:

$$\mathcal{L}_\lambda = \prod_j \mathcal{L}_\lambda(j). \quad (46)$$

Here, j runs over the relevant detector components which are the DIRC, DCH, and SVT. For DCH and SVT, the likelihood functions are calculated by dividing the difference between measured and expected energy loss per travelled distance ($\frac{dE}{dx}$) by its uncertainty. The expected value is calculated via the Bethe-Bloch formula [38] and the uncertainty is known from the calibration of the detector elements. For the DIRC, no direct formula exists to calculate the likelihood, hence a large lookup-table was generated in the variables momentum, Čerenkov angle, number of photons, and track quality.

Once all separate likelihoods are calculated, the total likelihood is determined for each particle hypothesis (pion, kaon, proton etc.). The results are subsequently evaluated by performing a likelihood ratio test [172].

In our case of the kaon likelihood selector, the ratios $\mathcal{L}_K/(\mathcal{L}_K + \mathcal{L}_p)$ (for protons) and $\mathcal{L}_K/(\mathcal{L}_K + \mathcal{L}_\pi)$ (for pions) are compared to threshold values depending on the required confidence level. These criteria in combination with electron and muon vetoes define the KLH selector, which achieves the clean yet efficient selection outlined below.

5.7 COMMON EVENT SELECTION

The event selection for the cross section consists of a variety of requirements, which will be described in detail in the following and are summarized in this list:

- $N(\text{good tracks}) = 2$
- $0.4 \leq \theta_{\text{reco}}(\text{good tracks}) \leq 2.4$
- $E_{\gamma_{\text{ISR}}}^{\text{lab}} > 3 \text{ GeV} \wedge E_{\gamma_{\text{ISR}}}^{\text{CM}} > 3 \text{ GeV}$, see App. A.2 for details
- $0.35 \leq \theta_\gamma \leq 2.4$
- $E_{\gamma_{\pi^0}}^{\text{lab}} > 0.05 \text{ GeV} \wedge \max_\gamma(E_{\gamma_{\pi^0}}^{\text{lab}}) > 0.1 \text{ GeV}$
- $\Delta_{\text{min}} \geq 1.2 \text{ rad}$
- $\chi_{3\pi}^2 \geq 25$
- None of the two charged tracks may be identified as a kaon.
- For events where the invariant mass of the two charged tracks is close to the nominal J/ψ mass, none of the two charged tracks may be identified as a muon.

The requirements on tracks and photons have been discussed in Section 5.4. They mainly restrict the events to the detector region of high acceptance and well understood efficiency. To exclude low energy photons and machine background, $E_\gamma > 0.05$ GeV is required. The remaining selection is split up into two parts: kinematic requirements (Δ_{\min} and $\chi_{3\pi}^2$) explained in Sec. 5.7.1 and selectors pertaining to particle identification (muons and kaons) presented in Sec. 5.7.2.

Beyond defining the selection, the introduced systematic uncertainties need to be determined. Type I and II errors [172] must be considered, which respectively translate to false rejection and false acceptance of events under the null hypothesis “the event was produced via the signal process”.

5.7.1 Kinematic Requirements

The variable Δ_{\min} measures the minimum angle spanned between the ISR photon and a charged track. In Fig. 46 the Δ_{\min} distributions are shown after applying the preselection and it is clearly visible that very little signal is lost but background can be effectively reduced by requiring $\Delta_{\min} > 1.2$ rad.

The requirement $\chi_{3\pi}^2 > 25$ is dedicated to removing the background channel $\pi^+\pi^-\pi^0\gamma$. Its effect can be studied in Fig. 47. Simulation shows that $(83.7 \pm 0.3)\%$ of $\pi^+\pi^-\pi^0\gamma$ events are removed by this requirement after the rest of the selection has already been applied. In contrast, $(98.39 \pm 0.01)\%$ of the $2\pi 2\pi^0\gamma$ events survive this requirement after the rest of the selection has been applied, a consequence of the $\chi_{3\pi}^2$ shapes seen in Fig. 48. When varying this requirement between $\chi_{3\pi}^2 > 15$ and $\chi_{3\pi}^2 > 35$, the fraction of surviving events subsequently varies by $\pm 13.0\%$ and $\pm 1.3\%$, respectively.

5.7.2 Background Reduction via PID

In this section, the specific selectors constructed to reject kaonic and muonic background are presented. For clarity, two variables are defined for this section: ε , the probability of a signal track to be falsely rejected, and η , the probability of a background track to be falsely accepted.

Kaon PID

Two kaon channels are relevant for the $\pi^+\pi^-2\pi^0\gamma$ analysis: $K_S K^\pm \pi^\mp \gamma$ and $K^+ K^- 2\pi^0 \gamma$. Their respective contributions before rejection, shown in Fig. 49, are on the percent-level and must be removed by a PID-selector like KLH. In the $\pi^+\pi^-3\pi^0\gamma$ analysis, background events are produced by channels like $K_L K^\pm \pi^\mp \gamma$ but are much less frequent. As will be shown in the following, a low systematic uncertainty is achieved by applying the veto

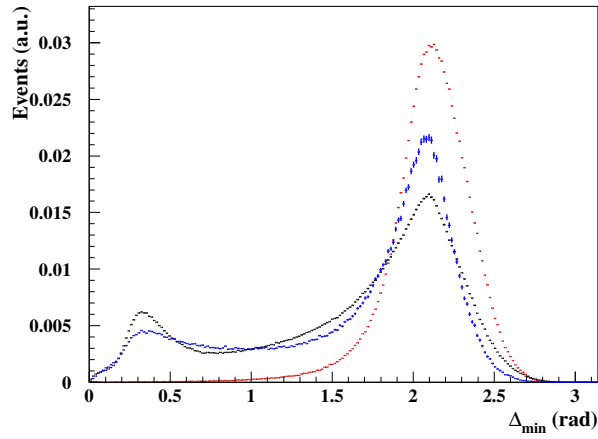


Figure 46.: Distributions of the variable Δ_{\min} for data (black), $2\pi 2\pi^0$ simulation (red) and continuum simulation (blue). (All samples normalized to same area, after pre-selection and requiring a converged kinematic fit in the $e^+e^- \rightarrow \pi^+\pi^-2\pi^0\gamma_{\text{ISR}}$ hypothesis.)

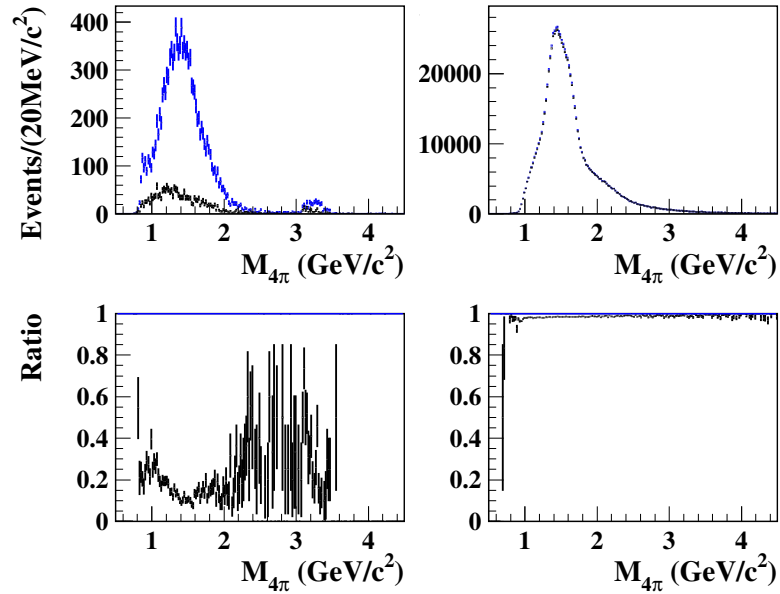


Figure 47.: Upper panels: $M_{4\pi}$ distributions for the 3π (left) and the $2\pi 2\pi^0$ (right) MC samples. For the black points the full selection has been applied, while for the blue points the requirement $\chi^2_{3\pi} > 25$ was omitted. In the lower panels the ratio of black and blue distributions is shown.

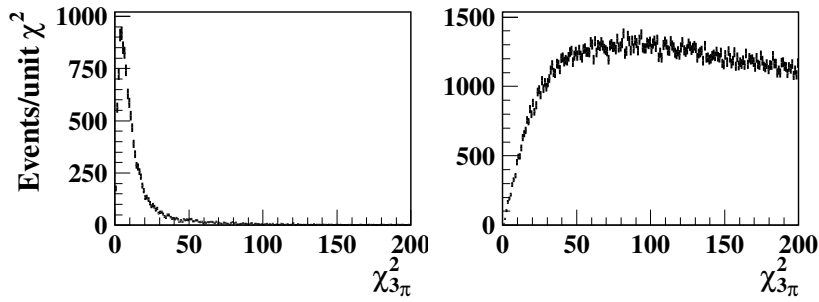


Figure 48.: $\chi^2_{3\pi}$ distributions for the 3π (left) and the $2\pi 2\pi^0$ (right) MC samples with the remaining selection applied.

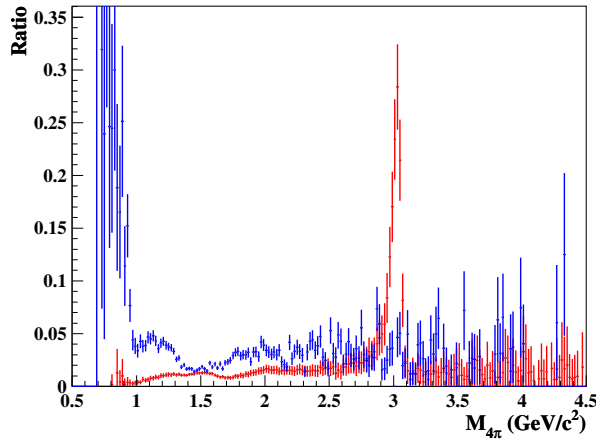


Figure 49.: Ratio of kaon backgrounds divided by $2\pi 2\pi^0$ simulation before rejection. $K_s K^\pm \pi^\mp \gamma$ in red, $K^+ K^- 2\pi^0 \gamma$ in blue. The peak at the J/ψ mass is due to the fact that no J/ψ is simulated in the $2\pi 2\pi^0$ sample.

$$(\text{KLH}(\text{Track1}) < \text{Tight}) \wedge (\text{KLH}(\text{Track2}) < \text{Tight}),$$

i.e. none of the tracks may be identified on the level “tight” or higher. In Fig. 50, the effect of this veto on $2\pi 2\pi^0$ simulation and data is shown as a function of $M_{4\pi}$, yielding the following points:

- The loss of $\pi^+ \pi^- 2\pi^0 \gamma$ in simulation is flat around 2.7 %, as expected from the *BABAR* PID-database⁵, where a pion-to-kaon misidentification probability of ~ 1.5 % per track is given, yielding ~ 3 % per event.
- In data, about 5 % of the events are rejected. Since 2.7 % of $\pi^+ \pi^- 2\pi^0 \gamma$ events are expected from simulation to be lost, the remaining roughly $(2.3 \pm 1.1)\%$ of data is removed as background, which is in agreement with the expectation.

⁵ This is a database, prepared by the *BABAR* PID working group, in which the performance of the different PID selectors is listed.

- According to the *BABAR* PID-database, the selection efficiency of KLHTight lies between 60 % and 90 % per track depending on its momentum. Taking the plain average value of 75 % (without weighting by the momentum distribution), in the channel $K_s K^\pm \pi^\mp \gamma$ 25 % are expected to survive, yielding good agreement with the value measured from simulation, which is 24.0 %. For $K^+ K^- 2\pi^0 \gamma$ $(25\%)^2 = 6.25\%$ are expected to survive, agreeing well with the 5.7 % obtained from simulation. The remaining contributions correspond to 0.3 % and 0.15 % of data, respectively, and are removed by subtracting simulation (see Sec. 7.2).
- Systematic Uncertainties: Taking the data-MC discrepancy as a measure of the systematic uncertainty, both the pion misidentification as well as the kaon selection efficiency of the KLH Tight selector have a relative systematic uncertainty of 20 %. The two aspects named at the beginning of Sec. 5.6 are of relevance here:
 1. Uncertainty of signal events removed by the kaon veto
 2. Uncertainty of the remaining kaon events

Regarding (1), we calculate $20\% \cdot 2.7\% = 0.54\%$ (2.7 % signal rejection).

Regarding (2), we calculate $20\% \cdot 0.3\% = 0.06\%$ for $K_s K^\pm \pi^\mp \gamma$ ($K_s K^\pm \pi^\mp \gamma$ amounts to 0.3 % of data after selection).

Regarding (2), we calculate $36\% \cdot 0.15\% = 0.054\%$ for $K^+ K^- 2\pi^0 \gamma$ ($K^+ K^- 2\pi^0 \gamma$ amounts to 0.15 % of data after selection), since $\varepsilon_{\text{data}} = 12\%$, and $\varepsilon_{\text{MC}} = 15\%$, such that for the two-track-case a relative discrepancy of $1 - \left(\frac{\varepsilon_{\text{data}}}{\varepsilon_{\text{MC}}}\right)^2 = 36\%$ exists.

The uncertainty from (2) is included in the background subtraction uncertainty outlined in Sec. 7.2.5, hence only the uncertainty from effect (1) (0.54 %) enters the total systematic uncertainty of the final result.

Muon PID

Regarding muon backgrounds, only one decay channel is relevant for each signal final state: $e^+ e^- \rightarrow \psi(2S)\gamma \rightarrow J/\psi 2\pi^0 \gamma \rightarrow \mu^+ \mu^- 2\pi^0 \gamma$ for $e^+ e^- \rightarrow \pi^+ \pi^- 2\pi^0 \gamma$ and $e^+ e^- \rightarrow \psi(2S)\gamma \rightarrow J/\psi 3\pi^0 \gamma \rightarrow \mu^+ \mu^- 3\pi^0 \gamma$ for $e^+ e^- \rightarrow \pi^+ \pi^- 3\pi^0 \gamma$. Since there is no simulation for this type of background, it has to be assessed purely in data. It contributes only at high masses (around the $\psi(2S)$ resonance) and a combined veto with low systematic uncertainties (as shown below) is constructed as

$$\neg \left((M_{J/\psi} - 3\sigma < M_{\pi^+ \pi^-} < M_{J/\psi} + 3\sigma) \wedge \left((\text{muMicro}(\text{Track1}) \geq \text{Loose}) \vee (\text{muMicro}(\text{Track2}) \geq \text{Loose}) \right) \right),$$

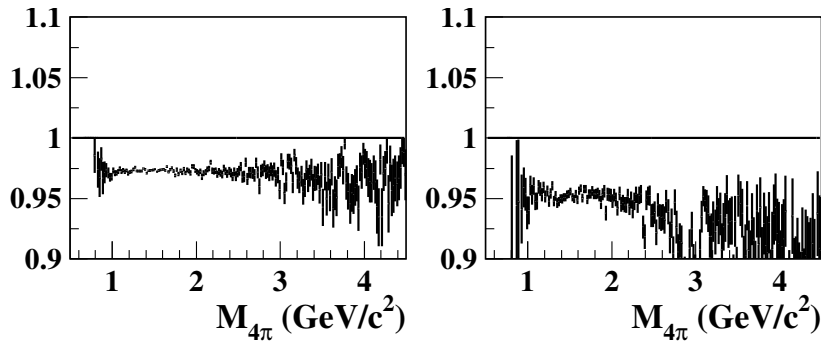


Figure 50.: Survival rates of the kaon-ID requirement (logic as described in the text) as a function of $M_{4\pi}$ for $\pi^+\pi^-2\pi^0\gamma$ simulation (left) and data containing kaons (right).

i.e. if the event's two-“pion” mass is near the J/ψ and one of the charged tracks is loosely identified as a muon, the event is rejected. (With $M_{J/\psi} = 3.102 \text{ GeV}/c^2$, $\sigma = 0.015 \text{ GeV}/c^2$, directly from data.) Tracks are identified as muons by the selector muMicro, which is using a cut-based approach combining information from the electromagnetic calorimeter and the instrumented flux return. In Fig. 51, the number of events after muon-rejection divided by the number of events before muon-rejection is shown as a function of $M_{4\pi}$ for data and $2\pi 2\pi^0$ simulation, exhibiting the following characteristics:

- Negligible rejection in signal simulation (few events in the relevant mass range, see Fig. 52).
- As expected, a large effect is observed at the $\psi(2S)$ mass. Up to 75 % of the events in this region are rejected as muonic background.
- Systematic uncertainties: According to the *BABAR* PID-database, the selector muMicro loose has a per track inefficiency of approximately $\eta = 15 \%$, and an inefficiency uncertainty (taking the data-MC discrepancy) of $\delta(\eta) = 2 \%$.

The uncertainty contribution relative to the number of signal events (N_{sig}) exclusively from this effect (falsely accepting a background event) where N_{b} is the number of background events and N_{tot} the total number of events, both before the

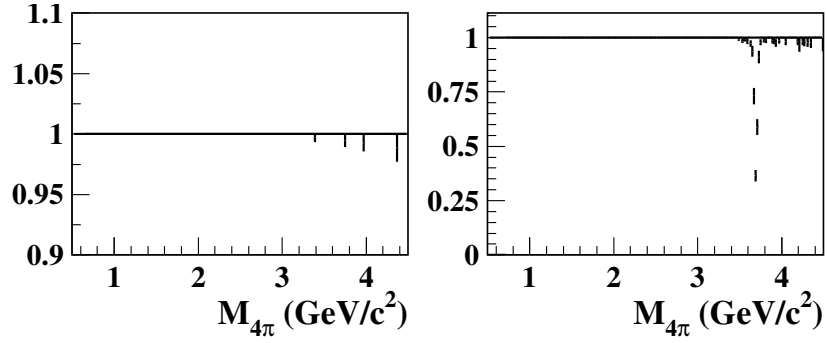


Figure 51.: Survival rates of the muon-ID requirement (logic as described in the text) as a function of $M_{4\pi}$ for $\pi^+\pi^-2\pi^0\gamma$ simulation (left, with binomial uncertainties [173]) and data (right) after background subtraction (see Sec. 7.2, uncertainties see App. C.1). In data, the effect of the removed $\psi(2S)$ peak is visible as a very pronounced dip, since a large fraction of this resonance decays into muonic final states.

veto, while N'_b and N'_{tot} are the values after the veto, can be calculated as

$$N'_{\text{tot}} = N_{\text{tot}} - (1 - \eta^2) N_b \quad (47)$$

$$q := \frac{N'_{\text{tot}}}{N_{\text{tot}}} \quad (48)$$

$$N_{\text{sig}} = N_{\text{tot}} - N_b = \frac{q - \eta^2}{1 - \eta^2} N_{\text{tot}} \quad (49)$$

$$\Rightarrow \delta(N_{\text{sig}}) = 2\eta\delta(\eta) \frac{1 - q}{(1 - \eta^2)^2} N_{\text{tot}} \quad (50)$$

$$\Rightarrow \frac{\delta(N_{\text{sig}})}{N_{\text{sig}}} = 2\eta\delta(\eta) \frac{1}{1 - \eta^2} \frac{1 - q}{q - \eta^2}. \quad (51)$$

The ratio q reaches as low as 25 % in the $\psi(2S)$ peak, as shown in Fig. 53. This gives the relative uncertainty of the number of events after the veto, thus in the $\psi(2S)$ region a relative uncertainty of $0.6\% \cdot \frac{1}{1 - 0.0225} \cdot \frac{0.75}{0.25 - 0.0225} = 2.0\%$ is calculated (with $2\eta\delta(\eta) = 0.6\%$), while outside this region the uncertainty approaches zero. The uncertainties from removed signal events and from the finite J/ψ -range ($\pm 3\sigma$) in $M_{\pi^+\pi^-}$ are negligible.

- The background events remaining due to inefficiency of the selector can be calculated as $\frac{N'_b}{N'_{\text{tot}}} = \frac{\eta^2}{1 - \eta^2} \cdot \frac{1 - q}{q}$, where q is the fraction of remaining events. The remaining contribution is removed as outlined in Sec. 7.2.

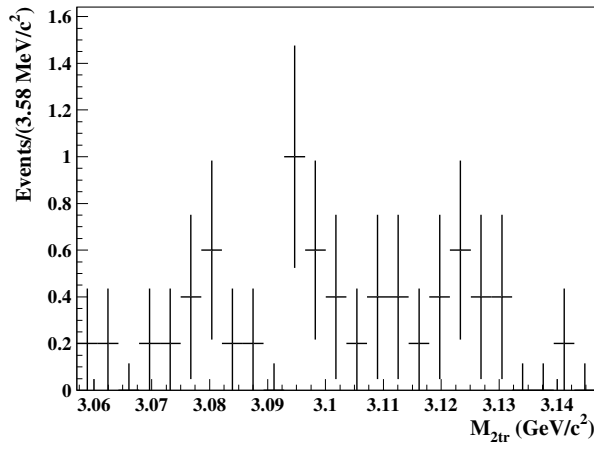


Figure 52.: Raw two-track mass in the J/ψ region for $2\pi 2\pi^0$ simulation before muon-PID on the charged tracks.

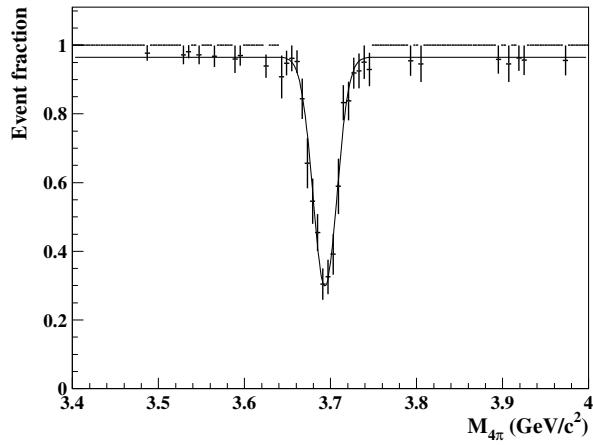


Figure 53.: Fit to data of the count rate after the μ -veto divided by the count rate before the μ -veto.

Proton PID

It was considered to apply a proton-veto to events in which both tracks are identified at least as “loose” by the proton likelihood selector. This veto can be dropped as it rejects next to no background-events, while the rejected fraction is predominantly misidentified signal channel events. The latter is evident from the fact that signal simulation and data have virtually the same survival rates. And furthermore from the observation that in data the rejection rate stays approximately the same over the whole mass spectrum, although in the low mass region (especially below the $p\bar{p}$ -threshold of $\sqrt{s} = 1.877 \text{ GeV}/c^2$) no protons can be produced. Thus this PID-selector is not necessary but would only introduce additional systematics. It can be deduced from the survival rates in data and signal simulation that the selector would remove less than 0.2% more events in data than in signal simulation. The uncertainty due to this effect is included in the background subtraction uncertainty outlined in Sec. 7.2.5 and hence does not need to be added separately.

SUMMARY OF THE GENERAL ANALYSIS ASPECTS

In the above chapter the first steps in the analyses of both final states – $e^+e^- \rightarrow \pi^+\pi^-2\pi^0\gamma$ and $e^+e^- \rightarrow \pi^+\pi^-3\pi^0\gamma$ – are described. A general preselection of ISR events is applied to the full data sample, leaving about 6×10^6 measured events. Subsequently, the kinematic fit and a series of requirements common to both analyses are summarized and their effects studied. This paves the way to the details of each analysis, which are outlined in the following chapters.

In the following chapter, the process $e^+e^- \rightarrow \pi^+\pi^-3\pi^0\gamma_{\text{ISR}}$ is investigated. For this final state only very imprecise cross section data exists up to now, with uncertainties in the range of 50 %-100 % shown in Fig. 18. Consequently, it is worthwhile investigating the channel more accurately, so that the resulting cross section measurement can be used to improve the background subtraction in the analysis of the channel $e^+e^- \rightarrow \pi^+\pi^-2\pi^0\gamma_{\text{ISR}}$, see Sec. 7.¹ Furthermore its contribution to $g_\mu - 2$ can be calculated according to the new measurement and Monte Carlo generators may be adapted to give more reliable predictions.

The analysis includes the generic steps of a cross section measurement, but has to be expanded to manage the additional difficulty of only having simulations of two intermediate states for the efficiency calculation: $\eta\pi^+\pi^-$ and $\omega2\pi^0$. Since the kinematics and mass distributions of these intermediate states are quite different, as observed in Fig. 54 for the mass distribution, a suitable signal simulation mixture or “cocktail” of both must be determined in order to represent the full channel. The analysis steps are

- Development of the event selection:
Sec. 6.1,
- Subtraction of background processes using the “Novosibirsk-method”:
Sec. 6.2,
- Calculation of efficiencies from $\eta\pi^+\pi^-$ and $\omega2\pi^0$ simulations:
Sec. 6.3,
- Determination of the production fractions of $\eta\pi^+\pi^-$ and $\omega2\pi^0$:
Sec. 6.4,
- Computation of cross sections via $\eta\pi^+\pi^-$ and $\omega2\pi^0$ -efficiency:
Sec. 6.5, \rightarrow weighted average for final result,
- Assessment of systematic uncertainties of the $2\pi3\pi^0$ cross section:
Sec. 6.6

¹ Isospin symmetry would allow a prediction of the $\pi^+\pi^-3\pi^0$ cross section from the measured $2(\pi^+\pi^-)\pi^0$ channel [138], projecting it to be precisely half the size of the latter [145], but this prediction does not hold exactly as can be seen by comparing measured cross sections.

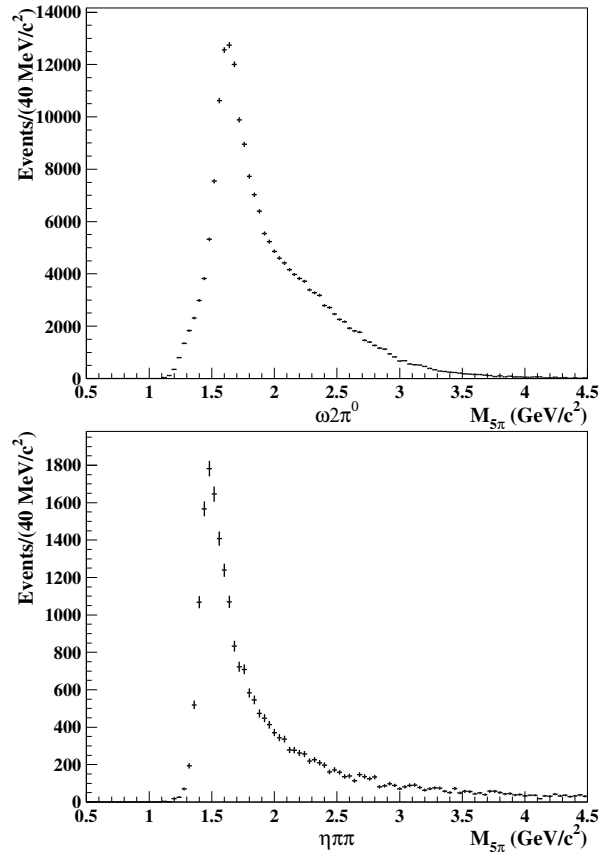


Figure 54.: $M_{5\pi}$ distributions of the available $2\pi 3\pi^0$ MC-channels $\omega 2\pi^0$ (top) and $\eta \pi^+ \pi^-$ (bottom) after the full $2\pi 3\pi^0$ selection.

6.1 EVENT SELECTION

In addition to the general selection (Sec. 5), requirements specific to the final state $2\pi 3\pi^0 \gamma_{\text{ISR}}$ are imposed as listed here and explained below:

- Number of photons $N_\gamma \geq 7$,
- $0 < \chi_{5\pi}^2 < 25$, where $\chi_{5\pi}^2$ serves as a test of the goodness of the kinematic fit in the $2\pi 3\pi^0 \gamma$ hypothesis,
- $\chi_{4\pi}^2 \geq 25$, where $\chi_{4\pi}^2$ serves as a test of the goodness of the kinematic fit in the $2\pi 2\pi^0 \gamma$ hypothesis,
- Events containing η mesons are rejected,
- Energy of excess photons $E_{\text{ph_add}} < 0.2 \text{ GeV}$.

The selector $N_\gamma \geq 7$ ensures that there is a sufficient number of photons in each event to execute the kinematic fit in the signal hypothesis. (Only the decay $\pi^0 \rightarrow \gamma\gamma$ is considered.²) The requirement on $\chi_{5\pi}^2$ is introduced to select events consistent with the signal hypothesis $e^+e^- \rightarrow \pi^+\pi^-3\pi^0\gamma$. The purpose of the requirement on $\chi_{4\pi}^2$ is to reject events from the channel $e^+e^- \rightarrow \pi^+\pi^-2\pi^0\gamma$, which has a kinematic structure similar to the signal process. Channels including η mesons, such as $e^+e^- \rightarrow \pi^+\pi^-\eta 2\pi^0\gamma$, $e^+e^- \rightarrow \pi^+\pi^-2\eta\pi^0\gamma$, and $e^+e^- \rightarrow \pi^+\pi^-3\eta\gamma$ with $\eta \rightarrow 2\gamma$ decay into the same detector signature as the signal channel. These backgrounds are removed by requiring that the event cannot be reconstructed in such a way that the invariant mass of at least one photon pair is within $30 \text{ MeV}/c^2$ of the nominal η meson mass.

Furthermore, a requirement was introduced to get rid of multi-photon backgrounds. The sum of the energies of the unused photons (photons which are neither assigned to a π^0 , nor determined to be the ISR photon), which is stored in the variable $E_{\text{ph_add}}$, can be used to achieve the desired effect. From Fig. 55 it is apparent that in the $\chi_{5\pi}^2$ -sideband region $25 < \chi_{5\pi}^2 < 50$, where a large fraction of data consists of background events, the $E_{\text{ph_add}}$ distributions are quite different between data and signal simulation. Thus the requirement $E_{\text{ph_add}} < 0.2 \text{ GeV}$ was introduced. The corresponding distributions in the $\chi_{5\pi}^2$ -signal region $\chi_{5\pi}^2 < 25$ are shown in Fig. 56, demonstrating much better agreement for samples dominated by signal events. In data, 57 % (35 %) of the events in the $\chi_{5\pi}^2$ -signal (sideband) region survive this requirement, while in the signal MC sample 75 % (68 %) get through. Figure 57 shows that the effect is mostly flat in $M_{5\pi}$. Figure 58 shows that the shape of the $\chi_{5\pi}^2$ distribution after applying the full selection including

² The cross section is corrected for only considering this decay by dividing by the cube of the branching fraction $\mathcal{B}(\pi^0 \rightarrow \gamma\gamma) = (98.823 \pm 0.034)\%$ [43].

the E_ph.add requirement is in reasonable agreement with signal simulation.

If a very clean event sample is selected by $\chi_{5\pi}^2 < 5$, a relative difference of 8 % remains between data and simulation, which gives a measure for the systematic uncertainty due differences between MC generation and data.

6.2 BACKGROUND SUBTRACTION

As explained below (Sec. 6.2.2), for the subtraction of ISR channels, the background shape is determined exclusively from data, while its normalization is calculated using simulation. Furthermore, background from continuum hadron production is estimated via a simulation sample which is normalized to data, see Sec. 6.2.1.

6.2.1 Continuum Background

The first background contribution to be subtracted is the continuum hadron production or “uds” for short, whose $M_{5\pi}$ and $\chi_{5\pi}^2$ distributions are shown in Figs. 59 and 60, especially demonstrating that the $\chi_{5\pi}^2$ requirement cannot effectively reject this contribution. The total cross section is around $\sigma_{\text{uds}} = 2090$ pb, but the simulation of its substructures, especially the low-multiplicity channels, is not reliable. Hence the normalization of this simulation is essentially unknown, so that it has to be calculated from data. In order to do this, an observable which allows a calibration is needed. The choice here is the $\gamma_{\text{ISR}}\gamma$ invariant mass. In case a photon from a π^0 decay is falsely identified as the ISR photon, the invariant mass of this photon and some other photon in the event will be equal to the π^0 mass (within uncertainties). The size of the π^0 yield is measured in continuum simulation as well as data and then compared to determine the appropriate scaling. To clean up the distributions, photons that have been identified as π^0 -photons by the kinematic fit are excluded and only the combinations of the ISR-photon with the remaining photons are plotted leading to a significant improvement. The $M_{\gamma\gamma}$ distributions are shown in Fig. 61, exhibiting similar peak sizes while the underlying distributions differ considerably.

If we calculate the global normalization factor f_{uds} from the ratio of the peak sizes in data and simulation (scaled to the same luminosity), the result is $f_{\text{uds}} = 0.9 \pm 0.3$. Due to low statistics, no mass-dependent uds-normalization can be calculated. The large uncertainty is not a problem for this analysis since the uds-contribution is small compared to data, especially in the low mass-region. As visible in Fig. 62, uds amounts to less than 10 % relative to data below 2 GeV, less than 20 % below 2.5 GeV and less than 40 % below 3.2 GeV, which results in uncertainties of less than 3 %, 7 % and

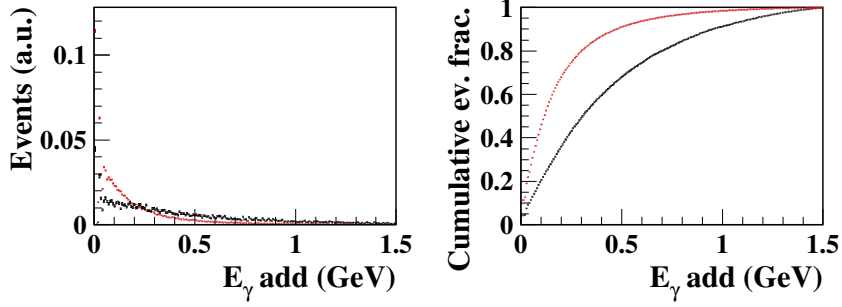


Figure 55.: Left: $E_{\text{ph_add}}$ distribution in data (black) and signal simulation (red, mixed according to the weights calculated in Sec. 6.4) in the $\chi_{5\pi}^2$ sideband region $25 < \chi_{5\pi}^2 < 50$. Right: the corresponding cumulative distributions.

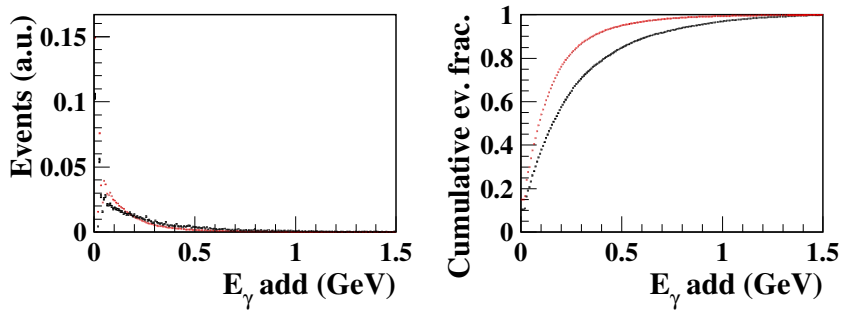


Figure 56.: Left: $E_{\text{ph_add}}$ distribution in data (black) and signal simulation (red, mixed according to the weights calculated in Sec. 6.4) in the $\chi_{5\pi}^2$ signal region $\chi_{5\pi}^2 < 25$. Right: the corresponding cumulative distributions.

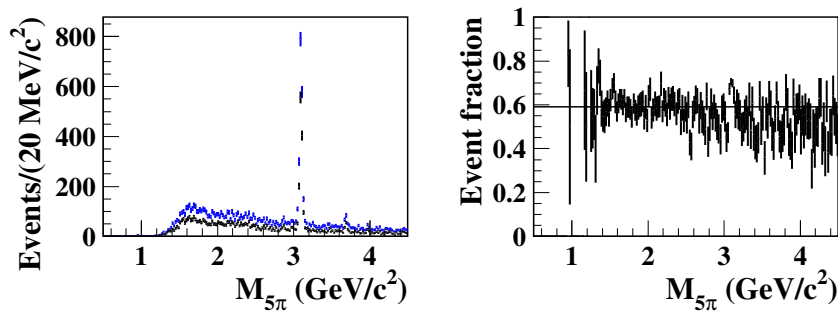


Figure 57.: The $M_{5\pi}$ distribution in data before (blue) and after (black) the $E_{\text{ph_add}}$ cut, and their ratio with binomial uncertainties [173].

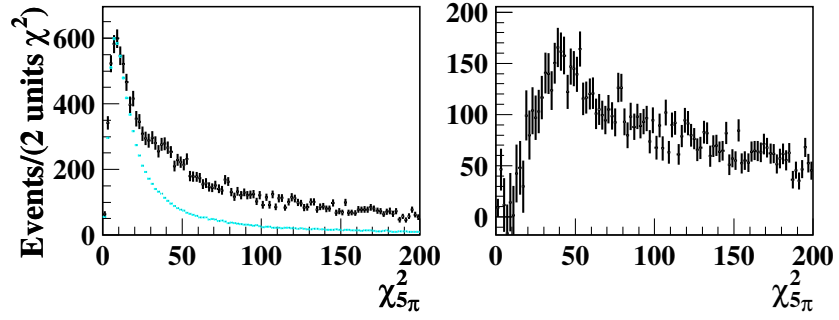


Figure 58.: Left: $\chi^2_{5\pi}$ distributions in data after subtraction of continuum background (black) and signal simulation (turquoise) mixed according to the measured contribution of each resonance and normalized to the same peak height as data. Right: remaining data after subtracting the signal cocktail (see Sec. 6.4).

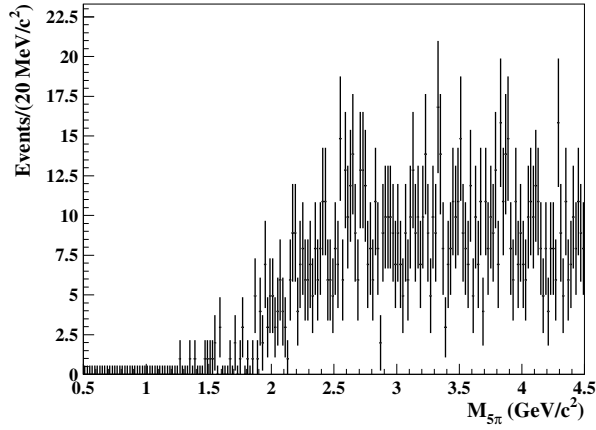


Figure 59.: Distribution of $M_{5\pi}$ in scaled uds simulation after selection.

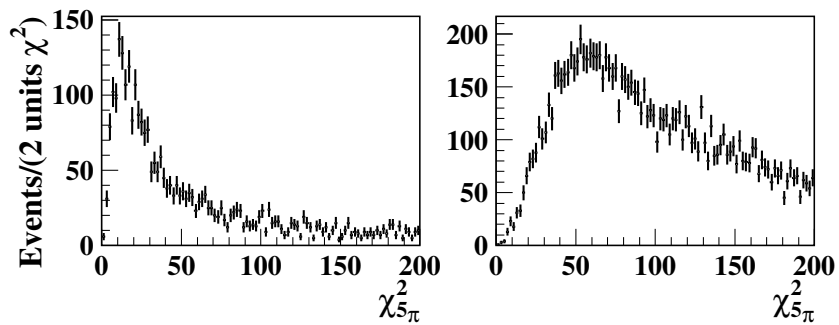


Figure 60.: $\chi^2_{5\pi}$ distributions for uds (left) and $2\pi 2\pi^0\gamma$ (right) simulation (both unnormalized).

13 %, respectively. In the high mass region, the uds contribution averages to less than 60 % of data, giving an uncertainty of 20 %.

6.2.2 Sideband Subtraction

To extract the remaining ISR backgrounds the comparison between the $\chi^2_{5\pi}$ -distributions in signal and background is exploited in the signal region ($0 < \chi^2_{5\pi} < 25$), as well as in a sideband region ($25 < \chi^2_{5\pi} < 50$). Figure 58 shows the $\chi^2_{5\pi}$ distributions of data and the $2\pi 3\pi^0\gamma$ MC cocktail (see Sec. 6.4) with the analysis selection. Only continuum background subtraction has been performed on the data.

The background subtraction is performed using the ‘‘Novosibirsk-Method’’³ As demonstrated in Fig. 63, N_{1s} is defined as the number of signal MC events in the signal region, N_{2s} the number of signal MC events in the sideband region, N_{1b} the number of background MC events in the signal region, and N_{2b} the number of background MC events in the sideband region. Furthermore $N_1 = N_{1s} + N_{1b}$ and $N_2 = N_{2s} + N_{2b}$. Then we can define

$$\alpha := \frac{N_{2s}}{N_{1s}}, \quad \beta := \frac{N_{2b}}{N_{1b}}. \quad (52)$$

If α and β can be calculated reliably (e.g. because signal and the dominating background have well known and simulated χ^2 -shapes), then it follows that

$$N_{1s} = \frac{\beta}{\beta - \alpha} \cdot N_1 - \frac{1}{\beta - \alpha} \cdot N_2 \equiv f_{\text{sig}} \cdot N_1 - f_{\text{bkg}} \cdot N_2, \quad (53)$$

where N_1 and N_2 are extracted from data and $f_{\text{sig}} := \beta/(\beta - \alpha)$, $f_{\text{bkg}} := 1/(\beta - \alpha)$. The above relation is proven to be correct by re-inserting the definitions:

$$\begin{aligned} N_{1s} &= \frac{N_{2b}/N_{1b}}{\frac{N_{2b}}{N_{1b}} - \frac{N_{2s}}{N_{1s}}} \cdot (N_{1s} + N_{1b}) - \frac{1}{\frac{N_{2b}}{N_{1b}} - \frac{N_{2s}}{N_{1s}}} \cdot (N_{2s} + N_{2b}) \\ \Rightarrow \frac{N_{2b}}{N_{1b}} \cdot N_{1s} - N_{2s} &= \frac{N_{2b}}{N_{1b}} \cdot N_{1s} + N_{2b} - N_{2s} - N_{2b} \quad \square \end{aligned} \quad (54)$$

Here, we assume the χ^2 -shape of background to be similar to the shape of the $2\pi 2\pi^0\gamma$ simulation in order to calculate β , as this is expected to be the dominating background process.

For high invariant masses, the final state $2\pi 4\pi^0\gamma$ would be dominant, but has been effectively removed by the requirement on $E_{\text{ph.add}}$. From Fig. 64 it is apparent that the $2\pi 2\pi^0\gamma$ simulation

³ Named after the Siberian city of Новосибирск, with its numerous research centers, especially the Budker Institute for Nuclear Physics, where this method was developed.

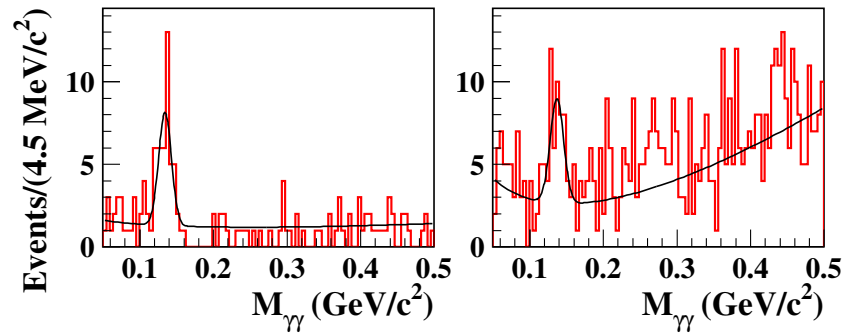


Figure 61.: Distributions of the invariant $\gamma_{\text{ISR}}\gamma$ mass for uds simulation (left) and data (right).

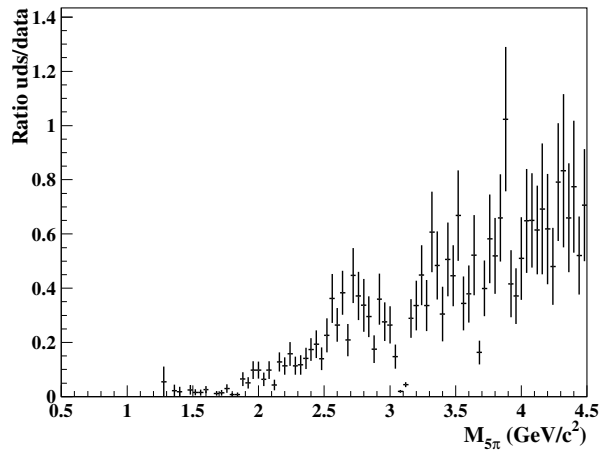


Figure 62.: Ratio of (scaled) continuum to data events.

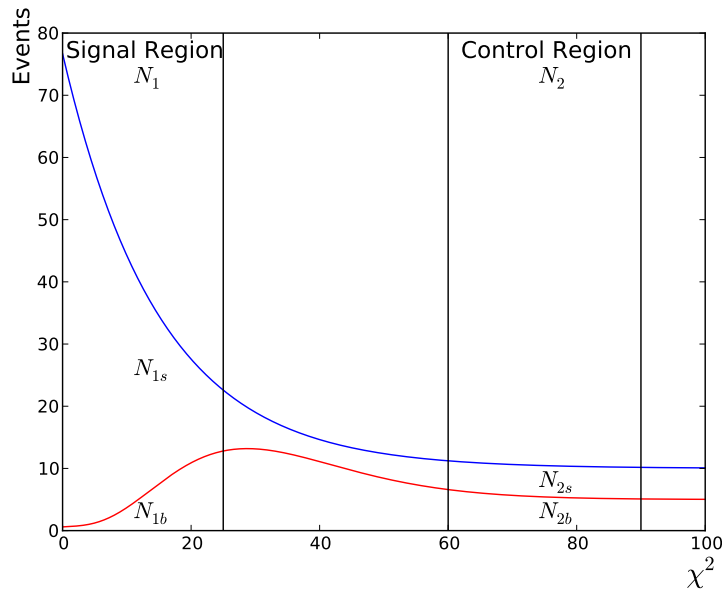


Figure 63.: Schematic representation of the “Novosibirsk-Method” for background normalization. N_{1s} is the number of signal MC events in the signal region, N_{2s} is the number of signal MC events in the sideband region. Correspondingly, N_{1b} is the number of background MC events in the signal region, N_{2b} is the number of background MC events in the sideband region.

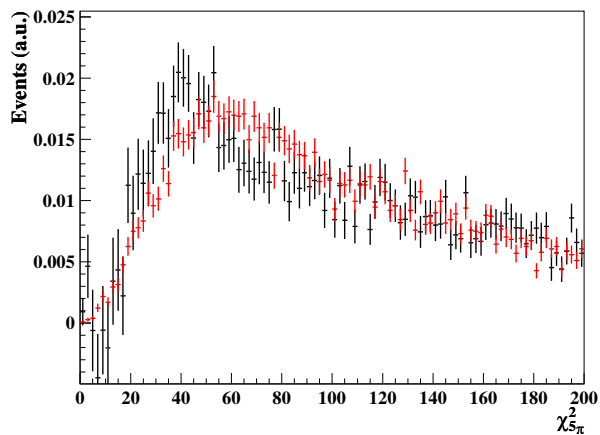


Figure 64.: $\chi^2_{5\pi}$ distributions for data after subtraction of signal simulation (mixed according to the weights calculated in Sec. 6.4) and uds (black) and for $2\pi 2\pi^0 \gamma$ simulation (red, scaled to equivalent areas).

Table 4.: Parameters for the background subtraction using the Novosibirsk method, where α is calculated using the different signal channels, while β results from the $2\pi2\pi^0\gamma$ background. $f_{\text{sig}} = \beta/(\beta - \alpha)$ and $f_{\text{bkg}} = 1/(\beta - \alpha)$ are the corresponding scaling factors for signal and background region, respectively.

Channel	α	β	f_{sig}	f_{bkg}
$\eta\pi^+\pi^-\gamma$	0.45	3.92	1.13	0.29
$\omega2\pi^0\gamma$	0.30	3.92	1.08	0.28
Average	0.37	3.92	1.11	0.28

shape agrees the background extracted from data (after subtraction of the signal cocktail (see Sec. 6.4) and uds). Hence, from the $2\pi2\pi^0\gamma$ simulation the value $\beta = 3.92$ is calculated. The variable α is calculated from the χ^2 -distributions of both $2\pi3\pi^0\gamma$ signal simulations ($\eta\pi^+\pi^-\gamma$ and $\omega2\pi^0\gamma$). For the scaling factors f_k , the arithmetic mean between both simulations is subsequently used, with the values listed in Tab. 4. They differ by less than 3 % from their average, giving a negligible uncertainty contribution. As can be observed already here, the two MC samples have different χ^2 shapes. This will be discussed further in the context of acceptance and efficiency in Sec. 6.3. The Novosibirsk scaling results in signal and sideband histograms shown in Fig. 65, also including their ratio. The scaled sideband amounts to approximately 20 % of scaled signal. The invariant mass distribution after employing this sideband subtraction method and uds subtraction is displayed in Fig. 66.

6.3 ACCEPTANCE AND EFFICIENCY

In order to measure any cross section, the detector acceptance (i.e. where the detector is sensitive to the final state in question) and the detection efficiency of the experimental setup must be determined. Once this has been achieved, the detected number of events is divided by the efficiency, giving the originally produced number of events, which is needed to calculate the cross section.

To measure acceptance and detection efficiency, simulation is used: the number of events after detector simulation and the full selection is divided by the number of events originally generated.

The efficiency of a process depends on the final state, the number and type of particles it contains, their angular and momentum distributions and many more variables. This means that different final states have different efficiencies. But it also follows that the same final state is detected with a different efficiency depending on the intermediate state through which it was produced. This effect

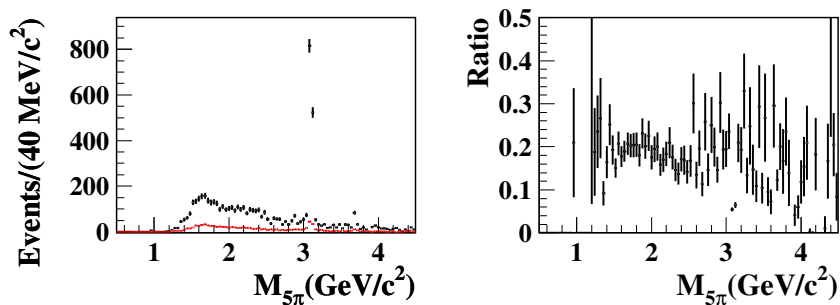


Figure 65.: Left: $M_{5\pi}$ distribution in data with the corresponding sideband (red), both scaled according to the Novosibirsk method. Right: sideband relative to signal in data.

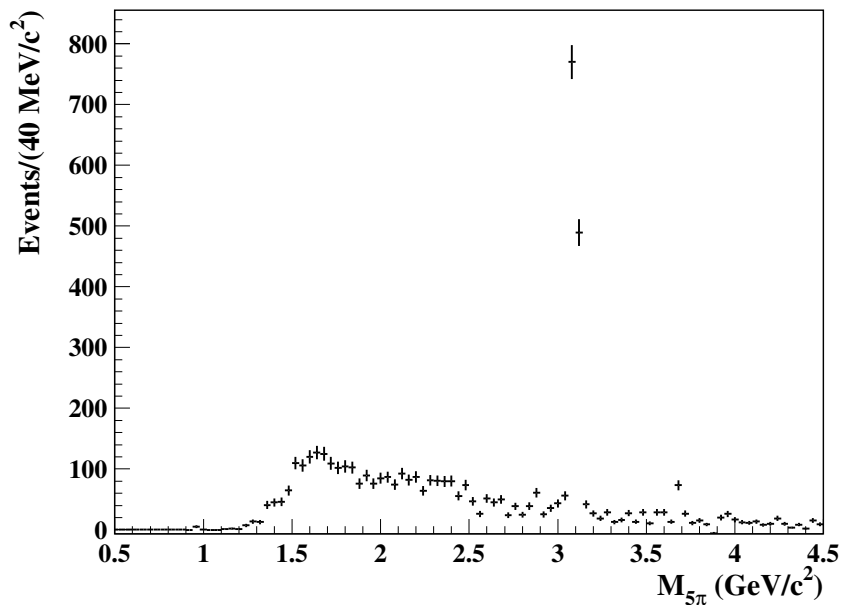


Figure 66.: $M_{5\pi}$ distribution after sideband and uds subtraction.

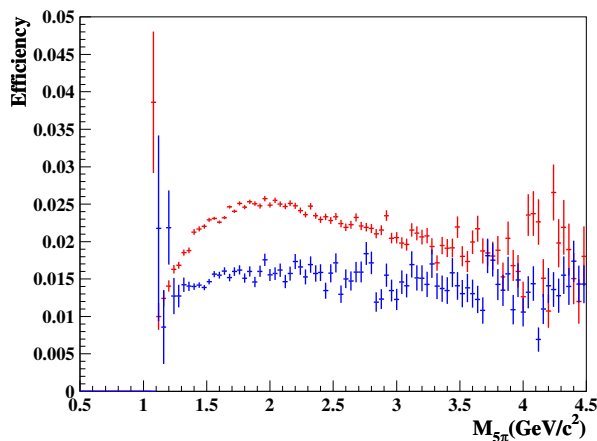


Figure 67.: Total efficiencies according to the $\omega 2\pi^0$ (red) and $\eta\pi^+\pi^-$ (blue) MC samples.

is due to the fact that each intermediate state leads to different kinematic distributions.

To account for this effect, ideally a full simulation of the production process of the final state in question is used, including all intermediate states with their corresponding weights. Since there are only two simulated signal channels ($e^+e^- \rightarrow \omega 2\pi^0$ and $e^+e^- \rightarrow \eta\pi^+\pi^-$) due to the fact that the full channel has never been measured accurately, the efficiency is determined from both simulated samples separately and the result is shown in Fig. 67. The global efficiencies significantly differ between these intermediate states, which is interesting, yet not unexpected due to the different kinematic structure.

Nonetheless, this effect is worthwhile studying. After thorough investigation, the different χ^2 shapes of the two channels have been found to be responsible for this effect. All other requirements in the event selection show compatible efficiencies. Figure 68 shows the $\chi^2_{5\pi}$ distributions of the $\omega 2\pi^0\gamma$ and $\eta\pi^+\pi^-\gamma$ intermediate states, the former being significantly more narrow than the latter.

As χ^2 is a variable compounded of various kinematic observables, an even closer look is instructive. Indeed, Figs. 69 & 70 show that the momentum distributions of the three π^0 are much more narrow in the $\eta\pi^+\pi^-\gamma$ MC sample than in the $\omega 2\pi^0\gamma$ MC sample. On the contrary, when mixing the two simulation samples according to the weights calculated in Sec.6.4, there is hardly any discrepancy between $2\pi 3\pi^0\gamma$ -data and the $2\pi 3\pi^0\gamma$ simulation cocktail (Figs. 71, 72), indicating a realistic simulation sample. Slight differences between data and simulation still exist, but are much smaller than the previously observed discrepancy in the efficiency and are therefore covered by the systematic uncertainty due to the efficiency difference calculated in Sec. 6.6. Hence the simulation cocktail

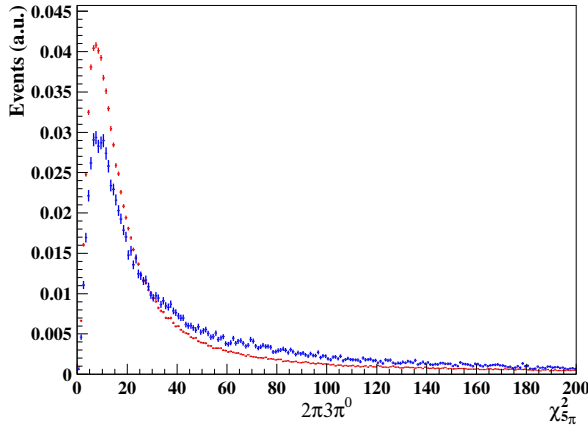


Figure 68.: $\chi^2_{5\pi}$ distributions for the $\omega 2\pi^0$ (red) and $\eta\pi^+\pi^-$ (blue) MC samples (both normalized to unit area).

can be used to reliably determine the efficiency of the full channel $e^+e^- \rightarrow \pi^+\pi^-3\pi^0\gamma$.

This is further proven in an independent cross check in the J/ψ mass region. As observed in Fig. 66, in the production of the final state $2\pi 3\pi^0$ a large contribution from this resonance exists. Therefore other intermediate states contribute only a small fraction ($\lesssim 10\%$) of the events around the J/ψ mass. Since neither of the existing simulation samples includes the J/ψ resonance, this region is the ideal testing ground to investigate how well the efficiency determined from the cocktail of $e^+e^- \rightarrow \omega 2\pi^0\gamma$ and $e^+e^- \rightarrow \eta\pi^+\pi^-\gamma$ simulation samples translates to events produced via different intermediate states in data. As the only selector showing a significant difference between the two simulation samples is the requirement $\chi^2_{2\pi 3\pi^0} < 25$, while all other selection efficiencies agree with each other, the $\chi^2_{2\pi 3\pi^0}$ requirement needs to be investigated. In Fig.73 (top) it is shown that the cumulative $\chi^2_{2\pi 3\pi^0}$ distributions in data and simulation are quite similar in this mass region. A more quantitative view is provided by Fig.73 (bottom), showing their ratio, which deviates from unity by less than 5%, confirming that the simulation cocktail describes $\pi^+\pi^-3\pi^0\gamma$ data very well, even for intermediate structures not included in the generators.

In summary, being restricted to merely two partial simulation samples leads to the effect that only the efficiency of events produced via the channels $e^+e^- \rightarrow \omega 2\pi^0$ and $e^+e^- \rightarrow \eta\pi^+\pi^-$ can be calculated directly, since their contributions are simulated by dedicated generators. The efficiency of the remaining fraction of events is not determined by a dedicated simulation but by an MC cocktail mixed from the existing generators. Although the cocktail is shown to describe the complete channel $e^+e^- \rightarrow \pi^+\pi^-3\pi^0\gamma$ very well, this procedure introduces an uncertainty which is determined in Sec. 6.6.

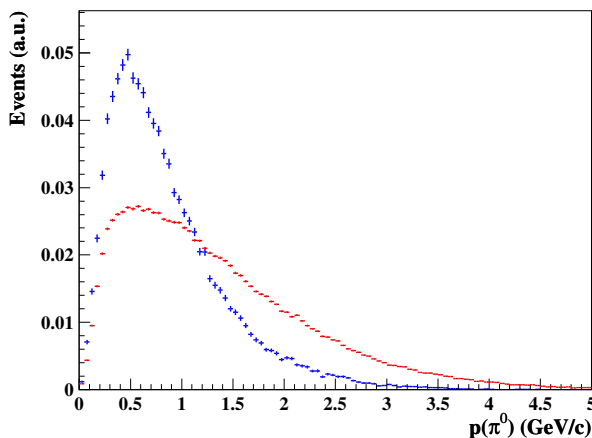


Figure 69.: p_{π^0} distributions for the $\omega 2\pi^0$ (red) and $\eta\pi^+\pi^-$ (blue) MC samples (both normalized to unit area). Each event contributes three entries to the calculation of this distribution, one for each π^0 . Full selection applied.

6.3.1 Correction of Track and π^0 Detection

The differences between data and simulation have been investigated in earlier *BABAR* analyses. Hence the resulting corrections can be used here and are summarized below, while detailed descriptions of each method with the corresponding references are given in App. C.4.

- Tracking correction: the efficiency of detecting a π^\pm in the final state $\pi^+\pi^-3\pi^0\gamma$ is overestimated in simulation by 0.47 % per charged track. This results in a correction of 0.9 % for both charged pions and an uncertainty of 0.8 %.
- π^0 correction: analyzing the process $e^+e^- \rightarrow \omega\pi^0\gamma$ shows that the efficiency of detecting a neutral pion is overestimated in simulation by 3.0 % with an uncertainty of 1.0 %. Hence for the channel $e^+e^- \rightarrow \pi^+\pi^-3\pi^0\gamma$ a correction of 9.0 ± 3.0 % results, contributing to the total systematic uncertainty.

6.4 RELATIVE FRACTIONS OF THE $\omega 2\pi^0\gamma$ AND $\eta\pi^+\pi^-\gamma$ INTERMEDIATE STATES

A precise determination of the respective production contributions via $\omega 2\pi^0$ and $\eta\pi^+\pi^-$ and the fraction not covered by these channels is interesting on its own, but moreover it is needed to evaluate efficiency of the full $\pi^+\pi^-3\pi^0$ channel reliably. Furthermore, it will be useful later when the channel $e^+e^- \rightarrow \pi^+\pi^-3\pi^0\gamma$ is subtracted as a background from the $e^+e^- \rightarrow \pi^+\pi^-2\pi^0\gamma$ data in Sec. 7, since the two available MC samples $e^+e^- \rightarrow \omega 2\pi^0\gamma \rightarrow \pi^+\pi^-3\pi^0\gamma$ and $e^+e^- \rightarrow \eta\pi^+\pi^-\gamma \rightarrow \pi^+\pi^-3\pi^0\gamma$ must be mixed properly.

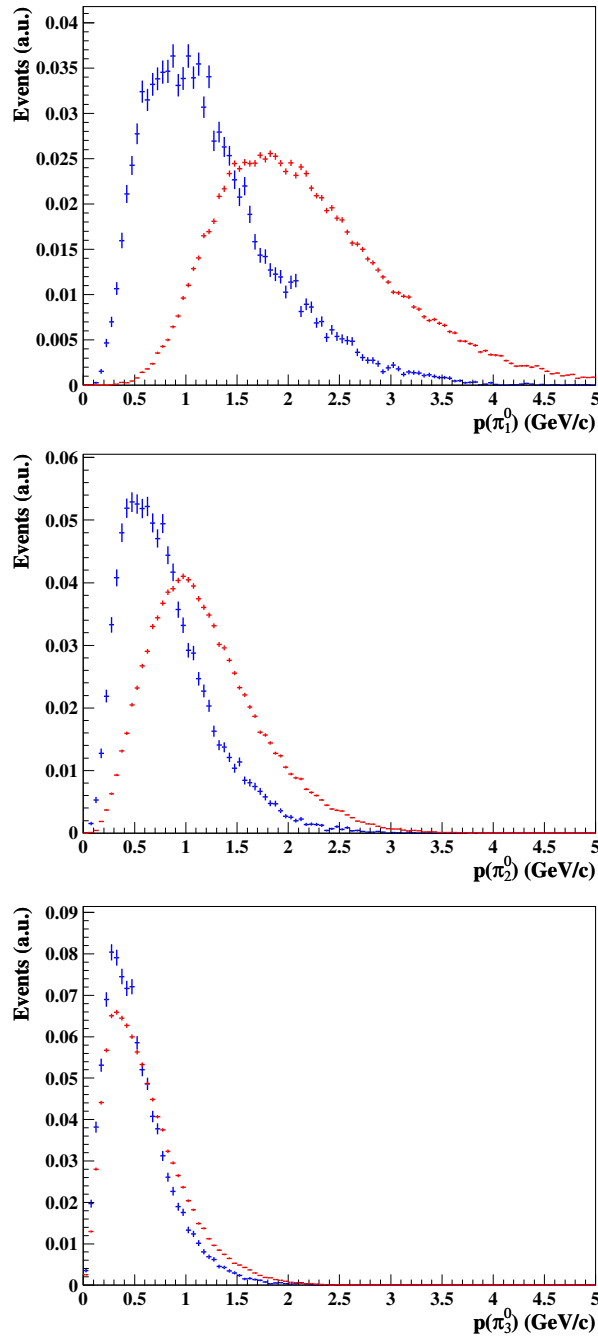


Figure 70.: p_{π^0} distributions for the $\omega 2\pi^0$ (red) and $\eta\pi^+\pi^-$ (blue) MC samples (both normalized to unit area) for the first (highest energetic, top), second (middle), and third (lowest energetic, bottom) π^0 . Full selection applied.

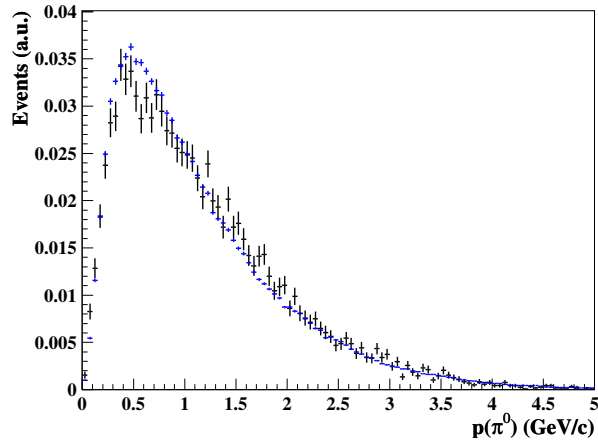


Figure 71.: p_{π^0} distribution for data (black) and $2\pi 3\pi^0$ simulation cocktail (blue). Each event contributes three entries to the calculation of this distribution, one for each π^0 . Full selection applied, both normalized to unit area.

Until this measurement the general assumption was that the intermediate states $\omega 2\pi^0 \gamma$ and $\eta \pi^+ \pi^- \gamma$ overwhelmingly dominate the production of the final state $\pi^+ \pi^- 3\pi^0 \gamma$. To inspect this hypothesis, the corresponding three pion mass distributions have been fitted phenomenologically with Gaussian distributions and a linear background in data in Fig. 74 and for simulation in Fig. 75.

As visible in Fig. 76, the distributions of $M_{3\pi^0}$ and $M_{\pi^+\pi^-\pi^0}$ have different shapes in data compared to the $\omega 2\pi^0$ and $\eta \pi^+ \pi^-$ simulations. This is due to the fact that in each simulated sample only one intermediate state is represented, while in data also events from other production channels pollute the plot of each resonance. In the case of $\omega 2\pi^0$ the background shape is different from the plane background in data. It is not possible to fit the $\omega 2\pi^0$ MC sample with a single Gaussian – as done successfully in data – but a double Gaussian has to be used in order to achieve a reasonable fit. Since the wider Gaussian is considered to be produced by combinatorics (which are submerged in the underlying distribution of the other channel(s) in data), the event yield is extracted from the central Gaussian's parameters.

In Figs. 77, 78, and 79, the 2D-distributions of $M_{3\pi^0}$ versus $M_{\pi^+\pi^-\pi^0}$ are shown as scatter plots. From the $\omega 2\pi^0$ and $\eta \pi^+ \pi^-$ simulations (Figs. 77 and 78, respectively) it can be deduced that no cross feed between the two resonances is expected from simulation.

Since the resonances J/ψ and $\psi(2S)$ are not included in the simulation samples, the production contributions are extracted for $M_{5\pi} < 2.9$ GeV in order to avoid possible bias. To extract the contributions we first measure the fit efficiency via simulation because we need to know the probability for a real resonance event to escape the fitting procedure. Thus we perform the fitting (see Fig. 75) and

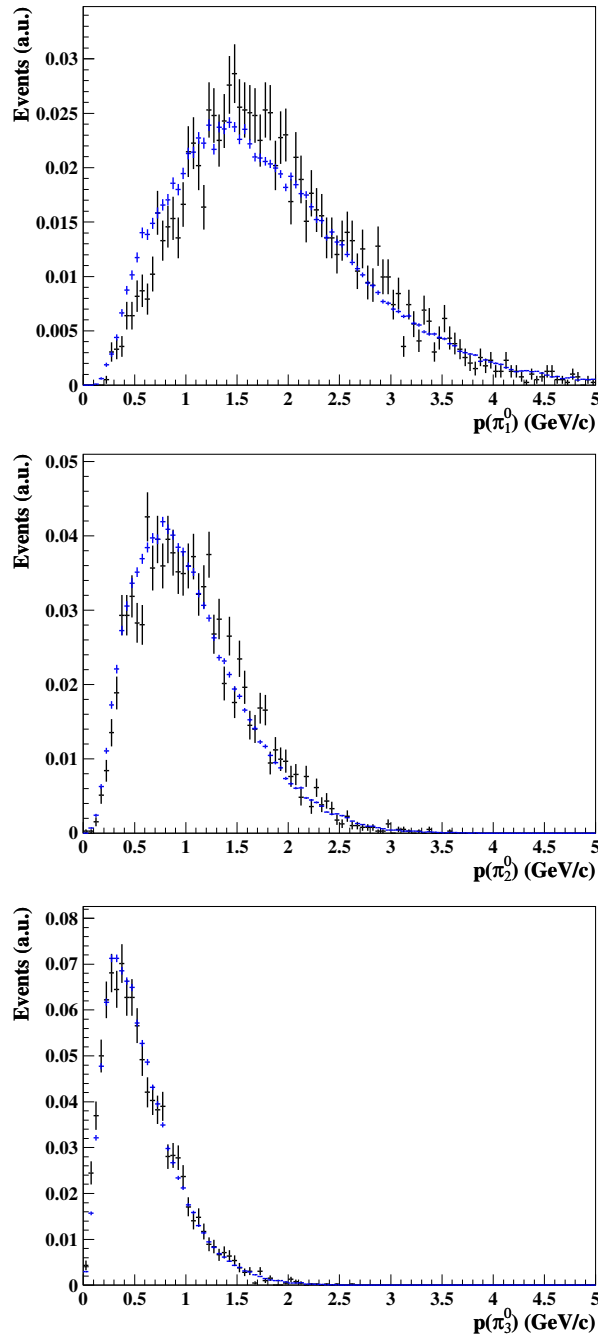


Figure 72.: p_{π^0} distributions for data (black) and $2\pi 3\pi^0$ simulation cocktail (blue) for the first (highest energetic, top), second (middle), and third (lowest energetic, bottom) π^0 . Full selection applied, all normalized to unit area.

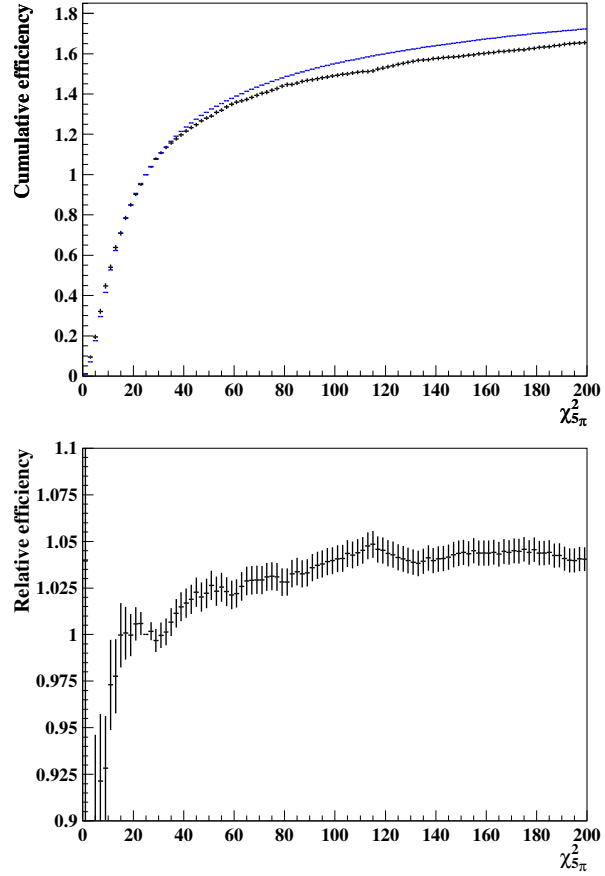


Figure 73.: Top: $\chi_{2\pi^3\pi^0}^2$ efficiency for data (black) and the simulation cocktail (blue) in the J/ψ region with the remaining selection applied. Both distributions normalized to unity at $\chi_{2\pi^3\pi^0}^2 = 25$. Bottom: ratio of the efficiencies (simulation/data).

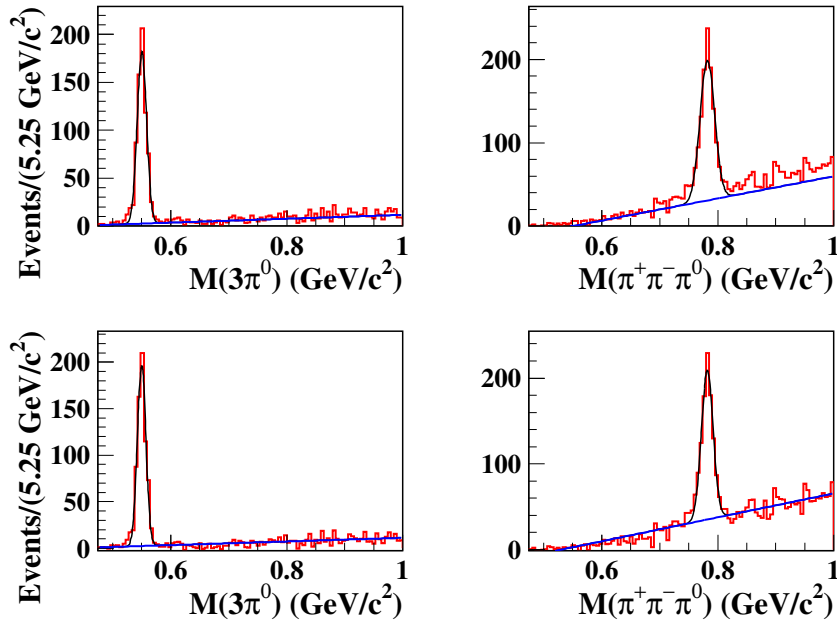


Figure 74.: η -peak in $M(3\pi^0)$ (left panels) and ω -peak in $M(\pi^+\pi^-\pi^0)$ (right panels) from data after continuum subtraction. The upper row shows the distributions without and the lower with sideband subtraction, the latter demonstrating improved fits after background is removed.

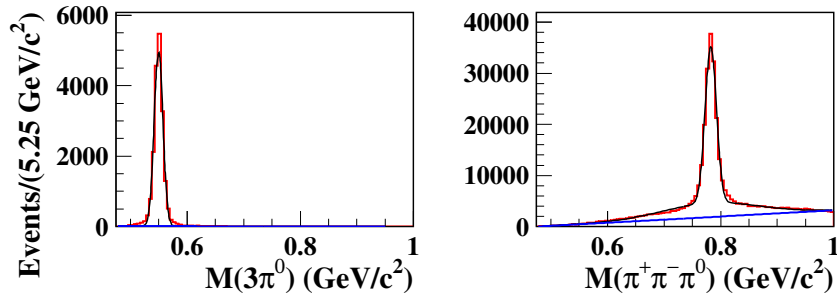


Figure 75.: η -peak in $M_{3\pi^0}$ (left panel) and ω -peak in $M_{\pi^+\pi^-\pi^0}$ (right panel) from each simulation.

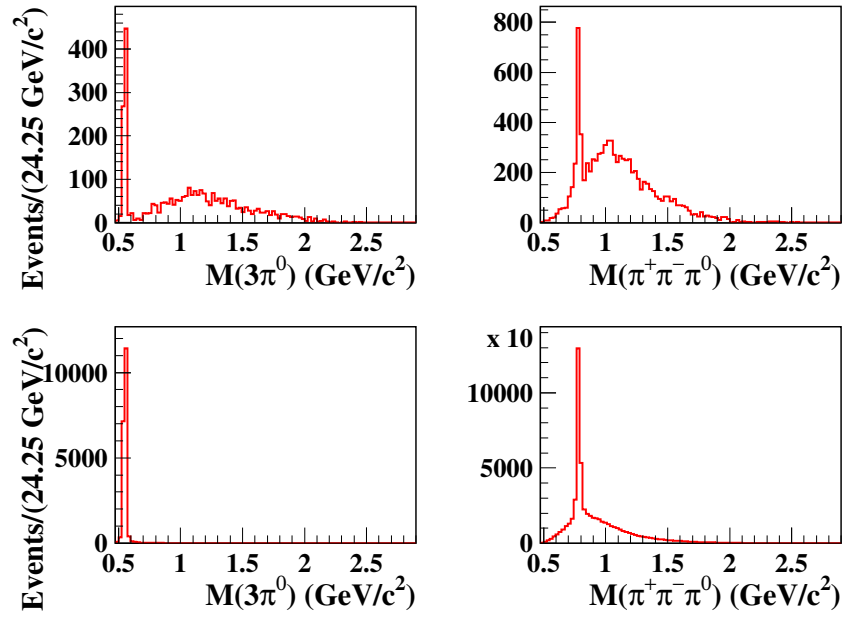


Figure 76.: η -peak in $M(3\pi^0)$ (left panels) and ω -peak in $M(\pi^+\pi^-\pi^0)$ (right panels). The top row shows the distributions in data with sideband and continuum subtraction, the bottom row shows the respective simulation samples.

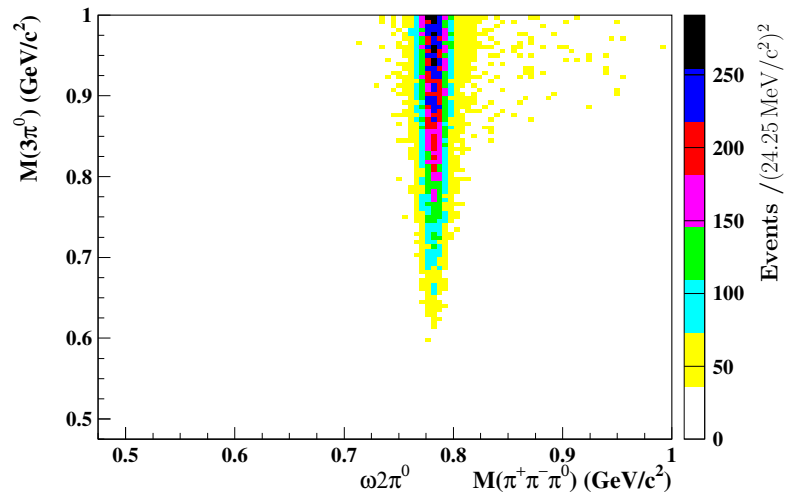


Figure 77.: Scatter plot of $M_{3\pi^0}$ and $M_{\pi^+\pi^-\pi^0}$ from $\omega 2\pi^0$ simulation with a clearly visible ω -peak.

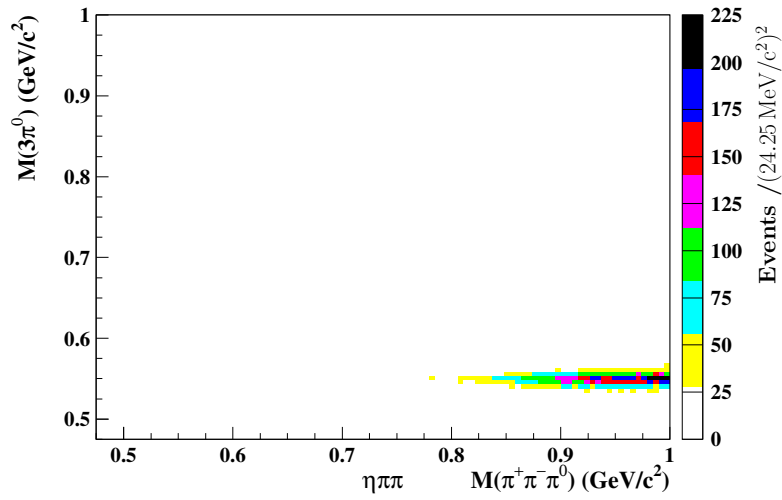


Figure 78.: Scatter plot of $M_{3\pi^0}$ and $M_{\pi^+\pi^-\pi^0}$ from $\eta\pi^+\pi^-$ simulation with a clearly visible η -peak.

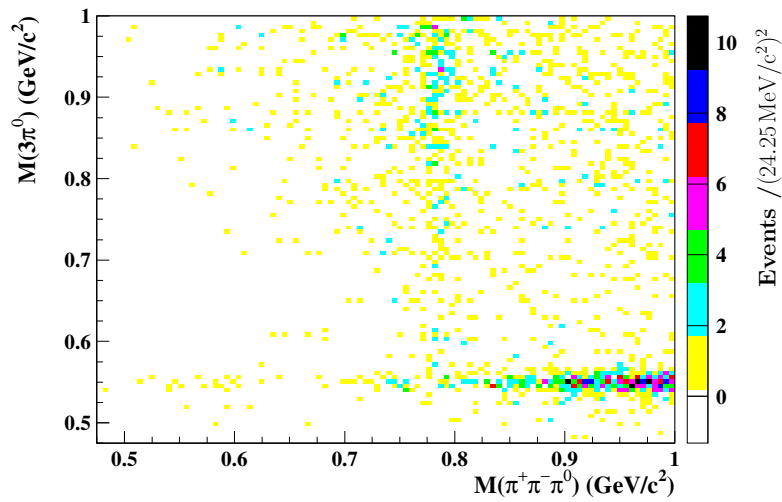


Figure 79.: Scatter plot of $M_{3\pi^0}$ and $M_{\pi^+\pi^-\pi^0}$ from data, with visible ω and η peaks.

contribution measurement in simulation, 100 % being the hypothetical result. The results in data are then normalized to ε , the efficiency determined from the MC samples:

$$\varepsilon := \frac{N_{\text{peak}}}{N_{\text{tot}}}(\text{MC}), \quad \mathcal{B} := \frac{\frac{N_{\text{peak}}}{N_{\text{tot}}}(\text{data})}{\varepsilon}. \quad (55)$$

N_{peak} is the number of events in the fitted peak, while N_{tot} is the total number of events. The weights to mix the $\pi^+\pi^-3\pi^0\gamma$ -MC cocktail are calculated accordingly:

$$w_\omega = \frac{\mathcal{B}(\omega)}{\mathcal{B}(\omega) + \mathcal{B}(\eta)}, \quad w_\eta = \frac{\mathcal{B}(\eta)}{\mathcal{B}(\omega) + \mathcal{B}(\eta)}, \quad (56)$$

where $\mathcal{B}(\omega)$ is the fraction \mathcal{B} evaluated for the ω peak, while $\mathcal{B}(\eta)$ is the fraction \mathcal{B} evaluated for the η peak. Hence w_ω and w_η are the weights calculated for the intermediate states $\omega 2\pi^0\gamma$ and $\eta\pi^+\pi^-\gamma$, respectively. The results can be studied in Tab. 5. In $\eta\pi^+\pi^-\gamma$ simulation we observe an efficiency of 0.914 ± 0.009 , while in the $\omega 2\pi^0\gamma$ sample it is 0.769 ± 0.003 . The raw event fractions are 0.234 ± 0.004 for $\eta\pi^+\pi^- \rightarrow \pi^+\pi^-3\pi^0$ and 0.290 ± 0.005 for $\omega 2\pi^0 \rightarrow \pi^+\pi^-3\pi^0$. When extracting the relative contributions corrected for the detection efficiency, the result is 0.257 ± 0.006 for η and 0.377 ± 0.007 for ω , which is in disagreement with the prior assumption that the final state $2\pi 3\pi^0$ was overwhelmingly dominated by the intermediate states $\eta\pi^+\pi^-$ and $\omega 2\pi^0$. Both simulation samples scaled to their respective contributions are shown in Fig. 80 in comparison to data, demonstrating the dominance of the simulated channels at low masses. At higher masses it is observed that a large fraction of events is not accounted for by the simulated channels, suggesting that they may be produced via different mechanisms.

A more thorough study regarding the evolution of these fractions as a function of the total invariant hadronic mass can be found in Tab. 6. This table also includes the J/ψ -region, which exhibits an especially small production fraction for the $\eta\pi^+\pi^-$ case. According to existing measurements the J/ψ -peak in $2\pi 3\pi^0$ has a much larger contribution from $\omega 2\pi^0$ than from $\eta\pi^+\pi^-$. This can be calculated from the respective branching fractions [43]:

$$\frac{\mathcal{B}(J/\psi \rightarrow \omega 2\pi^0 \rightarrow 2\pi 3\pi^0)}{\mathcal{B}(J/\psi \rightarrow \eta\pi^+\pi^- \rightarrow 2\pi 3\pi^0)} = 23 \pm 11. \quad (57)$$

This is in agreement with the newly measured production fractions in Tab. 6, where the ratio comes out as 14.9 ± 2.2 , which still includes the fraction of events not produced via the J/ψ resonance.

Table 5.: Production contributions and normalization factors for $M_{5\pi} < 2.9$ GeV. N_{peak} is the number of resonance events determined by the Gaussian fit, while N_{tot} is the total number of events (with Poisson errors). The production fraction \mathcal{B} is defined in the text.

Sample	$N_{\text{peak}}(\eta)$	$N_{\text{peak}}(\omega)$	N_{tot}	$\frac{N_{\text{peak}}}{N_{\text{tot}}}$	\mathcal{B}	w
$\eta\pi^+\pi^-$	18184.9 ± 137.6	–	19899	0.914 ± 0.009	–	–
$\omega 2\pi^0$	–	145153 ± 469	188785	0.769 ± 0.003	–	–
data	677.3 ± 3.1	–	2893	0.234 ± 0.004	0.257 ± 0.006	0.404 ± 0.007
data	–	837.6 ± 3.2	2893	0.290 ± 0.005	0.377 ± 0.007	0.595 ± 0.007

Table 6.: Production contributions and normalization factors for different invariant mass ranges. (For the lowest mass region, no ω signal can be fitted in data due to insufficient statistics.)

$M_{5\pi}$ (GeV)	(J/ψ)				
	< 1.4	1.4 – 1.9	1.9 – 2.4	2.4 – 2.9	2.9 – 3.3
$N_{\text{peak}}/N_{\text{tot}}(\eta\pi^+\pi^-)$	0.512 ± 0.059	0.361 ± 0.011	0.136 ± 0.005	0.110 ± 0.008	0.013 ± 0.001
$\epsilon(\eta\pi^+\pi^-)$	0.905 ± 0.037	0.919 ± 0.012	0.897 ± 0.022	0.895 ± 0.032	0.908 ± 0.047
$\mathcal{B}(\eta\pi^+\pi^-)$	0.566 ± 0.069	0.393 ± 0.013	0.152 ± 0.007	0.123 ± 0.010	0.014 ± 0.002
$w(\eta\pi^+\pi^-)$	–	0.430 ± 0.011	0.306 ± 0.013	0.298 ± 0.022	0.064 ± 0.007
$N_{\text{peak}}/N_{\text{tot}}(\omega2\pi^0)$	–	0.406 ± 0.012	0.234 ± 0.008	0.174 ± 0.010	0.140 ± 0.004
$\epsilon(\omega2\pi^0)$	0.864 ± 0.016	0.781 ± 0.004	0.678 ± 0.009	0.603 ± 0.015	0.671 ± 0.022
$\mathcal{B}(\omega2\pi^0)$	–	0.521 ± 0.016	0.345 ± 0.013	0.288 ± 0.018	0.209 ± 0.009
$w(\omega2\pi^0)$	–	0.570 ± 0.011	0.694 ± 0.013	0.702 ± 0.022	0.936 ± 0.007

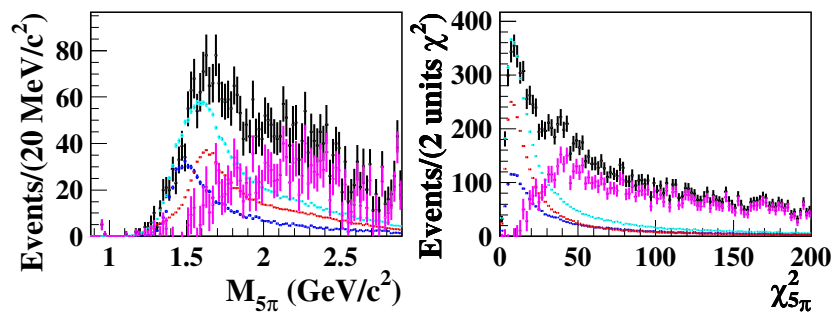


Figure 80.: $M_{5\pi}$ (left) and $\chi^2_{5\pi}$ (right) distributions in the range $0 \leq M_{5\pi}/(\text{GeV}/c^2) \leq 2.9$ in data after continuum subtraction (black) and the simulated signal channels $\eta\pi^+\pi^-$ (blue) and $\omega 2\pi^0$ (red) scaled according to the η and ω yields, respectively, as well as their sum (turquoise). The purple distributions show the difference between data and the sum of the simulations.

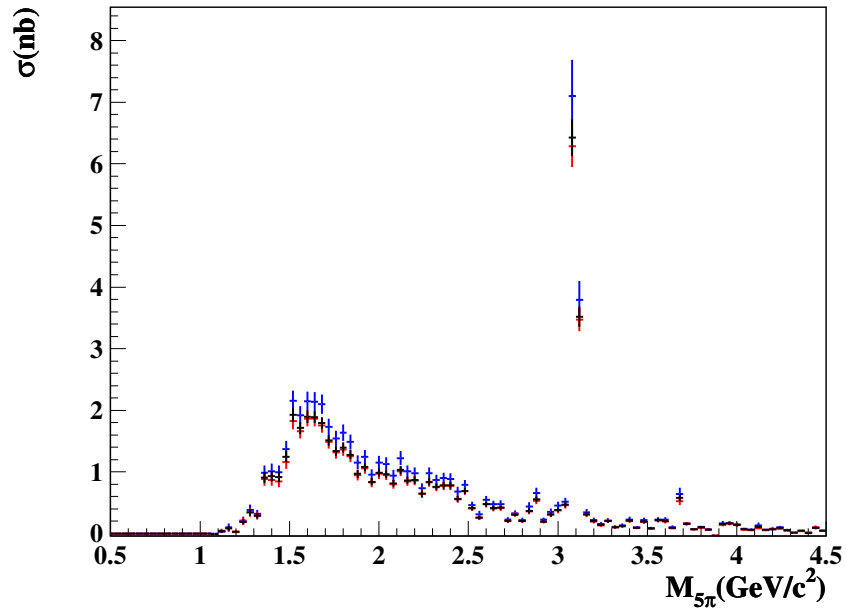


Figure 81.: The final $e^+e^- \rightarrow \pi^+\pi^-\pi^0\gamma_{\text{ISR}}$ cross section calculated as described in the text (black) as well as the extreme cases using the efficiency from the $\eta\pi^+\pi^-$ (blue) and $\omega 2\pi^0$ (red) simulations, respectively, for the unaccounted event fraction. Only statistical uncertainties are included.

6.5 CROSS SECTION

The differing calculations for the total efficiency (as seen in Fig. 67 from the simulation samples $\omega 2\pi^0$ and $\eta\pi^+\pi^-$) can be used in combination with the production fractions determined above to calculate the cross section. The approximately 26 % and 38 % of all events are produced via the intermediate states $\eta\pi^+\pi^-$ and $\omega 2\pi^0$, respectively, are simulated in the existing MC samples, so their total efficiency is well known. The remaining fraction of about 37 % does not have a dedicated sample to calculate its efficiency. Since the comparison of the momentum distributions in Figs. 71, 72 shows that the cocktail of the $\eta\pi^+\pi^-$ and $\omega 2\pi^0$ simulations mixed according to their measured production fractions describes data very well, this signal simulation cocktail is used to calculate the efficiency of the remaining fraction of events. The result is shown in Fig. 81, at low masses exhibiting a smooth distribution peaking around 1.6 GeV/c² with a strong tail even reaching 2.5 GeV/c². At higher masses the resonances J/ψ and $\psi(2S)$ are very prominently featured. The graph also includes the extreme cases, where instead of the cocktail either pure $\eta\pi^+\pi^-$ or $\omega 2\pi^0$ simulation is used to calculate the efficiency of the remaining fraction. These extreme cases give a measure of the systematic uncertainty due to the unknown efficiency of the unsimulated events, explored in detail in Sec. 6.6.

6.6 SYSTEMATIC UNCERTAINTIES OF THE CROSS SECTION

$$e^+e^- \rightarrow \pi^+\pi^-3\pi^0$$

Due to the different kinematics of the intermediate states $e^+e^- \rightarrow \omega 2\pi^0\gamma$ and $e^+e^- \rightarrow \eta\pi^+\pi^-\gamma$, their $\chi^2_{\pi^+\pi^-3\pi^0\gamma}$ distributions differ and hence the detection efficiencies determined from either the $\omega 2\pi^0\gamma$ or the $\eta\pi^+\pi^-\gamma$ simulation sample deviate by up to 67 % from each other, depending on the invariant mass $M_{5\pi}$.

As outlined above, 37 % of the $\pi^+\pi^-3\pi^0\gamma$ events are produced through other channels or phase space and the detection efficiency of these events is approximated by the efficiency of the signal simulation cocktail. It has been checked in an almost background-free data sample around the J/ψ resonance that the efficiency of the $\chi^2_{5\pi}$ requirement is in excellent agreement between data and the simulation cocktail, showing relative differences of less than 5 %. The difference between the $\omega 2\pi^0\gamma$ and $\eta\pi^+\pi^-\gamma$ efficiencies is taken as the uncertainty for the event fraction not simulated by the $\omega 2\pi^0\gamma$ or $\eta\pi^+\pi^-\gamma$ samples. This results in a total relative uncertainty of $37\% \cdot 67\% = 25\%$ for the $e^+e^- \rightarrow \pi^+\pi^-3\pi^0\gamma$ cross section. The only other considerable source of uncertainty is the subtraction of continuum background. Its uncertainty amounts to 3 %, 7 %, 13 %, and 20 %, respectively, for $M_{5\pi}$ below 2 GeV, 2.5 GeV, 3.2 GeV, and above. Hence, in the same intervals, the total systematic uncertainties become 25 %, 26 %, 28 %, and 32 %.

6.7 J/ψ BRANCHING FRACTION

The J/ψ resonance is also produced as an intermediate state of the process $e^+e^- \rightarrow \pi^+\pi^-3\pi^0$, as evidenced by the large peak around $3.1 \text{ GeV}/c^2$ in the cross section. This peak can be used to extract the branching fraction $\mathcal{B}_{J/\psi \rightarrow 2\pi 3\pi^0}$. By fitting a normal distribution (due to the extremely small width of the resonance $\Gamma^{J/\psi} = (92.9 \pm 2.8) \text{ keV}/c^2$, the peak shape is dominated by detector resolution) to the peak observed in data as shown in Fig. 82, the size of this production channel is determined. The ‘‘background’’ from other production mechanisms is flat and thus modeled by an additional first order polynomial. The parameters resulting from the fit can then be used to extract the J/ψ -yield after normalization to luminosity and efficiency:

$$\begin{aligned} \mathcal{B}_{J/\psi \rightarrow 2\pi 3\pi^0} \cdot \sigma_{\text{int}}^{J/\psi} &= \frac{N(J/\psi \rightarrow 2\pi 3\pi^0)}{d\mathcal{L}/dE \cdot \varepsilon} \\ &= 359 \pm 11_{\text{stat}} \pm 21_{\text{fit}} \pm 97_{\text{syst}} \text{ MeVnb} . \end{aligned} \quad (58)$$

Using $M_{J/\psi} = (3096.916 \pm 0.011)\text{MeV}/c^2$ [43] and the following relation [38], the product of branching fraction and electronic width can be calculated:

$$\begin{aligned} \mathcal{B}_{J/\psi \rightarrow 2\pi 3\pi^0} \cdot \Gamma_{ee}^{J/\psi} &= \frac{N(J/\psi \rightarrow 2\pi 3\pi^0) \cdot M_{J/\psi}^2 c^4}{6\pi^2 \cdot \hbar^2 c^2 \cdot d\mathcal{L}/dE \cdot \varepsilon} \\ &= 149 \pm 4_{\text{stat}} \pm 9_{\text{fit}} \pm 40_{\text{syst}} \text{eV}. \end{aligned} \quad (59)$$

With $\Gamma_{ee}^{J/\psi} = (5.55 \pm 0.14)\text{keV}$ [43], the branching fraction follows:

$$\mathcal{B}_{J/\psi \rightarrow 2\pi 3\pi^0} = (2.7 \pm 0.1_{\text{stat}} \pm 0.8_{\text{syst}} \pm 0.1_{\text{input}}) \times 10^{-2}. \quad (60)$$

Here, the model uncertainty due to the fit has been combined with the general systematic uncertainty of the cross section measurement. The model uncertainty due to the fit function is determined by repeating the fit using different functions. A normal distribution plus second order polynomial as well as a Voigt profile plus first order polynomial and also the sum of a normal distribution plus a Voigt profile over a first order polynomial (see Fig. 83) are studied. The maximum of the differences to the nominal result is taken as the systematic uncertainty. In addition, the systematic uncertainty of the general analysis is applied, which amounts to 28 %. Background subtraction is applied in the usual manner as shown in Fig. 84. The acceptance is determined from the $\omega 2\pi^0$ simulation due to its overwhelming dominance over the channel $\eta\pi^+\pi^-$ outlined above (Sec. 6.4). Furthermore the acceptance and efficiency has been fitted with a constant to minimize statistical fluctuations. The relative uncertainty of this fit is also added in quadrature to the uncertainty of the branching fraction.

The uncertainty due to the input values ($\Gamma_{ee}^{J/\psi}$, $M_{J/\psi}$, and $\hbar c$) is propagated to give $0.1_{\text{input}} \times 10^{-2}$.

SUMMARY OF THE CHANNEL $\pi^+\pi^-3\pi^0\gamma_{\text{ISR}}$

The cross section $e^+e^- \rightarrow \pi^+\pi^-3\pi^0$ had only been measured very crudely up to now. This leads to the effect that no Monte Carlo simulation generator for the full channel could be produced. Despite this obstacle, which makes the acceptance and efficiency determination exceptionally difficult, this cross section is now analyzed with a systematic uncertainty of 25 % to 32 %, resulting in a much clearer picture, as witnessed by the comparison to the previous world data set in Fig. 85. Besides being more precise, the new cross section also encompasses a wider energy range, especially the resonances J/ψ and $\psi(2S)$. Furthermore the intermediate structures are studied. This yields the unexpected result that the intermediate states $\omega 2\pi^0$ and $\eta\pi^+\pi^-$ only dominate production at low energies. Finally, the previously unknown branching fraction $J/\psi \rightarrow \pi^+\pi^-3\pi^0$ is extracted, with the result $2.7 \pm 0.8\%$.

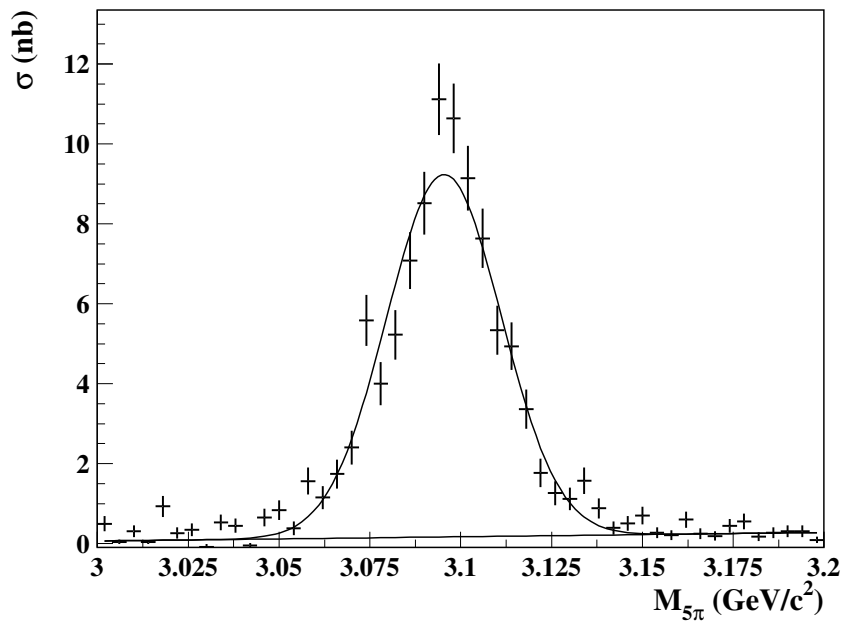


Figure 82.: J/ψ peak in the $e^+e^- \rightarrow \pi^+\pi^-3\pi^0$ cross section, including the fit of a normal distribution over linear background.

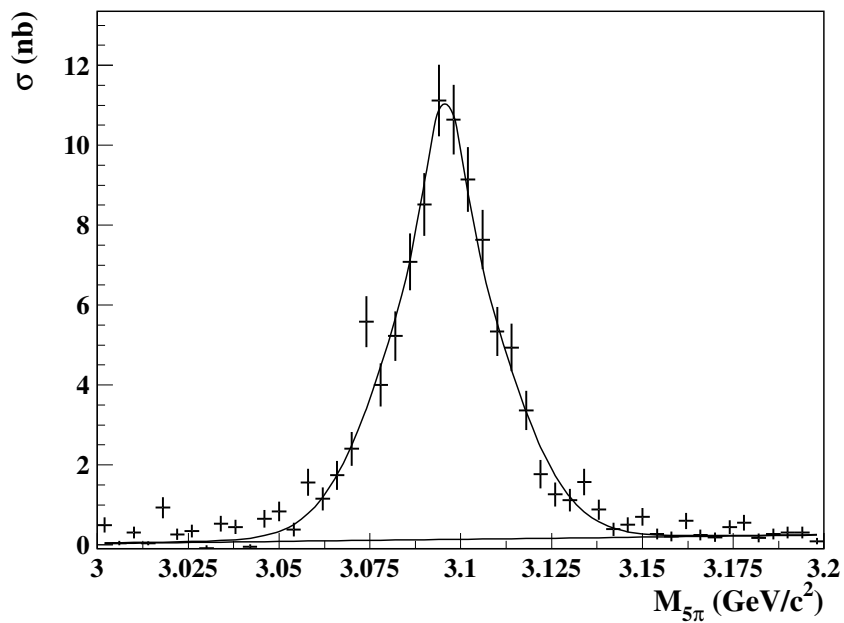


Figure 83.: J/ψ peak in the $e^+e^- \rightarrow \pi^+\pi^-3\pi^0$ cross section, including the fit of the sum of a Voigt profile plus a normal distribution over linear background.

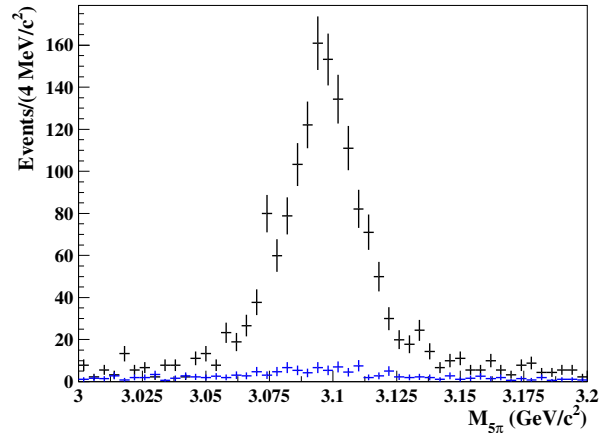


Figure 84.: The event rates from background (blue) and signal data (black) in the J/ψ range. No efficiency correction applied.

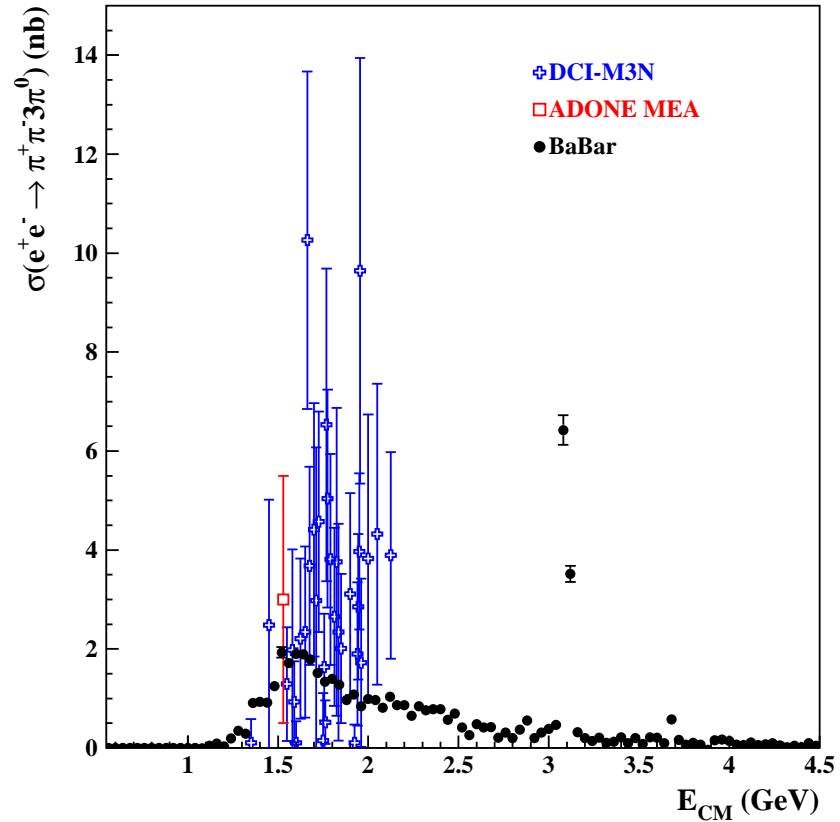


Figure 85.: Comparison of $e^+e^- \rightarrow \pi^+\pi^-\pi^0$ cross section measurements from different experiments [126, 131] with statistical uncertainties. The *BABAR* measurement reaches unprecedented precision and covers a greater range than the previous world data set.

Up to now, the cross section $e^+e^- \rightarrow \pi^+\pi^-2\pi^0$ had only been measured over small energy ranges below 2.2 GeV and with especially poor accuracy above 1.4 GeV, witnessed by the limited data sets in Fig. 17. Besides leaving a lot to be discovered about this process itself, this also means that its contribution to the prediction of the muon anomalous magnetic introduces a major part of the total uncertainty. After investigating the process $e^+e^- \rightarrow \pi^+\pi^-3\pi^0$, which also acts as a background to $e^+e^- \rightarrow \pi^+\pi^-2\pi^0$, a precise measurement of the cross section $e^+e^- \rightarrow \pi^+\pi^-2\pi^0$ can be pursued.

In this chapter, the cross section analysis of the channel $e^+e^- \rightarrow \pi^+\pi^-2\pi^0\gamma_{\text{ISR}}$ is summarized. It consists of an event selection closely adjusted to the final state, followed by two different background subtraction methods. Furthermore, the effect of the detector mass resolution is investigated before applying several efficiency corrections and radiative corrections. These additional steps are necessary to reach the accuracy goal of 5%. Finally, the cross section is extracted and the analysis is expanded by a deeper look into the internal structures of the production process.

7.1 EVENT SELECTION

The event selection for the $\pi^+\pi^-2\pi^0$ cross section determination consists of a variety of requirements, most of which have already been described among the more general selection in Ch. 5. The remaining requirements, which are specific to this final state, are summarized below:

- Number of photons $N_\gamma \geq 5$,
- $0 < \chi^2_{2\pi 2\pi^0} < 30$, where $\chi^2_{2\pi 2\pi^0}$ serves as a test of the goodness of the kinematic fit in the $2\pi 2\pi^0\gamma$ hypothesis,
- $\chi^2_{2\pi 2\pi^0} < \chi^2_{2\pi\pi^0\eta} \wedge \chi^2_{2\pi 2\pi^0} < \chi^2_{2\pi 2\eta}$, where $\chi^2_{2\pi\pi^0\eta}$ and $\chi^2_{2\pi 2\eta}$ serve as tests of the goodness of the kinematic fits in the $2\pi\pi^0\eta\gamma$ and $2\pi 2\eta\gamma$ hypotheses, respectively.

Requirements specific to the channel $e^+e^- \rightarrow \pi^+\pi^-2\pi^0\gamma_{\text{ISR}}$

For the final state $\pi^+\pi^-2\pi^0\gamma_{\text{ISR}}$, five photons are necessary, since only the decay $\pi^0 \rightarrow \gamma\gamma$ is considered.¹ This is enforced by the

¹ The cross section is corrected for only considering this decay by dividing by the square of the branching fraction $\mathcal{B}(\pi^0 \rightarrow \gamma\gamma) = (98.823 \pm 0.034)\%$ [43].

requirement $N_\gamma \geq 5$. Events with more than five photons can either come from physical background processes or radiative effects or machine background. The first case is treated in Sec. 7.2, while the second effect is corrected as described in Sec. 7.4. The latter pollution is cleaned up in two steps: in the first stage, only photons with an energy of more than 50 MeV are considered (see Sec. 5.4), leaving only a negligible fraction because machine background photons are predominantly low-energetic. The second phase is the kinematic fit, in which a random photon has an insignificant probability of matching the signal hypothesis for a given event, further reducing the contribution.

The most important requirement is $0 < \chi_{2\pi 2\pi^0}^2 < 30$, therefore its effect is studied in more detail in Sec. 7.3.2.

The requirement $\chi_{2\pi 2\pi^0}^2 < \chi_{2\pi\pi^0\eta}^2 \wedge \chi_{2\pi 2\pi^0}^2 < \chi_{2\pi 2\eta}^2$ suppresses events with one or two η mesons in the final state instead of π^0 . If the η meson decays into two photons ($\mathcal{B}(\eta \rightarrow \gamma\gamma) \approx 39.3\%$), the detector receives the same particles as in the case of the π^0 . To detect these events, the kinematic fit is also performed under the $\pi^+\pi^-\pi^0\eta$ and $\pi^+\pi^-\eta\eta$ hypotheses. In data $(2.02 \pm 0.02)\%$ of all events are rejected by the η -veto. We can study the false rejection rate using the $2\pi 2\pi^0$ simulation since it does not contain any η mesons. In the signal MC sample the η -veto has a survival rate of $(99.519 \pm 0.005)\%$ in the region $\chi_{2\pi 2\pi^0}^2 < 30$. Since this is the requirement for the analysis, it is concluded that $(0.481 \pm 0.005)\%$ of the signal events are falsely rejected, an effect which is compensated by dividing by the efficiency. Subtracting the mis-rejected events, $(1.54 \pm 0.02)\%$ of the events in data must originate from actual background processes like $e^+e^- \rightarrow \pi^+\pi^-\pi^0\eta\gamma$, $e^+e^- \rightarrow \pi^+\pi^-\eta\eta\gamma$.

Effect of the kinematic fit

During the kinematic fit outlined in Sec. 5.5 a large number of events is discarded since they do not fulfill the constraints imposed by energy-momentum conservation and the physical π^0 mass. These events and other events with non-converging kinematic fits are assigned values ≥ 20000 for $\chi_{4\pi}^2$. Furthermore, a cut is placed at $\chi_{4\pi}^2 < 30$ to reject most background processes while retaining a large fraction of the signal events. From the comparison of the shapes of the χ^2 distributions in data and signal simulation shown in Fig. 86 it is apparent that there are overwhelmingly many background events in the tail above $\chi_{4\pi}^2 = 30$. After applying the full selection, 167150 events are left in data, which can be observed in Fig. 87 in the $M_{4\pi}$ distribution, which shows a few structures not predicted by simulation. The corresponding distributions as a function of $\chi_{4\pi}^2$ are shown in Fig. 88, where data is slightly wider than simulation. This difference is due to the fact that no background subtraction has been performed yet and the simulation might be

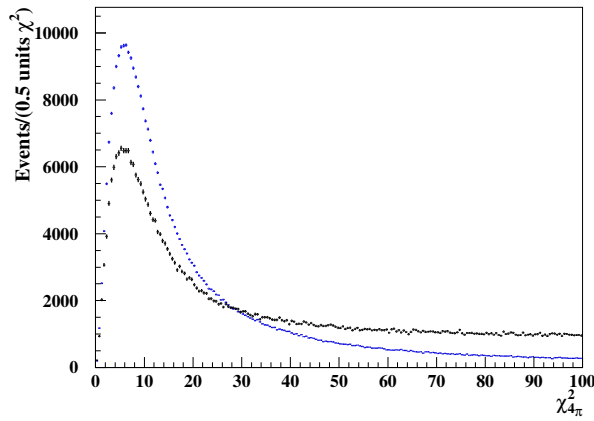


Figure 86.: Distributions of $\chi^2_{2\pi 2\pi^0}$ in data (black) and signal simulation (blue, scaled to the same area as data) in the Level 2 ntuples. A considerably heavier tail is seen in data due to background processes.

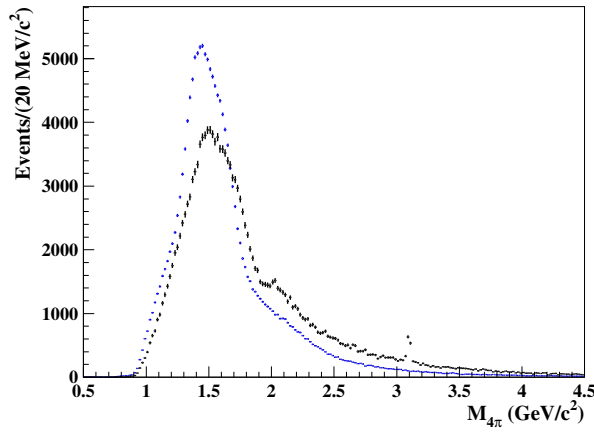


Figure 87.: Distributions of $M_{4\pi}$ after selection in data (black) and signal simulation (blue, scaled to the same area as data).

of limited accuracy, leading to different shapes in simulation compared to data. This discrepancy is resolved in Sec. 7.3.2, where the systematic uncertainty due to requiring particularly $\chi^2_{4\pi} < 30$ is assessed. The event numbers of the different samples after applying the full selection are listed in Tab. 7.

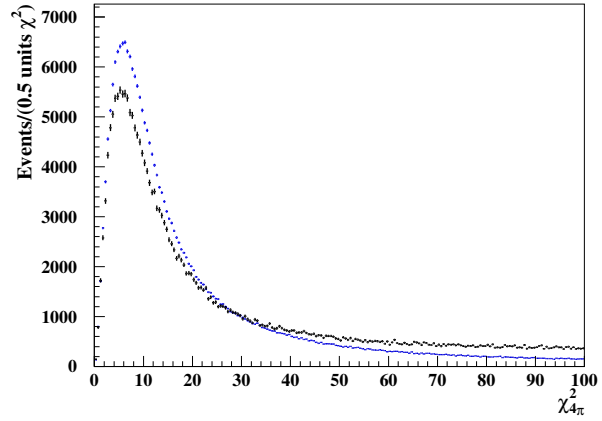


Figure 88.: Distributions of $\chi_{2\pi^2\pi^0}^2$ after selection in data (black) and signal simulation (blue, scaled to the same area as data).

Table 7.: The available data and simulation samples. All numbers after full selection. (N_{raw} is the produced number of events, f is the factor to scale each simulation to the same luminosity as observed in data, $N_{\text{eff}} = f \cdot N_{\text{raw}}$)

Channel	N_{raw}	f	N_{eff}	$N_{\text{raw}}/N_{\text{data}}$
data			167150	
signal	836662		836662	5.01
uds	10584	1.10	11678	0.06
$\tau^+\tau^-$	3	1.03	3	$2 \cdot 10^{-5}$
$\pi^+\pi^-\pi^0$	2047	0.122	249	0.012
$2(\pi^+\pi^-\pi^0)$	7	5.54	39	$4 \cdot 10^{-5}$
$K^+K^-2\pi^0$	220	1.15	254	10^{-3}
$K_s K^\pm \pi^\mp$	17474	0.04	679	0.1
$\eta\pi^+\pi^-$	18851	0.023	443	0.11
$\omega 2\pi^0$	72352	0.026	1860	0.43

7.2 BACKGROUND SUBTRACTION

A small fraction of background events survives the selection outlined in Secs. 5 & 7.1. These events fall into two main categories: ISR and continuum production. The contribution from the channel $e^+e^- \rightarrow \tau^+\tau^-(\gamma)$ is negligible as will be shown in Sec. 7.2.2. Background from $B\bar{B}$ and $D\bar{D}$ events is negligible as well due to the requirement of a high energetic photon. The amount of background surviving the event selection is determined from simulation (normalized by comparing to data) for continuum processes. ISR backgrounds are also subtracted using simulation (albeit possibly after reweighting to make the mass distributions more precise). The channel $e^+e^- \rightarrow \pi^+\pi^-3\pi^0\gamma_{\text{ISR}}$ has to be measured in order to subtract its contribution reliably. This measurement is described in Ch. 6 and its results are used here to subtract the corresponding background contribution.

As a cross check, a data-driven method will be applied in Sec. 7.2.5.

7.2.1 Continuum Background

As in the $e^+e^- \rightarrow \pi^+\pi^-3\pi^0$ analysis, the first contribution to be subtracted is continuum hadron production, whose $M_{4\pi}$ and $\chi_{4\pi}^2$ distributions are shown in Fig. 89. Also like before, it is advantageous to scale this MC sample by measuring the π^0 yield in data and simulation, using the same method outlined in Sec. 6.2.1. The π^0 yields in data and continuum simulation extracted over the full invariant mass spectrum are shown in Fig. 90.

An interesting feature in the data plot is a peak at very small masses ($M_{\gamma_{\text{ISR}}\gamma} \lesssim 0.1 \text{ GeV}$). This peak originates from the combination of the real (as opposed to fake) ISR photon with either an additional NLO ISR photon or simply with a low energetic background photon. It does not show up in the simulation, since machine background and NLO effects are not modeled properly.

The global normalization factor from comparing the π^0 yields in data and continuum simulation (scaled to the same luminosity) is $f_{\text{uds}} = 0.346 \pm 0.031$. Now it has to be checked whether this global (meaning $0.5 < M_{4\pi}/\text{GeV}/c^2 < 4.5$ and all other selection criteria) result holds for each slice of the whole energy spectrum.

In order to verify this, we split up our energy range into seven slices: $M_{4\pi} < 1.2 \text{ GeV}$, $1.2 \text{ GeV} < M_{4\pi} < 1.7 \text{ GeV}$, $1.7 \text{ GeV} < M_{4\pi} < 2.2 \text{ GeV}$, $2.2 \text{ GeV} < M_{4\pi} < 2.7 \text{ GeV}$, $2.7 \text{ GeV} < M_{4\pi} < 3.2 \text{ GeV}$, $3.2 \text{ GeV} < M_{4\pi} < 3.7 \text{ GeV}$ and $M_{4\pi} > 3.7 \text{ GeV}$. The same routine as above is applied for each slice in data and uds simulation. The result is shown in Fig. 91. In uds simulation the π^0 peak is well visible in all mass slices except the lowest mass region, as it contains hardly any entries. In data the low-mass slice shows no π^0 peak because combinatorial background is too high. In the intermediate

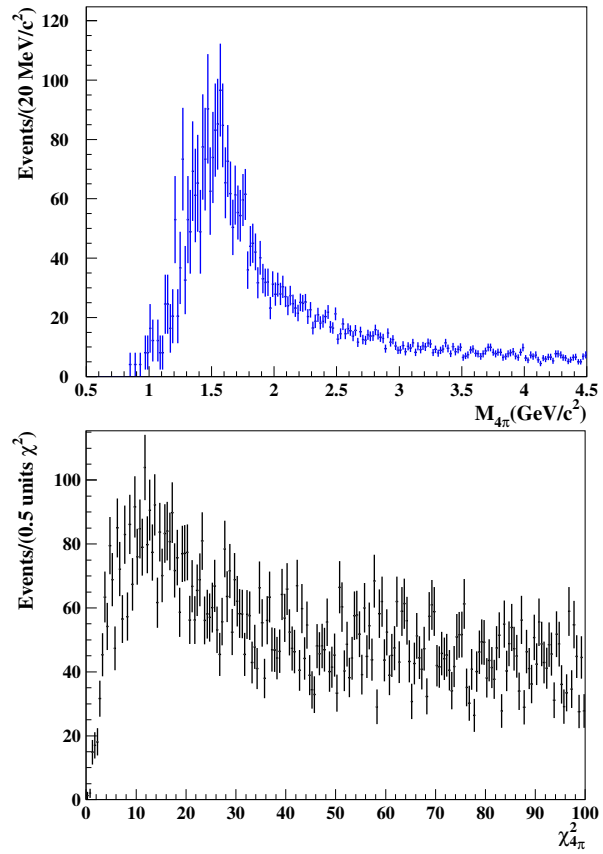


Figure 89.: Distributions of $M_{4\pi}$ (top) and $\chi_{2\pi 2\pi^0}^2$ (bottom) of the uds simulation after application of the selection. The results are already scaled, see text for explanation.

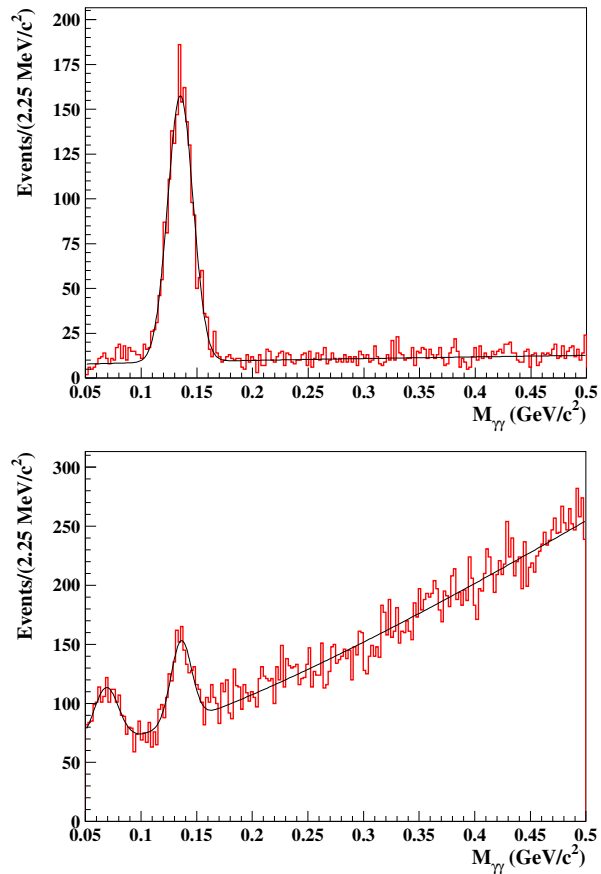


Figure 90.: Distributions the $\gamma_{\text{ISR}}\gamma$ invariant mass for all $\gamma_{\text{ISR}}\gamma$ combinations in uds simulation (top) and data (bottom). The peak at low masses in data is most likely due to machine background or additional NLO radiation. The full mass range $0.5 < M_{4\pi}/\text{GeV}/c^2 < 4.5$ is shown.

slices, the π^0 as well as the peak from machine background or NLO ISR is very pronounced. The high mass slices consist purely of the π^0 peak and some background. For the normalization factor π^0 peaks in both samples (data and simulation) are necessary. Thus the lowest mass slice cannot be used to study the mass-dependence or, effectively, there is virtually no continuum background in this mass region.

Table 8.: uds scaling factors f_{uds} in the whole range of mass bins with their statistical uncertainties δf_{uds} from the fit.

$M_{4\pi}(\text{GeV}/c^2)$	f_{uds}	δf_{uds}	$(\delta f_{\text{uds}})/f_{\text{uds}}$
1.2 – 1.7	3.73	0.71	0.19
1.7 – 2.2	0.583	0.109	0.19
2.2 – 2.7	0.216	0.042	0.20
2.7 – 3.2	0.243	0.038	0.16
3.2 – 3.7	0.139	0.032	0.23
3.7 – 4.5	0.142	0.027	0.19
total	0.346	0.031	0.09

As seen in Fig. 92, there is a significant deviation from the global scaling factor. At low masses, the normalization factor seems to be much larger than at high masses. The region $1.2 \text{ GeV} < M_{4\pi} < 1.7 \text{ GeV}$ produces a scaling factor an order of magnitude larger than the global value, but has very large uncertainties. The range $1.7 \text{ GeV} < M_{4\pi} < 2.2 \text{ GeV}$ also seems to include significantly more continuum background. Accordingly, the higher mass range values all lie below the global scaling. To account for this effect, a dynamic $M_{4\pi}$ -dependent scaling is introduced, which uses an exponential function plus constant fitted to the measured scaling factors (also shown in Fig. 92). Outside of the measured points, the function value at the corresponding edge is used. The uncertainties are taken from the measured points and are thus highly mass-dependent, which will be taken into account in the total systematics. From the numbers in Tab. 8 it can be deduced that the relative uncertainty of the scaling points is approximately 20 % or less in the complete mass spectrum. When figuring in the fact that the uds background contribution is less than 5 % up to $M_{4\pi} = 3.2 \text{ GeV}/c^2$ and averages to 10 % for higher masses (by rising from 5 % to 15 %), demonstrated in Fig. 93, it is estimated that the systematic uncertainty due to continuum subtraction is less than 1 % for $M_{4\pi} \leq 3.2 \text{ GeV}/c^2$ and approximately 2 % above.

An Aside: $\chi_{4\pi}^2$ Sideband Region

In order to increase the statistics of the uds normalization, it was suggested to extend the study to a wider $\chi_{4\pi}^2$ region. Improving statistics by this method proved to be infeasible since the results

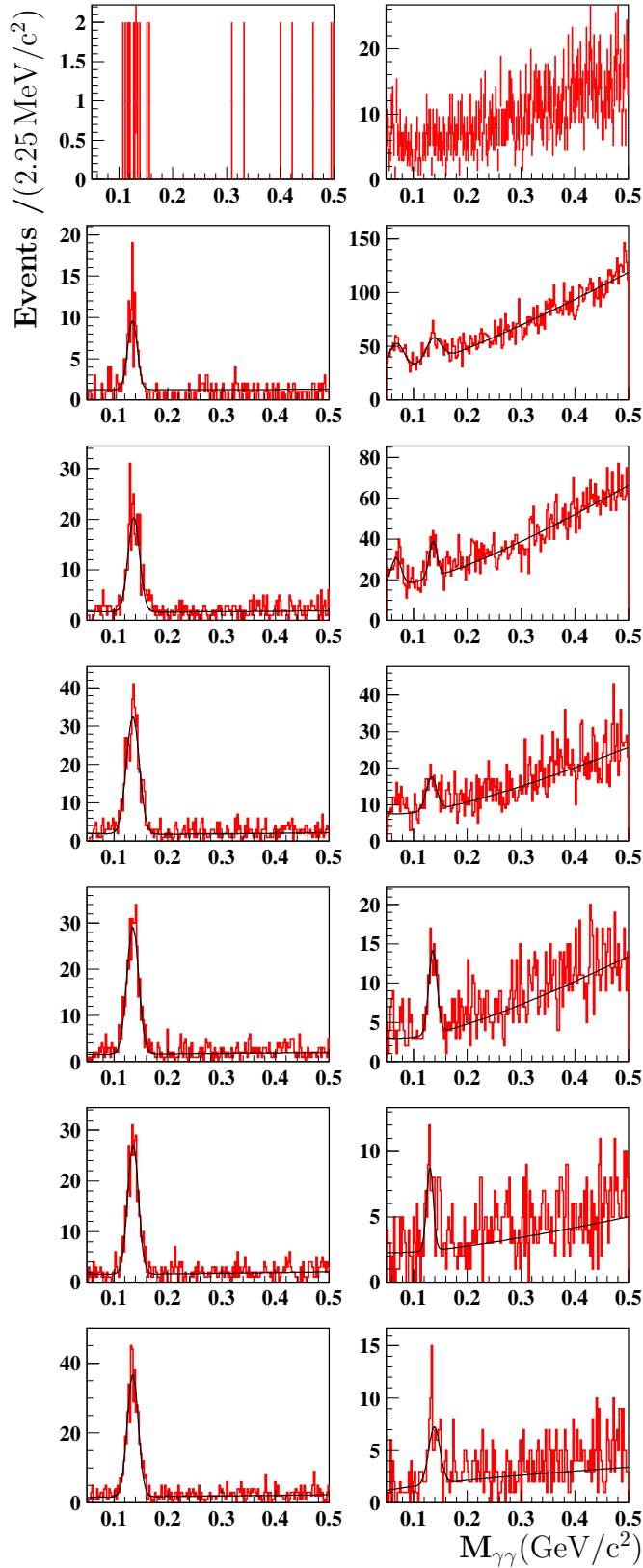


Figure 91.: Distributions of the invariant $\gamma_{\text{ISR}}\gamma$ mass for uds simulation (left panels) and data (right panels). Mass ranges from top to bottom: $M_{4\pi} < 1.2 \text{ GeV}/c^2$, $1.2 \text{ GeV}/c^2 < M_{4\pi} < 1.7 \text{ GeV}/c^2$, \dots , $3.2 \text{ GeV}/c^2 < M_{4\pi} < 3.7 \text{ GeV}/c^2$, $M_{4\pi} > 3.7 \text{ GeV}/c^2$.

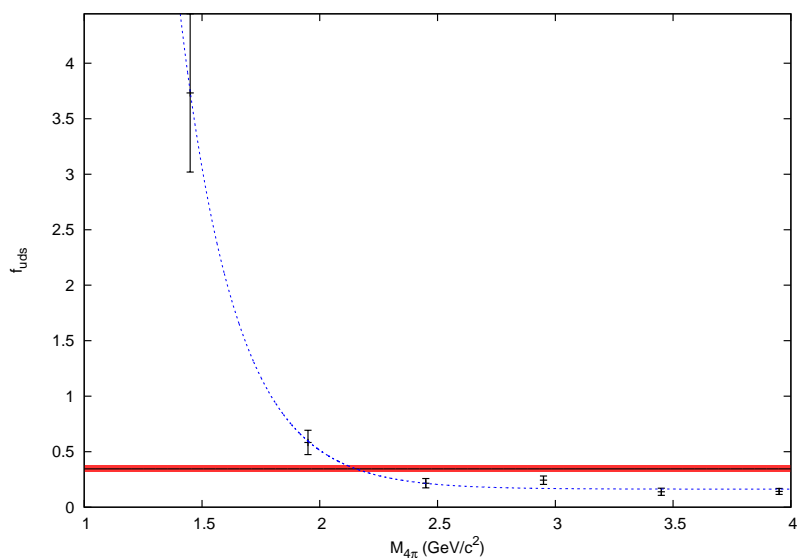


Figure 92.: Evolution of the uds scaling factor as a function of the corresponding $M_{4\pi}$ slices. The black line marks the global scaling factor with its 1σ -uncertainties in red, while the dashed blue line represents the fit of an exponential function plus a constant.

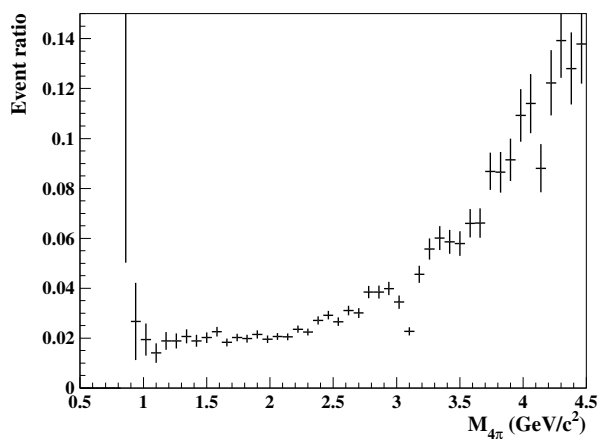


Figure 93.: Ratio of continuum simulation to data after application of the scaling procedure as a function of $M_{4\pi}$. The full selection is applied.

Table 9.: $\chi_{4\pi}^2$ sideband region: uds scaling factors f_{uds} in the whole range of mass bins with their statistical uncertainties δf_{uds} from the fit.

$M_{4\pi}(\text{GeV}/c^2)$	f_{uds}	δf_{uds}
1.2 – 1.7	0.709	0.054
1.7 – 2.2	0.551	0.065
2.2 – 2.7	0.447	0.040
2.7 – 3.2	0.446	0.044
3.2 – 3.7	0.606	0.056
> 3.7	0.622	0.055
total	0.517	0.012

inside the signal region $0 < \chi_{4\pi}^2 < 30$ turned out to be significantly different from the sideband $30 < \chi_{4\pi}^2 < 100$. The global result in the sideband region is 0.517 ± 0.012 (to be compared with 0.346 ± 0.031 in the signal region). The corresponding plots can be found in App. C.3 as Figs. 149, 150, 151 with the corresponding scaling factors listed in Tab. 9. Therefore including this wider region would only introduce an additional systematic uncertainty.

7.2.2 $e^+e^- \rightarrow \tau^+\tau^-(\gamma)$

The process $e^+e^- \rightarrow \tau^+\tau^-(\gamma)$ is simulated by the generator KK2f [166, 174–176] including radiative corrections up to order α , while using the library TAUOLA [177] for τ decays. In the first step, the generator produces the channel $e^+e^- \rightarrow \tau^+\tau^-(\gamma)$ as a spinless process but including radiative corrections. In the second step, the effect of possible polarization of the incoming e^\pm beam is calculated as well as the dependence of the τ decay on its polarization.

Since the process $e^+e^- \rightarrow \tau^+\tau^-(\gamma)$ can be calculated in QED, the theoretical scaling factor (1.03) is reliable for our simulated sample with respect to luminosity. Still, it is useful to cross check this expectation by comparing to data. Once the uds normalization has been completed, the variable called Δ_{min} (or Delta_min) can be used for this purpose. This variable gives the minimum value of all angles between a charged track and the ISR photon in each event. In ISR processes, large values of Δ_{min} are preferred due to the high-energy ISR photon. Thus, at small angles this distribution is dominated by two contributions: $\tau^+\tau^-(\gamma)$ and continuum background, while other contributions are negligible. Therefore after subtracting the normalized uds MC sample from data we can check the $\tau^+\tau^-(\gamma)$ MC normalization.

In Fig. 94 the Δ_{min} distributions for data, uds and $\tau^+\tau^-(\gamma)$ simulations are plotted on a logarithmic scale. A closer zoom is given in Fig. 95 on a linear scale with signal simulation shown as well. It

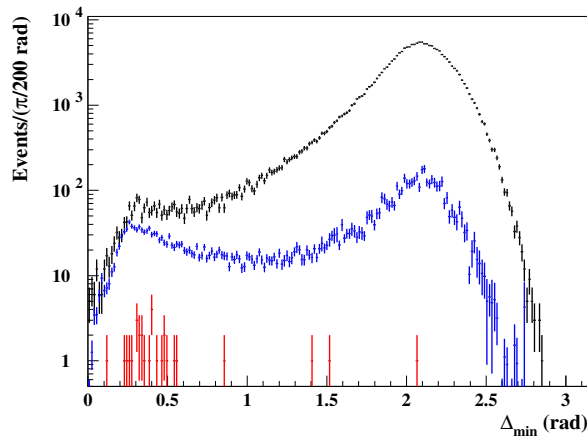


Figure 94.: Δ_{min} distributions (note the logarithmic scale), data in black, uds (blue) is scaled as explained above, $\tau^+\tau^-(\gamma)$ (red) is not scaled.

is clear that after subtracting uds from data only very little background is left. In fact this background is so small, it is not even necessary to determine an exact normalization factor. The lower panel in Fig. 95 proves that the maximum scaling factor could be in the order of 10. Taking into account the cut on $\Delta_{\text{min}} > 1.2$ rad (explained in Sec. 5.7) it is evident that no significant contribution remains even after a possible normalization, also rendering a τ -PID unnecessary.

7.2.3 $e^+e^- \rightarrow \mu^+\mu^-2\pi^0$

For the muon-events remaining after PID-rejection (see Sec. 5.7.2) no simulation is available, so they have to be removed by other means. If the selector inefficiency is well known, this can be implemented directly in data. From the PID-tables of the *BABAR* PID-database we see that the μ -selector has an inefficiency of $\eta_{1T} \approx 15\%$ per track, thus giving a survival rate of $\sim 2.25\%$ for two real muons to remain undetected. Therefore $\sim 2.25\%$ of the $\psi(2S) \rightarrow \mu^+\mu^-2\pi^0$ background is mistakenly not removed from data. This effect is addressed by fitting the $M_{4\pi}$ line shape of the survival rate for the μ -veto with a Gaussian, plotted in Fig. 53, where a dip down to approximately 25% is observed around the $\psi(2S)$ mass. The fitted function is then used to calculate the scaling factor for the remaining fraction of data, averaged over the bin width, shown in Fig. 96. Within $\pm 3\sigma$ of the peak this procedure essentially scales the data distribution such that the rejected background is augmented by the desired 2.25%. For a complete outline of the method see App. C.2.

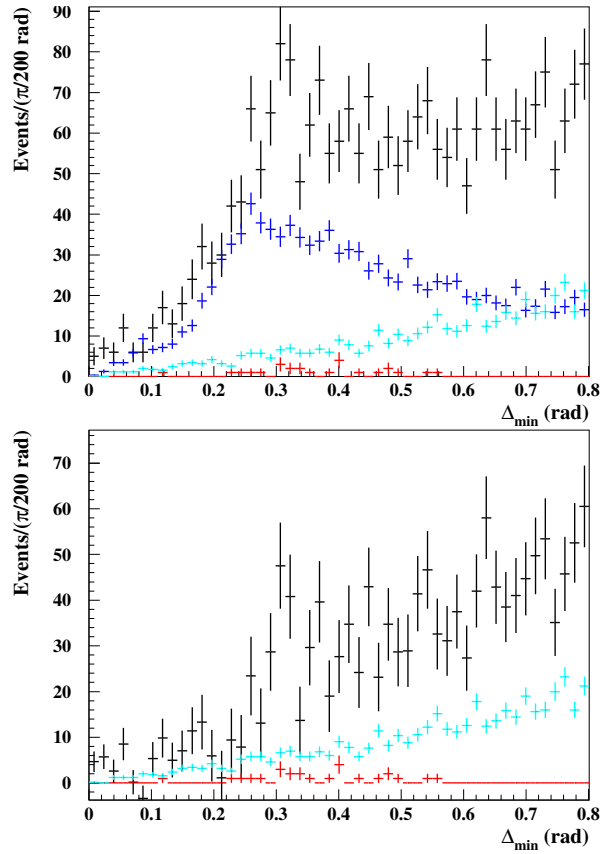


Figure 95.: Δ_{\min} distributions, data in black, $2\pi 2\pi^0$ simulation in turquoise, uds simulation in blue, $\tau^+\tau^-(\gamma)$ simulation in red. In the upper panel the three original distributions are shown ($2\pi 2\pi^0$ simulation is scaled to the same peak height as data, the uds sample is scaled as explained above, while the $\tau^+\tau^-(\gamma)$ sample is not scaled), in the lower panel the black points show the remainder after subtracting uds from data.

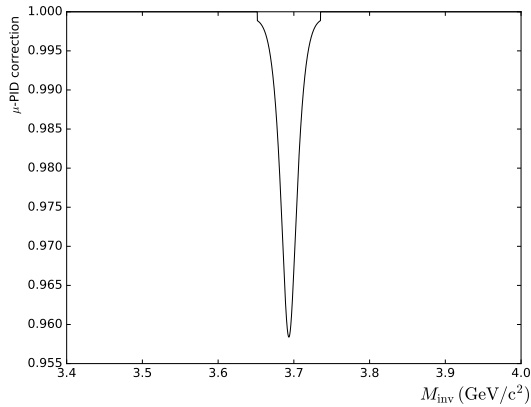


Figure 96.: Scale factor for removing the remaining muonic background from data.

7.2.4 ISR Background Channels

Besides the continuum, $\tau^+\tau^-(\gamma)$, and $\mu^+\mu^-2\pi^0$ backgrounds, there also are certain ISR channels that need to be studied as possible background contributions. These channels are:

- $e^+e^- \rightarrow 4\pi 2\pi^0\gamma_{\text{ISR}}$
- $e^+e^- \rightarrow \pi^+\pi^-\pi^0\gamma_{\text{ISR}}$
- $e^+e^- \rightarrow K_s K^\pm \pi^\mp \gamma_{\text{ISR}} (K_s \rightarrow 2\pi^0)$
- $e^+e^- \rightarrow K^+K^-2\pi^0\gamma_{\text{ISR}}$
- $e^+e^- \rightarrow \eta\pi^+\pi^-\gamma_{\text{ISR}}$
- $e^+e^- \rightarrow \omega 2\pi^0\gamma_{\text{ISR}} (\omega \rightarrow \pi^+\pi^-\pi^0)$

As shown in the following, the simulation samples of the channels $K_s K^\pm \pi^\mp \gamma_{\text{ISR}}$ & $\pi^+\pi^-\pi^0\gamma_{\text{ISR}}$ are reweighted according to existing measurements to improve the precision of their contributions, while the $2\pi 3\pi^0\gamma_{\text{ISR}}$ sample is reweighted according to the count rate result achieved in Sec. 6. All other ISR channels are globally scaled. The global scaling factors listed in Table 3 are obtained by convoluting the measured cross sections with the ISR-luminosity and integrating the resulting distribution. This gives the expected number of events in the respective channel (and, when divided by the integrated luminosity, an effective total cross section). The ratio of the expected number of events and the number of events available on MC-true level then defines the global scaling factor.

The Reweighting Procedure

In the case of some channels, the simulation is slightly outdated, such that cross section with higher precision have been measured experimentally ($K_s K^\pm \pi^\mp \gamma_{\text{ISR}}$ & $\pi^+\pi^-\pi^0\gamma_{\text{ISR}}$ by *BABAR* and *SND*). Therefore, a correction of the simulated mass distributions is applied. In order to do this, the measured cross section is converted into a radiative event distribution by convoluting it with the radiator function. A reweighting list is then computed by dividing the event distribution of measured data by the event distribution in MC-true invariant mass from simulation (both have to be normalized beforehand). That way, a list of scale factors corresponding to each bin of MC-true invariant mass is generated. The corresponding weight is now applied to each MC event. Thus the MC-true mass distribution is equivalent to the measured (radiative) distribution and can be used for further studies.

For the $2\pi 3\pi^0\gamma_{\text{ISR}}$ channel it is not necessary to take the detour via the cross section and the radiator function in order to get the radiative event distribution. Since we are performing this analysis as well, we simply extract the event yield directly from data.

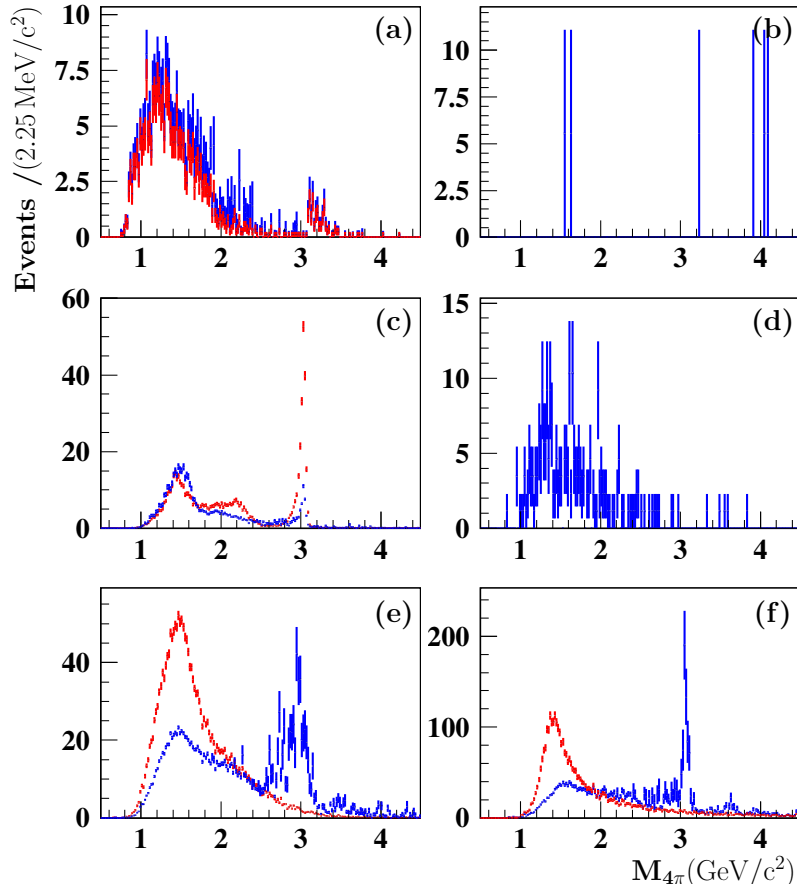


Figure 97: $M_{4\pi}$ -distributions for various background contributions: (a) $\pi^+\pi^-\pi^0$, (b) $2\pi^+2\pi^-2\pi^0$, (c) $K_s K^\pm \pi^\mp$, (d) $K^+K^-2\pi^0$, (e) $\omega 2\pi^0$, (f) $\eta \pi^+ \pi^-$. In panels (c), (e), and (f), where reweighting was performed in addition to the global scaling, the distribution before reweighting is shown in red.

$$\pi^+\pi^-\pi^0\gamma_{\text{ISR}}$$

This channel is reweighted in the mass range $0.645 \text{ GeV}/c^2 \leq M_{\text{inv}} \leq 3.0 \text{ GeV}/c^2$ according to a compilation of the measured cross sections from SND and *BABAR* in Ref. [118–120]. After the selection requirements, especially $\chi^2_{3\pi} \geq 25$, very few events of this channel still show up as seen in Fig. 97, where each bin contains less than 10 events. The remainder which is subtracted is about 0.2 % strong (in comparison to the $2\pi 2\pi^0$ signal in its peak region). The relative statistical uncertainty of the 3π simulation is $\lesssim 15\%$ in its peak, thus giving a negligible contribution of $0.2\% \cdot 15\% = 0.03\%$ to the $2\pi 2\pi^0$ cross section uncertainties.

$$2\pi^+2\pi^-2\pi^0\gamma_{\text{ISR}}$$

Unfortunately the simulated sample for this channel is very low in statistics. Nonetheless it is visible in Fig. 97 that the contribution in the peak region has a magnitude of less than 0.25 %. A more precise approximation than this very crude and conservative one is neither possible at present nor needed since in total less than 40 events from this background channel are expected after scaling to luminosity.

$$K_s K^\pm \pi^\mp \gamma_{\text{ISR}}$$

This channel is largely suppressed by the Kaon-PID requirement. It has been simulated with very high statistics, thus it was scaled down according to luminosity and total measured cross section. Its differential cross section had been measured at the *BABAR* experiment [178] and is shown in Fig. 98. Using the measured cross section to reweight the simulation sample, significant improvements are achieved, visible in Fig. 97. The relative statistical uncertainty in the peak region is approximately $\sim 4.5\%$. However, when weighted by its relative fraction of $\sim 0.3\%$, this results in a negligible contribution of $0.3\% \cdot 4.5\% = 0.0135\%$ to the $2\pi 2\pi^0$ cross section uncertainties.

$$K^+K^-2\pi^0\gamma_{\text{ISR}}$$

This background is strongly suppressed by the Kaon-PID requirement since it produces two charged kaonic tracks which can be identified. Hence only $(5.7 \pm 0.36)\%$ of the $K^+K^-2\pi^0$ events survive the selection, the rest is rejected. Similar to the 3π case, this is a small effect of about 0.15 % relative contribution. Given the statistical uncertainty of about 30 % in the peak region, its contribution of $0.15\% \cdot 30\% = 0.045\%$ to the total error is negligible.

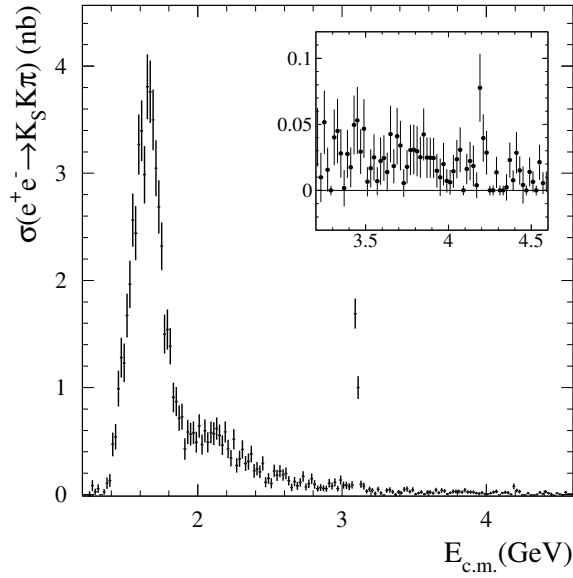


Figure 98.: The measured $e^+e^- \rightarrow K_s K^\pm \pi^\mp$ cross section. Reprinted with permission from Ref. [178], ©2008 by the American Physical Society.

$$\pi^+ \pi^- 3\pi^0 \gamma_{\text{ISR}}$$

The process $e^+e^- \rightarrow \pi^+ \pi^- 3\pi^0 \gamma$ has been studied in Chapter 6 since no complete simulation exists for this channel. In the same chapter, a $\pi^+ \pi^- 3\pi^0 \gamma$ simulation cocktail is constructed from the existing simulated subchannels $e^+e^- \rightarrow \omega 2\pi^0 \gamma \rightarrow \pi^+ \pi^- 3\pi^0 \gamma$ and $e^+e^- \rightarrow \eta \pi^+ \pi^- \gamma \rightarrow \pi^+ \pi^- 3\pi^0 \gamma$. This simulation cocktail can now be reweighted using the new precise measurement. The resulting $M_{4\pi}$ distribution is shown in Fig. 99 in red.

For comparison, the single MC samples $e^+e^- \rightarrow \eta \pi^+ \pi^- \gamma \rightarrow \pi^+ \pi^- 3\pi^0 \gamma$ and $e^+e^- \rightarrow \omega 2\pi^0 \gamma \rightarrow \pi^+ \pi^- 3\pi^0 \gamma$ are also reweighted, shown in blue and purple, respectively. It is clear from the plot that their shapes are similar, yet a significant difference exists even after reweighting to the same $M_{5\pi}$ distribution. The different efficiencies of surviving the $\pi^+ \pi^- 2\pi^0 \gamma$ selection of two intermediate states may be the result of differing kinematic distributions between the two channels. As observed in Figs. 69 & 70, the momentum distributions of the three π^0 are much more narrow in the $\eta \pi^+ \pi^-$ MC sample than in the $\omega 2\pi^0$ MC sample. This effects better compatibility of $\eta \pi^+ \pi^-$ with the $\pi^+ \pi^- 2\pi^0$ hypothesis since energy-momentum-conservation is violated to a lesser extent when one π^0 is not detected. Therefore the kinematic fit of the $\pi^+ \pi^- 2\pi^0$ hypothesis works better for events from the $\eta \pi^+ \pi^-$ sample, demonstrated by Fig. 100, yielding higher survival rates in the $\chi_{4\pi}^2 < 30$ requirement.

There is no significant discrepancy between data and the $\pi^+ \pi^- 3\pi^0 \gamma$ simulation cocktail in the π^0 momentum distributions as observed

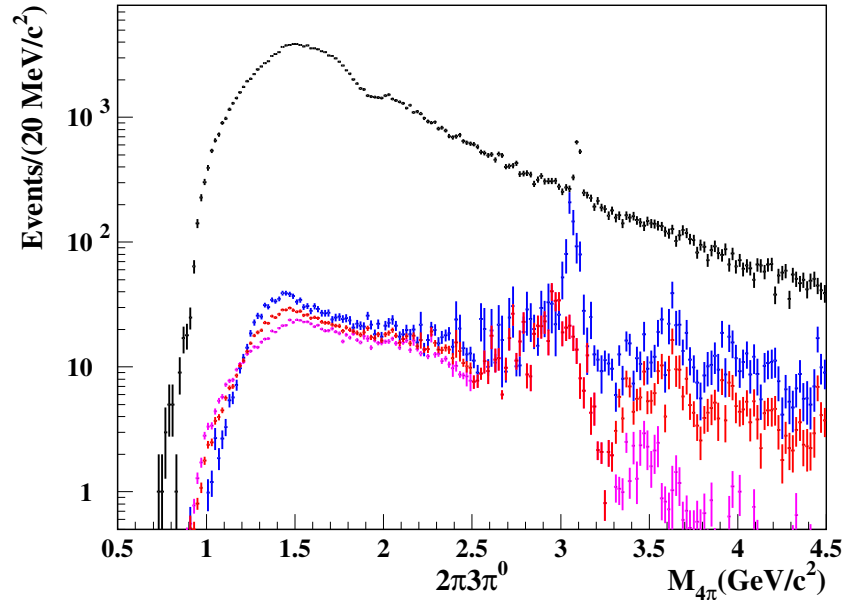


Figure 99.: The $\pi^+\pi^-3\pi^0$ contribution calculated using the reweighted simulation cocktail (red) together with $\pi^+\pi^-2\pi^0$ data (black). For comparison, the reweighted $\eta\pi^+\pi^-$ (blue) and $\omega2\pi^0$ (purple) simulations are shown. All histograms with the full $2\pi2\pi^0$ selection applied. Each histogram is scaled to represent the full expected event rate.

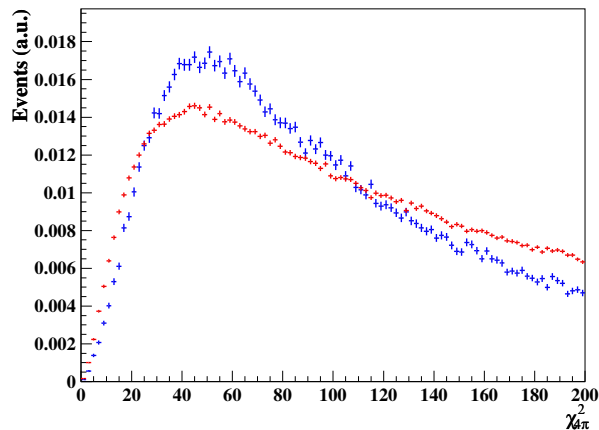


Figure 100.: $\chi^2_{4\pi}$ distributions for $\omega2\pi^0$ (red) and $\eta\pi^+\pi^-$ (blue) simulation. Full $\pi^+\pi^-2\pi^0\gamma$ -selection except $\chi^2_{4\pi}$ -requirement applied, both normalized to unit area.

in Figs. 71, 72. This indicates a realistic simulation sample and thus a reliable subtraction of the $\pi^+\pi^-3\pi^0\gamma$ channel.

As shown in Sec. 6.4, in the mass range around the J/ψ resonance a massive 15 : 1-dominance of $\omega2\pi^0$ production over $\eta\pi^+\pi^-$ production is observed. Hence only the reweighted $\omega2\pi^0$ simulation sample is used for background subtraction in the J/ψ -region $2.5 < M_{4\pi}/(\text{GeV}/c^2) < 3.3$. This is visible in Fig. 99 from the fact that the histograms of the simulation cocktail and the $\omega2\pi^0$ sample are identical in this mass region.

7.2.5 ISR Background Subtraction Uncertainty

In order to cross check the ISR background subtraction described above, which is based solely on simulation, the Novosibirsk subtraction method using a side band extracted from data ($30 < \chi_{4\pi}^2 < 60$) is applied. This is weighted according to the $\chi_{4\pi}^2$ shapes from signal simulation and background as outlined in Sec. 6.2.2, the latter being calculated by subtracting signal and uds simulations from data in the full χ^2 -spectrum. The ratio ($N_{\text{sideband}}/N_{\text{MCbkg}}$) comparing the resulting count rates using the two methods is shown in Fig. 101 and demonstrates good agreement between the methods on the level of $< 1\%$ in the peak region. From this distribution, the relative systematic uncertainties of the ISR background subtraction method are estimated as 6 % for $M_{4\pi} \geq 2.7 \text{ GeV}/c^2$ and 1 % for $1.2 \text{ GeV}/c^2 \leq M_{4\pi} < 2.7 \text{ GeV}/c^2$.

Since the ratio of two small numbers with statistical uncertainties can change quickly, no constant relative systematic uncertainty can be assigned in the low-mass region $M_{4\pi} < 1.2 \text{ GeV}/c^2$. Instead, an absolute systematic uncertainty is determined for each bin in this region. For this purpose, the difference between both subtraction methods is used, as shown in Fig. 102 after dividing the count rates by luminosity (see Sec. 3) and efficiency (see Sec. 7.3) to get the difference in the cross section. To minimize fluctuations, a fit is employed to extract the uncertainty. Observing that the difference vanishes below $M_{4\pi} = 0.65 \text{ GeV}/c^2$ the function $f(x) = b \cdot (x - 0.65)$ is fitted to the distribution (in the range $0.85 \text{ GeV}/c^2 \leq M_{4\pi} < 1.2 \text{ GeV}/c^2$, as the statistical and systematic uncertainties below $0.85 \text{ GeV}/c^2$ make a cross section determination infeasible in this region), yielding $b = -0.46 \pm 0.05$.² Taking the absolute value, in the region $0.85 \text{ GeV}/c^2 \leq M_{4\pi} < 1.2 \text{ GeV}/c^2$ the systematic uncertainty due to background subtraction is evaluated as $\delta_{\text{bkg}}\sigma(M_{4\pi}) = (M_{4\pi}/(\text{GeV}/c^2) - 0.65) \cdot 0.46 \text{ nb}$.

² Letting both parameters of the linear fit function float results in a similar description: $f(x) = 0.52 - 0.70x$.

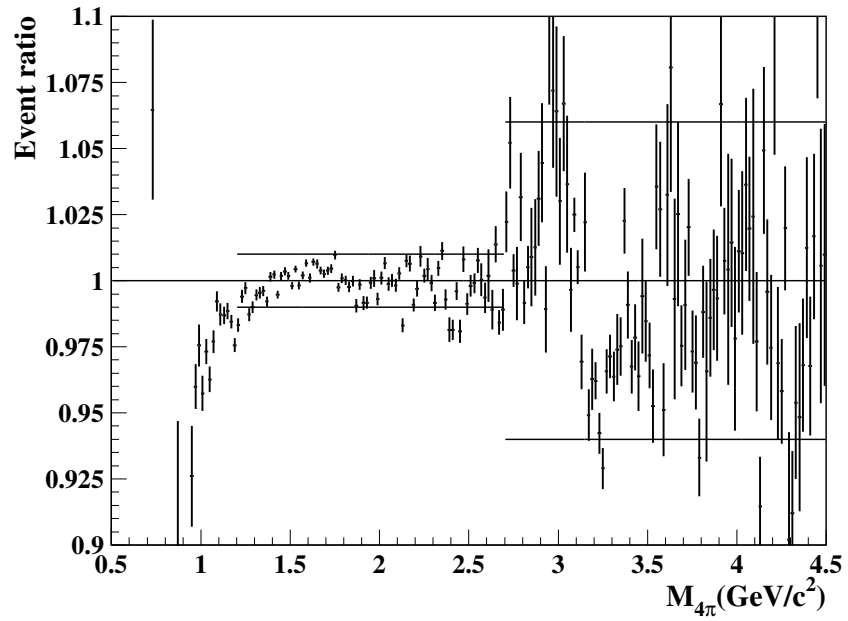


Figure 101.: Cross check of the count rate with the sideband subtraction: ratio $(N - N_{\text{sideband}})/(N - N_{\text{MCbkg}})$ including the error bands.

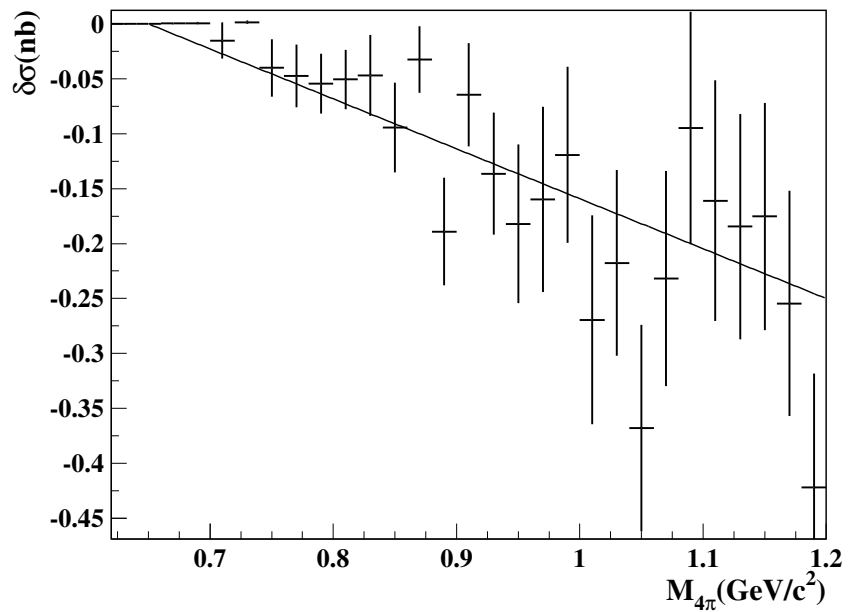


Figure 102.: Cross check of the cross section with the sideband subtraction: difference $\sigma_{\text{sideband}} - \sigma_{\text{MCbkg}}$ in the low-mass region. The black line indicates the fit used to determine the systematic uncertainty.

Summary of Background Subtraction

The description of continuum hadron production is refined by scaling its simulation sample to the π^0 yield measured in data. This scaling is performed as a function of the invariant mass $M_{4\pi}$, giving a very precise background subtraction procedure.

It is further shown that most ISR background channels can be subtracted from data using existing simulations, in some cases after reweighting according to measured cross sections. The only exception is the ISR final state $2\pi3\pi^0\gamma$, since it had not been measured with sufficient precision before. This measurement was performed in Sec. 6 with higher accuracy, such that the uncertainty it contributes is now well below our limiting uncertainties. After this, it is evident from Fig. 97 and Fig. 103 that all ISR background channels are either negligible, and therefore do not need to be studied any further, or can be reweighted according to a measurement and thus are subtracted reliably. The contributions of the background channels passing the $2\pi2\pi^0\gamma$ selection are shown as a function of $M_{4\pi}$ in Fig. 103 and as a function of $\chi_{4\pi}^2$ in Fig. 104. The major contributors in the $M_{4\pi}$ peak region are continuum (about 2 %) and $\pi^+\pi^-3\pi^0\gamma$ (about 0.8 %).

This results in uncertainties of less than 1 % below $3.2 \text{ GeV}/c^2$ and less than 2 % otherwise due to continuum background subtraction as well as less than 1 % for $1.2 \text{ GeV}/c^2 \leq M_{4\pi} < 2.7 \text{ GeV}/c^2$ and less than 6 % above due to ISR background subtraction. For $M_{4\pi} < 1.2 \text{ GeV}/c^2$, a mass dependent uncertainty due to ISR background subtraction must be applied.

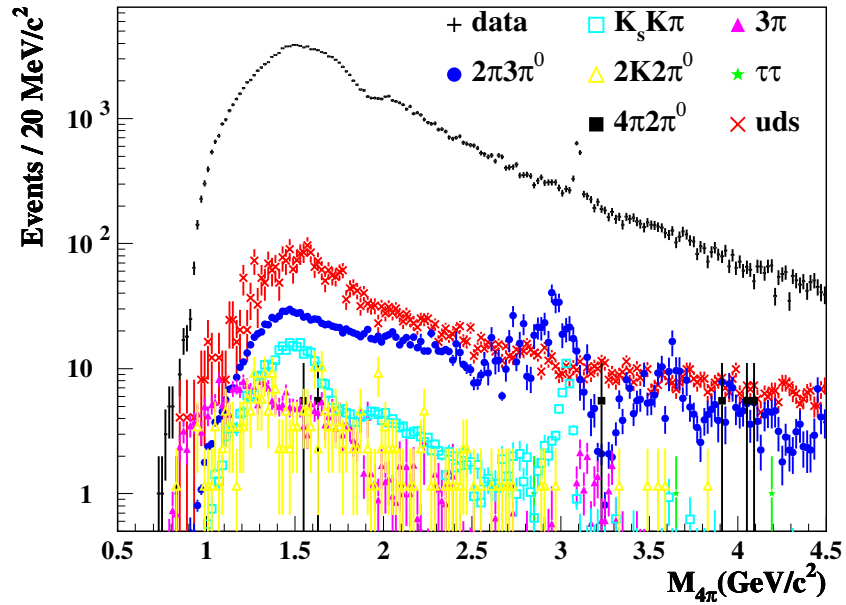


Figure 103.: The backgrounds to $2\pi 2\pi^0$ (data: black): uds (red), 3π (pink), $4\pi 2\pi^0$ (black), $K_s K\pi$ (turquoise), $K^+ K^- 2\pi^0$ (yellow), $\tau\tau$ (green), and $2\pi 3\pi^0$ (blue) as a function of $M_{4\pi}$.

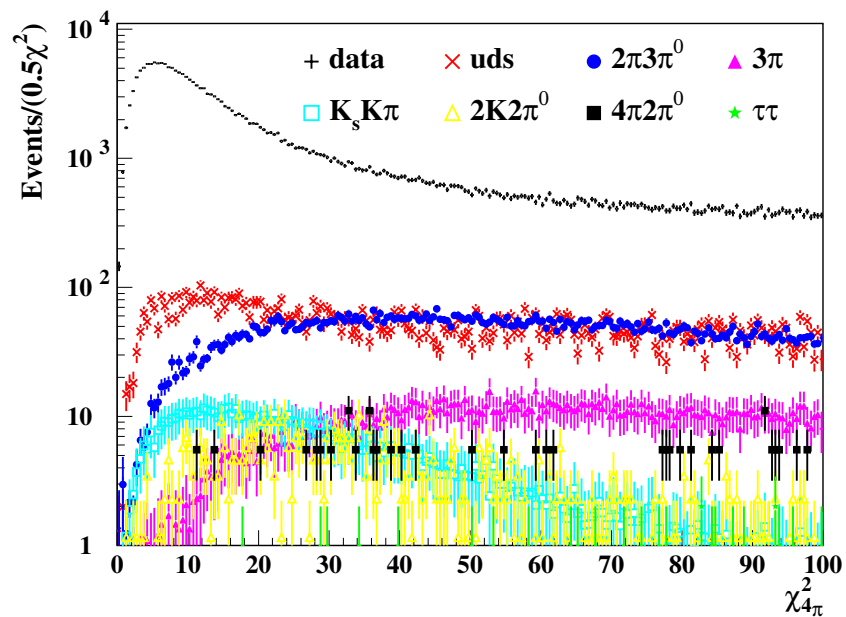


Figure 104.: The backgrounds to $2\pi 2\pi^0$ (data: black): uds (red), 3π (pink), $4\pi 2\pi^0$ (black), $K_s K\pi$ (turquoise), $K^+ K^- 2\pi^0$ (yellow), $\tau\tau$ (green), and $2\pi 3\pi^0$ (blue) as a function of $\chi_{4\pi}^2$.

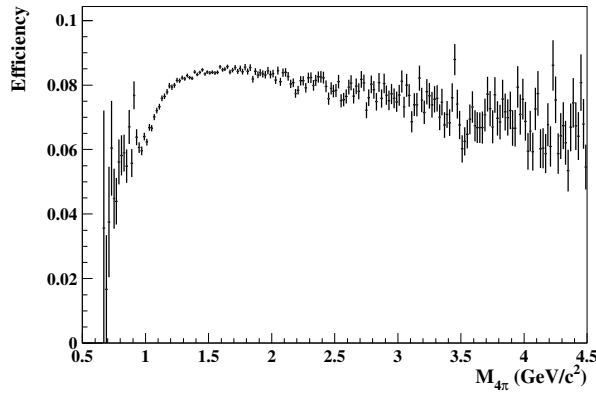


Figure 105.: Total efficiency without any corrections as a function of $M_{4\pi}$.

7.3 PRECISION EFFICIENCY CORRECTIONS AND MASS RESOLUTION

For a cross section measurement it is indispensable to know the acceptance and efficiency of the measurement precisely. The combination of acceptance and efficiency is calculated by dividing the number of events in signal simulation after selection and detector simulation by the number of events originally generated, leading to the distribution shown in Fig. 105. Since this procedure relies on the assumption that the simulation properly describes the physical process, it must be checked whether there are efficiency differences between data and simulation. Subsequently, these efficiency differences must be corrected wherever possible. Furthermore, the influence of the detector resolution must be investigated and, if necessary, reversed by an unfolding procedure.

7.3.1 Correction of Track, Photon and π^0 Detection

The differences between data and simulation have been investigated in earlier *BABAR* analyses. Hence the resulting corrections can be used here and are summarized below, while detailed descriptions of each method with the corresponding references are given in App. C.4.

- **Tracking correction:** the efficiency of detecting a π^\pm in the final state $\pi^+\pi^-2\pi^0\gamma$ is overestimated in simulation by 0.47 % per charged track. This results in a correction of 0.9 % for both charged pions and an uncertainty of 0.8 %.
- **γ correction:** this correction is dependent on the polar angle of the photon and hence applied to each event individually. On average, simulation overestimates the detection efficiency by 1.22 % with an uncertainty of 0.17 %.

- π^0 correction: analyzing the process $e^+e^- \rightarrow \omega\pi^0\gamma$ shows that the efficiency of detecting a neutral pion is overestimated in simulation by 3.0 % with an uncertainty of 1.0 %. Hence for the channel $e^+e^- \rightarrow \pi^+\pi^-2\pi^0\gamma$ a correction of 6.0 ± 2.0 % results, giving a leading systematic uncertainty.

7.3.2 The $\chi^2_{4\pi}$ Requirement

The requirement $\chi^2_{4\pi} < 30$, where $\chi^2_{4\pi}$ is extracted from the kinematic fit in the four pion hypothesis, separates the signal channel from production processes with different final states. It has to be assessed how this specific choice of the cut value affects the selection and whether a possible bias is introduced. It is particularly important to explore possible differences between data and simulation introduced by this specific cut value. For similar shapes of the $\chi^2_{4\pi}$ distributions in data (after background subtraction) and simulation after the full event selection except for the $\chi^2_{4\pi}$ requirement, such an effect is small, indicating a realistic background description. In Fig. 106 the effect of the background subtraction is observed, considerably reducing the difference in shape between data and simulation. Figure 107 shows the cumulative distributions, equivalent to the relative survival rate at a given $\chi^2_{4\pi}$ value. From this distribution it is seen that the effect is on the percent-level or even lower. To assess the effect more precisely the $\chi^2_{4\pi}$ requirement is then varied in fine steps. For the investigation of the survival rate differences between data and simulation, first the single rate for each case is calculated relative to the standard cut $\chi^2_{4\pi} < 30$:

$$\varepsilon(x) = \frac{N(\chi^2 < x)}{N(\chi^2 < 30)}. \quad (61)$$

To compare data and simulation, their ratio is obtained:

$$\eta(x) = \frac{\varepsilon_{\text{data}}(\chi^2 < x)}{\varepsilon_{\text{MC}}(\chi^2 < x)}. \quad (62)$$

In Fig. 108, the double ratio η is shown in the $\chi^2_{4\pi}$ region 30 ± 12.5 , reaching from $\chi^2_{4\pi} = 17.5$, which is dominated by signal events including detector resolution, up to $\chi^2_{4\pi} = 42.5$, where considerable background pollution exists as seen in Fig. 106. A difference due to background of $\sim \pm 2$ % between data and simulation is observed for the double ratio η . This deviation all but vanishes after background subtraction to the level of $\sim \pm 0.4$ %, as seen in Fig. 108 (bottom). This confirms the supposition that a reasonable background description has been found. Furthermore no systematic change of the shape of the $M_{4\pi}$ distributions in data or signal simulation is observed when varying the $\chi^2_{4\pi}$ requirement in this range, hence a systematic uncertainty of 0.4 % is assigned to the global result.

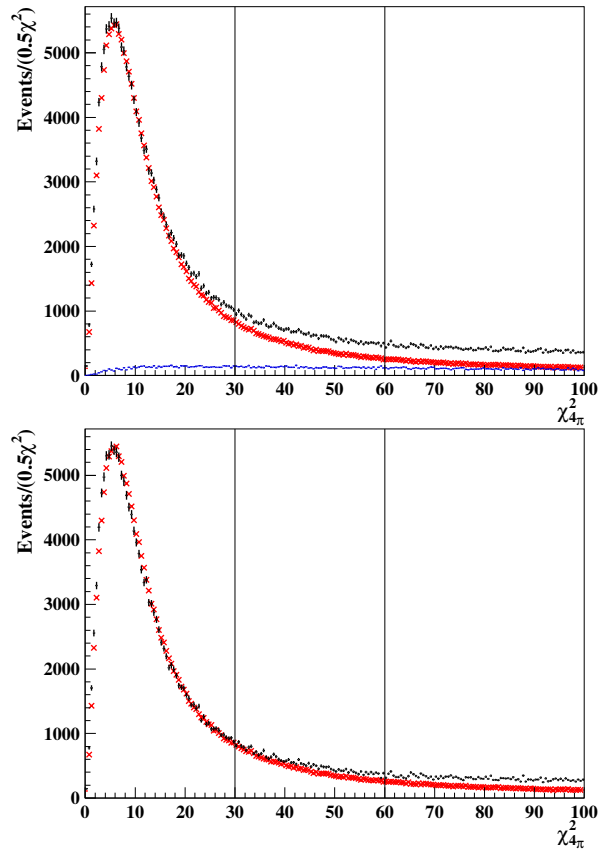


Figure 106.: χ^2 distributions for signal simulation (red, both plots, normalized to the same area as data in the range $\chi_{4\pi}^2 < 30$), data (black, top plot), total background (blue, top plot) and data-background (black, bottom plot).

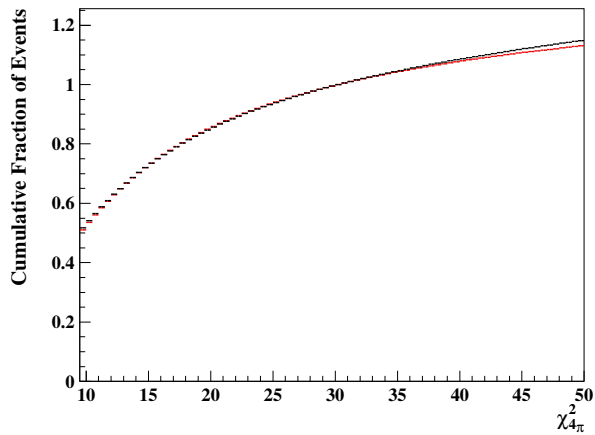


Figure 107.: Cumulative χ^2 distributions for data-background (black) and signal simulation (red), both scaled to unity at $\chi_{4\pi}^2 = 30$.

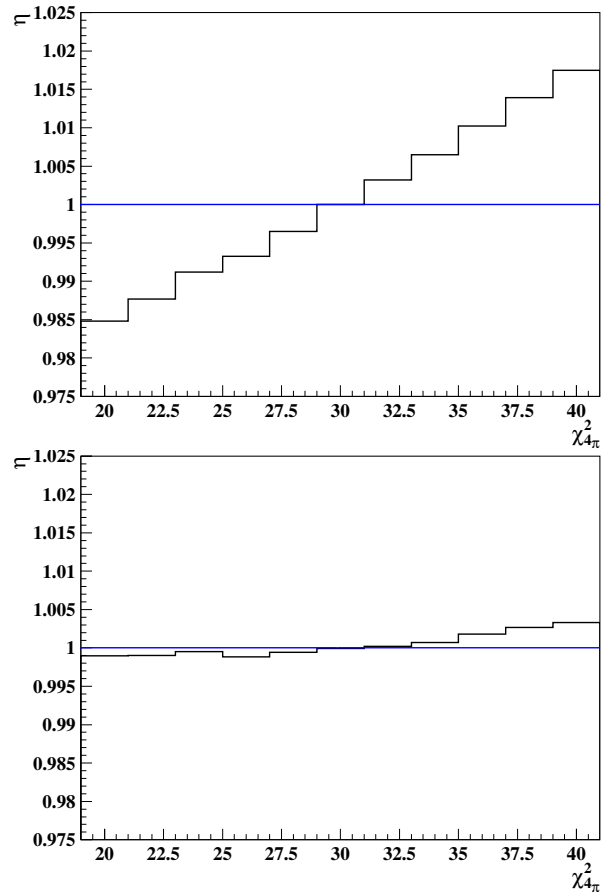


Figure 108.: Ratio of the $\chi_{4\pi}^2$ requirement survival rates η as a function of the cut-value as defined in Eq. 62 between data and signal simulation (top). The discrepancy almost vanishes when background subtraction is applied to data (bottom).

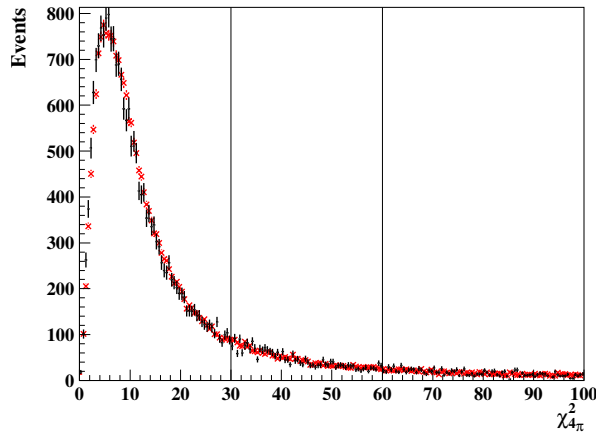


Figure 109.: χ^2 distributions for signal simulation (red, normalized to the same area as data in the range $\chi_{4\pi}^2 < 30$) and data-background (black).

Clean Sample

In order to investigate the effect of the χ^2 requirement in a wider range, a different method is necessary. Selecting a very clean sample and analyzing the effect of the χ^2 requirement on it on data and signal simulation is suitable for this purpose. This sample is achieved by selecting only events with exactly five photons in addition to the usual full selection (which especially includes the requirement of exactly two charged tracks). The resulting χ^2 distributions show good agreement in Fig. 109. Figure 110 displays – for the clean sample – the ratio $\eta(x)$ defined in Eq. 62. Varying the χ^2 requirement from its standard value of 30 up to 100, where no resolution effects are present, produces relative differences between data and the signal MC sample within the 0.4 % systematic uncertainty determined above. Hence this cross check confirms the systematic uncertainty to be sufficiently large, so that no additional uncertainty must be applied.

7.3.3 *Dependence on Resonance Weight*

The resonance weight may be slightly incorrect in the generator AFKQed which is used to calculate the detection efficiency, an effect which has to be checked. The model used in AFKQed includes the ρ , ρ' , and ρ'' resonances as well as the intermediate states $\omega\pi^0$, $a_1(1260)\pi$, and a small contribution from $\rho^0 f_0$. The most important and most narrow resonance to be considered here is the ω , with a mass of $782.65 \text{ GeV}/c^2$ and a width of $8.49 \text{ MeV}/c^2$ [43]. Therefore, the efficiency is calculated in the ω -region ($0.697 \text{ GeV}/c^2 < M_{3\pi} < 0.867 \text{ GeV}/c^2$) as well as a sideband directly above the ω peak ($0.867 \text{ GeV}/c^2 < M_{3\pi} < 1.037 \text{ GeV}/c^2$) in order to have comparable kinematic properties in both regions. Their ratio is shown

in Fig. 111. The same ratio is constructed between the ω -sideband region ($0.867 \text{ GeV}/c^2 < M_{3\pi} < 1.037 \text{ GeV}/c^2$) and a region of the same width just above ($1.037 \text{ GeV}/c^2 < M_{3\pi} < 1.197 \text{ GeV}/c^2$), the result is shown in Fig. 112.

It is observed that in both cases the ratio differs from unity on the order of 10 %, with slightly smaller effects seen in the second case. Hence the efficiency differences are predominantly not due to the presence of a resonance, but to kinematics. Nonetheless we assign a conservative 10 % uncertainty to the fraction of events which is generated via the ω by AfkQed although it should be produced non-resonantly.

Therefore, it is calculated from the fits shown in Fig. 113 that in data, approximately 32.1 % of the events are produced via the ω resonance, while in simulation about 36.4 % are generated this way, a difference of 4.3 %. The events corresponding to these 4.3 % are weighted with the wrong efficiency in the calculation of the cross section, thus they must be assigned the 10 % systematic uncertainty.

Hence, the global systematic uncertainty due to this effect is $10 \% \cdot 4.3 \% = 0.4 \%$.

Summary of Efficiency Corrections

Several corrections have to be applied to the efficiency calculated from simulation. Firstly, corrections for the γ and tracking efficiency differences between data and simulation must be considered (see Secs. C.4.1, C.4.2). Furthermore, the even larger correction due to the π^0 efficiency also has to be applied (Sec. C.4.3), which is a global factor and thus does not change the shape of the mass spectrum. Finally, it is shown that the $\chi^2_{4\pi}$ requirement and the weights of the individual resonances are in good agreement between data and simulation (Secs. 7.3.2, 7.3.3), so that no corrections are necessary, only systematic uncertainties need to be applied.

All efficiency corrections are listed in Tab. 10.

Table 10.: Table of efficiency corrections.

Category	Correction (%)
Tracking eff.	0.9 ± 0.8
γ eff.	1.2 ± 0.4
$2\pi^0$ eff.	6.0 ± 2.0
$\chi^2_{4\pi}$ requirement	0 ± 0.4
Resonance weighting	0 ± 0.4

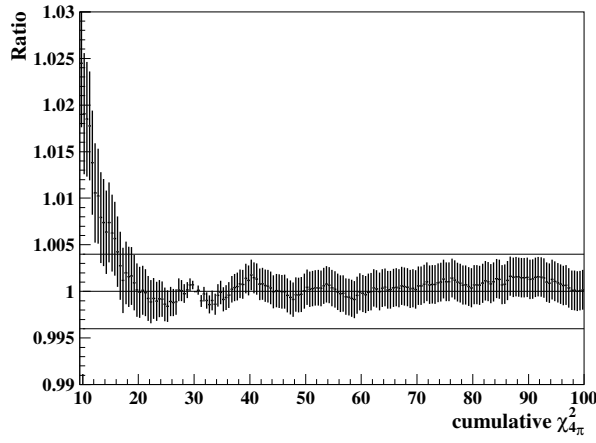


Figure 110.: Ratio of the event numbers is data and signal simulation as a function of the χ^2 requirement, normalized to unity at the standard requirement $\chi^2 < 30$. The horizontal lines indicate the $\pm 0.4\%$ uncertainty around unity assigned above, implying good agreement between the two methods.

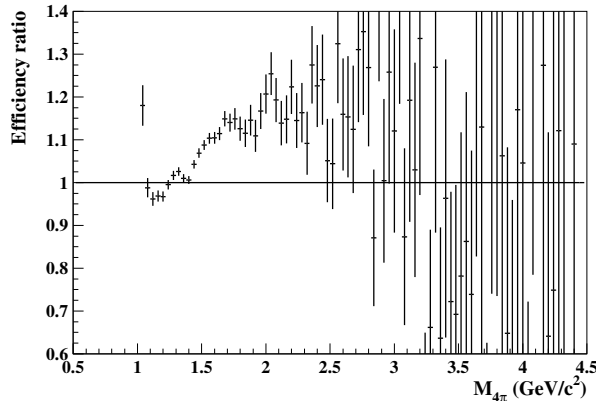


Figure 111.: Ratio of the efficiency in the ω region divided by the ω -sideband.

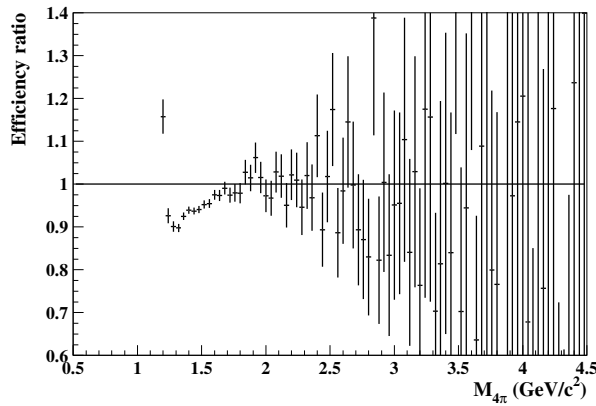


Figure 112.: Ratio of the efficiency in the ω -sideband region divided by the next-to-sideband region.

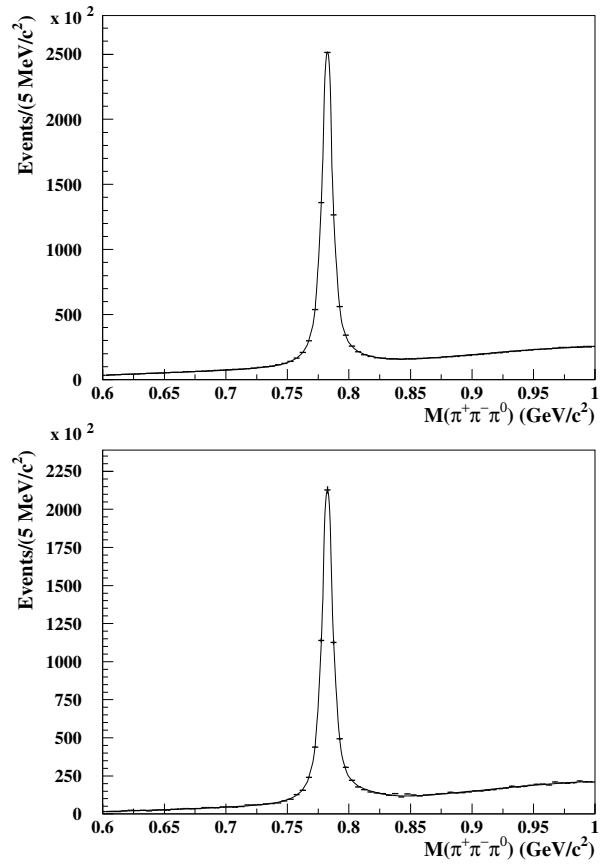


Figure 113.: Fits to the ω peak in AfkQED simulation (top) and data (bottom).

7.3.4 Unfolding the Mass Resolution

As observed in Fig. 45, even after kinematic fitting the measured mass of the hadronic system is blurred due to the finite detector resolution. The RMS width of the measured mass distribution around the “true” mass of the event is $15 \text{ MeV}/c^2$ in signal simulation. Since a bin width of $20 \text{ MeV}/c^2$ is aimed for in the cross section, it must be investigated whether the shape of the measured mass distribution is significantly affected by the accidental migration of events to a different bin. For this purpose, an *unfolding* of the mass spectrum is performed.

Trying to determine a fundamental distribution $\varphi(z)$ (the physical or “true” distribution) leads to the problem of unfolding defined by

$$\hat{\varphi}(\hat{z}) = \int dz p(\hat{z}, z) \varphi(z), \quad (63)$$

where $\hat{\varphi}$ and \hat{z} are the measured equivalents of φ and z , respectively. The function p incorporates the blurring resulting from finite detector resolution. When working with binned intervals of z and \hat{z} , the relation translates to

$$\hat{\varphi}(\hat{z}_i) = \sum_j A_{ij} \varphi(z_j), \quad (64)$$

where A is the transformation matrix (a discretized variant of p) mapping physical variables to measured observables. Hence, the distortion of a physical or true vector \vec{x} due to detector and other effects resulting in the measured vector \vec{y} can be modeled as³

$$\vec{y} = A\vec{x}. \quad (65)$$

Here, the observable \vec{y} contains the measured distribution, but \vec{x} is the fundamental distribution of interest we want to extract. Thus, the matrix A must effectively be inverted. The inversion of linear systems is extensively studied [182, 183] for matrices known to full numerical accuracy. The difficulty of unfolding is due to the limited knowledge of A and \vec{y} . As every measured observable, \vec{y} is affected by statistical fluctuations. Furthermore, A must be generated by Monte Carlo simulations leading to limited precision due to statistical fluctuations and model error. (The latter effect is not addressed by unfolding.) Inverting the linear system in Eq. 65 may lead to unstable solutions, massively enhancing small changes in A or \vec{y} . Therefore the challenge of unfolding becomes *regularizing* the problem so that the best estimate of \vec{x} is found given an imprecise approximation of A and measured \vec{y} , as illustrated in Fig. 114.

³ Note that the dimensions of the vectors \vec{x} and \vec{y} are in general not required to be equal, see e.g. [179]. Some methods require equality [180], while others require $\dim(\vec{x}) \leq \dim(\vec{y})$ [181].

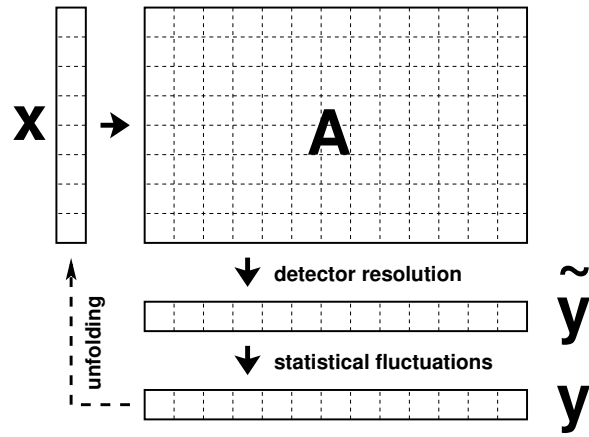


Figure 114.: Schematic depiction of the unfolding process from Ref. [181]. ©SISSA Medialab Srl. Reproduced by permission of IOP Publishing. All rights reserved.

Two possible solutions to this problem are outlined below and used in this analysis. The matrix A is constructed from the simulated two-dimensional distribution (after full selection) of the MC-true mass M_{inv} versus its counterpart after detector simulation and kinematic fitting $M_{4\pi}$, normalized to the total number of events in each true-bin.

SVD Unfolding

In the first method a Singular Value Decomposition [182] (SVD) is used in the unfolding procedure. Any real⁴ matrix M can be decomposed into

$$M = USW^T, \quad (66)$$

with U , W orthogonal (i.e. $U^T U = \mathbb{1}$, $W^T W = \mathbb{1}$) and S diagonal, $S_{ii} \geq 0$. The S_{ii} are called the *singular values* of M . The (pseudo)inverse of A is then given by

$$M^{-1} = WS^{-1}U^T, \quad (67)$$

where S^{-1} is easily determined to have $1/S_{ii}$ as its diagonal elements and zeros everywhere else. Therefore, the components corresponding to insignificantly small singular values S_{ii} should be neglected as they may introduce large fluctuations into the inversion.⁵ More specifically, it has been shown [184] that using a *truncated* SVD serves as a powerful means of regularization.

The first unfolding procedure applied in this analysis relies on a smoothly truncated SVD. In this method, the transfer matrix A

⁴ The brief introduction given here is restricted to the real case but can easily be generalized to complex matrices.

⁵ Effectively, this is a form of dimensionality reduction as the number of non-zero singular values of a matrix is equal to its rank and thus the dimension of the space its rows or columns span.

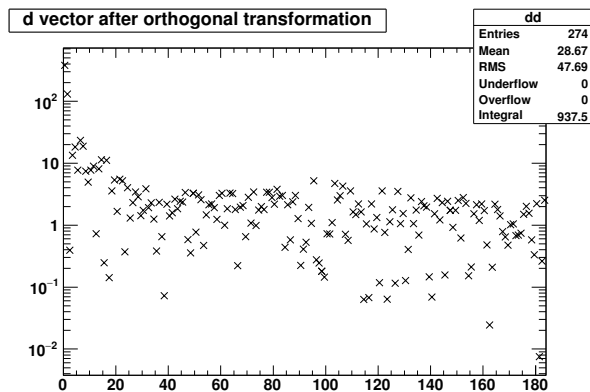


Figure 115.: d_i distribution for the SVD unfolding.

introduced above is combined with the covariance matrix of the measurement and then decomposed, for more details see Ref. [180].

Observing the distribution of the variable d_i (defined in Ref. [180]) shown in Fig. 115, 92 out of 184 components are retained. This selection is made following the method outlined in Ref. [180], stating that higher components become unreliable as soon the values of the d_i are of similar magnitude as the spread between them.

Applying this method to the measured mass spectrum after full selection while retaining 92 out of 184 components, the distribution shown in Fig. 116 is observed. Clearly, there are no major changes due to the unfolding, except in the region around the J/ψ resonance, where the unfolding is not reliable since the resonance is not simulated. It is obvious from the relative deviation in Fig. 117 that both spectra agree with each other within statistical uncertainties. This is quantified by fitting a constant to the peak region $1.0 \text{ GeV}/c^2 < M_{A\pi} < 2.7 \text{ GeV}/c^2$, yielding 0.0004 ± 0.0026 , good agreement with zero.

Unfolding using the Least Squares Method with Tikhonov Regularization and L-curve Optimization

The second unfolding method employed in this analysis calculates a regularized least squares solution. An unregularized least squares solution to Eq. 65 is defined by finding the vector \vec{x} so that

$$(A\vec{x} - \vec{y})^T V^{-1} (A\vec{x} - \vec{y}) \quad (68)$$

is minimized. The observable \vec{y} is measured, while \vec{x} is the variable to be extracted. The matrix V is the covariance matrix, generated from simulation assuming normal distribution. The matrix A is the transfer matrix describing the migration of events between true and reconstructed distribution. Just as inverting A in Eq. 65, the least squares method may become unstable, producing large fluctuations in \vec{x} for tiny changes in A or \vec{y} . Since both are known with limited precision, fluctuations in \vec{x} need to be suppressed. For

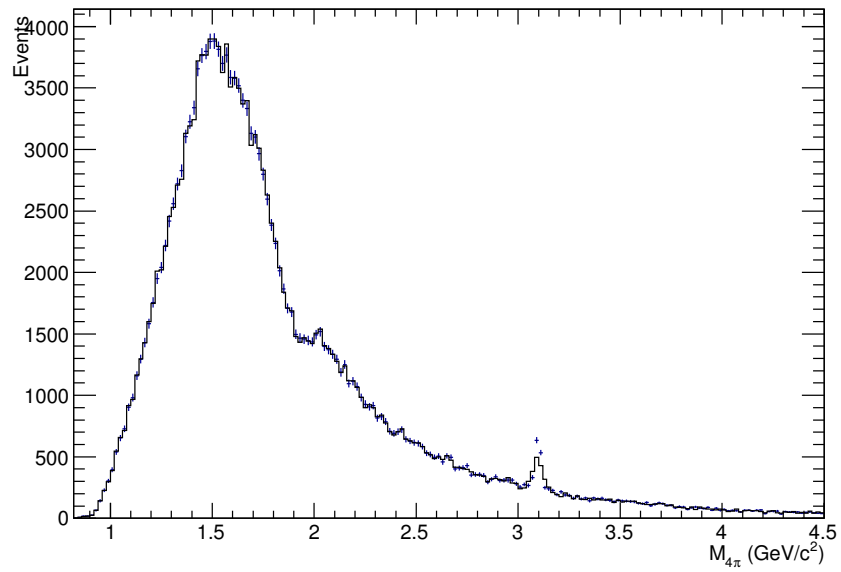


Figure 116.: Mass spectrum before (blue points) and after (black histogram) applying the SVD unfolding procedure.

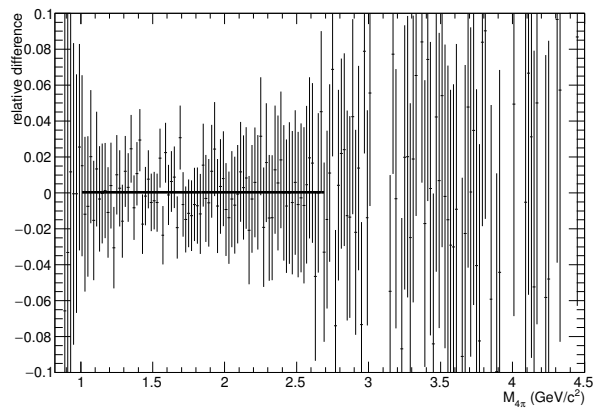


Figure 117.: Relative difference between the mass spectrum before and after applying the SVD unfolding procedure.

this purpose a matrix B is introduced, modifying the above formula to the new minimization problem

$$(A\vec{x} - \vec{y})^T V^{-1}(A\vec{x} - \vec{y}) + \tau^2 \vec{x}^T B^T B \vec{x}. \quad (69)$$

This modification is known as *Tikhonov regularization* [185, 186] and is one of the most widely-used regularization schemes, with applications including fields like machine learning (e.g. neural networks). The matrix B can be chosen to suit each problem individually. Common choices include the identity matrix $\mathbb{1}$ to regularize the size of $\|\vec{x}\|$, or regularizing the first derivative of \vec{x} by choosing B so that the difference between neighboring elements of \vec{x} is extracted. Another possibility is penalizing the second derivative of \vec{x} . All these choices of B are fixed matrices, which are then multiplied by a factor $\tau \in \mathbb{R}^+$ to achieve the desired regularization strength. For any choice of τ , the size of $\|B\vec{x}\|$ can be plotted versus $\|A\vec{x} - \vec{y}\|$. Varying τ systematically, the resulting plot should exhibit the shape of the letter “L”, hence commonly called the *L-curve* [187]. The value of τ where the L-curve has its kink – the maximum curvature – provides a good balance between regularization and perturbation from fluctuations [188] and can be found by numerical optimization.

The procedure outlined above is described in detail in Ref. [181]. A drawback of this implementation is that it requires $\dim(\vec{x})$ to be significantly smaller than $\dim(\vec{y})$, usually by around factor two, therefore the binning must be reduced in the resulting distribution. Nonetheless it is useful as a comparison to the SVD method since its regularization is optimized automatically without arbitrariness.

Applying the L-curve method to the measured mass spectrum after full selection results in the optimized regularization parameter $\tau = 0.00031$ and the curve in Fig. 118, where a narrow region around the kink of the L is already selected. After unfolding, the measured distribution shown in Fig. 119 is observed. Here also, there are no major changes due to the unfolding. Again, it is obvious from the relative deviation in Fig. 120 that both spectra agree with each other within statistical uncertainties. This is quantified by fitting a constant to the peak region $1.0 \text{ GeV}/c^2 < M_{4\pi} < 2.7 \text{ GeV}/c^2$, yielding -0.002 ± 0.003 , which is in good agreement with zero.

Region around 2 GeV/c²

Of particular interest is the question whether structures in the mass distribution persist after unfolding or whether they are due to resolution effects. Since an unknown structure is seen around $2 \text{ GeV}/c^2$, the SVD unfolding method is applied exclusively to this mass region. Retaining 15 out of the possible 21 components, the result in Fig. 121 is observed. The structure remains after unfolding, and is even slightly enhanced, but to negligible degree. Fitting a constant to the relative difference (Fig. 122) in the mass range

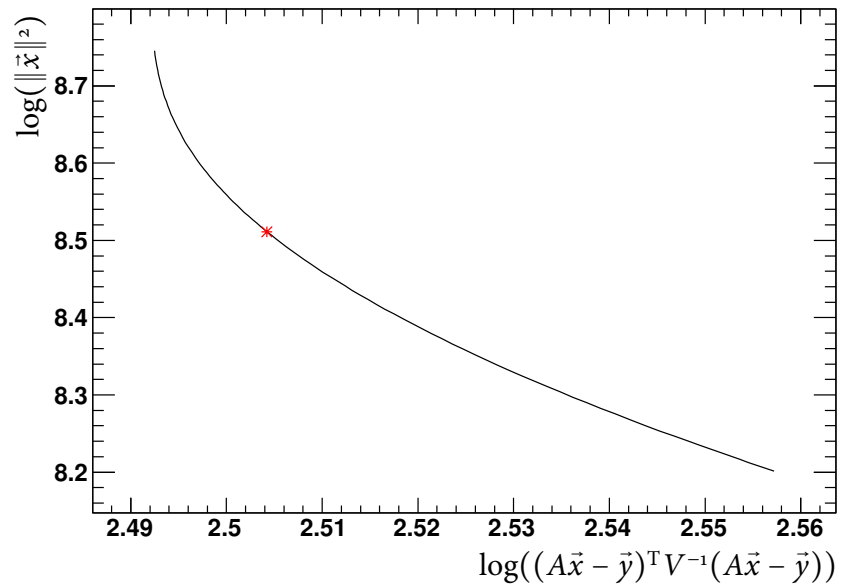


Figure 118.: The L-curve produced to optimize unfolding. The red dot indicates the best value for τ .

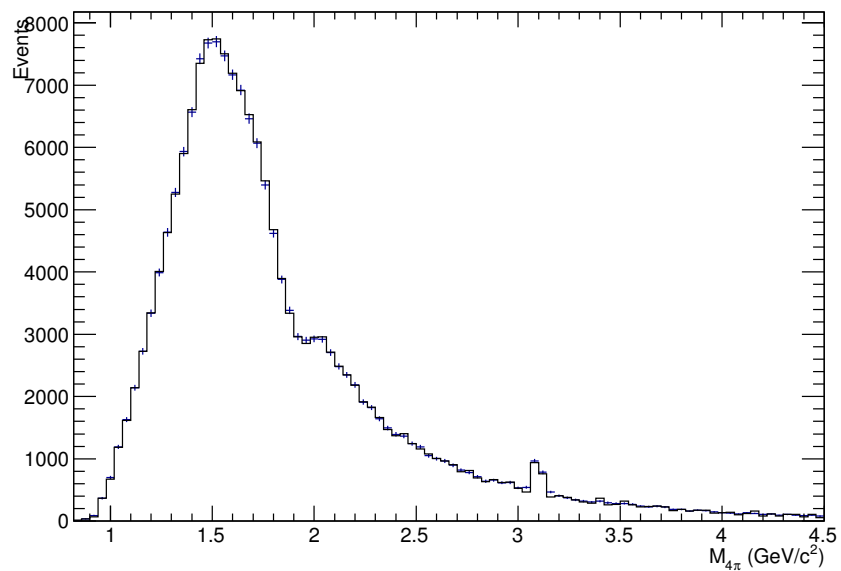


Figure 119.: Mass spectrum before (blue points) and after (black histogram) applying the L-curve unfolding procedure. Binning is widened from 20 MeV/c² to 40 MeV/c² as required by the algorithm.

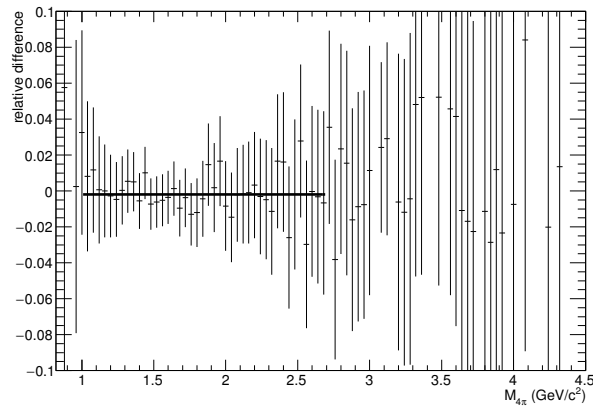


Figure 120.: Relative difference between the mass spectrum before and after applying the L-curve unfolding procedure.

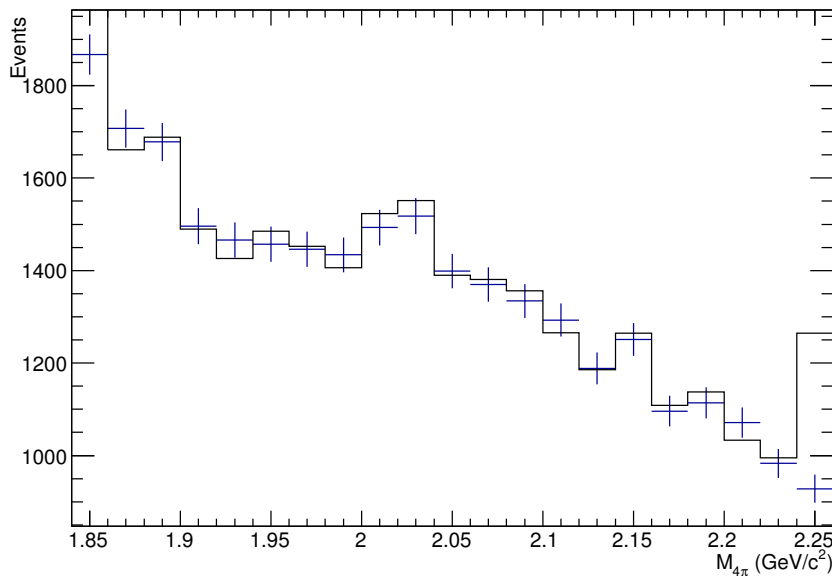


Figure 121.: Mass spectrum around 2 GeV/c² before (blue points) and after (black histogram) applying the SVD unfolding procedure.

$1.9 \text{ GeV}/c^2 < M_{4\pi} < 2.2 \text{ GeV}/c^2$ (the extreme side bins can be somewhat unreliable after unfolding) yields -0.003 ± 0.007 , also showing good agreement between both distributions.

Summary of Unfolding

Two unfolding procedures are applied in order to cross check whether the shape of the measured mass spectrum is significantly distorted due to detector blurring. Both methods show that this is not the case. Even the unknown excess of events above 2 GeV/c² persists after unfolding and thus is not due to resolution effects. The shape of the J/ψ is not well unfolded in the SVD procedure, but this is to be expected in this method since the simulation does

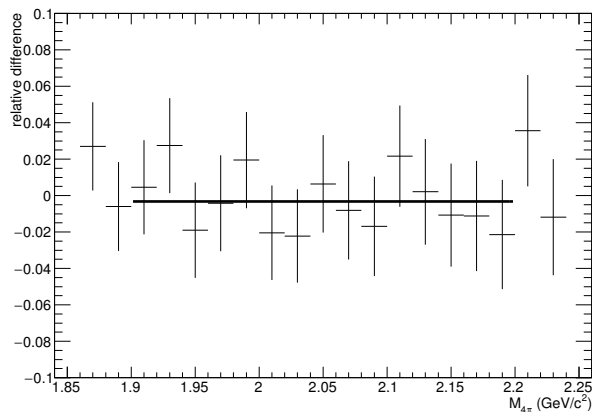


Figure 122.: Relative difference between the mass spectrum around $2 \text{ GeV}/c^2$ before and after applying the SVD unfolding procedure.

not contain this resonance [180]. Since the J/ψ is investigated in more detail and a different binning in Sec. 7.6.4 it is not discussed further here.

Since unfolding has negligible effect and in order not to introduce additional statistical fluctuations, the measured spectrum without unfolding is used to calculate the cross section. The uncertainty of the fits – 0.3 % – of a constant to the relative difference between the distributions with and without unfolding is introduced as the systematic uncertainty due to the mass resolution.

7.4 RADIATIVE CORRECTIONS

There are several categories of radiative corrections which need to be taken into account. Virtual corrections of the incoming particles are included in the signal simulation [153, 189] in leading-logarithmic order α^2 and vacuum polarization is considered in Sec. 7.5. The corrections concerning the detection efficiency calculated from simulation have been outlined in the previous section. Besides this, there are further physical effects which still need to be removed. Since we are dealing with a measurement using initial state radiation, additional photons are the main issue. These can either originate from the initial state, so that two photons are emitted in the initial state, or they can originate from the final state, altering the detected invariant mass of the hadrons. Both effects are described below.

7.4.1 NLO ISR Corrections

From the relation between the radiative and the non-radiative cross section – Eq. 38 – it can be deduced that the radiative cross sections (σ_γ) including leading order (LO) and next-to-leading order (NLO) ISR are connected to the corresponding radiator functions (W) via

$$\frac{\sigma_{\gamma\text{LO}}}{\sigma_{\gamma\text{NLO}}} = \frac{W_{\text{LO}}}{W_{\text{NLO}}}, \quad (70)$$

independent of the final state. Thus in order to be able to use the LO radiator function described in Sec. 3.1, we need to ensure that the cross sections are compatible or else correct for the difference. This is done by introducing the requirement $Q^2 := (p_{4\pi} + p_{\gamma\text{ISR}})^2 > 64 \text{ GeV}^2$ in simulation, which suppresses events with high-energetic NLO radiation. ($p_{4\pi}$ and $p_{\gamma\text{ISR}}$ correspond to the energy-momentum 4-vectors of the hadronic system and the ISR photon, respectively.) The value of this requirement was tuned so that in AfkQED the ratio $W_{\text{LO}}/W_{\text{NLO}}$ is unity (as observable in Fig. 123 (top) with a constant fitted for confirmation). But in the meantime more accurate calculations including full NLO radiation have become available, e.g. in PHOKHARA [163]. Thus it is checked whether the cross sections under the above requirement are also compatible using the improved simulation. In the simulation of the channel $e^+e^- \rightarrow \pi^+\pi^-\pi^0\pi^0\gamma$ a flat deviation of 0.8 % between NLO and LO simulation is observed as visible in Fig. 123 (bottom). The fit error is given as 0.02 %, but since we observe big variations in the count rates and therefore statistical uncertainties over the mass range, the resulting uncertainty is conservatively rounded up to 0.1 %. Thus a correction of $(0.8 \pm 0.1)\%$ is applied to account for NLO ISR effects. Since the model precision of PHOKHARA is estimated as 0.5 %, this has to be added to the fit uncertainty to get

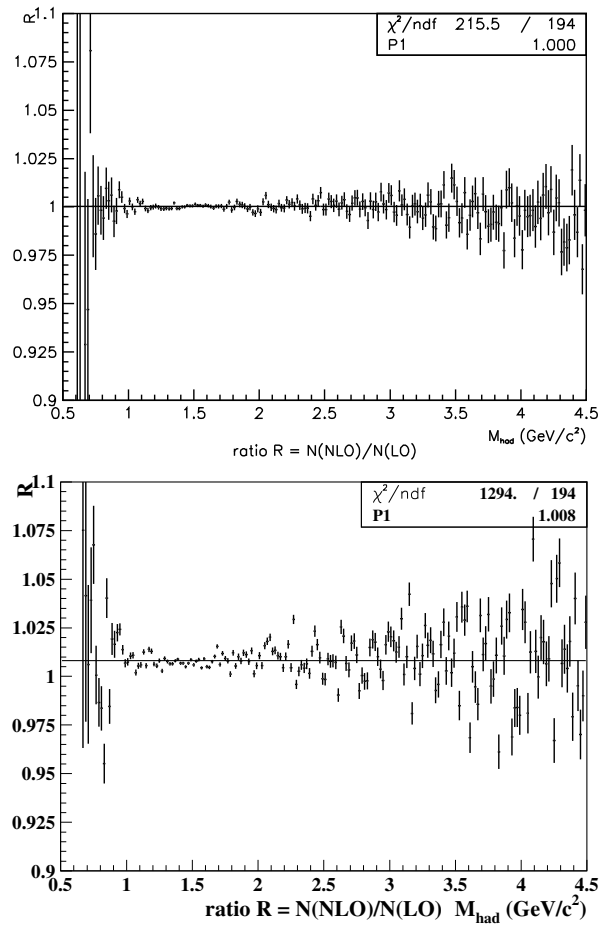


Figure 123.: Ratio of the count rates in next-to-leading and leading order simulated in AfkQED (top) and PHOKHARA (bottom).

the complete systematic uncertainty. Adding both up in quadrature yields 0.51 %.

7.4.2 FSR Correction of the Mass Spectrum

Since the production process of interest only contains ISR but not FSR, it is necessary to correct for the effects of additional FSR in nature. Therefore a study at generator level has been performed using AfkQED and PHOTOS (the latter for the additional FSR). In this study the distortion of the mass distribution by (not) including additional FSR is extracted. With this information, the mass distribution of the signal MC sample is corrected, which is subsequently used to calculate acceptance and efficiency. Therefore a simulation with 10^8 events was carried out for the ISR case as well as the ISR+FSR case. The corresponding mass distributions differ only slightly and are shown in Fig. 124. The ratio $R = \frac{N(\text{ISR}+\text{FSR})}{N(\text{ISR})}$ is depicted in Fig. 125, its features are discussed below. To correct

the existing efficiency distribution, a phenomenological function of the form

$$R(m) = p_0 + p_1 \cdot m + p_2 \cdot m^2 + A_g \cdot \exp\left(-\frac{1}{2} \cdot \left(\frac{m - m_g}{\sigma_g}\right)^2\right) + A_h \cdot \left(\frac{m - m_h}{\sigma_h}\right)^3 \cdot \exp\left(-\frac{1}{4} \cdot \left(\frac{m - m_h}{\sigma_h}\right)^4\right) \quad (71)$$

was fitted to the R distribution (see Fig. 125). The value $\chi^2_{\text{CV}}/n_{\text{dof}} = 0.294$ was obtained on a statistically independent cross validation data set, while $\chi^2_{\text{train}}/n_{\text{dof}} = 0.287$ (good agreement) was achieved on the training set to which the function was fitted. The resulting parameters are listed in Tab. 11.

Table 11.: The fit parameters of the FSR correction.

Parameter	Value	Uncertainty
p_0	1.02207	0.00088
p_1 [c^2/GeV]	-0.01799	0.00086
p_2 [$(\text{c}^2/\text{GeV})^2$]	0.00256	0.00019
A_g	0.04218	0.00023
m_g [GeV/c^2]	0.90422	0.00213
σ_g [GeV/c^2]	0.03280	0.00167
A_h	-0.00601	0.00018
m_h [GeV/c^2]	1.47231	0.00234
σ_h [GeV/c^2]	0.16123	0.00184

Applying the correction yields the result shown in Fig. 126 (original acceptance plot included for comparison). The most significant correction is applied around $M_{\text{had}} \approx 0.9 \text{ GeV}/\text{c}^2$. This bump is not due to any specific internal structure of the probability to radiate an FSR photon in this energy range. It is rather an effect of the steeply rising count rate above $M_{\text{had}} \approx 0.9 \text{ GeV}/\text{c}^2$. Since the invariant mass of the hadronic system is lowered if an FSR photon is emitted, in this region a relatively large number of events is shifted into a previously almost unpopulated area. This is verified by a toy simulation, coded in Python using the SciPy and NumPy libraries (see [190] and [191], respectively). To assess the effect of a global energy shift, this simulation artificially lowers the invariant mass of the hadronic system by the energy of the alleged FSR photon. The FSR photon energies are naïvely modeled to be distributed exponentially with a characteristic energy E_0 , while including the physical constraint that the resulting invariant mass must be at least the rest mass of four pions. After the new spectrum has been generated, it is compared to the actual spectrum including FSR by calculating the χ^2 of their deviation. This variable is then minimized by adjusting the parameter E_0 using the Golden Section Search algorithm (originally sketched in [192]). The result is $E_0^{\text{min}} = 1.1 \text{ MeV}$ with the

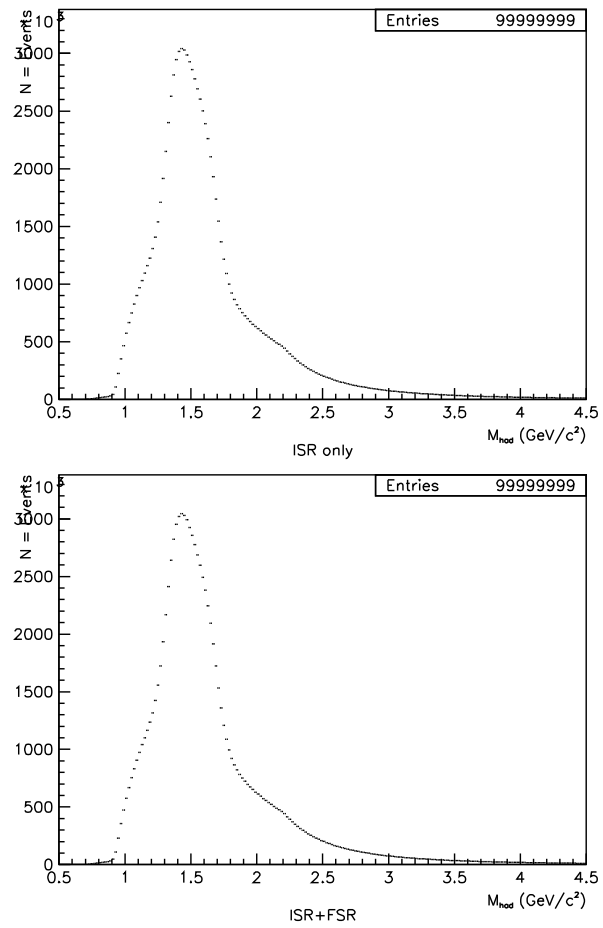


Figure 124.: Mass distributions including ISR only (top) and ISR+FSR (bottom).

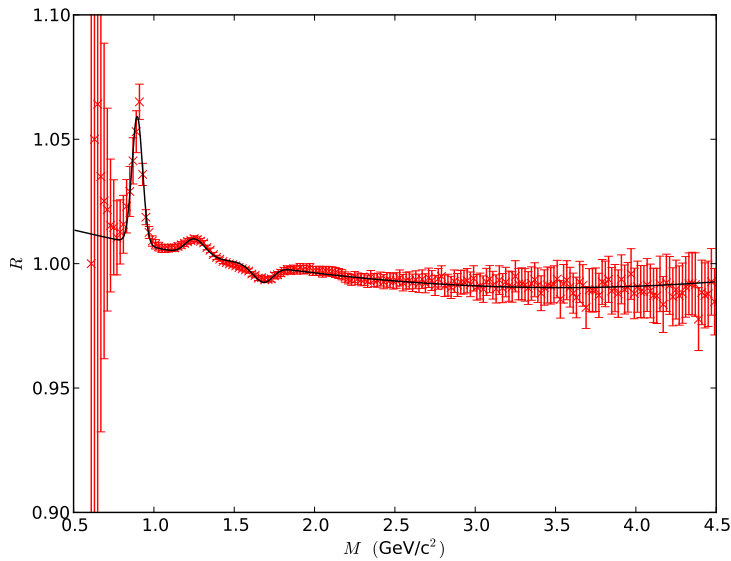


Figure 125.: Ratio of the mass distributions including FSR+ISR and ISR only. The black line depicts the phenomenological fit function.

corresponding plots showing good agreement in Fig. 127 (please note that for technical reasons a different simulation sample than for the original ratio had to be used).

Summary of Radiative Corrections

Since the virtual corrections of the initial state are included in the signal simulation, only two dedicated radiative corrections need to be applied to the measured cross section. These are the corrections for next to leading order ISR (Sec. 7.4.1) and for FSR

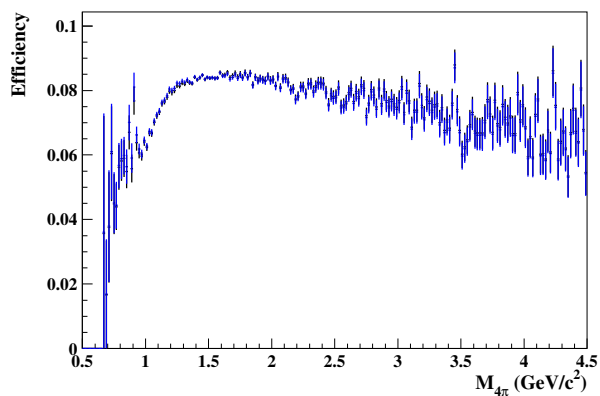


Figure 126.: Total efficiency before (black) and after (blue) FSR correction.

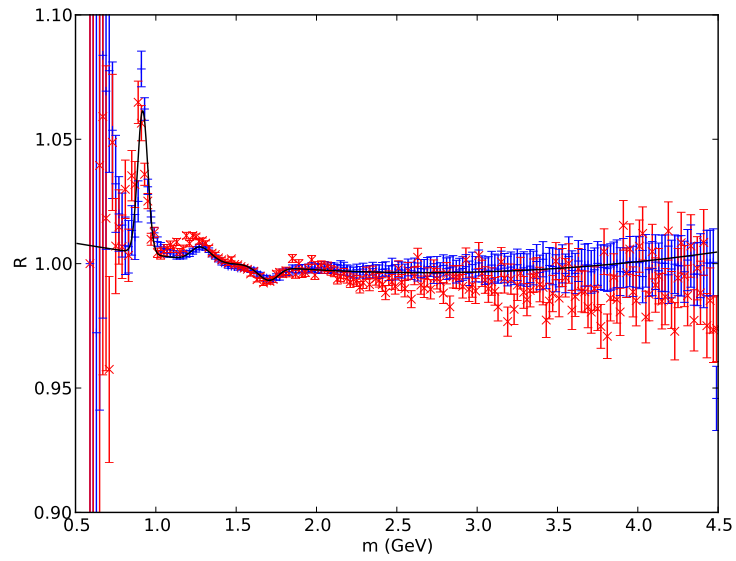


Figure 127.: Correction ratio R for the actual FSR simulation (red) and for the toy FSR simulation (blue). The black curve shows the correction function fit to the toy simulation.

effects (Sec. 7.4.2). The former results in a flat effect of $(0.8 \pm 0.1)\%$, while the latter is mass dependent. It is parameterized by a fitted function which gives a correction of up to 5%.

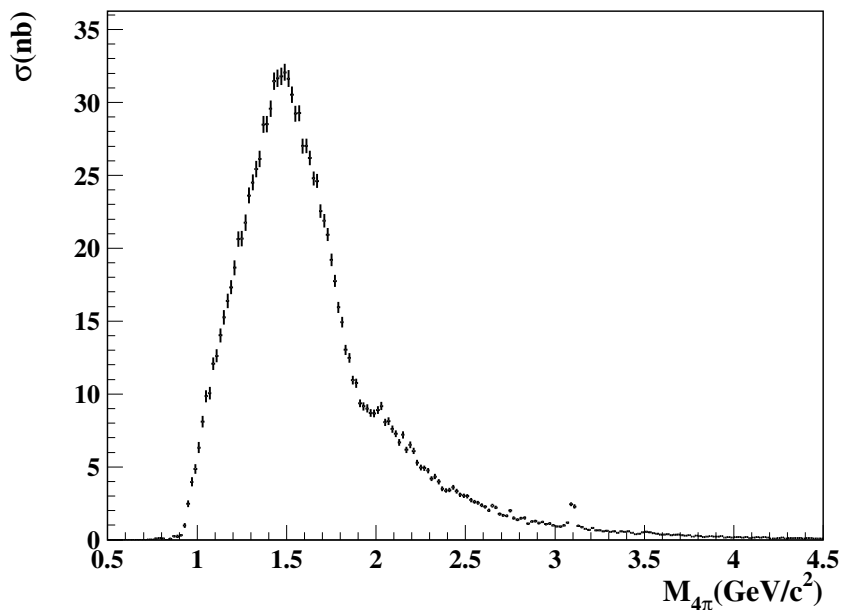


Figure 128.: The $e^+e^- \rightarrow \pi^+\pi^-2\pi^0$ cross section.

7.5 THE RESULTING CROSS SECTION

At this point in the analysis of the process $e^+e^- \rightarrow \pi^+\pi^-2\pi^0\gamma$, an effective event selection is established, the remaining background is subtracted accurately, efficiency including acceptance is simulated, luminosity as well as several precision corrections are calculated. Therefore, it is now possible to extract the final cross section $e^+e^- \rightarrow \pi^+\pi^-2\pi^0$ and the result in Fig. 128 is observed.

Additionally, the systematic uncertainties, compiled from the different sources and listed in Tab. 12, must be taken into account. Combining all systematic and statistical uncertainties, it is observed that the measurement is compatible with zero below $M_{4\pi} = 0.85 \text{ GeV}/c^2$.

For the computation of its contribution to $g - 2$, this cross section still has to be corrected for the effect of the running of the electroweak coupling α , which is performed as outlined in Refs. [145, 193]. The result – the Born cross section, also called “undressed” and denoted by $\sigma^{(0)}$ – is obtained by applying the correction factor in Fig. 129. Both cross sections, dressed and undressed, are listed in Tab. 13 in App. C.5.

Due to its unprecedented precision, this result also provides a much more meaningful benchmark than possible before for existing theoretical calculations. In Fig. 130, the prediction from chiral perturbation theory including ω , a_1 and double ρ exchange [194] is shown in comparison to data. The prediction exhibits similar behavior as the measured cross section, yet underestimates it con-

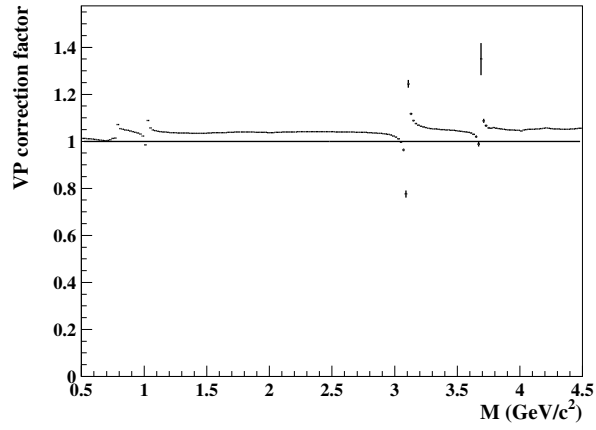


Figure 129.: Vacuum polarization correction factor according to Ref. [193].

siderably around $1 \text{ GeV}/c^2$, demonstrating the need for improved theoretical calculations.

Table 12.: Systematic uncertainties for different mass ranges.

$M(\pi^+\pi^-2\pi^0)(\text{GeV}/c^2)$	< 1.2	1.2 – 2.7	2.7 – 3.2	> 3.2
Tracking eff.	0.8%	0.8%	0.8%	0.8%
γ eff.	0.4%	0.4%	0.4%	0.4%
$2\pi^0$ eff.	2.0%	2.0%	2.0%	2.0%
$\chi^2_{4\pi\gamma}$ eff.	0.4%	0.4%	0.4%	0.4%
Resonances in AfkQed	0.4%	0.4%	0.4%	0.4%
Mass res.	0.3%	0.3%	0.3%	0.3%
FSR	1.0%	1.0%	1.0%	1.0%
NLO ISR	0.5%	0.5%	0.5%	0.5%
ISR luminosity	1.0%	1.0%	1.0%	1.0%
continuum Bkg	1.0%	1.0%	1.0%	2.0%
ISR Background	1 – 100%	1.0%	6.0%	6.0%
Kaon PID	0.5%	0.5%	0.5%	0.5%
Muon PID	0%	0%	0%	2.0%
total	3 – 100%	3.1%	6.7%	7.2%

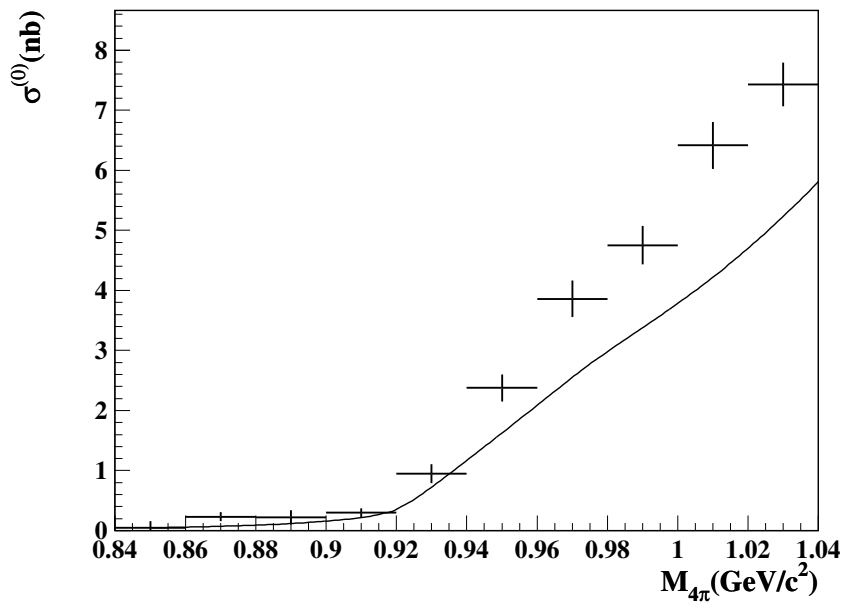


Figure 130.: The low-energy part of the Born cross section (points with statistical uncertainties) compared to the theoretical prediction (line) of Ref. [194].

7.6 INTERMEDIATE RESONANCES

Besides the contribution to $a_\mu = g_\mu/2 - 1$, the channel $e^+e^- \rightarrow \pi^+\pi^-\pi^0\pi^0$ is of importance due to its manifold internal structures. These shed light on the production process of hadrons and can (in-)validate theoretical models or provide input for the latter, e.g. Ref. [195].

It is observed that there is a large ρ^0 contribution in the $\pi^+\pi^-$ mass spectrum of data from the size of the peak around $M_{\pi^+\pi^-} = 0.78 \text{ GeV}/c^2$. In the $\pi^0\pi^0$ mass distribution, a slight shoulder is present just below $1 \text{ GeV}/c^2$, which is not visible in PHOKHARA simulation and is further explored in Sec. 7.6.1. In the two-dimensional distribution of the $\pi^+\pi^0$ vs. the $\pi^-\pi^0$ mass a $\rho^+\rho^-$ -peak is found in data, which is studied in Sec. 7.6.2.

While otherwise being very similar to the prediction from simulation, the three pion mass distributions show slightly stronger tails towards high masses as do all invariant mass contributions, including the full four pion mass $M_{\pi^+\pi^-2\pi^0}$. The most prominent resonance observed in the three pion mass subsystems is the ω , whose contribution is investigated in Sec. 7.6.3.

Two structures decaying into four pions are visible directly in the cross section (Fig. 144): the J/ψ resonance and possibly an excited ρ state at $M_{\pi^+\pi^-2\pi^0} \approx 2.05 \text{ GeV}/c^2$. In Sec. 7.6.4 the branching fraction of the decay $J/\psi \rightarrow \pi^+\pi^-2\pi^0$ is calculated.

In the following sections data is compared with PHOKHARA 5.0 [196, 197], which is not processed through detector simulation. The efficiencies applied to data are calculated from AflQED. No background subtraction is applied to the data shown in this section.

7.6.1 Production of $\rho^0 f_0$

Intriguingly, the intermediate state $\rho^0\pi^0\pi^0$ was not observed by the CMD-2 experiment in the energy range $1.05 < E_{\text{CM}} < 1.38 \text{ GeV}$ [198]. Nonetheless, a small peak at the ρ^0 mass is seen in the $\pi^+\pi^-$ mass in Fig. 131 and also a shoulder around the f_0 mass in the $\pi^0\pi^0$ mass. One possible production channel for $\pi^+\pi^-2\pi^0\gamma$ is given by $e^+e^- \rightarrow \rho^0(770)f_0(980)\gamma \rightarrow \pi^+\pi^-2\pi^0\gamma$, thus at higher CM energies the intermediate state $\rho^0\pi^0\pi^0$ should be observed. The relevant decays $f_0(980) \rightarrow \pi^0\pi^0$ and $\rho^0(770) \rightarrow \pi^+\pi^-$ are listed [43] as dominant and almost exclusive, respectively. The opposite decay is forbidden because the decay $\rho^0 \rightarrow \pi^0\pi^0$ violates \mathcal{C} -parity ($J^{PC}(\rho^0) = 1^{--}$). In the *BABAR* data the intermediate states $\rho^0 f_0$ and hence $\rho^0\pi^0\pi^0$ are clearly observed. The correlated production of $\rho^0(770)$ and $f_0(980)$ is especially well visible in the $M_{\pi^0\pi^0}$ vs. $M_{\pi^+\pi^-}$ scatter plot restricted to the invariant mass interval $1.7 \text{ GeV}/c^2 < M_{\pi^+\pi^-2\pi^0} < 2.3 \text{ GeV}/c^2$, Fig. 132. The effect is even more pronounced in the $M_{\pi^0\pi^0}$ spectrum seen in Fig. 133a, where a clear peak is observed at

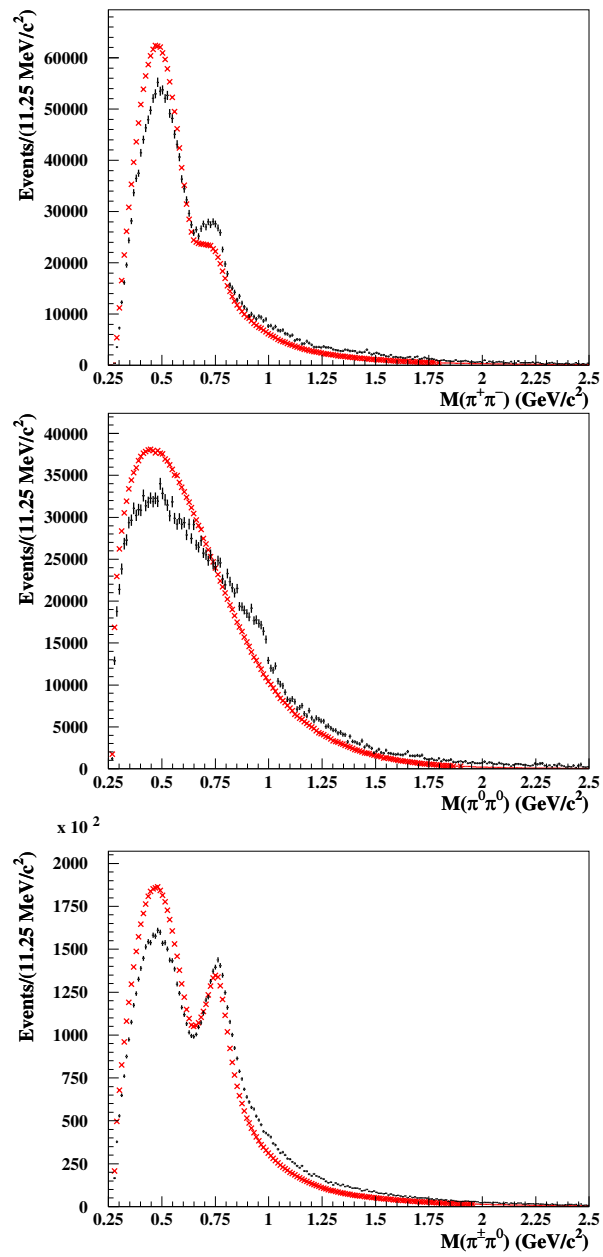


Figure 131.: $M(\pi^+\pi^-)$ (top), $M(\pi^0\pi^0)$ (middle), and $M(\pi^\pm\pi^0)$ (bottom) for data (black) and PHOKHARA-MC (red). Data after efficiency correction and MC sample scaled to the same area.

the nominal $f_0(980)$ mass $M_{f_0} \approx 990 \text{ MeV}/c^2$. This peak vanishes (Fig. 133b) if an additional requirement is applied to remove the $\rho^0(770)$: $M_{\pi^+\pi^-} < 0.6 \text{ GeV}/c^2 \vee M_{\pi^+\pi^-} > 0.9 \text{ GeV}/c^2$. This indicates that $f_0(980)$ is produced exclusively in combination with $\rho^0(770)$, an important insight into the production mechanism of the final state.⁶ The converse is not true: as visible in Fig. 134b a significant $\rho^0(770)$ -peak remains when removing $f_0(980)$, the signal is simply smaller than when including $f_0(980)$ (Fig. 134a).

The influence on the cross section $e^+e^- \rightarrow \pi^+\pi^-2\pi^0$ is illustrated in Fig. 135 by selecting only events within ± 1 width of the ρ -resonance in $M(\pi^+\pi^-)$ and of the f_0 -resonance in $M(\pi^0\pi^0)$, visualized by the ellipse in Fig. 132. It must be noted that this region still includes a sizable fraction of events from other production mechanisms as is apparent from Fig. 131. Nonetheless, in Fig. 136 different shapes can be observed in data and signal simulation in the cross section restricted to the $\rho^0 f_0$ region. The production rate in data is larger by a factor 2.2 ± 0.4 than in PHOKHARA 5.0 simulation, hinting at potential improvement opportunities in the model describing this process.

7.6.2 Production of $\rho^+\rho^-$

Another possible production mechanism is $e^+e^- \rightarrow \rho^+\rho^-\gamma \rightarrow \pi^+\pi^-2\pi^0\gamma$. The individual ρ^\pm peak is visible in the $\pi^\pm\pi^0$ mass in Fig. 131 (bottom), but no conclusion about the correlation between the resonances ρ^+ and ρ^- can be drawn from this distribution. However, Fig. 137 illustrates that a much larger number of events is observed in the $\rho^+\rho^-$ region in data than in AfkQED-MC. Simulation contains independent ρ^\pm bands but no correlated production. This seems insufficient to describe the shape measured from data. The cross section (Fig. 135&136) in the $\rho^+\rho^-$ region (nominal ρ mass ± 1 width in each variable, which, as above, may also contain a large fraction of non- $\rho^+\rho^-$ events), is larger by a factor 1.6 ± 0.1 in data than in PHOKHARA 5.0 simulation.

⁶ In order to correct the effect of the phase space limitation due to the requirements on $M_{\pi^+\pi^-}$, data is divided by the efficiency calculated from AfkQED simulation.

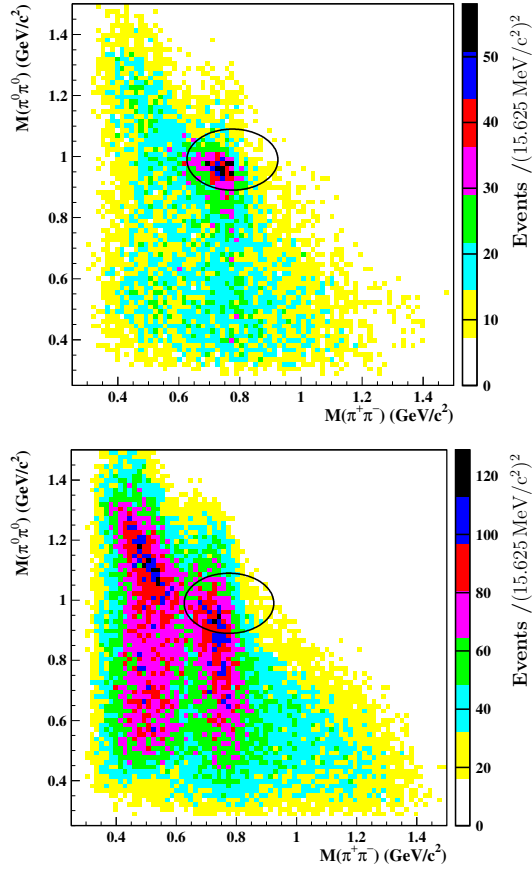
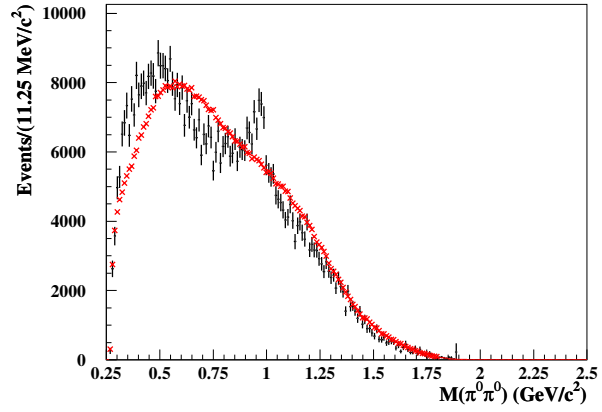


Figure 132.: $M_{\pi^0\pi^0}$ vs. $M_{\pi^+\pi^-}$ scatter plot of data (top) and AfkQED signal simulation (bottom) in the invariant mass interval $1.7 \text{ GeV}/c^2 < M_{\pi^+\pi^-\pi^0} < 2.3 \text{ GeV}/c^2$ after full selection without efficiency correction and background subtraction. The black ellipse indicates the region used to select $\rho^0 f_0$ events.



(a) Full spectrum.

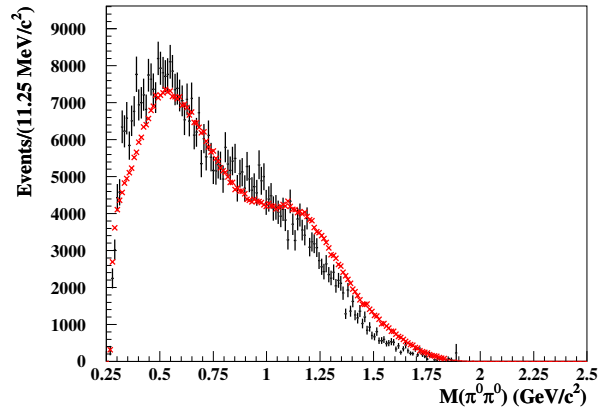
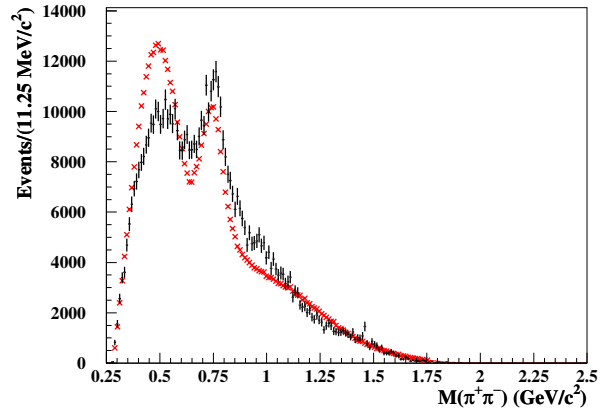
(b) Spectrum excluding the ρ^0 region in $M_{\pi^+\pi^-}$.

Figure 133.: $M(\pi^0\pi^0)$ in the invariant mass interval $1.7 \text{ GeV}/c^2 < M_{\pi^+\pi^-\pi^0} < 2.3 \text{ GeV}/c^2$ for data (black) and PHOKHARA-MC (red). Data after full selection and efficiency correction, MC sample scaled to the same area.



(a) Full spectrum.

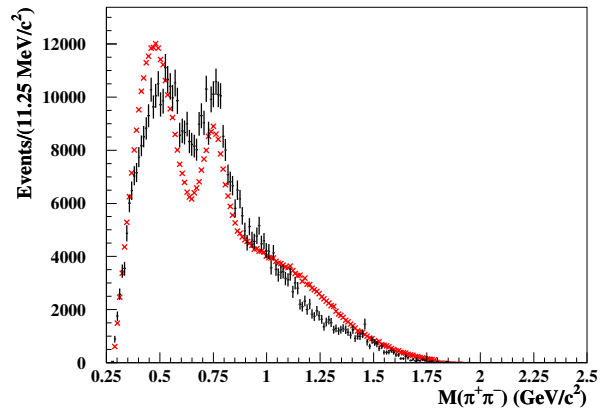
(b) Spectrum excluding the f^0 region in $M_{\pi^0\pi^0}$.

Figure 134.: $M(\pi^+\pi^-)$ in the invariant mass interval $1.7 \text{ GeV}/c^2 < M_{\pi^+\pi^-2\pi^0} < 2.3 \text{ GeV}/c^2$ for data (black) and PHOKHARA-MC (red). Data after full selection and efficiency correction, MC sample scaled to the same area.

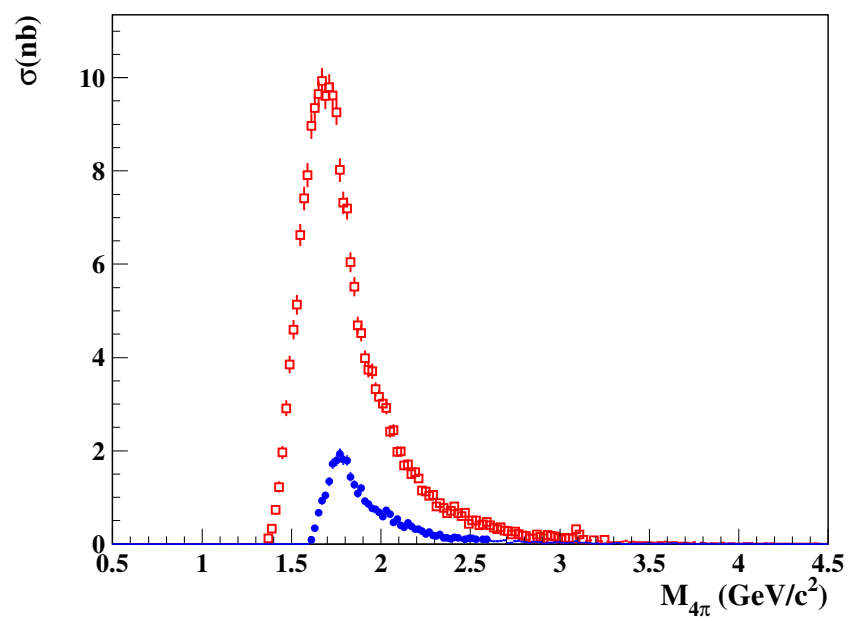


Figure 135.: The $e^+e^- \rightarrow \pi^+\pi^-2\pi^0$ cross section in the $\rho^+\rho^-$ (red) and ρ^0f_0 (blue) regions as indicated in Figs. 132&137.

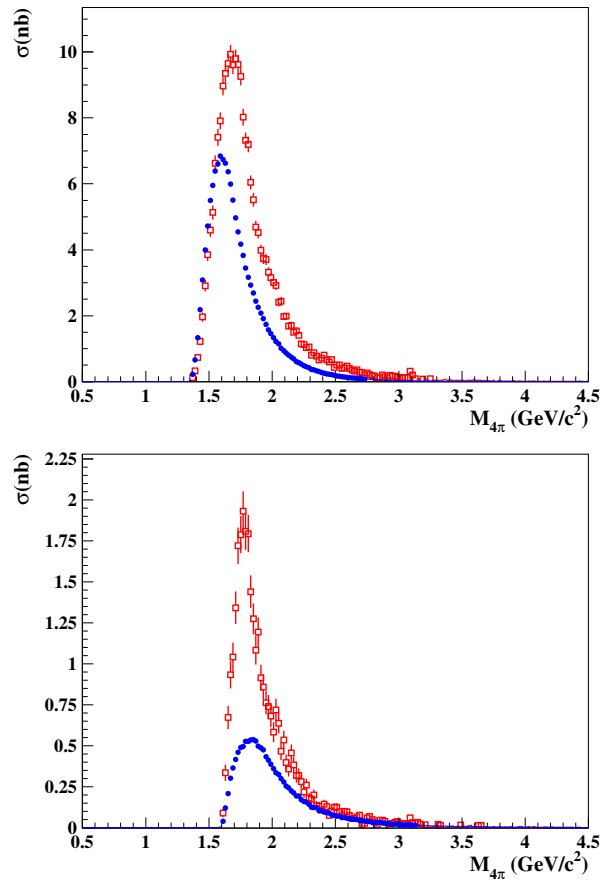


Figure 136.: The $e^+e^- \rightarrow \pi^+\pi^-2\pi^0$ cross section in the $\rho^+\rho^-$ (upper panel) and $\rho^0 f_0$ (lower panel) regions as indicated in Figs. 132&137 for data (red) and PHOKHARA-MC (blue).

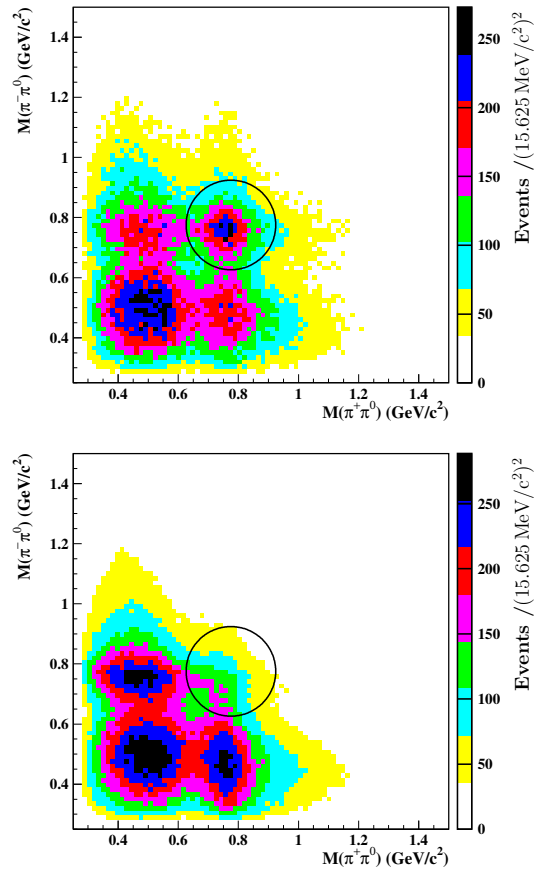


Figure 137.: $M(\pi^+\pi^0)$ vs. $M(\pi^-\pi^0)$ for data (top) and AfkQED-MC (bottom). No efficiency correction or scaling applied. The black circle indicates the region used to select $\rho^+\rho^-$ events.

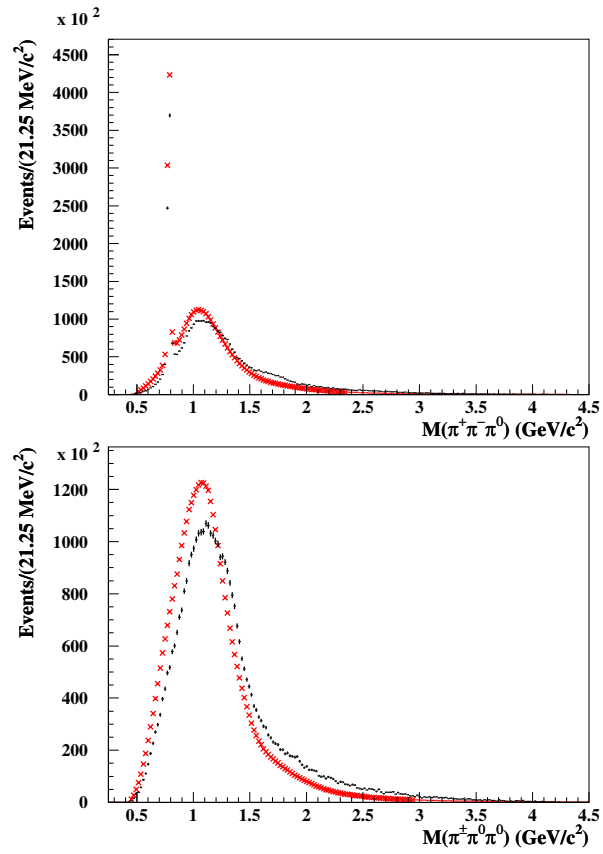


Figure 138.: The $M(\pi^+\pi^-\pi^0)$ (top) and $M(\pi^\pm\pi^0\pi^0)$ (bottom) distributions for data (black) and PHOKHARA-MC (red). Data after efficiency correction and MC sample scaled to the same area.

7.6.3 Production of $\omega\pi^0$

A large number of events is observed in the ω peak in the three-pion masses shown in Fig.138. Hence it is interesting to investigate the events coming from the subchannel $e^+e^- \rightarrow \omega\pi^0\gamma \rightarrow \pi^+\pi^-2\pi^0\gamma$, provided by the large branching fraction $\mathcal{B}(\omega \rightarrow \pi^+\pi^-\pi^0) = (89.2 \pm 0.2)\%$ [43]. This can be achieved by studying the three-pion mass $M(\pi^+\pi^-\pi^0)$ distribution, seen in Fig. 139, which exhibits a very clear peak. The peak is fitted with the sum of a Voigt profile [199, 200] (convolution of normal distribution and Breit-Wigner function with fixed ω width) added to a normal distribution to account for the radiative tail. The underlying background is modeled by

$$\text{bkg}(x) = (1 - \exp(-((x - x_0)/w)^3)) \cdot (p_0 + p_1x + p_2x^2 + p_3x^3) .$$

In this fit a resonance mass compatible with the current world average of $782.65 \pm 0.12 \text{ MeV}/c^2$ [43] is found. The extracted $\omega\pi^0$ production fraction is $(32.1 \pm 0.2)\%$ (the uncertainty is taken from the fit and thus purely statistical).

Using the same fit in steps of $M_{\pi^+\pi^-2\pi^0}$ and normalizing to luminosity, the $\omega\pi^0$ production cross section can be studied in order to characterize the production of the $\pi^+\pi^-2\pi^0$ final state. The resulting cross section is shown in Fig. 140 as a function of the total invariant mass. For very low values just above the $\omega\pi^0$ production threshold, the intermediate state $\omega\pi^0\gamma$ saturates the process $e^+e^- \rightarrow \pi^+\pi^-2\pi^0\gamma$. The production fraction then decreases rapidly, such that it is on the level of 10 % already at $M_{\pi^+\pi^-2\pi^0} \approx 1.8 \text{ GeV}/c^2$, decreasing further towards higher masses. After the sharp drop observed between $1.5 \text{ GeV}/c^2$ and $2.0 \text{ GeV}/c^2$, there is a small bump at approximately $2.1 \text{ GeV}/c^2$. Its significance and possible connection to the shoulder seen in the full $e^+e^- \rightarrow \pi^+\pi^-2\pi^0$ cross section at the same energy could be investigated in a partial wave analysis.

Systematic uncertainties are determined by repeating the fits using a simpler fit function. In the full energy range this gives $(29.5 \pm 0.2)\%$ instead of the nominal $(32.1 \pm 0.2)\%$ ω -fraction, thus a relative deviation of $\sim 8\%$. In the individual mass slices the deviation is somewhat larger, giving a relative systematic uncertainty of $\sim 10\%$. In Fig. 141 the cross section is shown in comparison to the existing world data set [201–204], exhibiting good agreement with the recent measurement by the SND collaboration, yet the new *BABAR* measurement has smaller statistical uncertainties.

7.6.4 J/ψ Branching Fraction

As visible in the cross section, the J/ψ resonance is also produced as an intermediate state. Analogous to the to the procedure outlined in Sec. 6.7, the branching fraction $\mathcal{B}_{J/\psi \rightarrow 2\pi 2\pi^0}$ is extracted. By fitting a normal distribution (due to the extremely small width of the

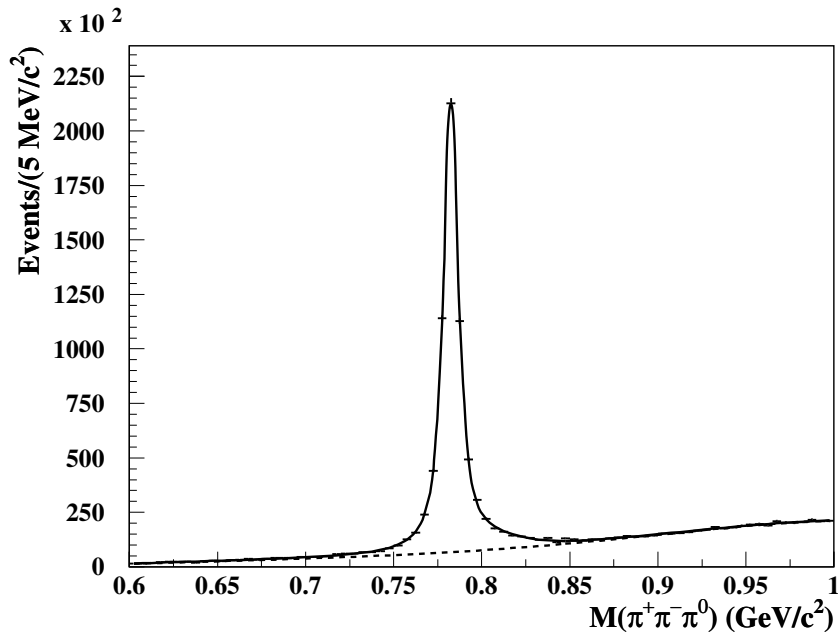


Figure 139.: The measured ω data peak in the complete $M(\pi^+\pi^-2\pi^0)$ range after full selection and efficiency correction.

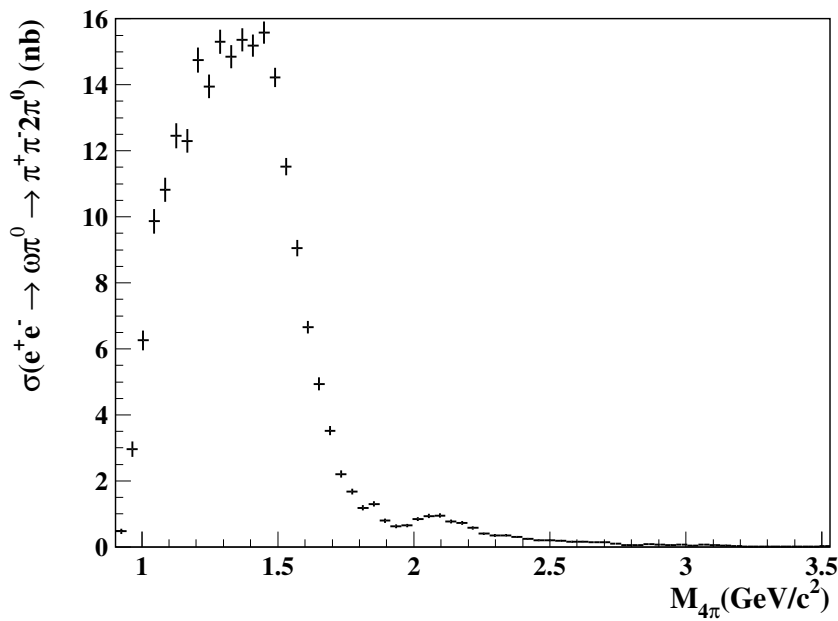


Figure 140.: The measured $e^+e^- \rightarrow \omega\pi^0 \rightarrow \pi^+\pi^-2\pi^0$ cross section as a function of $M(\pi^+\pi^-2\pi^0)$, statistical uncertainties from the fit shown only.

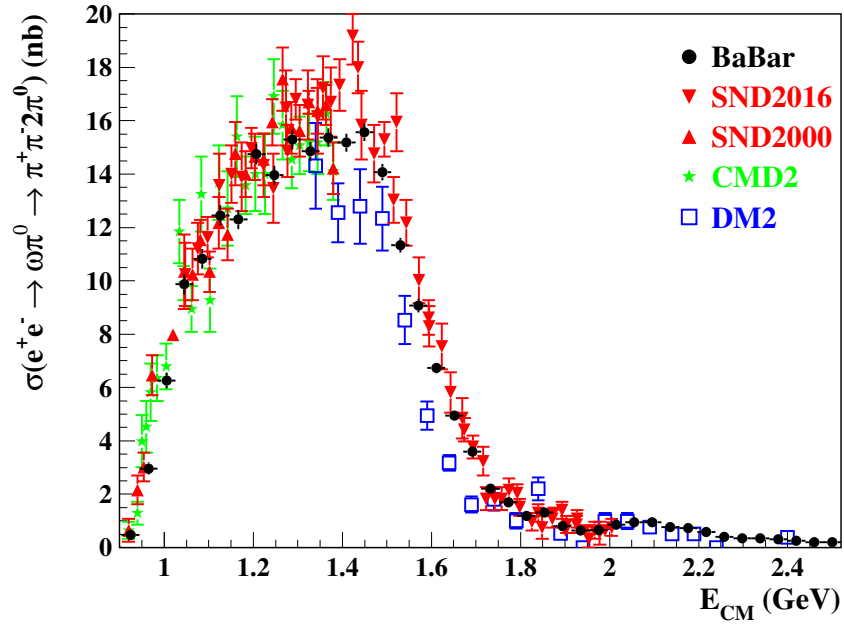


Figure 141.: The measured $e^+e^- \rightarrow \omega\pi^0 \rightarrow \pi^+\pi^-2\pi^0$ cross section world data set as a function of $M(\pi^+\pi^-2\pi^0)$, statistical uncertainties shown only.

resonance $\Gamma^{J/\psi} = (92.9 \pm 2.8)\text{keV}/c^2$, the peak shape is dominated by detector resolution $\sim 15\text{MeV}/c^2$ to the peak observed in data as shown in Fig. 142, the size of this production channel is determined. The background from other channels and other $\pi^+\pi^-2\pi^0$ production mechanisms is flat and thus not subtracted but instead modeled by an additional first order polynomial. The parameters resulting from the fit can then be used to extract the J/ψ -yield after normalization to luminosity and efficiency:

$$\mathcal{B}_{J/\psi \rightarrow 2\pi 2\pi^0} \cdot \sigma_{\text{int}}^{J/\psi} = \frac{N(J/\psi \rightarrow 2\pi 2\pi^0)}{d\mathcal{L}/dE \cdot \varepsilon} = 64 \pm 4_{\text{stat}} \pm 5_{\text{fit}} \text{MeVnb}. \quad (72)$$

Using $M_{J/\psi} = (3096.916 \pm 0.011)\text{MeV}/c^2$ [43] and the following relation [38], the product of branching fraction and electronic width can be calculated:

$$\mathcal{B}_{J/\psi \rightarrow 2\pi 2\pi^0} \cdot \Gamma_{ee}^{J/\psi} = \frac{N(J/\psi \rightarrow 2\pi 2\pi^0) \cdot M_{J/\psi}^2 c^4}{6\pi^2 \cdot \hbar^2 c^2 \cdot d\mathcal{L}/dE \cdot \varepsilon} = 26 \pm 2_{\text{stat}} \pm 2_{\text{fit}} \text{eV}. \quad (73)$$

With $\Gamma_{ee}^{J/\psi} = (5.55 \pm 0.14)\text{keV}$ [43], the branching fraction follows:

$$\mathcal{B}_{J/\psi \rightarrow 2\pi 2\pi^0} = (4.8 \pm 0.3_{\text{stat}} \pm 0.4_{\text{syst}} \pm 0.1_{\text{input}}) \times 10^{-3}. \quad (74)$$

Here, the model uncertainty due to the fit has been combined with the general systematic uncertainty of the cross section measurement. The model uncertainty due to the fit is determined by repeating the fit using different functions. A normal distribution plus second order polynomial as well as a Voigt profile plus first

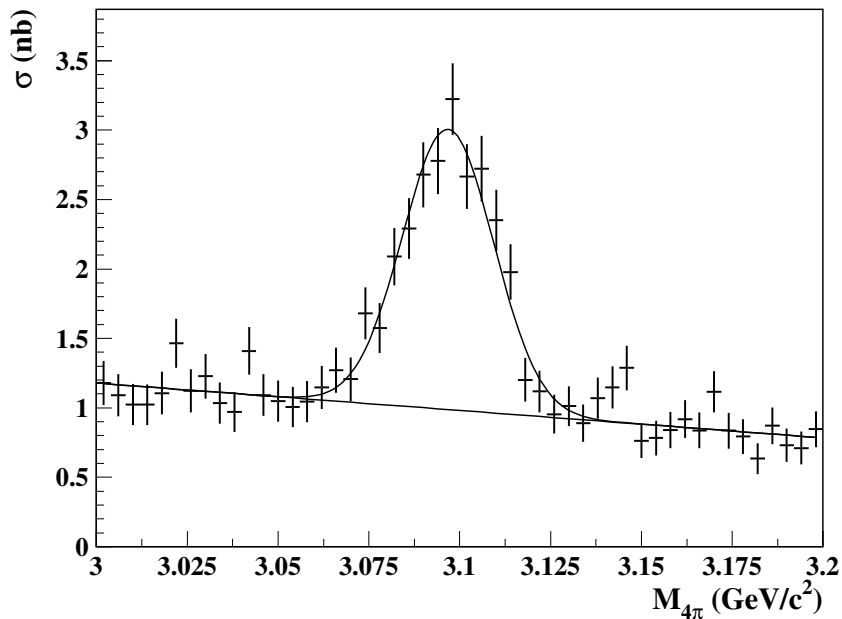


Figure 142.: J/ψ peak in the $e^+e^- \rightarrow \pi^+\pi^-2\pi^0$ cross section.

order polynomial are studied. The absolute sum of the differences to the result using the nominal fit model is taken as the systematic uncertainty. In addition, the systematic uncertainty of the general analysis is applied, which amounts to 2.7 % in this mass range since no background subtraction is applied. This is justified as all backgrounds in this energy range are reasonably flat (see Fig. 103) thus the fit takes care of them. The only background channel showing any structure near the J/ψ mass is the $e^+e^- \rightarrow 2\pi_3\pi^0\gamma$ contribution but its peak is shifted towards lower energies and therefore does not interfere with the fitting procedure. Its contribution in the fit range is shown in Fig. 143. Furthermore the acceptance and efficiency has been fitted with a constant to minimize statistical fluctuations. The relative uncertainty of the fit parameter is also added in quadrature to the uncertainty of the branching fraction.

The uncertainty due to the input values ($\Gamma_{ee}^{J/\psi}$, $M_{J/\psi}$, and $\hbar c$) is propagated to give $0.1_{\text{input}} \times 10^{-3}$.

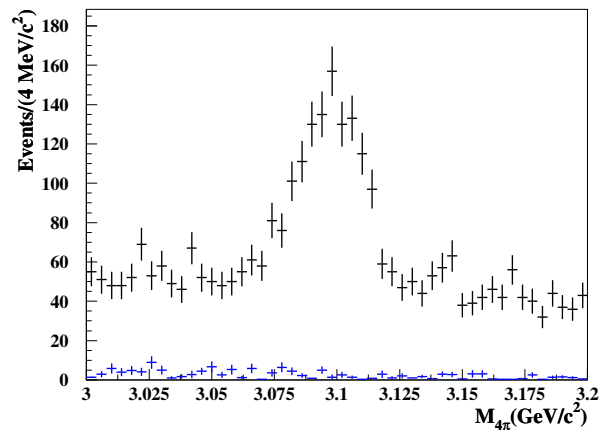


Figure 143.: The event rates from $2\pi 3\pi^0\gamma$ background (blue) and data (black) in the J/ψ range. No efficiency correction applied.

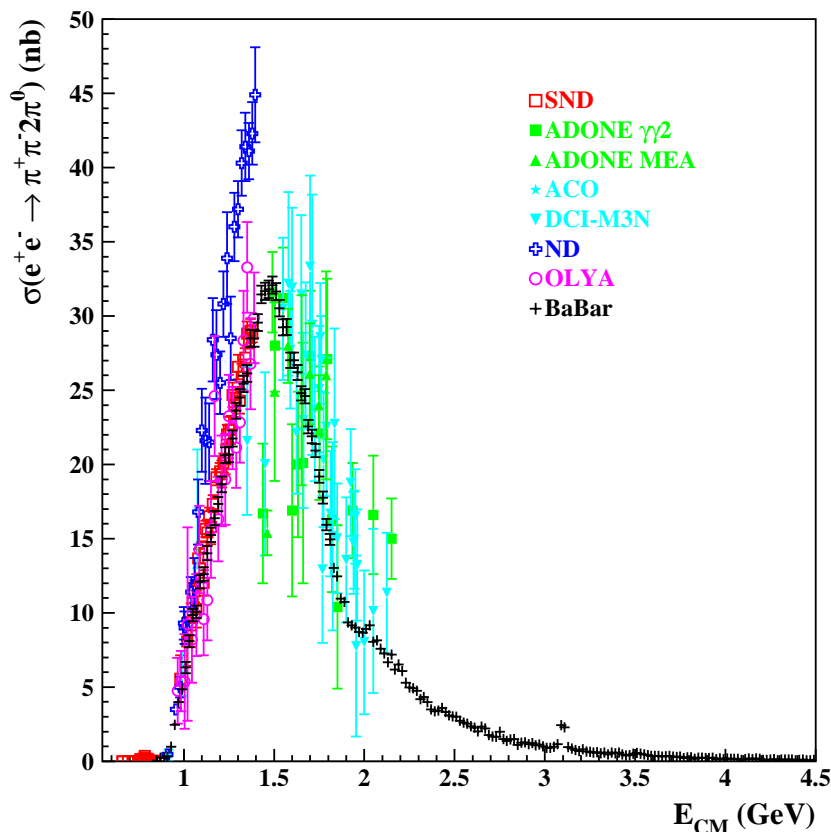


Figure 144.: Comparison of $e^+e^- \rightarrow \pi^+\pi^-2\pi^0$ cross section measurements as a function of $E_{\text{CM}} = M_{4\pi}c^2$ from different experiments with statistical uncertainties. It is observed that the *BABAR* measurement reaches unprecedented precision and covers a greater range than any other experiment.

Summary of the Channel $e^+e^- \rightarrow \pi^+\pi^-2\pi^0$

The cross section of this channel has been analyzed with unprecedented precision and in a wider energy range than previously available in the world data set, which is shown in Fig. 144 in comparison to the new *BABAR* data.

The precision of this new measurement far exceeds all others, statistically and systematically. In the peak region around $M_{4\pi} \approx 1.5 \text{ GeV}/c^2$, systematic precision of 3.1 % is reached, surpassing the original goal of 5 %, owed mostly to the improvement of the background subtraction. Moreover, it is the first measurement to cover a wide energy range, almost from threshold up to $4.5 \text{ GeV}/c^2$. This leads to the effect that resonances like the J/ψ are observed in this channel for the first time, and can be studied in detail in Sec. 7.6.4. Furthermore the structure around $2 \text{ GeV}/c^2$ has never been seen before, due to insufficient precision of the previously existing data. This excess of events has been suspected to be an excited ρ state,

but definitive conclusions can only be drawn in the future after a partial wave analysis or similar investigations. Besides the cross section, the subprocesses in producing the final state $\pi^+\pi^-\pi^0\pi^0$ are studied, yielding insight into such intermediate states as $\rho^+\rho^-$, $\rho^0 f_0$, and $\omega\pi^0$.

Using the new cross section result, it is now possible to significantly reduce the uncertainty introduced into the theoretical prediction of a_μ , which is calculated in the following chapter.

CALCULATION OF a_μ AND $\Delta\alpha$

One of the main motivations for measuring the $e^+e^- \rightarrow \pi^+\pi^-2\pi^0$ and $e^+e^- \rightarrow \pi^+\pi^-3\pi^0$ cross sections is the improvement of the Standard Model prediction of $g_\mu - 2$ or $a_\mu := \frac{g_\mu - 2}{2}$. In this chapter a routine is described which has been developed to extract the contribution to the lepton magnetic moment for given hadronic Born cross section data. Special attention is paid to ensuring that the algorithm produces robust results, meaning that small changes in the data must not lead to disproportionately large differences in the result.

The hadronic contribution a_μ^{had} is given by the integral derived in Sec. 2.3

$$a_\mu^{\text{had}} = \frac{1}{4\pi^3} \int_{s_{\min}}^{\infty} K_\mu(s) \cdot \frac{\sqrt{1 - \frac{4m_e^2}{s}}}{1 + \frac{2m_e^2}{s}} \cdot \sigma_{\text{had}}^{(o)}(s) ds. \quad (75)$$

The kernel function depicted in Fig. 145 is given by¹

$$K_\mu(s) = \begin{cases} \frac{1}{h^2} \left(4(h-2) \ln \frac{h}{4} - h \left(4 - \frac{h}{2} \right) \right. \\ \quad \left. - 2(h^2 - 8h + 8) \frac{\arctan(\sqrt{h-1})}{\sqrt{h-1}} \right) & s < 4m_\mu^2 \\ \frac{1}{h^2} \left(4(h-2) \ln \frac{h}{4} - h \left(4 - \frac{h}{2} \right) \right. \\ \quad \left. - 2(h^2 - 8h + 8) \frac{\operatorname{arctanh}(\sqrt{1-h})}{\sqrt{1-h}} \right) & s > 4m_\mu^2 \end{cases} \quad (76)$$

with $h := \frac{4m_\mu^2}{s}$. The singularity at $h = 1$ is removable with $K_\mu(4m_\mu^2) = 8 \ln(2) - \frac{11}{2} \approx 0.045$. The $e^+e^- \rightarrow \pi^+\pi^-2\pi^0$ and $e^+e^- \rightarrow \pi^+\pi^-3\pi^0$ cross sections only contribute in the region $s > 4m_\mu^2$.

In order to evaluate the integral from experimental cross section data and the analytic kernel function, several steps are taken. First, the cross section is interpolated by a monotone cubic spline [205, 206] (end-slopes determined in a one-sided scheme [207]). Using a monotone interpolator ensures that no artificial extrema are introduced. The interpolation methods employed here further guarantee that a change in one data point remains *local*, i.e. does not

¹ For $h \ll 1$, catastrophic cancellations occur if the formula is implemented directly. This problem can be remedied by expanding the corresponding terms and simplifying the formula into a convergent series, see App. D.

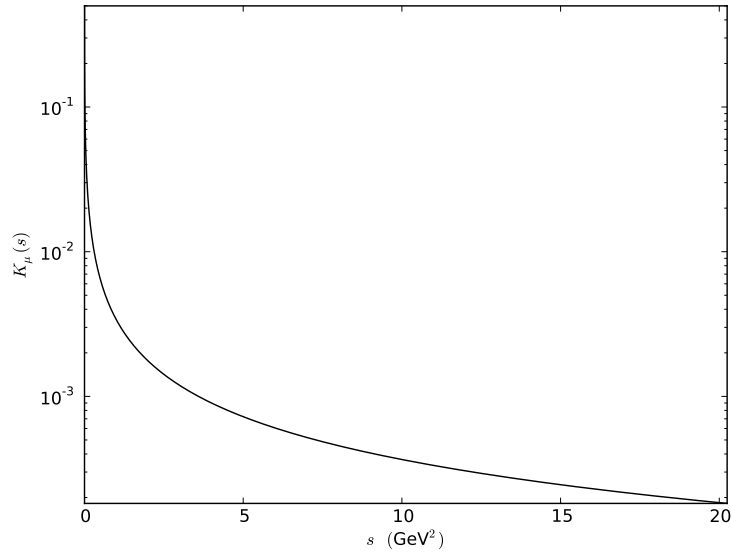


Figure 145.: Muon kernel function in Eq. 76 on a logarithmic scale.

influence the shape of the interpolation curve far from the affected point. The spline is furthermore once continuously differentiable fulfilling the requirements on functions evaluated with the dispersion relation. Applying this interpolation to the newly measured $e^+e^- \rightarrow \pi^+\pi^-2\pi^0$ and $e^+e^- \rightarrow \pi^+\pi^-3\pi^0$ cross section data yields the results shown in Figs. 146 and 147, respectively.

The produced spline is then weighted by the kernel function and the kinematic term. (The order of operations is important, since especially for a quickly (on the scale of the cross section bin width) varying kernel the reversed order (first weighting by the kernel, then interpolating) would result in an incorrect weighting.) The resulting function may then be integrated numerically to arbitrary precision, which is achieved via an adaptive Gaussian quadrature method (see e.g. Ref. [58, 208, 209]). To ensure that the error from the integration is negligible, the precision of the integration is required to be at least a factor 10^3 better than the statistical and than the systematic uncertainty. These are computed from the uncertainties of the cross section measurement. Basically for each bin, the uncertainty is weighted by the bin width and then summed up quadratically for the statistical and absolutely for the systematic uncertainties.

This algorithm – in part implemented using routines from the open source libraries SciPy [190] and GSL [210] – has been cross checked against the method HVPTools described in Ref. [211], giving consistent results.

For the process $e^+e^- \rightarrow \pi^+\pi^-2\pi^0$ the world data value before *BABAR* covered the energy range $1.02 \text{ GeV} \leq E_{\text{CM}} \leq 1.8 \text{ GeV}$ and

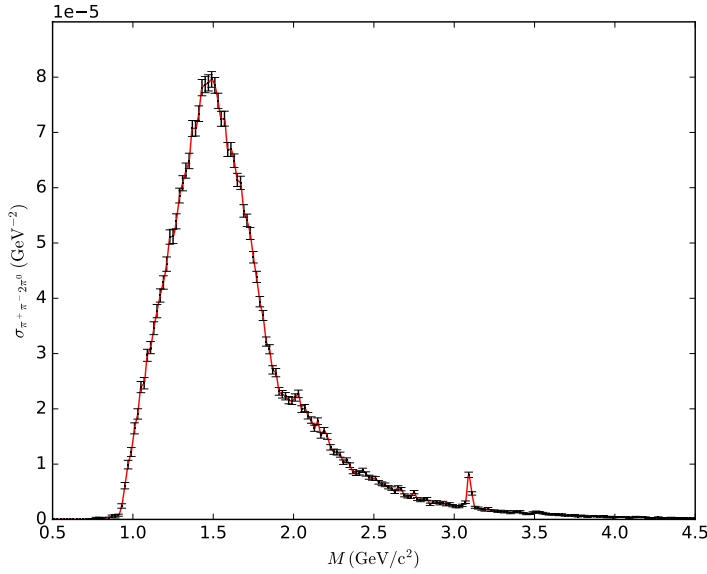


Figure 146.: Cubic spline interpolating the cross section $e^+e^- \rightarrow \pi^+\pi^-2\pi^0$.

yielded the result² $(16.76 \pm 1.31 \pm 0.20_{\text{rad}}) \times 10^{-10}$ [137], implying a total relative precision of 8%. Evaluating a_μ by integrating the new measurement, shown in Fig. 146, restricted to the same energy region as used in the analysis of the previous world data, yields $a_\mu(\pi^+\pi^-2\pi^0) = (17.4 \pm 0.1_{\text{stat}} \pm 0.6_{\text{syst}}) \times 10^{-10}$, corresponding to a total relative precision of 3.2%. Hence, the relative precision of the *BABAR* measurement alone is a factor 2.5 higher than the previous world data set's relative precision.

In the commonly used energy region $0.85 \text{ GeV} < E_{\text{CM}} < 1.8 \text{ GeV}$ the new data yields

$$a_\mu(\pi^+\pi^-2\pi^0) = (17.9 \pm 0.1_{\text{stat}} \pm 0.6_{\text{syst}}) \times 10^{-10}, \quad (77)$$

giving a total relative precision of 3.3%.

Furthermore, since the new measurement covers a much larger energy range than available up to now, it is possible to extract the a_μ up to higher energies. In the interval $0.85 \text{ GeV} < E_{\text{CM}} < 3.0 \text{ GeV}$ the value $a_\mu(\pi^+\pi^-2\pi^0) = (21.8 \pm 0.1_{\text{stat}} \pm 0.7_{\text{syst}}) \times 10^{-10}$ is found with a total relative precision of 3.3%.

Before *BABAR*, the latest published value for the a_μ contribution from the complete process $e^+e^- \rightarrow \pi^+\pi^-3\pi^0$ was estimated using isospin relations [109]:

$$a_\mu = (1.29 \pm 0.22 \pm 0.02_{\text{rad}}) \times 10^{-10} \quad (78)$$

in the range $1.019 \text{ GeV} \leq E_{\text{CM}} \leq 1.8 \text{ GeV}$, where the second uncertainty corresponds to a correction of radiative effects. This implies

² The second uncertainty corresponds to a correction of radiative effects.

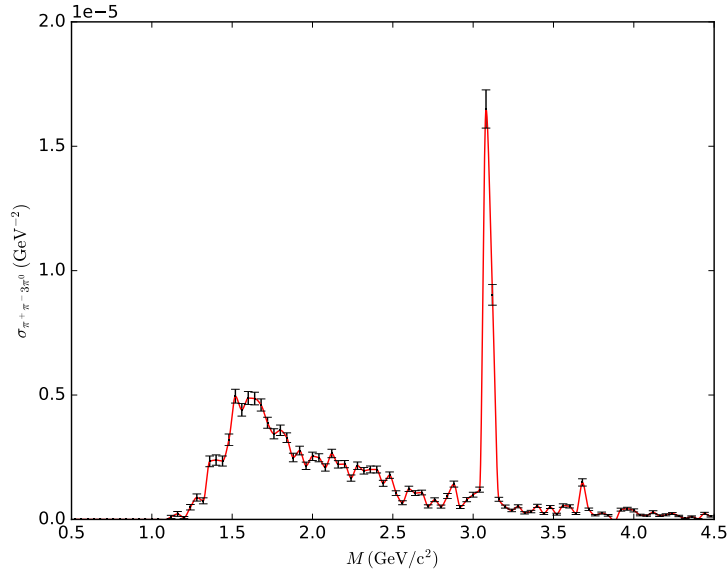


Figure 147: Cubic spline interpolating the cross section $e^+e^- \rightarrow \pi^+\pi^-3\pi^0$.

a total relative precision of 17 % but since it is calculated via isospin relations, a model uncertainty is present. Since the magnitude of the model error cannot be established, this presents an unknown unknown, which cannot be quantified explicitly. Therefore a direct, precise measurement is essential to reliably calculate the a_μ contribution from the channel $e^+e^- \rightarrow \pi^+\pi^-3\pi^0$.

After *BABAR* this contribution – from the data shown in Fig. 147 – is given by

$$a_\mu = (0.67 \pm 0.01_{\text{stat}} \pm 0.17_{\text{syst}}) \times 10^{-10}, \quad (79)$$

where the first uncertainty is of statistical nature and the second is systematic. Due to this new measurement, this channel's contribution to the muon $g-2$ can for the first time be calculated directly, disagreeing with the isospin-estimate above. The negligible size of the cross section at low masses makes the contribution to a_μ in the range $0.85 \text{ GeV} \leq E_{\text{CM}} \leq 1.8 \text{ GeV}$ identical to the value in the above interval. Extending the upper integration limit yields $a_\mu(\pi^+\pi^-3\pi^0) = (1.20 \pm 0.01_{\text{stat}} \pm 0.31_{\text{syst}}) \times 10^{-10}$ for $0.85 \text{ GeV} \leq E_{\text{CM}} \leq 3.0 \text{ GeV}$.

Furthermore, when comparing the $e^+e^- \rightarrow \pi^+\pi^-\pi^+\pi^-\pi^0$ cross sections used as input for the isospin-driven a_μ calculation to the more recent *BABAR* measurement [138], a difference of roughly a factor two is observed. In order to use the new measurement to estimate $a_\mu(\pi^+\pi^-3\pi^0)$ via isospin relations, the $\eta\pi^+\pi^-$ contribution must be subtracted, since the decay $\eta \rightarrow \pi^+\pi^-\pi^0$ is isospin breaking. This gives $a_\mu(\pi^+\pi^-3\pi^0 \text{ excluding } \eta) = (0.36 \pm 0.04) \times 10^{-10}$ [136]. Adding on the contribution to a_μ from the process

$e^+e^- \rightarrow \eta\pi^+\pi^-$ ($a_\mu(\eta\pi^+\pi^-) = (1.15 \pm 0.10) \times 10^{-10}$) [136] weighted with the branching fraction $\mathcal{B}(\eta \rightarrow 3\pi^0) = 0.3268 \pm 0.0023$ [43] yields $a_\mu(\pi^+\pi^-3\pi^0) = (0.74 \pm 0.07) \times 10^{-10}$, in good agreement with the direct calculation, yet also here an unknown model uncertainty is present.

The same routine as outlined above can be applied to compute the contribution to the running of the fine-structure constant α simply by replacing the kernel function K_μ with $1/(1-s/q^2)$ in Eq. 75. After also adjusting the proportionality constant to $1/(4\pi^2\alpha)$, the relation from Sec. 2.8 is recovered:

$$\Delta\alpha_{\text{had}}(q^2) = \frac{1}{4\pi^2\alpha} \int_{s_{\text{min}}}^{\infty} ds \frac{\sqrt{1 - \frac{4m_e^2}{s}}}{1 + \frac{2m_e^2}{s}} \frac{\sigma_{\text{had}}^{(o)}(s)}{1 - \frac{s}{q^2}}. \quad (80)$$

For $q^2 = M_Z^2 c^2 \approx (91 \text{ GeV}/c)^2$ the principal value does not apply since the measured cross sections only cover the energy range below 4.5 GeV, so that the singularity does not arise in the integration.

For the channel $e^+e^- \rightarrow \pi^+\pi^-2\pi^0$ in the energy region $0.85 \text{ GeV} < E_{\text{CM}} < 1.8 \text{ GeV}$ this results in

$$\Delta\alpha(M_Z^2 c^2) = (4.44 \pm 0.02_{\text{stat}} \pm 0.14_{\text{syst}}) \times 10^{-4}, \quad (81)$$

where the first uncertainty is of statistical nature and the second systematic. For $0.85 \text{ GeV} \leq E_{\text{CM}} \leq 3.0 \text{ GeV}$ the result becomes $\Delta\alpha(M_Z^2 c^2) = (6.58 \pm 0.02_{\text{stat}} \pm 0.22_{\text{syst}}) \times 10^{-4}$.

Similarly, for $e^+e^- \rightarrow \pi^+\pi^-3\pi^0$ this yields

$$\Delta\alpha(M_Z^2 c^2) = (0.20 \pm 0.01_{\text{stat}} \pm 0.05_{\text{syst}}) \times 10^{-4} \quad (82)$$

in the range $0.85 \text{ GeV} \leq E_{\text{CM}} \leq 1.8 \text{ GeV}$. For $0.85 \text{ GeV} \leq E_{\text{CM}} \leq 3.0 \text{ GeV}$ the result becomes $\Delta\alpha(M_Z^2 c^2) = (0.52 \pm 0.01_{\text{stat}} \pm 0.13_{\text{syst}}) \times 10^{-4}$.

SUMMARY OF THE CALCULATION OF a_μ AND $\Delta\alpha$

An algorithm was developed to evaluate the integral connection between a measured cross section and a_μ as well as $\Delta\alpha$. The interpolation does not introduce artificial structures (minima/maxima) while simultaneously guaranteeing differentiability, as required by the dispersion relation. As a result, improved values for a_μ and $\Delta\alpha$ are achieved for the channel $e^+e^- \rightarrow \pi^+\pi^-2\pi^0$, closing a long-standing gap in the pursuit of precision. Furthermore, the channel $e^+e^- \rightarrow \pi^+\pi^-3\pi^0$ has now been evaluated for the first time. For both processes, the observables are not only calculated in the standard interval up to $E_{\text{CM}} = 1.8 \text{ GeV}$ but also up to 3.0 GeV.

CONCLUSION

The *BABAR* experiment has resulted in a tremendous wealth of impressive physics results. From CP -violation [212] to the bottomonium ground state η_b [213], it has achieved more insight than could be imagined at its conception as a B Factory. However, the most remarkable property of this experiment is the diversity of physics topics it covers. The detector design and especially the flexibility of the trigger opened up the possibility of performing ISR measurements with high statistics and precision. This resulted in the analysis of many ISR channels, including among others the important $\pi^+\pi^-$ [120] and $\pi^+\pi^-\pi^+\pi^-$ [121] channels. ISR cross section analyses are still ongoing with emphasis on the investigation of heavier final states. Their cross sections carry major importance for the theoretical prediction of the muon $g - 2$, one of the most important tests of the validity of the Standard Model of Particle Physics. Its hadronic contribution needs experimental input and is the leading uncertainty at the moment.

In this work, the cross sections $e^+e^- \rightarrow \pi^+\pi^-2\pi^0$ and $e^+e^- \rightarrow \pi^+\pi^-3\pi^0$ are analyzed with unprecedented precision.

Up to now, the channel $e^+e^- \rightarrow \pi^+\pi^-2\pi^0$ was the leading contributor to the uncertainty of the hadronic part of the muon $g - 2$. Before *BABAR* the world data yielded [137]

$$a_\mu = (16.76 \pm 1.31 \pm 0.20_{\text{rad}}) \times 10^{-10} \quad (83)$$

in the range $1.02 \text{ GeV} \leq E_{\text{CM}} \leq 1.8 \text{ GeV}$, where the second uncertainty corresponds to a correction of radiative effects, implying a total relative precision of 8 %.

After *BABAR* this contribution is given by

$$a_\mu = (17.4 \pm 0.1_{\text{stat}} \pm 0.6_{\text{syst}}) \times 10^{-10} . \quad (84)$$

By this new measurement alone, the relative precision improved by a factor of 2.5, leaving other channels dominating the total uncertainty. While its uncertainty amounted to 28 % [136] of the total uncertainty of the hadronic part of a_μ^{had} , this fraction would be reduced to approximately 12 % assuming the same numbers for the other channels.

Before *BABAR* the contribution from $e^+e^- \rightarrow \pi^+\pi^-3\pi^0$ could only be estimated using isospin relations [137]:

$$a_\mu = (1.29 \pm 0.22 \pm 0.02_{\text{rad}}) \times 10^{-10} \quad (85)$$

in the range $1.019 \text{ GeV} \leq E_{\text{CM}} \leq 1.8 \text{ GeV}$. This implies a total relative precision of 17 % but since it is calculated via isospin relations, a model error of unknown magnitude is present.

After *BABAR* this contribution is given by

$$a_\mu = (0.67 \pm 0.01_{\text{stat}} \pm 0.17_{\text{syst}}) \times 10^{-10}. \quad (86)$$

Due to this new measurement, this channel's contribution to the muon $g - 2$ can for the first time be calculated directly.

In addition to $g - 2$, the influence on the running of the fine-structure constant α can also be extracted from the new data. In the range $0.85 \text{ GeV} \leq E_{\text{CM}} \leq 1.8 \text{ GeV}$ this yields

$$\Delta\alpha(M_Z^2) = (4.44 \pm 0.02_{\text{stat}} \pm 0.14_{\text{syst}}) \times 10^{-4} \quad (87)$$

and

$$\Delta\alpha(M_Z^2) = (0.20 \pm 0.01_{\text{stat}} \pm 0.05_{\text{syst}}) \times 10^{-4} \quad (88)$$

from $e^+e^- \rightarrow \pi^+\pi^-2\pi^0$ and $e^+e^- \rightarrow \pi^+\pi^-3\pi^0$, respectively.

Furthermore, in the $\pi^+\pi^-2\pi^0$ channel previously unobserved resonant substructures are seen, in particular $\rho^+\rho^-$ and $\rho^0 f_0(980)$. The production fraction of $\omega\pi^0$ is extracted, yielding $(32.1 \pm 0.2_{\text{stat}} \pm 2.6_{\text{syst}})\%$ over the full mass range, but is also shown to peak sharply at low energy, decreasing below 10 % already around 1.8 GeV.

Moreover, the first measurement of the branching fraction $J/\psi \rightarrow \pi^+\pi^-2\pi^0$ is achieved, giving

$$\mathcal{B}_{J/\psi \rightarrow 2\pi 2\pi^0} = (4.8 \pm 0.3_{\text{stat}} \pm 0.4_{\text{syst}} \pm 0.1_{\text{input}}) \times 10^{-3}. \quad (89)$$

In the channel $e^+e^- \rightarrow \pi^+\pi^-3\pi^0$ it is shown that the intermediate resonances $\eta\pi^+\pi^-$ and $\omega 2\pi^0$ dominate only at low energies $\lesssim 2 \text{ GeV}$. At higher energies, it is seen that more than half of the $\pi^+\pi^-3\pi^0$ events are produced via other production mechanisms, a previously unexpected result.

Additionally, the first measurement of the branching fraction $J/\psi \rightarrow \pi^+\pi^-3\pi^0$ is achieved:

$$\mathcal{B}_{J/\psi \rightarrow 2\pi 3\pi^0} = (2.7 \pm 0.1_{\text{stat}} \pm 0.8_{\text{syst}} \pm 0.1_{\text{input}}) \times 10^{-2}, \quad (90)$$

giving an interesting comparison to its isospin-partner $e^+e^- \rightarrow \pi^+\pi^-\pi^+\pi^-\pi^0$, which has a branching fraction [43] of $\mathcal{B} = (4.1 \pm 0.3) \times 10^{-2}$.

These results, especially the new values for $g_\mu - 2$, allow improved comparisons between Standard Model predictions and direct measurements. Therefore they may facilitate the means necessary to discern whether a deviation from theory has been found, which would hint at modifications to the Standard Model.

Furthermore, the Monte Carlo generators of both channels can now be improved by adapting them to the measured internal distributions (momentum, angle etc.) and using the measured resonance fractions. This is particularly important for the channel $e^+e^- \rightarrow \pi^+\pi^-3\pi^0$ where no generator of the full process exists, since it has never been measured in detail.

KINEMATIC CONSIDERATIONS

A.1 EQUIVALENCE $1 - \frac{s'}{s} = \frac{2E_\gamma^*}{\sqrt{s}}$

A short kinematic calculation to prove $1 - \frac{s'}{s} = \frac{2E_\gamma^*}{\sqrt{s}}$.

$$M := \sqrt{s} \quad (91)$$

$$m := \sqrt{s'} \quad (92)$$

$$\begin{pmatrix} M \\ \vec{0} \end{pmatrix} = \begin{pmatrix} E_\gamma^* \\ \vec{p}_\gamma^* \end{pmatrix} + \begin{pmatrix} \sqrt{m^2 + p_m^2} \\ \vec{p}_m \end{pmatrix} \quad (93)$$

$$\Rightarrow M^2 = \left(E_\gamma^* + \sqrt{m^2 + p_m^2} \right)^2 - \underbrace{(\vec{p}_\gamma^* + \vec{p}_m)^2}_{=0} \quad (94)$$

$$\Rightarrow M^2 = E_\gamma^{*2} + m^2 + \underbrace{p_m^2}_{=E_\gamma^{*2}} + 2E_\gamma^* \cdot \underbrace{\sqrt{m^2 + p_m^2}}_{=M-E_\gamma^*} \quad (95)$$

$$\Rightarrow M^2 = m^2 + 2ME_\gamma^* \quad (96)$$

$$\Rightarrow s = s' + 2\sqrt{s}E_\gamma^* \quad (97)$$

$$\Leftrightarrow 1 - \frac{s'}{s} = \frac{2E_\gamma^*}{\sqrt{s}} \quad \square \quad (98)$$

A.2 EQUIVALENCE OF RESTRICTING THE ISR PHOTON ENERGY AND THE INVARIANT HADRONIC MASS

In this section it is shown that restricting the energy of the ISR photon (e.g. $E_{\gamma\text{ISR}}^* > 3 \text{ GeV}$ ¹ or $E_{\gamma\text{ISR}}^{\text{lab}} > 3 \text{ GeV}$) is equivalent to restricting the invariant mass of the hadronic system.

We see immediately from App. A.1, that in the center-of-mass system, with a collider energy of \sqrt{s} , producing a hadronic system with invariant mass $m = \sqrt{s'}$ and an additional photon with energy E_γ^* leads to:

$$E_\gamma^* = \frac{1}{2} \left(\sqrt{s} - \frac{m^2}{\sqrt{s}} \right). \quad (99)$$

For $\sqrt{s} = 10.58 \text{ GeV}$ and m between 0 and $4.5 \text{ GeV}/c^2$, we get $4.33 \text{ GeV} < E_\gamma^* < 5.29 \text{ GeV}$, well within the preselection-range $E_\gamma^* > 3 \text{ GeV}$. Hence the preselection does not limit the range of the measurement.

Restricting the laboratory frame energy of the ISR photon also leads to a limited range of the CM-energy of the ISR photon. For

¹ As usual, variables with an asterisk x^* are set in the center-of-mass system.

this calculation, the Lorentz transformation between CM and laboratory system due to the asymmetric beam energies and the angular range of the detector must be taken into account.

At *BABAR*, the magnitude of the Lorentz boost is given by $\beta\gamma = 0.56$ [162]. The fiducial volume of the detector is restricted in the laboratory polar angle to $0.35 \text{ rad} \leq \theta \leq 2.4 \text{ rad}$. It is useful to decompose the laboratory momentum of the ISR photon into a component parallel (\parallel) and a component orthogonal (\perp) to the boost direction:

$$\vec{p} = \begin{pmatrix} p_{\parallel} \\ p_{\perp} \end{pmatrix} = \begin{pmatrix} |p| \cos \theta \\ |p| \sin \theta \end{pmatrix}. \quad (100)$$

The Lorentz boost only acts on the parallel component, hence the orthogonal component is conserved: $p_{\perp}^* = p_{\perp}$. For the magnitude of the photon momentum (or energy) we have [43]

$$\begin{aligned} |p^*| &= \gamma|p| - \gamma\beta p_{\parallel} \\ &= \gamma|p|(1 - \beta \cos \theta) \end{aligned} \quad (101)$$

Thus, restricting the laboratory ISR photon energy to $E_{\gamma\text{ISR}}^{\text{lab}} > 3 \text{ GeV}$ leads to the following limits on the CM energy/momentum of the ISR photon:

$$\begin{aligned} E_{\gamma\text{ISR}}^* &> 4.67 \text{ GeV} && \text{for } \theta = 2.4 \text{ rad}, \\ E_{\gamma\text{ISR}}^* &> 4.33 \text{ GeV} && \forall \theta > 2.13 \text{ rad}. \end{aligned} \quad (102)$$

This shows that imposing $E_{\gamma\text{ISR}}^{\text{lab}} > 3 \text{ GeV}$ translates to a slightly tighter restriction on the CM energy of the ISR photon than limiting the range of the invariant hadronic mass to values below $4.5 \text{ GeV}/c^2$, but with an angular dependence. Events with an ISR photon of laboratory energy above 3 GeV traveling in the extreme backward direction $\theta > 2.13 \text{ rad}$ are exceptionally rare. In both data and signal simulation, it was studied that only a relative fraction of $\mathcal{O}(10^{-4})$ of either sample is affected. This effect is negligible and furthermore cancels out since the same selection is applied to data and simulation.

INTERMEDIATE CALCULATIONS IN THE DERIVATION OF a_e

B.1 REPLACING THE VACUUM POLARIZATION TENSOR BY THE AMPLITUDE

To be shown:

$$\begin{aligned}
& \bar{v}(p)(-ie)\gamma^\mu u(k) \frac{-i\mathcal{G}^{\mu\nu}}{(p+k)^2 + i\varepsilon} (i\Pi^{\nu\rho}(p+k)) \\
& \cdot \frac{-i\mathcal{G}^{\rho\sigma}}{(p+k)^2 + i\varepsilon} \bar{u}(k)(-ie)\gamma^\sigma v(p) \\
= & \frac{-ie^2\Pi_{\text{ren}}(q^2)}{q^2 + i\varepsilon} \bar{v}(p)\gamma^\mu u(k)\bar{u}(k)\gamma_\mu v(p) \quad (103)
\end{aligned}$$

with $q = p + k$, using the Dirac equation corollary

$$\bar{v}(p)\not{q}u(k) = 0,$$

as well as the relation between vacuum polarization tensor $\Pi^{\nu\rho}$ and renormalized vacuum polarization amplitude Π_{ren}

$$\Pi^{\nu\rho}(q) \equiv -(q^2 g^{\nu\rho} - q^\nu q^\rho) \cdot \Pi_{\text{ren}}(q^2).$$

$$\begin{aligned}
& \bar{v}(p)(-ie)\gamma^\mu u(k) \frac{-i\mathcal{G}^{\mu\nu}}{(p+k)^2 + i\varepsilon} (i\Pi^{\nu\rho}(p+k)) \\
& \cdot \frac{-i\mathcal{G}^{\rho\sigma}}{(p+k)^2 + i\varepsilon} \bar{u}(k)(-ie)\gamma^\sigma v(p) \\
= & ie^2 \bar{v}(p)\gamma^\mu u(k) \frac{\mathcal{G}^{\mu\nu}}{q^2 + i\varepsilon} \Pi^{\nu\rho}(q) \frac{\mathcal{G}^{\rho\sigma}}{q^2 + i\varepsilon} \bar{u}(k)\gamma^\sigma v(p) \\
= & -ie^2 \bar{v}(p)\gamma^\mu u(k) \frac{\mathcal{G}^{\mu\nu}}{q^2 + i\varepsilon} (q^2 g^{\nu\rho} - q^\nu q^\rho) \\
& \cdot \Pi_{\text{ren}}(q^2) \frac{\mathcal{G}^{\rho\sigma}}{q^2 + i\varepsilon} \bar{u}(k)\gamma^\sigma v(p) \\
= & \frac{-ie^2\Pi_{\text{ren}}(q^2)}{q^2 + i\varepsilon} \bar{v}(p)\gamma^\mu u(k) \left(g_{\mu\sigma} - \frac{1}{q^2 + i\varepsilon} q_\mu q_\sigma \right) \bar{u}(k)\gamma^\sigma v(p) \\
= & \frac{-ie^2\Pi_{\text{ren}}(q^2)}{q^2 + i\varepsilon} \bar{v}(p)\gamma^\mu u(k)\bar{u}(k)\gamma_\mu v(p) \quad \square \quad (104)
\end{aligned}$$

B.2 EXTRACTING THE KINEMATIC FACTOR $s + 2m^2$

To be shown:

$$(\bar{v}(p)\gamma^\mu u(k)) (\bar{u}(k)\gamma_\mu v(p)) = -s \left(1 + \frac{2m^2}{s}\right)$$

using the completeness relations

$$\sum_s u^s(k)\bar{u}^s(k) = \not{k} + m, \quad \sum_s v^s(p)\bar{v}^s(p) = \not{p} - m$$

and

$$s \equiv (p+k)^2 = p^2 + k^2 + 2p \cdot k = 2m^2 + 2p \cdot k.$$

$$\begin{aligned} & (\bar{v}(p)\gamma^\mu u(k)) (\bar{u}(k)\gamma_\mu v(p)) = \\ &= \frac{1}{4} \sum_{s,s'} \bar{v}_a^{s'}(p) \gamma_{ab}^\mu u_b^s(k) \bar{u}_c^s(k) \gamma_{\mu cd} v_d^{s'}(k) \\ &= \frac{1}{4} (\not{p} - m)_{da} \gamma_{ab}^\mu (\not{k} + m)_{bc} \gamma_{\mu cd} = \\ &= \frac{1}{4} \text{Tr} [(\not{p} - m) \gamma^\mu (\not{k} + m) \gamma_\mu] = \\ &= \frac{1}{4} \text{Tr} [\gamma_\rho p^\rho \gamma^\mu \gamma^\nu k_\nu \gamma_\mu] - \frac{m^2}{4} \text{Tr} [\gamma^\mu \gamma_\mu] \\ &\quad - \frac{m}{4} \underbrace{\text{Tr} [\gamma^\mu \gamma^\nu k_\nu \gamma_\mu]}_{=0} + \frac{m}{4} \underbrace{\text{Tr} [\gamma_\rho p^\rho \gamma^\mu \gamma_\mu]}_{=0} \\ &= \frac{1}{4} \text{Tr} [p^\rho k_\nu \gamma_\rho \gamma^\mu \gamma^\nu \gamma_\mu] - 4m^2 \\ &= -4m^2 + \frac{1}{4} \text{Tr} [p^\rho k_\nu \gamma_\rho (2g^{\mu\nu} - \gamma^\nu \gamma^\mu) \gamma_\mu] \\ &= -4m^2 + \frac{1}{2} \text{Tr} [p^\rho k_\nu \gamma_\rho \gamma^\nu] - \text{Tr} [p^\rho k_\nu \gamma_\rho \gamma^\nu] \\ &= -4m^2 - 2p^\rho k_\nu g_\rho^\nu \\ &= -4m^2 - 2p \cdot k \\ &= -s \left(1 + \frac{2m^2}{s}\right) \quad \square \end{aligned} \tag{105}$$

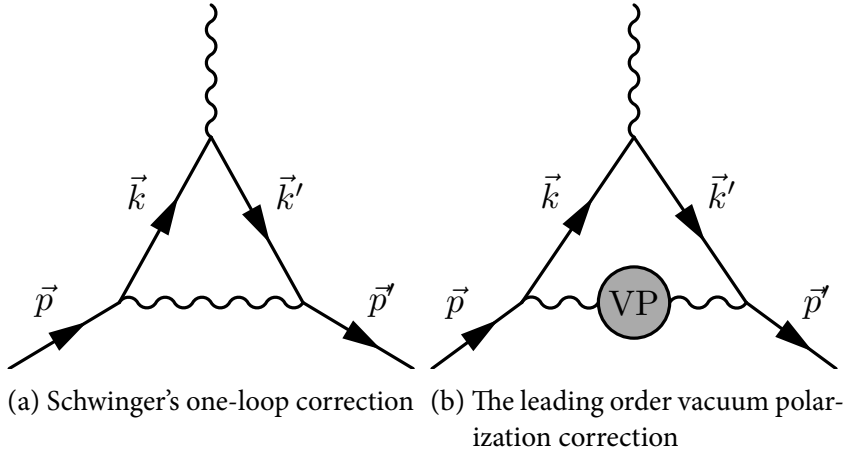


Figure 148.: Feynman diagrams of the considered processes.

B.3 INCLUDING THE VACUUM POLARIZATION AMPLITUDE INTO THE PHOTON PROPAGATOR

To calculate the hadronic contribution to $g - 2$, the vacuum polarization amplitude needs to be included in the internal photon propagator. In this section, it is shown that this is achieved by modifying¹ the photon propagator:

$$\frac{-i g_{\mu\nu}}{(k-p)^2 + i\varepsilon} \rightarrow \frac{i g_{\mu\nu}}{(k-p)^2 + i\varepsilon} \Pi_{\text{ren}}((k-p)^2). \quad (106)$$

Schwinger's one-loop contribution (Fig. 148a) is given by [90]

$$\begin{aligned} \bar{u}(p') \delta\Gamma^\mu u(p) &= \\ &= \int \frac{d^4k}{(2\pi)^4} \frac{-i g_{\nu\rho}}{(k-p)^2 + i\varepsilon} \bar{u}(p') (-ie\gamma^\nu) \\ &\quad \cdot \frac{i(\not{k}' + m)}{k'^2 - m^2 + i\varepsilon} \gamma^\mu \frac{i(\not{k} + m)}{k^2 - m^2 + i\varepsilon} (-ie\gamma^\rho) u(p). \end{aligned} \quad (107)$$

When including vacuum polarization as shown in Fig. 148b this becomes

¹ This replacement is commonly used, e.g. in Ref. [147], but often without justification.

$$\begin{aligned}
& \bar{u}(p') \delta^{(2)} \Gamma^\mu u(p) = \\
& = \int \frac{d^4 k}{(2\pi)^4} \frac{-i g_{\nu\sigma}}{(k-p)^2 + i\varepsilon} (i \Pi^{\sigma\tau}(k-p)) \cdot \frac{-i g_{\tau\rho}}{(k-p)^2 + i\varepsilon} \\
& \quad \cdot \bar{u}(p') (-i e \gamma^\nu) \frac{i(\not{k}' + m)}{k'^2 - m^2 + i\varepsilon} \gamma^\mu \frac{i(\not{k} + m)}{k^2 - m^2 + i\varepsilon} (-i e \gamma^\rho) u(p) \\
& = \int \frac{d^4 k}{(2\pi)^4} i \Pi_{\text{ren}}((k-p)^2) \frac{g_{\nu\sigma}}{(k-p)^2 + i\varepsilon} \\
& \quad \cdot ((k-p)^2 g^{\sigma\tau} - (k-p)^\sigma (k-p)^\tau) \frac{g_{\tau\rho}}{(k-p)^2 + i\varepsilon} \\
& \quad \cdot \bar{u}(p') (-i e \gamma^\nu) \frac{i(\not{k}' + m)}{k'^2 - m^2 + i\varepsilon} \gamma^\mu \frac{i(\not{k} + m)}{k^2 - m^2 + i\varepsilon} (-i e \gamma^\rho) u(p) \\
& = \int \frac{d^4 k}{(2\pi)^4} i \Pi_{\text{ren}}((k-p)^2) \frac{(k-p)^2 g_{\nu\rho}}{((k-p)^2 + i\varepsilon)^2} \\
& \quad \cdot \bar{u}(p') (-i e \gamma^\nu) \frac{i(\not{k}' + m)}{k'^2 - m^2 + i\varepsilon} \gamma^\mu \frac{i(\not{k} + m)}{k^2 - m^2 + i\varepsilon} (-i e \gamma^\rho) u(p) \\
& - \int \frac{d^4 k}{(2\pi)^4} i \Pi_{\text{ren}}((k-p)^2) \frac{(k-p)_\nu (k-p)_\rho}{((k-p)^2 + i\varepsilon)^2} \\
& \quad \cdot \bar{u}(p') (-i e \gamma^\nu) \frac{i(\not{k}' + m)}{k'^2 - m^2 + i\varepsilon} \gamma^\mu \frac{i(\not{k} + m)}{k^2 - m^2 + i\varepsilon} (-i e \gamma^\rho) u(p) \quad (108)
\end{aligned}$$

The second integral might not vanish but reduces to

$$i e^2 \int \frac{d^4 k}{(2\pi)^4} \bar{u}(p') \gamma^\mu \frac{\Pi_{\text{ren}}((k-p)^2)}{((k-p)^2 + i\varepsilon)^2} u(p). \quad (109)$$

Due to the decomposition into terms proportional to $\sigma^{\mu\nu} q_\nu$ for F_2 and terms proportional to γ^μ for F_1 , this part is absorbed into F_1 . Since $g-2$ is determined by $F_2(o)$, the above term does not contribute. Hence we can conclude for the determination of $g-2$

$$\begin{aligned}
& \bar{u}(p') \delta^{(2)} \Gamma_{g-2}^\mu u(p) = \quad (110) \\
& = \int \frac{d^4 k}{(2\pi)^4} \frac{i g_{\nu\rho} \Pi_{\text{ren}}((k-p)^2)}{(k-p)^2 + i\varepsilon} \\
& \quad \cdot \bar{u}(p') (-i e \gamma^\nu) \frac{i(\not{k}' + m)}{k'^2 - m^2 + i\varepsilon} \gamma^\mu \frac{i(\not{k} + m)}{k^2 - m^2 + i\varepsilon} (-i e \gamma^\rho) u(p).
\end{aligned}$$

SPECIFICS OF THE ANALYSES

C.1 CALCULATION OF UNCERTAINTIES IN BACKGROUND-REDUCED PROPORTIONS

When calculating the ratio of events before and after selection, usually a binomial error [173] can be used. Here it is derived how this changes when background subtraction is also performed. Since we are only interested in the uncertainty introduced by the selection, the original event numbers are considered to be fixed (without uncertainty). For simplicity only one background source is considered, but this may easily be generalized to any number. N_1 (N_2) is the total number of data (background) events, n_1 (n_2) the number after selection. We are interested in the ratio r :

$$r := \frac{n_1 - n_2}{N_1 - N_2} = \frac{n_1}{N_1 - N_2} + \frac{n_2}{N_2 - N_1} =: r_1 + r_2 \quad (111)$$

$$\delta r = \sqrt{(\delta r_1)^2 + (\delta r_2)^2} \quad (112)$$

$$r_i = \frac{n}{N - M} = \frac{n}{N} \cdot \frac{N}{N - M} \quad (113)$$

with $n := n_i$, $N := N_i$, $M := N_{\neq i}$

$$\begin{aligned} (\delta r_i)^2 &= \left(\frac{N}{N - M} \right)^2 \cdot \underbrace{\left(\delta \left(\frac{n}{N} \right) \right)^2}_{\text{binomial error}} + \underbrace{\left(\frac{n}{N} \right)^2 \cdot \left(\delta \left(\frac{N}{N - M} \right) \right)^2}_{=0} \\ &= \left(\frac{N}{N - M} \right)^2 \cdot \frac{n}{N} \left(1 - \frac{n}{N} \right) / N \end{aligned} \quad (114)$$

$$q_i := \frac{n_i}{N_i}$$

$$\Rightarrow \delta r = \frac{\sqrt{N_1 \cdot q_1 \cdot (1 - q_1) + N_2 \cdot q_2 \cdot (1 - q_2)}}{N_1 - N_2} \quad (115)$$

As a consistency check, it is obvious that we regain the binomial uncertainty for the background-free case $n_2 = 0$, $N_2 = 0$. In the above calculation, the normal (Gaussian) approximation is used for the binomial error interval. The same derivation can be carried out using a different confidence interval, such as the Wilson score interval [214] or the Agresti-Coull interval [215]. Extensive reviews of their properties can be found in Refs. [173, 216].

C.2 μ -PID CORRECTION

In Sec. 5.7.2 it is outlined that the Muon-background rejected by the combined μ -veto is slightly too small since the Muon selector mu-Micro does not possess perfect efficiency. Due to this inefficiency, with a probability of $p_\mu \approx 2.25\%$, a muon event is mistakenly not rejected. But as the relative fraction of muon events in data is highly mass dependent, the inefficiency-correction is as well. Assuming the simple case in which only the background in question pollutes the data sample, two relative fractions of events make up the data sample: the signal fraction f_s and the background fraction f_b . They satisfy the equality $f_s + f_b = 1$. Hence in order to correct the extracted number of events, the amount of background to be subtracted must be scaled up. Technically this is facilitated by scaling the remaining data distribution by

$$s = \frac{1 - c \cdot f_b}{f_s} = \frac{1 - c \cdot (1 - f_s)}{f_s}, \quad (116)$$

where c is the constant inefficiency correction factor $1 + \frac{p_\mu}{1 - p_\mu} \approx 1.023$ to scale the rejected background up by $\sim 2.3\%$. The signal fraction is extracted from the fit shown in Fig. 53. It is important to note that the width of the fitted curve ($\sigma \approx 14$ MeV) is smaller than the bin width (20 MeV) of the cross section to which the correction is applied. Therefore the correction has to be calculated from the mean signal fraction in each bin. Since the distribution is modeled by a Gaussian, an error function (from Ref. [217]) is employed to facilitate the averaging. This correction is applied within $\pm 3\sigma$ of the μ -peak, as its effect is negligible outside of this range. The result of this procedure is shown in Fig. 96.

C.3 ADDITIONAL PLOTS ON THE CONTINUUM SUBTRACTION FROM THE FINAL STATE $\pi^+\pi^-2\pi^0\gamma$

In this section, the plots of the continuum background determination in the $\chi_{4\pi}^2$ sideband region are shown. As mentioned in Sec. 7.2.1, the sideband region gives a significantly different result for the scaling function than the signal region, hence the sideband region cannot be used to increase the statistics of the fit of the scaling function. Figure 149 shows the $M_{\gamma\gamma}$ distributions in the full mass range, while Fig. 150 shows it in mass slices. The resulting scale function is seen in Fig. 151, giving a considerably different result than in the signal region (see Fig. 92).

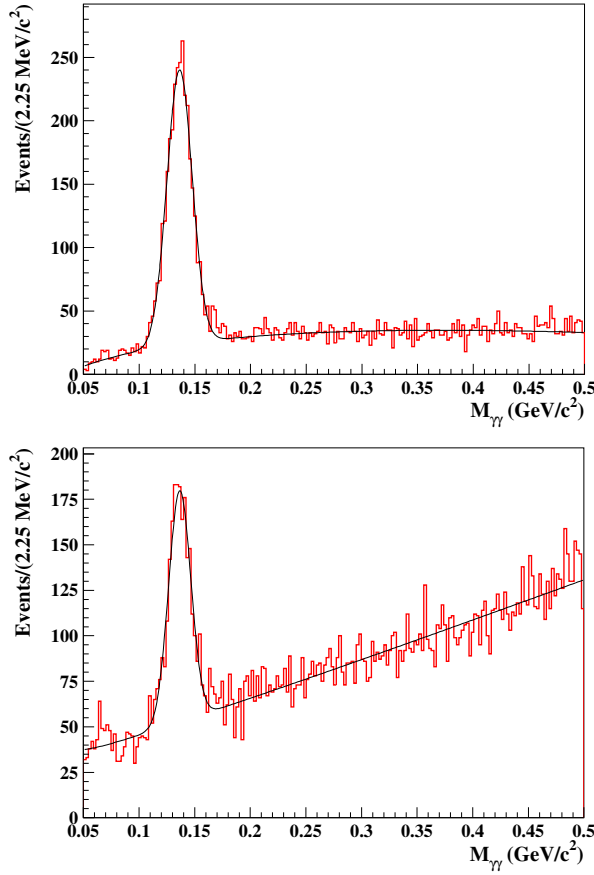


Figure 149.: $\chi_{4\pi}^2$ sideband region: Distributions of the invariant $\gamma_{\text{ISR}}\gamma$ mass for uds MC (top) and data (bottom). The peak at low masses in data is most likely due to processes with additional NLO radiation.

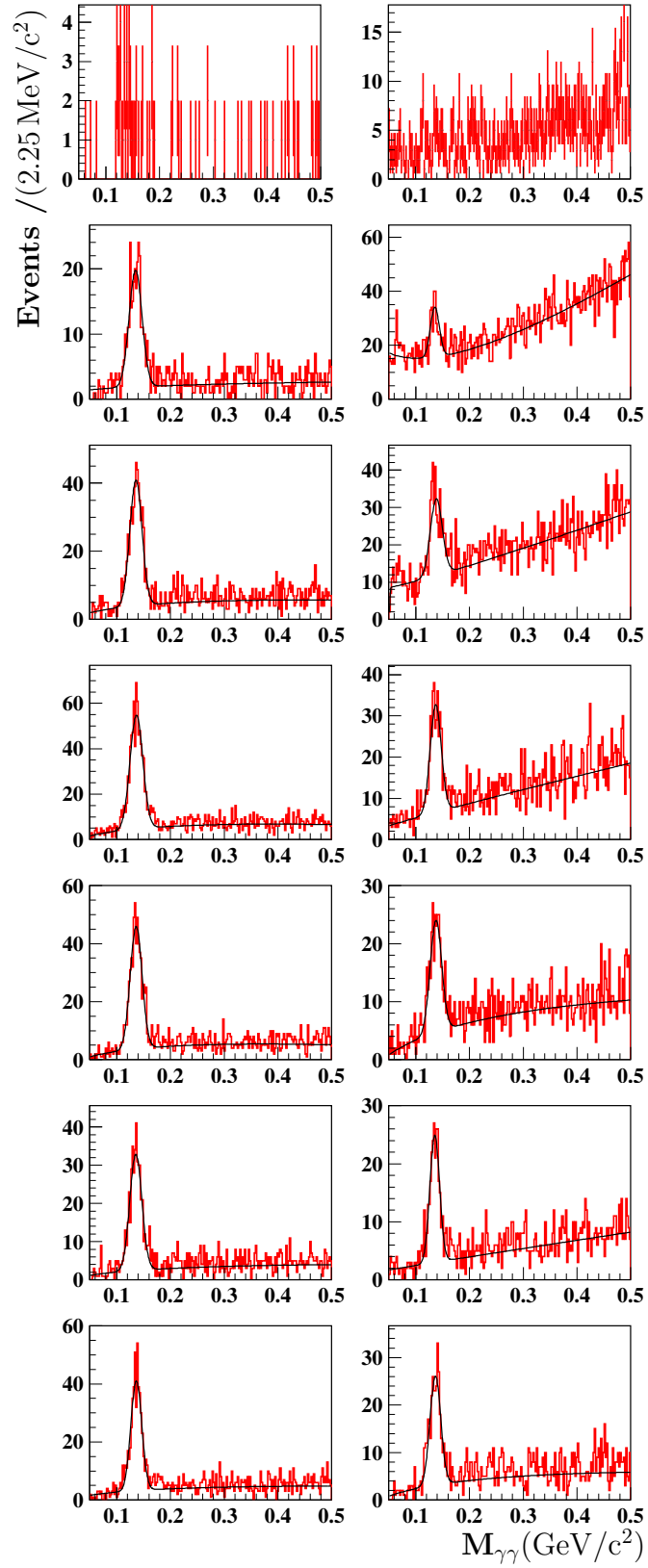


Figure 150.: $\chi_{4\pi}^2$ sideband region: Distributions of the invariant $\gamma_{\text{ISR}}\gamma$ mass for uds MC (left panels) and data (right panels). Mass ranges from top to bottom: $M_{4\pi} < 1.2 \text{ GeV}/c^2$, $1.2 \text{ GeV}/c^2 < M_{4\pi} < 1.7 \text{ GeV}/c^2$, ..., $3.2 \text{ GeV}/c^2 < M_{4\pi} < 3.7 \text{ GeV}/c^2$, $M_{4\pi} > 3.7 \text{ GeV}/c^2$.

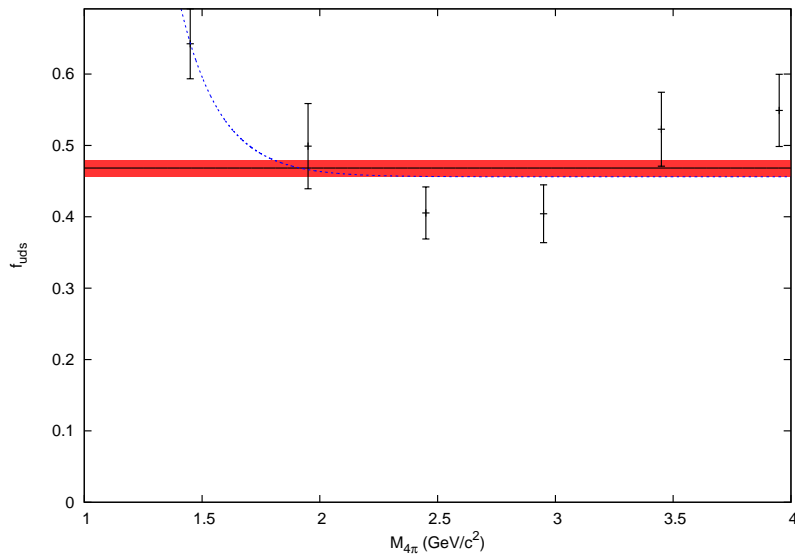


Figure 151.: $\chi_{4\pi}^2$ sideband region: Evolution of the uds scaling factor as a function of the corresponding $M_{4\pi}$ slices. The black line marks the global scaling factor with its 1σ -uncertainties in red, while the dashed blue line represents the fit of an exponential function plus a constant.

C.4 EFFICIENCY CORRECTIONS

C.4.1 Tracking

The data-simulation efficiency difference in detecting charged tracks has been studied in the *BABAR* analysis of the channel $e^+e^- \rightarrow \pi^+\pi^-\pi^+\pi^-\gamma_{\text{ISR}}$ [162, 218]. The results of this previous ISR tracking efficiency study can be used here since its final state has a very similar event topology. It was found that the general tracking inefficiency difference is

$$\Delta\eta_{\text{no overlap}} = (0.38 \pm 0.08_{\text{stat}} \pm 0.34_{\text{syst}})\% . \quad (117)$$

Furthermore an inefficiency is calculated including the effect of tracks overlapping in the detector, which leads to difficulty distinguishing between the signals of the tracks:

$$\Delta\eta_{\text{incl. overlap}} = (0.75 \pm 0.08_{\text{stat}} \pm 0.39_{\text{syst}})\% . \quad (118)$$

Since the study was carried out for the 4-charged-track case of $e^+e^- \rightarrow \pi^+\pi^-\pi^+\pi^-\gamma_{\text{ISR}}$, the probability of track overlap is considerably higher than in the 2-charged-track case of this analysis. More specifically, we have to consider the number of combinations for overlap of oppositely charged tracks, since no difference between data and simulation is observed for overlap of equally charged tracks. In the 4-charged-track case there are 4 possible combinations of oppositely charged tracks, while in the 2-track case there is obviously only one combination. Thus the effective inefficiency difference for the 2-track case is calculated as

$$\begin{aligned} \Delta\eta_{\text{eff}}(\pi^+\pi^-\pi^0) &= \Delta\eta_{\text{no overlap}} + \frac{1}{4} \cdot (\Delta\eta_{\text{incl. overlap}} - \Delta\eta_{\text{no overlap}}) \\ &= (0.47 \pm 0.08_{\text{stat}} \pm 0.39_{\text{syst}})\% \end{aligned} \quad (119)$$

per track. The total uncertainty of this inefficiency difference is included in the systematics of the cross section.

C.4.2 γ Efficiency Correction

The difference in photon efficiency between data and simulation has been studied specifically for the ISR case [121] and the subsequent corrections have been calculated. This comparison shows that globally the efficiency in MC is overestimated. It is analyzed as a function of the ISR photon's polar angle θ and the result can be studied in Fig. 152. These corrections are applied to each event in signal MC during the efficiency calculation. From Fig. 153 it is apparent that the angular dependence translates into a flat correction in the mass of the hadrons. When fitting a constant to the

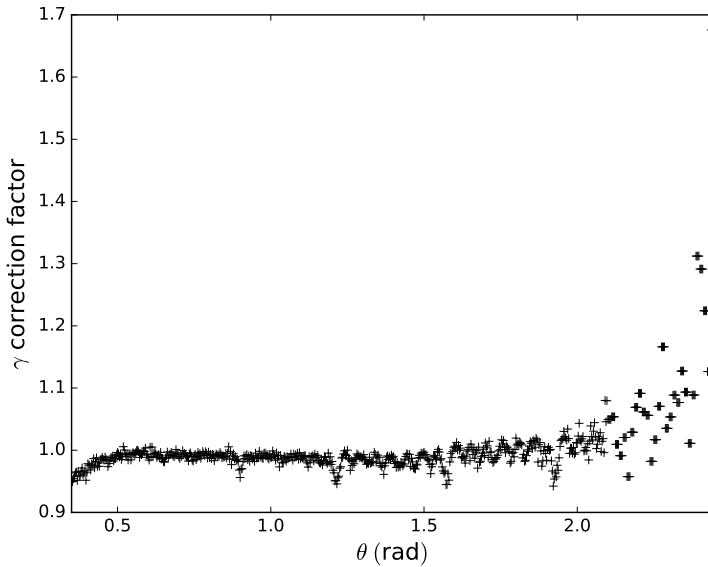


Figure 152.: The γ correction as a function of the polar angle θ .

distribution in Fig. 153, a global correction factor of 0.9878 ± 0.0017 is obtained. Therefore $(1.22 \pm 0.17)\%$ change in the cross section is expected, as can be observed in the corrected efficiency plot in Fig. 154.

C.4.3 π^0 Efficiency Correction

The π^0 efficiency difference between data and simulation had already been investigated using the channel $e^+e^- \rightarrow \omega\pi^0$. It was employed for the *BABAR* measurement of the ISR cross section $e^+e^- \rightarrow K^+K^-2\pi^0$ [219]. In this efficiency analysis, the number of events in the ω peak is studied in process $e^+e^- \rightarrow \omega\pi^0\gamma \rightarrow \pi^+\pi^-2\pi^0\gamma$.

To facilitate suitable samples in data and $e^+e^- \rightarrow \pi^+\pi^-2\pi^0\gamma$ signal simulation, events with two charged tracks and at least three photons are selected (the photon with the highest energy is assumed to be the ISR photon). Since only three photons are required, one π^0 may not have been detected, hence could be missing. The detected π^0 is required to be from the ω decay by selecting only events where the $\pi^+\pi^-\pi^0$ invariant mass is close to the mass of the ω resonance. All events must be accepted by a kinematic fit in the hypothesis $e^+e^- \rightarrow \pi^+\pi^-2\pi^0\gamma$, where only two constraints are imposed: the reconstructed photon pair is required to have the nominal π^0 mass and the missing particle must also have the nominal π^0 mass. No energy-momentum requirement is imposed in this kinematic fit.

The efficiency is determined by fitting the ω peak in two samples. One sample consists of events which are accepted by the 6-constraint (6C) kinematic fit in the hypothesis $e^+e^- \rightarrow \pi^+\pi^-2\pi^0\gamma$

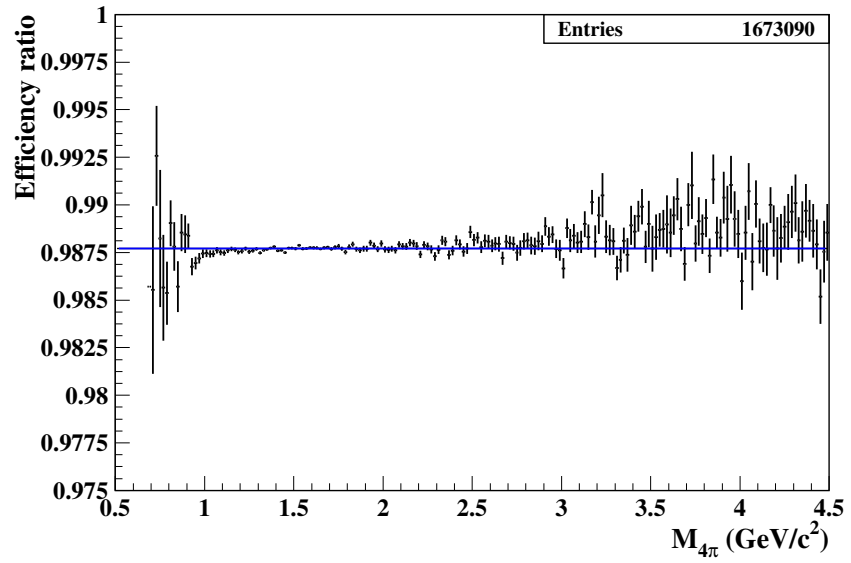


Figure 153.: Effect of the γ correction as a function of $M_{4\pi}$:
 $\mathcal{E}_{\text{corr}}/\mathcal{E}_{\text{uncorr}}$.

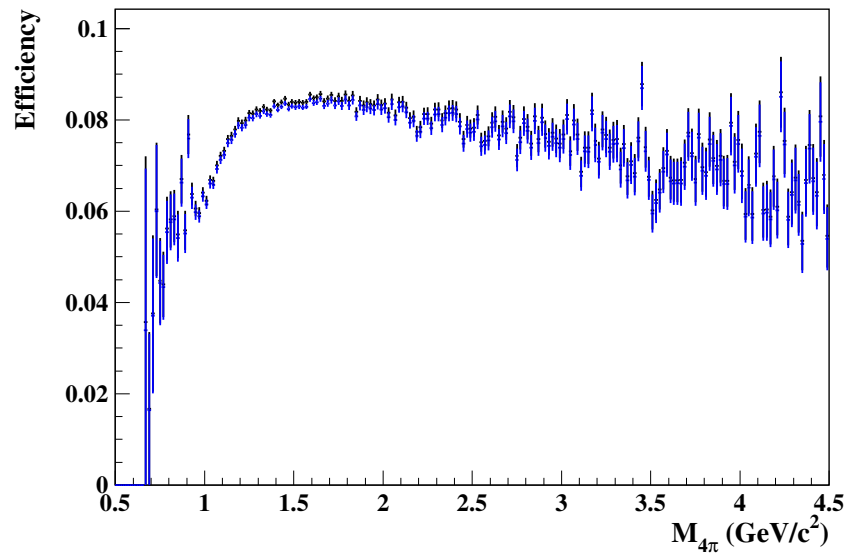


Figure 154.: Total efficiency without (black) and with (blue) γ correction as a function of $M_{4\pi}$.

(also used in the cross section analysis), which requires five photons and imposes energy-momentum conservation as well as the π^0 mass for both photon pairs. The other sample consists of the events not selected by the 6C kinematic fit. The ω peak is then fitted in both samples. The ratio of the ω yield of the sample selected in the 6C kinematic fit divided by the sum of both yields determines the π^0 efficiency. This method is used on data and simulation, so that their relative difference can be used to determine the correction needed in simulation.

Since the efficiency analysis was performed also using the case of neutral pions in ISR production, also employing an energy-momentum constrained kinematic fit, the result can be applied here:

$$\frac{\varepsilon_{\text{data}}}{\varepsilon_{\text{MC}}} - 1 = -(3.0 \pm 1.0)\% \quad (120)$$

per π^0 , where ε is the respective efficiency. Systematic studies were performed, confirming this result over the full range of π^0 momenta and χ_{6C}^2 requirements. For the two channels studied in this work, this results in the following corrections:

- $e^+e^- \rightarrow \pi^+\pi^-2\pi^0\gamma$: $(-6.0 \pm 2.0)\%$,
- $e^+e^- \rightarrow \pi^+\pi^-3\pi^0\gamma$: $(-9.0 \pm 3.0)\%$.

These values are used to correct for data-MC differences and their uncertainties contribute to the total uncertainties.

C.5 $e^+e^- \rightarrow \pi^+\pi^-\pi^0$ CROSS SECTION TABLE

Table 13.: The measured $e^+e^- \rightarrow \pi^+\pi^-\pi^0$ cross section. σ is the *dressed* (including VP) and $\sigma^{(o)}$ the *undressed* (without VP) cross section, each with the corresponding statistical and systematic uncertainties.

$E_{CM}(\text{GeV})$	$\sigma(\text{nb})$	$\sigma^{(o)}(\text{nb})$
0.850	$0.053 \pm 0.116 \pm 0.091$	$0.050 \pm 0.111 \pm 0.087$
0.870	$0.243 \pm 0.077 \pm 0.100$	$0.232 \pm 0.073 \pm 0.096$
0.890	$0.234 \pm 0.124 \pm 0.109$	$0.224 \pm 0.118 \pm 0.105$
0.910	$0.310 \pm 0.076 \pm 0.119$	$0.298 \pm 0.073 \pm 0.114$
0.930	$0.983 \pm 0.164 \pm 0.131$	$0.947 \pm 0.157 \pm 0.126$
0.950	$2.460 \pm 0.233 \pm 0.155$	$2.376 \pm 0.225 \pm 0.149$
0.970	$3.979 \pm 0.312 \pm 0.187$	$3.860 \pm 0.302 \pm 0.182$
0.990	$4.861 \pm 0.324 \pm 0.211$	$4.753 \pm 0.317 \pm 0.206$
1.010	$6.322 \pm 0.383 \pm 0.248$	$6.414 \pm 0.388 \pm 0.252$
1.030	$8.092 \pm 0.398 \pm 0.295$	$7.429 \pm 0.366 \pm 0.271$
1.050	$9.846 \pm 0.417 \pm 0.343$	$9.321 \pm 0.395 \pm 0.325$
1.070	$10.063 \pm 0.421 \pm 0.354$	$9.593 \pm 0.402 \pm 0.337$
1.090	$12.081 \pm 0.444 \pm 0.410$	$11.558 \pm 0.425 \pm 0.392$
1.110	$12.621 \pm 0.447 \pm 0.428$	$12.102 \pm 0.428 \pm 0.410$
1.130	$14.023 \pm 0.471 \pm 0.469$	$13.467 \pm 0.453 \pm 0.450$
1.150	$15.256 \pm 0.484 \pm 0.505$	$14.669 \pm 0.465 \pm 0.486$
1.170	$16.388 \pm 0.485 \pm 0.539$	$15.772 \pm 0.466 \pm 0.519$
1.190	$17.327 \pm 0.490 \pm 0.568$	$16.688 \pm 0.472 \pm 0.547$
1.210	$18.657 \pm 0.525 \pm 0.583$	$17.981 \pm 0.506 \pm 0.561$
1.230	$20.624 \pm 0.524 \pm 0.644$	$19.890 \pm 0.506 \pm 0.621$
1.250	$20.659 \pm 0.521 \pm 0.645$	$19.932 \pm 0.503 \pm 0.622$
1.270	$21.753 \pm 0.547 \pm 0.679$	$20.996 \pm 0.528 \pm 0.656$
1.290	$23.623 \pm 0.539 \pm 0.738$	$22.810 \pm 0.520 \pm 0.712$
1.310	$24.514 \pm 0.553 \pm 0.765$	$23.677 \pm 0.534 \pm 0.739$
1.330	$25.431 \pm 0.551 \pm 0.794$	$24.568 \pm 0.533 \pm 0.767$
1.350	$26.128 \pm 0.562 \pm 0.816$	$25.248 \pm 0.543 \pm 0.788$
1.370	$28.489 \pm 0.579 \pm 0.890$	$27.537 \pm 0.560 \pm 0.860$
1.390	$28.502 \pm 0.568 \pm 0.890$	$27.552 \pm 0.549 \pm 0.861$
1.410	$29.564 \pm 0.570 \pm 0.923$	$28.577 \pm 0.551 \pm 0.893$
1.430	$31.453 \pm 0.591 \pm 0.982$	$30.412 \pm 0.572 \pm 0.950$
1.450	$31.663 \pm 0.585 \pm 0.989$	$30.622 \pm 0.566 \pm 0.957$
1.470	$31.800 \pm 0.591 \pm 0.993$	$30.749 \pm 0.572 \pm 0.960$
1.490	$32.069 \pm 0.579 \pm 1.001$	$30.999 \pm 0.559 \pm 0.968$
1.510	$31.639 \pm 0.574 \pm 0.988$	$30.571 \pm 0.555 \pm 0.955$
1.530	$30.525 \pm 0.561 \pm 0.953$	$29.476 \pm 0.542 \pm 0.920$
1.550	$29.238 \pm 0.546 \pm 0.913$	$28.214 \pm 0.527 \pm 0.881$
1.570	$29.262 \pm 0.545 \pm 0.914$	$28.227 \pm 0.526 \pm 0.881$
1.590	$27.013 \pm 0.512 \pm 0.844$	$26.055 \pm 0.494 \pm 0.814$

continued

$E_{\text{CM}}(\text{GeV})$	$\sigma(\text{nb})$	$\sigma^{(0)}(\text{nb})$
1.610	$27.022 \pm 0.509 \pm 0.844$	$26.064 \pm 0.491 \pm 0.814$
1.630	$26.194 \pm 0.499 \pm 0.818$	$25.263 \pm 0.482 \pm 0.789$
1.650	$24.798 \pm 0.481 \pm 0.774$	$23.911 \pm 0.464 \pm 0.747$
1.670	$24.603 \pm 0.480 \pm 0.768$	$23.710 \pm 0.463 \pm 0.740$
1.690	$22.556 \pm 0.458 \pm 0.704$	$21.728 \pm 0.441 \pm 0.678$
1.710	$21.886 \pm 0.449 \pm 0.683$	$21.073 \pm 0.432 \pm 0.658$
1.730	$20.929 \pm 0.443 \pm 0.653$	$20.142 \pm 0.426 \pm 0.629$
1.750	$19.198 \pm 0.421 \pm 0.599$	$18.467 \pm 0.405 \pm 0.577$
1.770	$17.759 \pm 0.406 \pm 0.554$	$17.084 \pm 0.391 \pm 0.533$
1.790	$15.944 \pm 0.377 \pm 0.498$	$15.335 \pm 0.362 \pm 0.479$
1.810	$14.939 \pm 0.367 \pm 0.467$	$14.365 \pm 0.353 \pm 0.449$
1.830	$13.028 \pm 0.337 \pm 0.407$	$12.527 \pm 0.324 \pm 0.391$
1.850	$12.466 \pm 0.335 \pm 0.389$	$11.986 \pm 0.322 \pm 0.374$
1.870	$10.951 \pm 0.306 \pm 0.342$	$10.534 \pm 0.294 \pm 0.329$
1.890	$10.742 \pm 0.304 \pm 0.335$	$10.339 \pm 0.293 \pm 0.323$
1.910	$9.365 \pm 0.279 \pm 0.292$	$9.018 \pm 0.269 \pm 0.282$
1.930	$9.152 \pm 0.275 \pm 0.286$	$8.815 \pm 0.265 \pm 0.275$
1.950	$9.012 \pm 0.273 \pm 0.281$	$8.681 \pm 0.263 \pm 0.271$
1.970	$8.715 \pm 0.265 \pm 0.272$	$8.399 \pm 0.255 \pm 0.262$
1.990	$8.656 \pm 0.265 \pm 0.270$	$8.348 \pm 0.256 \pm 0.261$
2.010	$8.906 \pm 0.268 \pm 0.278$	$8.588 \pm 0.259 \pm 0.268$
2.030	$9.172 \pm 0.276 \pm 0.286$	$8.842 \pm 0.266 \pm 0.276$
2.050	$8.056 \pm 0.251 \pm 0.252$	$7.764 \pm 0.242 \pm 0.243$
2.070	$8.141 \pm 0.258 \pm 0.254$	$7.842 \pm 0.248 \pm 0.245$
2.090	$7.590 \pm 0.242 \pm 0.237$	$7.308 \pm 0.233 \pm 0.228$
2.110	$7.273 \pm 0.235 \pm 0.227$	$6.999 \pm 0.226 \pm 0.219$
2.130	$6.674 \pm 0.225 \pm 0.208$	$6.421 \pm 0.217 \pm 0.201$
2.150	$7.198 \pm 0.238 \pm 0.225$	$6.923 \pm 0.229 \pm 0.216$
2.170	$6.169 \pm 0.217 \pm 0.193$	$5.932 \pm 0.209 \pm 0.185$
2.190	$6.513 \pm 0.228 \pm 0.203$	$6.261 \pm 0.219 \pm 0.196$
2.210	$6.087 \pm 0.218 \pm 0.190$	$5.851 \pm 0.210 \pm 0.183$
2.230	$5.282 \pm 0.198 \pm 0.165$	$5.076 \pm 0.190 \pm 0.159$
2.250	$4.964 \pm 0.191 \pm 0.155$	$4.770 \pm 0.183 \pm 0.149$
2.270	$4.913 \pm 0.193 \pm 0.153$	$4.720 \pm 0.185 \pm 0.147$
2.290	$4.748 \pm 0.185 \pm 0.148$	$4.561 \pm 0.178 \pm 0.142$
2.310	$4.191 \pm 0.171 \pm 0.131$	$4.025 \pm 0.165 \pm 0.126$
2.330	$4.335 \pm 0.178 \pm 0.135$	$4.164 \pm 0.171 \pm 0.130$
2.350	$3.980 \pm 0.168 \pm 0.124$	$3.823 \pm 0.162 \pm 0.119$
2.370	$3.501 \pm 0.155 \pm 0.109$	$3.363 \pm 0.149 \pm 0.105$
2.390	$3.374 \pm 0.152 \pm 0.105$	$3.241 \pm 0.146 \pm 0.101$
2.410	$3.416 \pm 0.153 \pm 0.107$	$3.281 \pm 0.147 \pm 0.102$
2.430	$3.594 \pm 0.161 \pm 0.112$	$3.453 \pm 0.155 \pm 0.108$
2.450	$3.331 \pm 0.158 \pm 0.104$	$3.200 \pm 0.152 \pm 0.100$
2.470	$3.095 \pm 0.148 \pm 0.097$	$2.973 \pm 0.142 \pm 0.093$
2.490	$3.022 \pm 0.147 \pm 0.094$	$2.904 \pm 0.141 \pm 0.091$

continued

$E_{CM}(\text{GeV})$	$\sigma(\text{nb})$	$\sigma^{(o)}(\text{nb})$
2.510	$2.991 \pm 0.146 \pm 0.093$	$2.874 \pm 0.140 \pm 0.090$
2.530	$2.721 \pm 0.135 \pm 0.085$	$2.616 \pm 0.130 \pm 0.082$
2.550	$2.611 \pm 0.138 \pm 0.082$	$2.510 \pm 0.133 \pm 0.078$
2.570	$2.534 \pm 0.136 \pm 0.079$	$2.436 \pm 0.130 \pm 0.076$
2.590	$2.364 \pm 0.129 \pm 0.074$	$2.273 \pm 0.124 \pm 0.071$
2.610	$2.261 \pm 0.126 \pm 0.071$	$2.175 \pm 0.121 \pm 0.068$
2.630	$2.015 \pm 0.115 \pm 0.063$	$1.938 \pm 0.111 \pm 0.060$
2.650	$2.339 \pm 0.129 \pm 0.073$	$2.250 \pm 0.124 \pm 0.070$
2.670	$2.215 \pm 0.122 \pm 0.069$	$2.132 \pm 0.117 \pm 0.067$
2.690	$1.762 \pm 0.109 \pm 0.055$	$1.696 \pm 0.105 \pm 0.053$
2.710	$1.675 \pm 0.104 \pm 0.112$	$1.613 \pm 0.100 \pm 0.108$
2.730	$1.645 \pm 0.106 \pm 0.110$	$1.584 \pm 0.102 \pm 0.106$
2.750	$1.996 \pm 0.122 \pm 0.134$	$1.923 \pm 0.118 \pm 0.129$
2.770	$1.493 \pm 0.101 \pm 0.100$	$1.439 \pm 0.098 \pm 0.096$
2.790	$1.389 \pm 0.096 \pm 0.093$	$1.339 \pm 0.092 \pm 0.090$
2.810	$1.464 \pm 0.097 \pm 0.098$	$1.412 \pm 0.094 \pm 0.095$
2.830	$1.496 \pm 0.101 \pm 0.100$	$1.444 \pm 0.097 \pm 0.097$
2.850	$1.103 \pm 0.084 \pm 0.074$	$1.065 \pm 0.081 \pm 0.071$
2.870	$1.258 \pm 0.093 \pm 0.084$	$1.216 \pm 0.090 \pm 0.081$
2.890	$1.274 \pm 0.091 \pm 0.085$	$1.233 \pm 0.088 \pm 0.083$
2.910	$1.149 \pm 0.089 \pm 0.077$	$1.113 \pm 0.087 \pm 0.074$
2.930	$1.224 \pm 0.091 \pm 0.082$	$1.187 \pm 0.089 \pm 0.079$
2.950	$1.072 \pm 0.089 \pm 0.072$	$1.042 \pm 0.087 \pm 0.070$
2.970	$1.120 \pm 0.091 \pm 0.075$	$1.091 \pm 0.088 \pm 0.073$
2.990	$0.996 \pm 0.086 \pm 0.067$	$0.973 \pm 0.084 \pm 0.065$
3.010	$0.913 \pm 0.078 \pm 0.061$	$0.897 \pm 0.076 \pm 0.060$
3.030	$0.906 \pm 0.076 \pm 0.061$	$0.897 \pm 0.075 \pm 0.060$
3.050	$0.984 \pm 0.084 \pm 0.066$	$0.987 \pm 0.084 \pm 0.066$
3.070	$1.166 \pm 0.087 \pm 0.078$	$1.210 \pm 0.090 \pm 0.081$
3.090	$2.440 \pm 0.146 \pm 0.163$	$3.143 \pm 0.188 \pm 0.219$
3.110	$2.278 \pm 0.147 \pm 0.152$	$1.831 \pm 0.118 \pm 0.125$
3.130	$0.953 \pm 0.078 \pm 0.064$	$0.854 \pm 0.070 \pm 0.057$
3.150	$0.870 \pm 0.076 \pm 0.058$	$0.799 \pm 0.070 \pm 0.053$
3.170	$0.765 \pm 0.064 \pm 0.051$	$0.711 \pm 0.060 \pm 0.048$
3.190	$0.686 \pm 0.064 \pm 0.046$	$0.642 \pm 0.059 \pm 0.043$
3.210	$0.821 \pm 0.072 \pm 0.059$	$0.771 \pm 0.068 \pm 0.056$
3.230	$0.652 \pm 0.060 \pm 0.047$	$0.615 \pm 0.057 \pm 0.044$
3.250	$0.645 \pm 0.060 \pm 0.046$	$0.610 \pm 0.057 \pm 0.044$
3.270	$0.586 \pm 0.058 \pm 0.042$	$0.554 \pm 0.055 \pm 0.040$
3.290	$0.621 \pm 0.059 \pm 0.045$	$0.589 \pm 0.056 \pm 0.042$
3.310	$0.536 \pm 0.054 \pm 0.039$	$0.509 \pm 0.051 \pm 0.037$
3.330	$0.588 \pm 0.060 \pm 0.042$	$0.559 \pm 0.057 \pm 0.040$
3.350	$0.473 \pm 0.051 \pm 0.034$	$0.450 \pm 0.048 \pm 0.032$
3.370	$0.585 \pm 0.062 \pm 0.042$	$0.557 \pm 0.059 \pm 0.040$
3.390	$0.536 \pm 0.057 \pm 0.039$	$0.511 \pm 0.054 \pm 0.037$

continued

$E_{\text{CM}}(\text{GeV})$	$\sigma(\text{nb})$	$\sigma^{(0)}(\text{nb})$
3.410	$0.588 \pm 0.061 \pm 0.042$	$0.560 \pm 0.058 \pm 0.040$
3.430	$0.468 \pm 0.050 \pm 0.034$	$0.447 \pm 0.048 \pm 0.032$
3.450	$0.389 \pm 0.042 \pm 0.028$	$0.372 \pm 0.040 \pm 0.027$
3.470	$0.413 \pm 0.048 \pm 0.030$	$0.395 \pm 0.046 \pm 0.028$
3.490	$0.506 \pm 0.057 \pm 0.036$	$0.484 \pm 0.054 \pm 0.035$
3.510	$0.554 \pm 0.063 \pm 0.040$	$0.530 \pm 0.061 \pm 0.038$
3.530	$0.519 \pm 0.060 \pm 0.037$	$0.498 \pm 0.058 \pm 0.036$
3.550	$0.463 \pm 0.056 \pm 0.033$	$0.445 \pm 0.053 \pm 0.032$
3.570	$0.416 \pm 0.050 \pm 0.030$	$0.400 \pm 0.049 \pm 0.029$
3.590	$0.366 \pm 0.045 \pm 0.026$	$0.353 \pm 0.043 \pm 0.025$
3.610	$0.367 \pm 0.048 \pm 0.026$	$0.355 \pm 0.047 \pm 0.025$
3.630	$0.379 \pm 0.051 \pm 0.027$	$0.368 \pm 0.049 \pm 0.026$
3.650	$0.311 \pm 0.044 \pm 0.022$	$0.305 \pm 0.043 \pm 0.022$
3.670	$0.348 \pm 0.047 \pm 0.025$	$0.352 \pm 0.047 \pm 0.026$
3.690	$0.361 \pm 0.044 \pm 0.026$	$0.268 \pm 0.033 \pm 0.024$
3.710	$0.306 \pm 0.039 \pm 0.022$	$0.282 \pm 0.036 \pm 0.020$
3.730	$0.293 \pm 0.040 \pm 0.021$	$0.275 \pm 0.037 \pm 0.020$
3.750	$0.320 \pm 0.043 \pm 0.023$	$0.302 \pm 0.041 \pm 0.022$
3.770	$0.215 \pm 0.031 \pm 0.015$	$0.204 \pm 0.030 \pm 0.015$
3.790	$0.278 \pm 0.038 \pm 0.020$	$0.263 \pm 0.036 \pm 0.019$
3.810	$0.265 \pm 0.038 \pm 0.019$	$0.251 \pm 0.036 \pm 0.018$
3.830	$0.180 \pm 0.029 \pm 0.013$	$0.171 \pm 0.028 \pm 0.012$
3.850	$0.233 \pm 0.034 \pm 0.017$	$0.222 \pm 0.033 \pm 0.016$
3.870	$0.254 \pm 0.037 \pm 0.018$	$0.242 \pm 0.035 \pm 0.017$
3.890	$0.215 \pm 0.033 \pm 0.015$	$0.205 \pm 0.031 \pm 0.015$
3.910	$0.206 \pm 0.034 \pm 0.015$	$0.197 \pm 0.033 \pm 0.014$
3.930	$0.252 \pm 0.037 \pm 0.018$	$0.240 \pm 0.035 \pm 0.017$
3.950	$0.142 \pm 0.025 \pm 0.010$	$0.135 \pm 0.024 \pm 0.010$
3.970	$0.199 \pm 0.032 \pm 0.014$	$0.190 \pm 0.031 \pm 0.014$
3.990	$0.139 \pm 0.025 \pm 0.010$	$0.133 \pm 0.024 \pm 0.009$
4.010	$0.189 \pm 0.031 \pm 0.014$	$0.181 \pm 0.029 \pm 0.013$
4.030	$0.178 \pm 0.032 \pm 0.013$	$0.170 \pm 0.031 \pm 0.012$
4.050	$0.165 \pm 0.030 \pm 0.012$	$0.157 \pm 0.029 \pm 0.011$
4.070	$0.179 \pm 0.033 \pm 0.013$	$0.171 \pm 0.031 \pm 0.012$
4.090	$0.105 \pm 0.022 \pm 0.008$	$0.100 \pm 0.021 \pm 0.007$
4.110	$0.148 \pm 0.025 \pm 0.011$	$0.141 \pm 0.024 \pm 0.010$
4.130	$0.195 \pm 0.033 \pm 0.014$	$0.185 \pm 0.031 \pm 0.013$
4.150	$0.157 \pm 0.030 \pm 0.011$	$0.149 \pm 0.028 \pm 0.011$
4.170	$0.187 \pm 0.033 \pm 0.013$	$0.177 \pm 0.032 \pm 0.013$
4.190	$0.162 \pm 0.029 \pm 0.012$	$0.153 \pm 0.027 \pm 0.011$
4.210	$0.086 \pm 0.022 \pm 0.006$	$0.081 \pm 0.021 \pm 0.006$
4.230	$0.102 \pm 0.019 \pm 0.007$	$0.096 \pm 0.018 \pm 0.007$
4.250	$0.121 \pm 0.022 \pm 0.009$	$0.114 \pm 0.021 \pm 0.008$
4.270	$0.157 \pm 0.030 \pm 0.011$	$0.149 \pm 0.028 \pm 0.011$
4.290	$0.075 \pm 0.019 \pm 0.005$	$0.071 \pm 0.018 \pm 0.005$

continued

$E_{CM}(\text{GeV})$	$\sigma(\text{nb})$	$\sigma^{(o)}(\text{nb})$
4.310	$0.128 \pm 0.025 \pm 0.009$	$0.121 \pm 0.023 \pm 0.009$
4.330	$0.124 \pm 0.025 \pm 0.009$	$0.118 \pm 0.024 \pm 0.009$
4.350	$0.132 \pm 0.028 \pm 0.009$	$0.125 \pm 0.027 \pm 0.009$
4.370	$0.114 \pm 0.023 \pm 0.008$	$0.109 \pm 0.022 \pm 0.008$
4.390	$0.081 \pm 0.018 \pm 0.006$	$0.077 \pm 0.017 \pm 0.005$
4.410	$0.107 \pm 0.022 \pm 0.008$	$0.102 \pm 0.021 \pm 0.007$
4.430	$0.120 \pm 0.024 \pm 0.009$	$0.114 \pm 0.023 \pm 0.008$
4.450	$0.073 \pm 0.017 \pm 0.005$	$0.069 \pm 0.016 \pm 0.005$
4.470	$0.078 \pm 0.019 \pm 0.006$	$0.074 \pm 0.018 \pm 0.005$
4.490	$0.089 \pm 0.023 \pm 0.006$	$0.085 \pm 0.022 \pm 0.006$

NUMERICAL STABILITY OF THE KERNEL FUNCTION

For $s > 4m_\ell^2$ the Kernel function is given by [46, 103]

$$\begin{aligned}
 K_\ell(s) &= \\
 &= \frac{1}{h^2} \left(4(h-2) \ln \frac{h}{4} - h \left(4 - \frac{h}{2} \right) \right. \\
 &\quad \left. - 2(h^2 - 8h + 8) \frac{\operatorname{arctanh}(\sqrt{1-h})}{\sqrt{1-h}} \right) \\
 &= \frac{1+x}{1-x} x^2 \ln x + x^2 \left(1 - \frac{x^2}{2} \right) \\
 &\quad + (1+x)^2 \left(1 + \frac{1}{x^2} \right) \left(\ln(1+x) - x + \frac{x^2}{2} \right)
 \end{aligned} \tag{121}$$

with $h := \frac{4m_\ell^2}{s}$, $x := \frac{1-\sqrt{1-h}}{1+\sqrt{1-h}}$. Since $\ln(1+x) = x - \frac{x^2}{2} + \frac{x^3}{3} + \dots$ for $|x| < 1$, it is obvious that large cancellations occur for very small x . Hence it is advantageous for the numerical precision to express the Kernel function as

$$\begin{aligned}
 K_\ell(s) &= \\
 &= \frac{1+x}{1-x} x^2 \ln x + x^2 \left(1 - \frac{x^2}{2} \right) \\
 &\quad + (1+x)^2 (x^2 + 1) \sum_{k=1}^{\infty} \frac{(-1)^{k+1}}{k+2} x^k \\
 &= \frac{1+x}{1-x} x^2 \ln x + \frac{1}{3}x + \frac{17}{12}x^2 + \frac{11}{30}x^3 - \frac{1}{10}x^4 \\
 &\quad + \sum_{k=5}^{\infty} (-1)^{k+1} \frac{4k^2 + 8}{k^5 - 5k^3 + 4k} x^k
 \end{aligned} \tag{122}$$

This alternating series converges quickly (asymptotically $\sim k^{-3}$), is numerically stable and trivial to implement efficiently. The first few coefficients are given by $\frac{3}{70}$, $-\frac{19}{840}$, $\frac{17}{1260}$, $-\frac{11}{1260}$ for $k = 5, 6, 7, 8$, respectively.

COPYRIGHT



Unless stated otherwise, the work (as defined below) is provided under the terms of the Creative Commons Public License Attribution-NonCommercial-ShareAlike 4.0 (printed below).

E.1 CREATIVE COMMONS LEGAL CODE

E.1.1 *Attribution-NonCommercial-ShareAlike 4.0 International*

Official translations of this license are available in other languages.

Creative Commons Corporation (“Creative Commons”) is not a law firm and does not provide legal services or legal advice. Distribution of Creative Commons public licenses does not create a lawyer-client or other relationship. Creative Commons makes its licenses and related information available on an “as-is” basis. Creative Commons gives no warranties regarding its licenses, any material licensed under their terms and conditions, or any related information. Creative Commons disclaims all liability for damages resulting from their use to the fullest extent possible.

Using Creative Commons Public Licenses

Creative Commons public licenses provide a standard set of terms and conditions that creators and other rights holders may use to share original works of authorship and other material subject to copyright and certain other rights specified in the public license below. The following considerations are for informational purposes only, are not exhaustive, and do not form part of our licenses.

Considerations for licensors: Our public licenses are intended for use by those authorized to give the public permission to use material in ways otherwise restricted by copyright and certain other rights. Our licenses are irrevocable. Licensors should read and understand the terms and conditions of the license they choose before applying it. Licensors should also secure all rights necessary before applying our licenses so that the public can reuse the material as expected. Licensors should clearly mark any material not subject to the license. This includes other CC-licensed material, or material used under an exception or limitation to copyright. More considerations for licensors.

Considerations for the public: By using one of our public licenses, a licensor grants the public permission to use the licensed material under specified terms and conditions. If the licensor’s permission is not necessary for any reason—for example, because of any applicable exception or limitation to copyright—then that use is not regulated by the license. Our licenses grant only permissions under copyright and certain other rights that a licensor has authority to grant. Use of the licensed material may still be restricted for other reasons, including because others have copyright or other rights in the material. A licensor may make special requests, such as asking that all changes be marked or described. Although not required by our licenses, you are encouraged to respect those requests where reasonable. More considerations for the public.

Creative Commons Attribution-NonCommercial-ShareAlike 4.0 International Public License

By exercising the Licensed Rights (defined below), You accept and agree to be bound by the terms and conditions of this Creative Commons Attribution-NonCommercial-ShareAlike 4.0 International Public License (“Public License”). To the extent this Public License may be interpreted as a contract, You are granted the Licensed Rights in consideration of Your acceptance of these terms and conditions, and the Licensor grants You such rights in consideration of benefits the Licensor receives from making the Licensed Material available under these terms and conditions.

Section 1 – Definitions.

1. **Adapted Material** means material subject to Copyright and Similar Rights that is derived from or based upon the Licensed Material and in which the Licensed Material is translated, altered, arranged, transformed, or otherwise modified in a manner requiring permission under the Copyright and Similar Rights held by the Licensor. For purposes of this Public License, where the Licensed Material is a musical work, performance, or sound recording, Adapted Material is always produced where the Licensed Material is synched in timed relation with a moving image.
2. **Adapter’s License** means the license You apply to Your Copyright and Similar Rights in Your contributions to Adapted Material in accordance with the terms and conditions of this Public License.
3. **BY-NC-SA Compatible License** means a license listed at creativecommons.org/compatiblelicenses, approved by Cre-

ative Commons as essentially the equivalent of this Public License.

4. **Copyright and Similar Rights** means copyright and/or similar rights closely related to copyright including, without limitation, performance, broadcast, sound recording, and Sui Generis Database Rights, without regard to how the rights are labeled or categorized. For purposes of this Public License, the rights specified in Section 2(b)(1)-(2) are not Copyright and Similar Rights.
5. **Effective Technological Measures** means those measures that, in the absence of proper authority, may not be circumvented under laws fulfilling obligations under Article 11 of the WIPO Copyright Treaty adopted on December 20, 1996, and/or similar international agreements.
6. **Exceptions and Limitations** means fair use, fair dealing, and/or any other exception or limitation to Copyright and Similar Rights that applies to Your use of the Licensed Material.
7. **License Elements** means the license attributes listed in the name of a Creative Commons Public License. The License Elements of this Public License are Attribution, NonCommercial, and ShareAlike.
8. **Licensed Material** means the artistic or literary work, database, or other material to which the Licensor applied this Public License.
9. **Licensed Rights** means the rights granted to You subject to the terms and conditions of this Public License, which are limited to all Copyright and Similar Rights that apply to Your use of the Licensed Material and that the Licensor has authority to license.
10. **Licensor** means the individual(s) or entity(ies) granting rights under this Public License.
11. **NonCommercial** means not primarily intended for or directed towards commercial advantage or monetary compensation. For purposes of this Public License, the exchange of the Licensed Material for other material subject to Copyright and Similar Rights by digital file-sharing or similar means is NonCommercial provided there is no payment of monetary compensation in connection with the exchange.
12. **Share** means to provide material to the public by any means or process that requires permission under the Licensed Rights,

such as reproduction, public display, public performance, distribution, dissemination, communication, or importation, and to make material available to the public including in ways that members of the public may access the material from a place and at a time individually chosen by them.

13. **Sui Generis Database Rights** means rights other than copyright resulting from Directive 96/9/EC of the European Parliament and of the Council of 11 March 1996 on the legal protection of databases, as amended and/or succeeded, as well as other essentially equivalent rights anywhere in the world.
14. **You** means the individual or entity exercising the Licensed Rights under this Public License. **Your** has a corresponding meaning.

Section 2 – Scope.

1. License grant.

- a) Subject to the terms and conditions of this Public License, the Licensor hereby grants You a worldwide, royalty-free, non-sublicensable, non-exclusive, irrevocable license to exercise the Licensed Rights in the Licensed Material to:
 - i. reproduce and Share the Licensed Material, in whole or in part, for NonCommercial purposes only; and
 - ii. produce, reproduce, and Share Adapted Material for NonCommercial purposes only.
- b) Exceptions and Limitations. For the avoidance of doubt, where Exceptions and Limitations apply to Your use, this Public License does not apply, and You do not need to comply with its terms and conditions.
- c) Term. The term of this Public License is specified in Section 6(a).
- d) Media and formats; technical modifications allowed. The Licensor authorizes You to exercise the Licensed Rights in all media and formats whether now known or hereafter created, and to make technical modifications necessary to do so. The Licensor waives and/or agrees not to assert any right or authority to forbid You from making technical modifications necessary to exercise the Licensed Rights, including technical modifications necessary to circumvent Effective Technological Measures. For purposes of this Public License, simply making modifications authorized by this Section 2(a)(4) never produces Adapted Material.

- e) Downstream recipients.
 - i. Offer from the Licensor – Licensed Material. Every recipient of the Licensed Material automatically receives an offer from the Licensor to exercise the Licensed Rights under the terms and conditions of this Public License.
 - ii. Additional offer from the Licensor – Adapted Material. Every recipient of Adapted Material from You automatically receives an offer from the Licensor to exercise the Licensed Rights in the Adapted Material under the conditions of the Adapter's License You apply.
 - iii. No downstream restrictions. You may not offer or impose any additional or different terms or conditions on, or apply any Effective Technological Measures to, the Licensed Material if doing so restricts exercise of the Licensed Rights by any recipient of the Licensed Material.
- f) No endorsement. Nothing in this Public License constitutes or may be construed as permission to assert or imply that You are, or that Your use of the Licensed Material is, connected with, or sponsored, endorsed, or granted official status by, the Licensor or others designated to receive attribution as provided in Section 3(a)(1)(A)(i).

Other rights.

- 2.
 - a) Moral rights, such as the right of integrity, are not licensed under this Public License, nor are publicity, privacy, and/or other similar personality rights; however, to the extent possible, the Licensor waives and/or agrees not to assert any such rights held by the Licensor to the limited extent necessary to allow You to exercise the Licensed Rights, but not otherwise.
 - b) Patent and trademark rights are not licensed under this Public License.
 - c) To the extent possible, the Licensor waives any right to collect royalties from You for the exercise of the Licensed Rights, whether directly or through a collecting society under any voluntary or waivable statutory or compulsory licensing scheme. In all other cases the Licensor expressly reserves any right to collect such royalties, including when the Licensed Material is used other than for NonCommercial purposes.

Section 3 – License Conditions.

Your exercise of the Licensed Rights is expressly made subject to the following conditions.

1. Attribution.

- a) If You Share the Licensed Material (including in modified form), You must:
 - i. retain the following if it is supplied by the Licensor with the Licensed Material:
 - A. identification of the creator(s) of the Licensed Material and any others designated to receive attribution, in any reasonable manner requested by the Licensor (including by pseudonym if designated);
 - B. a copyright notice;
 - C. a notice that refers to this Public License;
 - D. a notice that refers to the disclaimer of warranties;
 - E. a URI or hyperlink to the Licensed Material to the extent reasonably practicable;
 - ii. indicate if You modified the Licensed Material and retain an indication of any previous modifications; and
 - iii. indicate the Licensed Material is licensed under this Public License, and include the text of, or the URI or hyperlink to, this Public License.
- b) You may satisfy the conditions in Section 3(a)(1) in any reasonable manner based on the medium, means, and context in which You Share the Licensed Material. For example, it may be reasonable to satisfy the conditions by providing a URI or hyperlink to a resource that includes the required information.
- c) If requested by the Licensor, You must remove any of the information required by Section 3(a)(1)(A) to the extent reasonably practicable.

2. ShareAlike.

In addition to the conditions in Section 3(a), if You Share Adapted Material You produce, the following conditions also apply.

- a) The Adapter's License You apply must be a Creative Commons license with the same License Elements, this version or later, or a BY-NC-SA Compatible License.

- b) You must include the text of, or the URI or hyperlink to, the Adapter's License You apply. You may satisfy this condition in any reasonable manner based on the medium, means, and context in which You Share Adapted Material.
- c) You may not offer or impose any additional or different terms or conditions on, or apply any Effective Technological Measures to, Adapted Material that restrict exercise of the rights granted under the Adapter's License You apply.

Section 4 – Sui Generis Database Rights.

Where the Licensed Rights include Sui Generis Database Rights that apply to Your use of the Licensed Material:

1. for the avoidance of doubt, Section 2(a)(1) grants You the right to extract, reuse, reproduce, and Share all or a substantial portion of the contents of the database for NonCommercial purposes only;
2. if You include all or a substantial portion of the database contents in a database in which You have Sui Generis Database Rights, then the database in which You have Sui Generis Database Rights (but not its individual contents) is Adapted Material, including for purposes of Section 3(b); and
3. You must comply with the conditions in Section 3(a) if You Share all or a substantial portion of the contents of the database.

For the avoidance of doubt, this Section 4 supplements and does not replace Your obligations under this Public License where the Licensed Rights include other Copyright and Similar Rights.

Section 5 – Disclaimer of Warranties and Limitation of Liability.

1. **Unless otherwise separately undertaken by the Licensor, to the extent possible, the Licensor offers the Licensed Material as-is and as-available, and makes no representations or warranties of any kind concerning the Licensed Material, whether express, implied, statutory, or other. This includes, without limitation, warranties of title, merchantability, fitness for a particular purpose, non-infringement, absence of latent or other defects, accuracy, or the presence or absence of errors, whether or not known or discoverable. Where disclaimers of warranties are not allowed in full or in part, this disclaimer may not apply to You.**
2. **To the extent possible, in no event will the Licensor be liable to You on any legal theory (including, without limitation, negligence) or otherwise for any direct, special,**

indirect, incidental, consequential, punitive, exemplary, or other losses, costs, expenses, or damages arising out of this Public License or use of the Licensed Material, even if the Licensor has been advised of the possibility of such losses, costs, expenses, or damages. Where a limitation of liability is not allowed in full or in part, this limitation may not apply to You.

1. The disclaimer of warranties and limitation of liability provided above shall be interpreted in a manner that, to the extent possible, most closely approximates an absolute disclaimer and waiver of all liability.

Section 6 – Term and Termination.

1. This Public License applies for the term of the Copyright and Similar Rights licensed here. However, if You fail to comply with this Public License, then Your rights under this Public License terminate automatically.
2. Where Your right to use the Licensed Material has terminated under Section 6(a), it reinstates:
 - a) automatically as of the date the violation is cured, provided it is cured within 30 days of Your discovery of the violation; or
 - b) upon express reinstatement by the Licensor.

For the avoidance of doubt, this Section 6(b) does not affect any right the Licensor may have to seek remedies for Your violations of this Public License.

3. For the avoidance of doubt, the Licensor may also offer the Licensed Material under separate terms or conditions or stop distributing the Licensed Material at any time; however, doing so will not terminate this Public License.
4. Sections 1, 5, 6, 7, and 8 survive termination of this Public License.

Section 7 – Other Terms and Conditions.

1. The Licensor shall not be bound by any additional or different terms or conditions communicated by You unless expressly agreed.
2. Any arrangements, understandings, or agreements regarding the Licensed Material not stated herein are separate from and independent of the terms and conditions of this Public License.

Section 8 – Interpretation.

1. For the avoidance of doubt, this Public License does not, and shall not be interpreted to, reduce, limit, restrict, or impose conditions on any use of the Licensed Material that could lawfully be made without permission under this Public License.
2. To the extent possible, if any provision of this Public License is deemed unenforceable, it shall be automatically reformed to the minimum extent necessary to make it enforceable. If the provision cannot be reformed, it shall be severed from this Public License without affecting the enforceability of the remaining terms and conditions.
3. No term or condition of this Public License will be waived and no failure to comply consented to unless expressly agreed to by the Licensor.
4. Nothing in this Public License constitutes or may be interpreted as a limitation upon, or waiver of, any privileges and immunities that apply to the Licensor or You, including from the legal processes of any jurisdiction or authority.

Creative Commons is not a party to its public licenses. Notwithstanding, Creative Commons may elect to apply one of its public licenses to material it publishes and in those instances will be considered the “Licensor.” The text of the Creative Commons public licenses is dedicated to the public domain under the CCo Public Domain Dedication. Except for the limited purpose of indicating that material is shared under a Creative Commons public license or as otherwise permitted by the Creative Commons policies published at creativecommons.org/policies, Creative Commons does not authorize the use of the trademark “Creative Commons” or any other trademark or logo of Creative Commons without its prior written consent including, without limitation, in connection with any unauthorized modifications to any of its public licenses or any other arrangements, understandings, or agreements concerning use of licensed material. For the avoidance of doubt, this paragraph does not form part of the public licenses.

Creative Commons may be contacted at creativecommons.org.

BIBLIOGRAPHY

- [1] H. Yukawa. On the Interaction of Elementary Particles. *Proc.Phys.Math.Soc.Jap.*, 17:48–57, 1935.
- [2] C.D. Anderson and S.H. Neddermeyer. Cloud chamber observations of cosmic rays at 4300 meters elevation and near sea-level. *Phys. Rev.*, 50:263–271, Aug 1936.
- [3] M. Schein and V.C. Wilson. Mesotron production in the atmosphere. *Rev. Mod. Phys.*, 11:292–295, Jul 1939.
- [4] E.L. Gettier. Is justified true belief knowledge? *Analysis*, 23(6):121–123, 1963.
- [5] S.L. Glashow. Partial Symmetries of Weak Interactions. *Nucl.Phys.*, 22:579–588, 1961.
- [6] S. Weinberg. A Model of Leptons. *Phys.Rev.Lett.*, 19:1264–1266, 1967.
- [7] G. 't Hooft. Renormalization of Massless Yang-Mills Fields. *Nucl.Phys.*, B33:173–199, 1971.
- [8] G. 't Hooft. Renormalizable Lagrangians for Massive Yang-Mills Fields. *Nucl.Phys.*, B35:167–188, 1971.
- [9] C. Berger et al. Jet Analysis of the Υ (9.46) Decay Into Charged Hadrons. *Phys.Lett.*, B82:449, 1979.
- [10] G. Arnison et al. Experimental Observation of Isolated Large Transverse Energy Electrons with Associated Missing Energy at $\sqrt{s} = 540\text{GeV}$. *Phys.Lett.*, B122:103–116, 1983.
- [11] M. Banner et al. Observation of Single Isolated Electrons of High Transverse Momentum in Events with Missing Transverse Energy at the CERN $\bar{p}p$ Collider. *Phys.Lett.*, B122:476–485, 1983.
- [12] G. Arnison et al. Experimental Observation of Lepton Pairs of Invariant Mass Around $95\text{GeV}/c^2$ at the CERN SPS Collider. *Phys.Lett.*, B126:398–410, 1983.
- [13] P. Bagnaia et al. Evidence for $Z^0 \rightarrow e^+e^-$ at the CERN $\bar{p}p$ Collider. *Phys.Lett.*, B129:130–140, 1983.
- [14] G. Arnison et al. Further Evidence for Charged Intermediate Vector Bosons at the SPS Collider. *Phys.Lett.*, B129:273–282, 1983.

- [15] G. Aad et al. Observation of a new particle in the search for the Standard Model Higgs boson with the ATLAS detector at the LHC. *Phys.Lett.*, B716:1–29, 2012.
- [16] S. Chatrchyan et al. Observation of a new boson at a mass of 125 GeV with the CMS experiment at the LHC. *Phys.Lett.*, B716:30–61, 2012.
- [17] R. Aaij et al. Measurement of the $B_s^0 \rightarrow \mu^+ \mu^-$ branching fraction and search for $B^0 \rightarrow \mu^+ \mu^-$ decays at the LHCb experiment. *Phys.Rev.Lett.*, 111:101805, 2013.
- [18] S. Chatrchyan et al. Measurement of the $B_s^0 \rightarrow \mu^+ \mu^-$ branching fraction and search for $B^0 \rightarrow \mu^+ \mu^-$ with the CMS Experiment. *Phys.Rev.Lett.*, 111:101804, 2013.
- [19] P. Mery, S.E. Moubarik, M. Perrottet, and F.M. Renard. Constraints on Nonstandard Effects From Present and Future Muon $g - 2$ Measurements. *Z. Phys.*, C46:229, 1990.
- [20] M. Pospelov. Secluded $U(1)$ below the weak scale. *Phys. Rev.*, D80:095002, 2009.
- [21] H. Merkel et al. Search at the Mainz Microtron for Light Massive Gauge Bosons Relevant for the Muon $g - 2$ Anomaly. *Phys. Rev. Lett.*, 112(22):221802, 2014.
- [22] J.P. Lees et al. Search for a Dark Photon in $e^+ e^-$ Collisions at BaBar. *Phys. Rev. Lett.*, 113(20):201801, 2014.
- [23] D. Stöckinger. The Muon Magnetic Moment and Supersymmetry. *J. Phys.*, G34:R45–R92, 2007.
- [24] K.S. Babu, I. Gogoladze, Q. Shafi, and C.S. Ün. Muon $g - 2$, 125 GeV Higgs boson, and neutralino dark matter in a flavor symmetry-based MSSM. *Phys. Rev.*, D90(11):116002, 2014.
- [25] C. Biggio and M. Bordone. Minimal muon anomalous magnetic moment. *JHEP*, 02:099, 2015.
- [26] D. Zhuridov. Leptomeson contribution to the muon $g - 2$. *Phys. Rev.*, D93(3):035025, 2016.
- [27] M. Bauer and M. Neubert. One Leptoquark to Rule Them All: A Minimal Explanation for $R_{D^{(*)}}$, R_K and $(g - 2)_\mu$. *Phys. Rev. Lett.*, 116:141802, 2016.
- [28] J.D. Jackson. *Classical Electrodynamics*. Wiley, 3rd edition, 1998.

- [29] C. Cohen-Tannoudji, J. Dupont-Roc, and G. Grynberg. *Photons and Atoms: Introduction to Quantum Electrodynamics*. Wiley-VCH, 1997.
- [30] P. A. M. Dirac. The Quantum Theory of the Electron. *Proc. Roy. Soc. Lond.*, A117:610–624, 1928.
- [31] P. A. M. Dirac. The Quantum Theory of the Electron. Part II. *Proc. Roy. Soc. Lond.*, A118:351–361, 1928.
- [32] G. Charpak, F.J.M. Farley, and R.L. Garwin. A New Measurement of the Anomalous Magnetic Moment of the Muon. *Phys. Lett.*, 1:16, 1962.
- [33] J. Bailey, W. Bartl, G. von Bochmann, R.C.A. Brown, F.J.M. Farley, M. Giesch, H. Jostlein, S. van der Meer, E. Picasso, and R.W. Williams. Precise Measurement of the Anomalous Magnetic Moment of the Muon. *Nuovo Cim.*, A9:369–432, 1972.
- [34] J. Bailey et al. Final Report on the CERN Muon Storage Ring Including the Anomalous Magnetic Moment and the Electric Dipole Moment of the Muon, and a Direct Test of Relativistic Time Dilation. *Nucl.Phys.*, B150:1, 1979.
- [35] G.W. Bennett et al. Final Report of the Muon E821 Anomalous Magnetic Moment Measurement at BNL. *Phys.Rev.*, D73:072003, 2006. <http://dx.doi.org/10.1103/PhysRevD.73.072003>.
- [36] V. Bargmann, L. Michel, and V.L. Telegdi. Precession of the polarization of particles moving in a homogeneous electromagnetic field. *Phys.Rev.Lett.*, 2:435, 1959.
- [37] J. Bailey, F.J.M. Farley, and H. Jöstlein. Proposal for a measurement of the anomalous magnetic moment of the muon at a level of 10-20 ppm. Technical Report CERN-PH-I-COM-69-20, CERN, Geneva, 1969.
- [38] Y. Nagashima. *Elementary Particle Physics: Quantum Field Theory and Particles*, volume 1. Wiley, 2010.
- [39] K.P. Jungmann. A precise measurement of the muon magnetic anomaly. *Phys. Scripta*, T104:44–48, 2003.
- [40] S. Gasiorowicz. *Elementary Particle Physics*. Wiley, 1966.
- [41] W. Liu, M.G. Boshier, S. Dhawan, O. van Dyck, P. Egan, et al. High precision measurements of the ground state hyperfine structure interval of muonium and of the muon magnetic moment. *Phys.Rev.Lett.*, 82:711–714, 1999.

- [42] P.J. Mohr, B.N. Taylor, and D.B. Newell. CODATA Recommended Values of the Fundamental Physical Constants: 2006. *Rev.Mod.Phys.*, 80:633–730, 2008.
- [43] K.A. Olive et al. Review of Particle Physics. *Chin.Phys.*, C38:090001, 2014.
- [44] G. Venanzoni. The Fermilab Muon $g - 2$ Experiment. *PoS, EPS-HEP2015*:568, 2015.
- [45] M. Otani. Status of the Muon $g-2$ /EDM Experiment at J-PARC (E34). *JPS Conf. Proc.*, 8:025008, 2015.
- [46] F. Jegerlehner and A. Nyffeler. The Muon $g-2$. *Phys.Rept.*, 477:1–110, 2009.
- [47] J. Schwinger. On quantum-electrodynamics and the magnetic moment of the electron. *Phys. Rev.*, 73:416–417, Feb 1948.
- [48] J. Schwinger. On radiative corrections to electron scattering. *Phys. Rev.*, 75:898–899, Mar 1949.
- [49] R. Karplus and N.M. Kroll. Fourth-order corrections in quantum electrodynamics and the magnetic moment of the electron. *Phys. Rev.*, 77:536–549, Feb 1950.
- [50] C.M. Sommerfield. Magnetic dipole moment of the electron. *Phys. Rev.*, 107:328–329, Jul 1957.
- [51] C.M. Sommerfield. The Magnetic Moment of the Electron. *Annals Phys.*, 5:26–57, 1958.
- [52] A. Petermann. Fourth order magnetic moment of the electron. *Helv.Phys.Acta*, 30:407–408, 1957.
- [53] A. Petermann. Magnetic moment of the electron. *Nucl.Phys.*, 3:689–690, 1957.
- [54] H. Suura and E.H. Wichmann. Magnetic Moment of the Mu Meson. *Phys.Rev.*, 105:1930–1931, 1957.
- [55] A. Petermann. Magnetic moment of the μ meson. *Phys.Rev.*, 105:1931, 1957.
- [56] T. Aoyama, M. Hayakawa, T. Kinoshita, and M. Nio. Complete tenth-order qed contribution to the muon $g - 2$. *Phys. Rev. Lett.*, 109:111808, Sep 2012.
- [57] B. Riemann. Ueber die Anzahl der Primzahlen unter einer gegebenen Grösse. *Monatsberichte der Berliner Akademie*, November 1859.

- [58] M. Abramowitz and I.A. Stegun. *Handbook of Mathematical Functions: with Formulas, Graphs, and Mathematical Tables*. National Bureau of Standards Applied Mathematics Series. United States Government Printing Office, 1972.
- [59] H.H. Elend. On the anomalous magnetic moment of the muon. *Physics Letters*, 20(6):682 – 684, 1966. Erratum-ibid. 21(6):720, 1966.
- [60] M. Passera. The Standard model prediction of the muon anomalous magnetic moment. *J.Phys.*, G31:R75–R94, 2005.
- [61] L. Lewin. *Polylogarithms and Associated Functions*. North Holland, 1981.
- [62] S. Laporta and E. Remiddi. The analytical value of the electron ($g-2$) at order α^3 in QED. *Phys.Lett.*, B379:283–291, 1996.
- [63] M.A. Samuel and G.W. Li. Improved analytic theory of the muon anomalous magnetic moment. *Phys.Rev.*, D44:3935, 1991. Erratum-ibid. D48:1879, 1993.
- [64] G. Li, R. Mendel, and M.A. Samuel. Precise mass ratio dependence of fourth order lepton anomalous magnetic moments: The Effect of a new measurement of m_τ . *Phys.Rev.*, D47:1723–1725, 1993.
- [65] S. Laporta. The Analytical contribution of the sixth order graphs with vacuum polarization insertions to the muon ($g-2$) in QED. *Nuovo Cim.*, A106:675–683, 1993.
- [66] S. Laporta and E. Remiddi. The Analytical value of the electron light-light graphs contribution to the muon ($g-2$) in QED. *Phys.Lett.*, B301:440–446, 1993.
- [67] A. Czarnecki and M. Skrzypek. The Muon anomalous magnetic moment in QED: Three loop electron and tau contributions. *Phys.Lett.*, B449:354–360, 1999.
- [68] S. Laporta. The Analytical contribution of some eighth order graphs containing vacuum polarization insertions to the muon ($g-2$) in QED. *Phys.Lett.*, B312:495–500, 1993.
- [69] T. Kinoshita and M. Nio. Improved α^4 term of the electron anomalous magnetic moment. *Phys.Rev.*, D73:013003, 2006.
- [70] T. Aoyama, M. Hayakawa, T. Kinoshita, and M. Nio. Revised value of the eighth-order electron $g - 2$. *Phys.Rev.Lett.*, 99:110406, 2007.

- [71] T. Aoyama, M. Hayakawa, T. Kinoshita, and M. Nio. Revised value of the eighth-order QED contribution to the anomalous magnetic moment of the electron. *Phys.Rev.*, D77:053012, 2008.
- [72] T. Aoyama, M. Hayakawa, T. Kinoshita, and M. Nio. Tenth-Order QED Contribution to the Electron $g - 2$ and an Improved Value of the Fine Structure Constant. *Phys.Rev.Lett.*, 109:111807, 2012.
- [73] T. Aoyama, M. Hayakawa, T. Kinoshita, and M. Nio. Tenth-Order Electron Anomalous Magnetic Moment — Contribution of Diagrams without Closed Lepton Loops. *Phys. Rev.*, D91(3):033006, 2015.
- [74] A. Kurz, T. Liu, P. Marquard, A. Smirnov, V. Smirnov, and M. Steinhauser. Electron contribution to the muon anomalous magnetic moment at four loops. *Phys. Rev.*, D93(5):053017, 2016.
- [75] A. Kurz, T. Liu, P. Marquard, A.V. Smirnov, V.A. Smirnov, and Matthias Steinhauser. Light-by-light-type corrections to the muon anomalous magnetic moment at four-loop order. *Phys. Rev.*, D92(7):073019, 2015.
- [76] S. Weinberg. Physical Processes in a Convergent Theory of the Weak and Electromagnetic Interactions. *Phys.Rev.Lett.*, 27:1688–1691, 1971.
- [77] S. Weinberg. General Theory of Broken Local Symmetries. *Phys.Rev.*, D7:1068–1082, 1973.
- [78] A. Czarnecki, W.J. Marciano, and A. Vainshtein. Refinements in electroweak contributions to the muon anomalous magnetic moment. *Phys.Rev.*, D67:073006, 2003. Erratum-ibid., 73:119901, 2006.
- [79] A. Czarnecki, B. Krause, and W.J. Marciano. Electroweak Fermion loop contributions to the muon anomalous magnetic moment. *Phys.Rev.*, D52:2619–2623, 1995.
- [80] S. Peris, M. Perrottet, and E. de Rafael. Two loop electroweak corrections to the muon $g - 2$: A New class of hadronic contributions. *Phys.Lett.*, B355:523–530, 1995.
- [81] M. Knecht, S. Peris, M. Perrottet, and E. De Rafael. Electroweak hadronic contributions to the muon ($g - 2$). *JHEP*, 0211:003, 2002.

- [82] R. Jackiw and S. Weinberg. Weak interaction corrections to the muon magnetic moment and to muonic atom energy levels. *Phys.Rev.*, D5:2396–2398, 1972.
- [83] A.I. Studenikin. Contributions of bosons of various types to the anomalous magnetic moment of charged leptons. *Sov.Phys.JETP*, 70:795–800, 1990.
- [84] T. Gribouk and A. Czarnecki. Electroweak interactions and the muon $g-2$: Bosonic two-loop effects. *Phys.Rev.*, D72:053016, 2005.
- [85] C. Gnendiger, D. Stöckinger, and H. Stöckinger-Kim. The electroweak contributions to $(g - 2)_\mu$ after the Higgs boson mass measurement. *Phys.Rev.*, D88(5):053005, 2013.
- [86] H.D. Politzer. Reliable Perturbative Results for Strong Interactions? *Phys.Rev.Lett.*, 30:1346–1349, 1973.
- [87] D.J. Gross and F. Wilczek. Ultraviolet Behavior of Non-abelian Gauge Theories. *Phys.Rev.Lett.*, 30:1343–1346, 1973.
- [88] C. Itzykson and J.B. Zuber. *Quantum Field Theory*. McGraw-Hill, 1980.
- [89] G. Källén. *Elementary Particle Physics*. Addison-Wesley Pub. Co, 1964.
- [90] M.E. Peskin and D.V. Schroeder. *An Introduction to Quantum Field Theory*. Advanced book classics. Addison-Wesley Publishing Company, 1995.
- [91] R. de L. Kronig. On the Theory of Dispersion of X-Rays. *J. Opt. Soc. Am.*, 12(6):547–557, Jun 1926.
- [92] H.A. Kramers. La diffusion de la lumiere par les atomes. *Atti Cong. Intern. Fisici, (Transactions of Volta Centenary Congress) Como*, 2:545–557, 1927.
- [93] W. Rudin. *Real and Complex Analysis*. Mathematics Series. McGraw-Hill, 3rd edition, 1987.
- [94] D. Iagolnitzer. *The S Matrix*. North-Holland Publishing Company, 1978.
- [95] C. Carathéodory. *Theory of Functions of a Complex Variable*, volume 1. Chelsea Publishing Company, 1954.
- [96] S. Weinberg. *The Quantum Theory of Fields*, volume 1. Cambridge University Press, 2005.

- [97] M. Reed and B. Simon. *Methods of Modern Mathematical Physics I: Functional Analysis*. Academic Press, San Diego, 1980.
- [98] A.I. Akhiezer and V.B. Berestetskii. *Quantum Electrodynamics*. Interscience Monographs and Texts in Physics and Astronomy. John Wiley & Sons, 1965.
- [99] V.B. Berestetskii, O.N. Krokhin, and A.K. Khlebnikov. Concerning the Radiative Correction to the μ -Meson Magnetic Moment. *Sov.Phys.JETP*, 3:761–762, 1956.
- [100] R.P. Feynman. Relativistic cut-off for quantum electrodynamics. *Phys. Rev.*, 74:1430–1438, Nov 1948.
- [101] R.P. Feynman. Space-time approach to quantum electrodynamics. *Phys. Rev.*, 76:769–789, Sep 1949.
- [102] G.B. Arfken and H.J. Weber. *Mathematical Methods for Physicists*. Academic Press, 6th edition, 2005.
- [103] N.N. Achasov and A.V. Kiselev. Contribution to muon $g - 2$ from the $\pi^0\gamma$ and $\eta\gamma$ intermediate states in the vacuum polarization. *Phys.Rev.*, D65:097302, 2002.
- [104] C. Bouchiat and L. Michel. La résonance dans la diffusion méson π - méson π et le moment magnétique anormal du méson μ . *J. Phys. Radium*, 22:121, Feb 1961.
- [105] K. Ackerstaff et al. Measurement of the strong coupling constant $\alpha(s)$ and the vector and axial vector spectral functions in hadronic tau decays. *Eur. Phys. J.*, C7:571–593, 1999.
- [106] S. Anderson et al. Hadronic structure in the decay $\tau^- \rightarrow \pi^- \pi^0 \nu_\tau$. *Phys. Rev.*, D61:112002, 2000.
- [107] S. Schael et al. Branching ratios and spectral functions of τ decays: Final ALEPH measurements and physics implications. *Phys. Rept.*, 421:191–284, 2005.
- [108] M. Fujikawa et al. High-Statistics Study of the $\tau^- \rightarrow \pi^- \pi^0 \nu_\tau$ Decay. *Phys. Rev.*, D78:072006, 2008.
- [109] M. Davier, S. Eidelman, A. Höcker, and Z. Zhang. Confronting spectral functions from e^+e^- annihilation and τ decays: Consequences for the muon magnetic moment. *Eur. Phys. J.*, C27:497–521, 2003.
- [110] M. Davier, A. Hoecker, G. Lopez Castro, B. Malaescu, X.H. Mo, G. Toledo Sanchez, P. Wang, C.Z. Yuan, and Z. Zhang. The Discrepancy Between τ and e^+e^- Spectral Functions

- Revisited and the Consequences for the Muon Magnetic Anomaly. *Eur. Phys. J.*, C66:127–136, 2010.
- [111] F. Jegerlehner and R. Szafron. $\rho^0 - \gamma$ mixing in the neutral channel pion form factor F_π^e and its role in comparing e^+e^- with τ spectral functions. *Eur. Phys. J.*, C71:1632, 2011.
- [112] R. R. Akhmetshin et al. Reanalysis of hadronic cross-section measurements at CMD-2. *Phys. Lett.*, B578:285–289, 2004.
- [113] R.R. Akhmetshin et al. High-statistics measurement of the pion form factor in the ρ -meson energy range with the CMD-2 detector. *Phys. Lett.*, B648:28–38, 2007.
- [114] M.N. Achasov et al. Study of the process $e^+e^- \rightarrow \pi^+\pi^-$ in the energy region $400 < \sqrt{s} < 1000\text{MeV}$. *J. Exp. Theor. Phys.*, 101(6):1053–1070, 2005. [Zh. Eksp. Teor. Fiz.128,no.6,1201(2005)].
- [115] J.P. Lees et al. Precise Measurement of the $e^+e^- \rightarrow \pi^+\pi^-(\gamma)$ Cross Section with the Initial-State Radiation Method at BABAR. *Phys.Rev.*, D86:032013, 2012.
- [116] D. Babusci et al. Precision measurement of $\sigma(e^+e^- \rightarrow \pi^+\pi^-\gamma)/\sigma(e^+e^- \rightarrow \mu^+\mu^-\gamma)$ and determination of the $\pi^+\pi^-$ contribution to the muon anomaly with the KLOE detector. *Phys.Lett.*, B720:336–343, 2013.
- [117] M. Ablikim et al. Measurement of the $e^+e^- \rightarrow \pi^+\pi^-$ cross section between 600 and 900 MeV using initial state radiation. *Phys. Lett.*, B753:629–638, 2016.
- [118] M.N. Achasov, V.M. Aulchenko, K.I. Beloborodov, A.V. Berdyugin, A.G. Bogdanchikov, et al. Study of the process $e^+e^- \rightarrow \pi^+\pi^-\pi^0$ in the energy region \sqrt{s} from 0.98 GeV to 1.38 GeV. *Phys.Rev.*, D66:032001, 2002.
- [119] M.N. Achasov, K.I. Beloborodov, A.V. Berdyugin, A.G. Bogdanchikov, A.V. Bozhenok, et al. Study of the process $e^+e^- \rightarrow \pi^+\pi^-\pi^0$ in the energy region \sqrt{s} below 0.98 GeV. *Phys.Rev.*, D68:052006, 2003.
- [120] B. Aubert et al. Study of the $e^+e^- \rightarrow \pi^+\pi^-\pi^0$ process using initial state radiation with BaBar. *Phys.Rev.*, D70:072004, 2004.
- [121] J.P. Lees et al. Initial-State Radiation Measurement of the $e^+e^- \rightarrow \pi^+\pi^-\pi^+\pi^-$ Cross Section. *Phys.Rev.*, D85:112009, 2012.

- [122] M.R. Whalley. A Compilation of data on hadronic total cross-sections in e^+e^- interactions. *J.Phys.*, G29:A1–A133, 2003.
- [123] M.N. Achasov, K.I. Beloborodov, A.V. Berdyugin, A.G. Bogdanchikov, A.V. Bozhenok, et al. Analysis of $e^+e^- \rightarrow \pi^+\pi^-\pi^+\pi^-$ and $e^+e^- \rightarrow \pi^+\pi^-\pi^0\pi^0$ Processes in the Energy Range of $\sqrt{s} = 0.98 - 1.38\text{GeV}$ in Experiments with a Spherical Neutral Detector. *J.Exp.Theor.Phys.*, 96:789–800, 2003.
- [124] M.N. Achasov et al. Study of Process $e^+e^- \rightarrow \pi^+\pi^-\pi^0\pi^0$ at Energies $\sqrt{s} < 1\text{GeV}$ with the Spherical Neutral Detector. *J. Exp. Theor. Phys.*, 109:379–392, 2009. [*Zh. Eksp. Teor. Fiz.*136,442(2009)].
- [125] B. Esposito et al. Multi-Hadron Production from e^+e^- Annihilation at 1.6 Center-of-Mass Energy. *Lett. Nuovo Cim.*, 19:21–31, 1977.
- [126] B. Esposito et al. Multihadron Production in e^+e^- Annihilation at 1.45 - 1.61GeV c.m. Energy. *Lett. Nuovo Cim.*, 25:5–12, 1979.
- [127] B. Esposito et al. Measurement on $\pi^+\pi^-\pi^0\pi^0$, $\pi^+\pi^-\pi^+\pi^-\pi^0$, $\pi^+\pi^-\pi^+\pi^-\pi^0\pi^0$, $\pi^+\pi^-\pi^+\pi^-\pi^+\pi^-$ Production Cross-sections in e^+e^- Annihilation at 1.45-GeV - 1.80-GeV Center-of-mass Energy. *Lett. Nuovo Cim.*, 31:445–452, 1981.
- [128] C. Bacci et al. Measurement of Hadronic Exclusive Cross-sections in e^+e^- Annihilation From 1.42-GeV to 2.20-GeV. *Nucl. Phys.*, B184:31, 1981.
- [129] G. Cosme, B. Jean-Marie, S. Jullian, F. Laplanche, J. Lefrancois, A. D. Liberman, G. Parrour, J. P. Repellin, G. Sauvage, and G. Szklarz. Hadronic production by e^+e^- collisions at the energy 990 mev with the orsay storage ring. *Phys. Lett.*, B40:685–688, 1972.
- [130] G. Cosme et al. Multi-Pion Production Below 1.1-GeV by e^+e^- Annihilation. *Phys. Lett.*, B63:349–351, 1976.
- [131] G. Cosme, B. Dudelzak, B. Grelaud, B. Jean-Marie, S. Jullian, et al. Hadronic Cross-Sections Study in e^+e^- Collisions from 1.350GeV to 2.125GeV. *Nucl.Phys.*, B152:215, 1979.
- [132] S.I. Dolinsky et al. Summary of experiments with the neutral detector at the e^+e^- storage ring VEPP-2M. *Phys. Rept.*, 202:99–170, 1991.

- [133] L.M. Kurdadze, M. Yu. Lelchuk, E.V. Pakhtusova, V.A. Sidorov, A.N. Skrinsky, A.G. Chilingarov, Yu. M. Shatunov, B.A. Shvarts, and S.I. Eidelman. Study of the Reaction $e^+e^- \rightarrow \pi^+\pi^-\pi^0\pi^0$ at $2E$ Up to 1.4-GeV. *JETP Lett.*, 43:643–645, 1986. [Pisma Zh. Eksp. Teor. Fiz.43,497(1986)].
- [134] J.S. Schwinger. *Particles, Sources, and Fields*, volume 3. Addison-Wesley, 1989.
- [135] M. Drees and K.I. Hikasa. Scalar top production in e^+e^- annihilation. *Phys. Lett.*, B252:127–134, 1990.
- [136] M. Davier, A. Hoecker, B. Malaescu, and Z. Zhang. Reevaluation of the Hadronic Contributions to the Muon $g-2$ and to $\alpha(M_Z^2)$. *Eur.Phys.J.*, C71:1515, 2011. Erratum-ibid. C72:1874, 2012.
- [137] M. Davier, S. Eidelman, A. Höcker, and Z. Zhang. Updated estimate of the muon magnetic moment using revised results from e^+e^- annihilation. *Eur. Phys. J.*, C31:503–510, 2003.
- [138] B. Aubert et al. The $e^+e^- \rightarrow 2(\pi^+\pi^-)\pi^0$, $2(\pi^+\pi^-)\eta$, $K^+K^-\pi^+\pi^-\pi^0$ and $K^+K^-\pi^+\pi^-\eta$ Cross Sections Measured with Initial-State Radiation. *Phys.Rev.*, D76:092005, 2007. Erratum-ibid. D77:119902, 2008.
- [139] A. Kurz, T. Liu, P. Marquard, and M. Steinhauser. Hadronic contribution to the muon anomalous magnetic moment to next-to-next-to-leading order. *Phys.Lett.*, B734:144–147, 2014.
- [140] T. Blum, S. Chowdhury, M. Hayakawa, and T. Izubuchi. Hadronic light-by-light scattering contribution to the muon anomalous magnetic moment from lattice QCD. *Phys. Rev. Lett.*, 114(1):012001, 2015.
- [141] J. Green, O. Gryniuk, G. von Hippel, H.B. Meyer, and V. Pascalutsa. Lattice QCD calculation of hadronic light-by-light scattering. *Phys. Rev. Lett.*, 115(22):222003, 2015.
- [142] G. Colangelo, M. Hoferichter, A. Nyffeler, M. Passera, and P. Stoffer. Remarks on higher-order hadronic corrections to the muon $g-2$. *Phys.Lett.*, B735:90–91, 2014.
- [143] K. Hagiwara, R. Liao, A.D. Martin, D. Nomura, and T. Teubner. $(g-2)_\mu$ and $\alpha(M_Z^2)$ re-evaluated using new precise data. *J. Phys.*, G38:085003, 2011.
- [144] F. Jegerlehner. Leading-order hadronic contribution to the electron and muon $g-2$. *EPJ Web Conf.*, 118:01016, 2016.

- [145] S. Eidelman and F. Jegerlehner. Hadronic contributions to $(g - 2)$ of the leptons and to the effective fine structure constant $\alpha(M_Z^2)$. *Z.Phys.*, C67:585–602, 1995.
- [146] F. Jegerlehner. Hadronic vacuum polarization contribution to $g - 2$ of the leptons and $\alpha(M_Z)$. *Nucl. Phys. Proc. Suppl.*, 51C:131–141, 1996.
- [147] F. Jegerlehner. The Anomalous Magnetic Moment of the Muon. *Springer Tracts Mod.Phys.*, 226:1, 2008.
- [148] I. Levine et al. Measurement of the electromagnetic coupling at large momentum transfer. *Phys.Rev.Lett.*, 78:424–427, 1997.
- [149] M. Baak, J. Cúth, J. Haller, A. Hoecker, R. Kogler, K. Mönig, M. Schott, and J. Stelzer. The global electroweak fit at NNLO and prospects for the LHC and ILC. *Eur. Phys. J.*, C74:3046, 2014.
- [150] V.N. Baier and V.A. Khoze. Photon emission in muon pair production in electron - positron collisions. *Sov.Phys.JETP*, 21:629–632, 1965.
- [151] V.N. Baier and V.A. Khoze. Radiation accompanying two particle annihilation of an electron - positron pair. *Sov.Phys.JETP*, 21:1145–1150, 1965.
- [152] V. P. Druzhinin, S.I. Eidelman, S.I. Serednyakov, and E.P. Solodov. Hadron Production via e^+e^- Collisions with Initial State Radiation. *Rev. Mod. Phys.*, 83:1545, 2011.
- [153] H. Czyż and J.H. Kühn. Four pion final states with tagged photons at electron positron colliders. *Eur.Phys.J.*, C18:497–509, 2001.
- [154] G. Bonneau and F. Martin. Hard photon emission in e^+e^- reactions. *Nucl.Phys.*, B27:381–397, 1971.
- [155] G. Rodrigo, H. Czyż, J.H. Kühn, and M. Szopa. Radiative return at NLO and the measurement of the hadronic cross-section in electron positron annihilation. *Eur. Phys. J.*, C24:71–82, 2002.
- [156] National Communications System Technology & Standards Division. *Federal Standard 1037C*. General Services Administration Information Technology Service, 1996.
- [157] B. Aubert et al. The BaBar detector. *Nucl.Instrum.Meth.*, A479:1–116, 2002.
- [158] B. Aubert et al. The BABAR Detector: Upgrades, Operation and Performance. *Nucl.Instrum.Meth.*, A729:615–701, 2013.

- [159] A. Abashian, K. Gotow, N. Morgan, L. Piilonen, S. Schrenk, et al. The Belle Detector. *Nucl.Instrum.Meth.*, A479:117–232, 2002.
- [160] J.P. Lees et al. Time-Integrated Luminosity Recorded by the BABAR Detector at the PEP-II e^+e^- Collider. *Nucl.Instrum.Meth.*, A726:203–213, 2013.
- [161] P.A. Cherenkov. Visible luminescence of pure fluids induced by γ rays. *Doklady Akademii Nauk SSSR*, 2:451–454, 1934.
- [162] A.J. Bevan et al. The Physics of the B Factories. *Eur. Phys. J.*, C74:3026, 2014.
- [163] H. Czyż, J.H. Kühn, and A. Wapienik. Four-pion production in tau decays and e^+e^- annihilation: An Update. *Phys.Rev.*, D77:114005, 2008.
- [164] H. Czyż, A. Grzelinska, and J.H. Kühn. Narrow resonances studies with the radiative return method. *Phys.Rev.*, D81:094014, 2010.
- [165] E. Barberio and Z. Was. PHOTOS: A Universal Monte Carlo for QED radiative corrections. Version 2.0. *Comput.Phys.Commun.*, 79:291–308, 1994.
- [166] S. Jadach, B.F.L. Ward, and Z. Was. The Precision Monte Carlo event generator KK for two fermion final states in e^+e^- collisions. *Comput. Phys. Commun.*, 130:260–325, 2000.
- [167] T. Sjostrand. High-energy physics event generation with PYTHIA 5.7 and JETSET 7.4. *Comput.Phys.Commun.*, 82:74–90, 1994.
- [168] S. Brandt. *Statistical and Computational Methods in Data Analysis*. North-Holland Publishing Company, 2nd edition, 1983.
- [169] T. Hastie, R. Tibshirani, and J. Friedman. *The Elements of Statistical Learning: Data Mining, Inference, and Prediction*. Springer Series in Statistics. Springer New York, 2013.
- [170] T.G. Dietterich and G. Bakiri. Solving Multiclass Learning Problems via Error-Correcting Output Codes. *Journal of Artificial Intelligence Research*, 2:263, 1995.
- [171] I. Narsky and F.C. Porter. *Statistical analysis techniques in particle physics*. Wiley-VCH, Weinheim, Germany, 2014.
- [172] F. James. *Statistical Methods in Experimental Physics*. World Scientific Publishing, 2nd edition, 2006.

- [173] J.L. Fleiss, B. Levin, and M.C. Paik. *Statistical Methods for Rates and Proportions*. Wiley Series in Probability and Statistics. Wiley, 3rd edition, 2003.
- [174] S. Jadach and Z. Was. Koralb: An Upgrade to version 2.4. *Comput.Phys.Commun.*, 85:453–462, 1995.
- [175] S. Jadach and Z. Was. KORALB version 2.1: An Upgrade with TAUOLA library of τ decays. *Comput. Phys. Commun.*, 64:267–274, 1991.
- [176] S. Jadach and Z. Was. Monte Carlo Simulation of the Process $e^+e^- \rightarrow \tau^+\tau^-$ Including Radiative $\mathcal{O}(\alpha^3)$ QED Corrections, Mass and Spin Effects. *Comput. Phys. Commun.*, 36:191–211, 1985.
- [177] S. Jadach, Z. Was, R. Decker, and J.H. Kühn. The tau decay library TAUOLA: Version 2.4. *Comput. Phys. Commun.*, 76:361–380, 1993.
- [178] B. Aubert et al. Measurements of $e^+e^- \rightarrow K^+K^-\eta$, $K^+K^-\pi^0$ and $K_s^0K^\pm\pi^\mp$ cross- sections using initial state radiation events. *Phys.Rev.*, D77:092002, 2008.
- [179] G. D'Agostini. A Multidimensional unfolding method based on Bayes' theorem. *Nucl. Instrum. Meth.*, A362:487–498, 1995.
- [180] A. Höcker and V. Kartvelishvili. SVD Approach to Data Unfolding. *Nucl. Instrum. Meth.*, A372:469–481, 1996.
- [181] S. Schmitt. TUnfold, an algorithm for correcting migration effects in high energy physics. *JINST*, 7:T10003, 2012.
- [182] G.H. Golub and C.F. Van Loan. *Matrix Computations*. Johns Hopkins Studies in the Mathematical Sciences. Johns Hopkins University Press, 4th edition, 2013.
- [183] N.J. Higham. *Accuracy and Stability of Numerical Algorithms: Second Edition*. Society for Industrial and Applied Mathematics, 2002.
- [184] P.C. Hansen. The Truncated SVD as a Method for Regularization. *BIT Numerical Mathematics*, 27(4):534–553, 1987.
- [185] D.L. Phillips. A technique for the numerical solution of certain integral equations of the first kind. *J. ACM*, 9(1):84–97, January 1962.
- [186] A.N. Tikhonov. Solution of incorrectly formulated problems and the regularization method. *Soviet Math. Dokl.*, 4:1035–1038, 1963.

- [187] C.L. Lawson and R.J. Hanson. *Solving Least Squares Problems*. SIAM, 1995.
- [188] P.C. Hansen and D. Prost O’Leary. The Use of the L-Curve in the Regularization of Discrete Ill-Posed Problems. *SIAM Journal on Scientific Computing*, 14(6):1487–1503, 1993.
- [189] M. Caffo, H. Czyż, and E. Remiddi. Order- α^2 leading-logarithmic corrections in Bhabha scattering at LEP/SLC energies. *Phys. Lett.*, B327:369–376, 1994.
- [190] E. Jones, T. Oliphant, P. Peterson, et al. SciPy: Open source scientific tools for Python, 2001–. <http://www.scipy.org>.
- [191] T. Oliphant et al. NumPy: the fundamental package for scientific computing in Python, 1995–. <http://www.numpy.org>.
- [192] J. Kiefer. Sequential minimax search for a maximum. *Proceedings of the American Mathematical Society*, 4(3):pp. 502–506, 1953.
- [193] F. Jegerlehner. Electroweak effective couplings for future precision experiments. *Nuovo Cim.*, C034S1:31–40, 2011.
- [194] G. Ecker and R. Unterdorfer. Four-Pion Production in e^+e^- Annihilation. *Eur. Phys. J.*, C24:535–545, 2002.
- [195] B. Aubert et al. Observation of $e^+e^- \rightarrow \rho^+\rho^-$ near $\sqrt{s} = 10.58$ GeV. *Phys.Rev.*, D78:071103, 2008.
- [196] H. Czyż, A. Grzelinska, and J.H. Kühn. Charge asymmetry and radiative phi decays. *Phys.Lett.*, B611:116–122, 2005.
- [197] H. Czyż, A. Grzelinska, J.H. Kühn, and G. Rodrigo. Electron-positron annihilation into three pions and the radiative return. *Eur.Phys.J.*, C47:617–624, 2006.
- [198] R.R. Akhmetshin et al. $a_1(1260)\pi$ dominance in the process $e^+e^- \rightarrow 4\pi$ at energies 1.05 – 1.38GeV. *Phys. Lett.*, B466:392–402, 1999.
- [199] J. Humlíček. An efficient method for evaluation of the complex probability function: The voigt function and its derivatives. *Journal of Quantitative Spectroscopy and Radiative Transfer*, 21(4):309 – 313, 1979.
- [200] S.J. McKenna. A method of computing the complex probability function and other related functions over the whole complex plane. *Astrophysics and Space Science*, 107(1):71–83, 1984.

- [201] D. Bisello et al. e^+e^- annihilation into multi-hadrons in the 1350MeV - 2400MeV energy range. *Nucl. Phys. Proc. Suppl.*, 21:111–117, 1991.
- [202] M.N. Achasov et al. The Process $e^+e^- \rightarrow \omega\pi^0 \rightarrow \pi^0\pi^0\gamma$ up to 1.4GeV. *Phys. Lett.*, B486:29–34, 2000.
- [203] R.R. Akhmetshin et al. Study of the process $e^+e^- \rightarrow \omega\pi^0 \rightarrow \pi^0\pi^0\gamma$ in c.m. energy range 920MeV - 1380MeV at CMD-2. *Phys. Lett.*, B562:173–181, 2003.
- [204] M.N. Achasov et al. Updated measurement of the $e^+e^- \rightarrow \omega\pi^0 \rightarrow \pi^0\pi^0\gamma$ cross section with the SND detector. *Phys. Rev.*, D94:112001, 2016.
- [205] F.N. Fritsch and J. Butland. A method for constructing local monotone piecewise cubic interpolants. *SIAM Journal on Scientific and Statistical Computing*, 5(2):300–304, 1984.
- [206] M. Steffen. A simple method for monotonic interpolation in one dimension. *Astronomy and Astrophysics*, 239:443–450, 1990.
- [207] D.R. Kincaid and E.W. Cheney. *Numerical Analysis: Mathematics of Scientific Computing*. Brooks/Cole Publishing Company, 1991.
- [208] G.H. Golub and J.H. Welsch. Calculation of Gauss Quadrature Rules. *Mathematics of Computation*, 23(106):221–230 + s1–s10, 1969.
- [209] J.R. Rice. *Numerical Methods, Software, and Analysis*. Academic Press, 2nd edition, 1993.
- [210] M. Galassi, J. Davies, J. Theiler, B. Gough, G. Jungman, P. Alken, M. Booth, and F. Rossi. *GNU Scientific Library: Reference Manual*. Network Theory Ltd., 3rd edition, January 2009.
- [211] M. Davier, A. Hoecker, B. Malaescu, C.Z. Yuan, and Z. Zhang. Reevaluation of the hadronic contribution to the muon magnetic anomaly using new $e^+e^- \rightarrow \pi^+\pi^-$ cross section data from BABAR. *Eur.Phys.J.*, C66:1–9, 2010.
- [212] B. Aubert et al. Measurement of CP violating asymmetries in B^0 decays to CP eigenstates. *Phys. Rev. Lett.*, 86:2515–2522, 2001.
- [213] B. Aubert et al. Observation of the bottomonium ground state in the decay $\nu_{3S} \rightarrow \gamma\eta_b$. *Phys. Rev. Lett.*, 101:071801, 2008. [Erratum: *Phys. Rev. Lett.*102,029901(2009)].

- [214] E.B. Wilson. Probable inference, the law of succession, and statistical inference. *Journal of the American Statistical Association*, 22(158):209–212, 1927.
- [215] A. Agresti and B.A. Coull. Approximate is better than “exact” for interval estimation of binomial proportions. *The American Statistician*, 52(2):119–126, 1998.
- [216] L.D. Brown, T.T. Cai, and A. DasGupta. Interval estimation for a binomial proportion. *Statist. Sci.*, 16(2):101–133, 05 2001.
- [217] S. Zhang and J.M. Jin. *Computation of Special functions*. A Wiley-Interscience Publication. John Wiley, 1996.
- [218] T. Allmendinger et al. Track Finding Efficiency in BaBar. *Nucl. Instrum. Meth.*, A704:44–59, 2013.
- [219] J.P. Lees et al. Cross Sections for the Reactions $e^+e^- \rightarrow K^+K^-\pi^+\pi^-$, $K^+K^-\pi^0\pi^0$, and $K^+K^-K^+K^-$ Measured Using Initial-State Radiation Events. *Phys.Rev.*, D86:012008, 2012.